EFFECTS OF TERMINATION SHOCK ACCELERATION ON COSMIC RAYS IN THE HELIOSPHERE

U.W. Langner M.Sc.

Thesis accepted for the degree Philosophiae Doctor in Physics at the Potchefstroomse Universiteit vir Christelike Hoër Onderwys

Promoter: Prof. M.S. Potgieter

January 2004
Potchefstroom
South Africa

ABSTRACT

The interest in the role of the solar wind termination shock (TS) and heliosheath in cosmic ray (CR) modulation studies has increased significantly as the Voyager 1 and 2 spacecraft approach the estimated position of the TS. For this work the modulation of galactic CR protons, anti-protons, electrons with a Jovian source, positrons, Helium, and anomalous protons and Helium, and the consequent charge-sign dependence, are studied with an improved and extended two-dimensional numerical CR modulation model including a TS with diffusive shock acceleration, a heliosheath and drifts. The modulation is computed using improved local interstellar spectra (LIS) for almost all the species of interest to this study and new fundamentally derived diffusion coefficients, applicable to a number of CR species during both magnetic polarity cycles of the Sun. The model also allows comparisons of modulation with and without a TS and between solar minimum and moderate maximum conditions. The modulation of protons and Helium with their respective anomalous components are also studied to establish the consequent charge-sign dependence at low energies and the influence on the computed $\overline{\mathrm{p}}/\mathrm{p}$, e^-/p, and e^-/He. The level of modulation in the simulated heliosheath, and the importance of this modulation 'barrier' and the TS for the different species are illustrated. From the computations it is possible to estimate the ratio of modulation occurring in the heliosheath to the total modulation between the heliopause and Earth for the mentioned species. It has been found that the modulation in the heliosheath depends on the particle species, is strongly dependent on the energy of the CRs, on the polarity cycle and is enhanced by the inclusion of the TS. The computed modulation for the considered species is surprisingly different and the heliosheath is important for CR modulation, although 'barrier' modulation is more prominent for protons, anti-protons and Helium, while the heliosheath cannot really be considered a modulation 'barrier' for electrons and positrons above energies of ~150 MeV. The effects of the TS on modulation are more pronounced for polarity cycles when particles are drifting primarily in the equatorial regions of the heliosphere along the heliospheric current sheet to the Sun, e.g. the $A < 0$ polarity cycle for protons, positrons, and Helium, and the $A > 0$ polarity cycle for electrons and anti-protons. This study also shows that the proton and Helium LIS may not be known at energies $\lesssim$ 200 MeV until a spacecraft actually approaches the heliopause because of the strong modulation that occurs in the heliosheath, the effect of the TS, and the presence of anomalous protons and Helium. For anti-protons, in contrast, these effects are less pronounced. For positrons, with a completely different shape LIS, the modulated spectra have very mild energy dependencies $\lesssim$ 300 MeV, even at Earth, in contrast to the other species. These characteristic spectral features may be helpful to distinguish between electron and positron spectra when they are measured near and at Earth. These simulations can be of use for future missions to the outer heliosphere and beyond.

Keywords: cosmic rays, modulation, heliosphere, heliosheath, termination shock, protons, anti-protons, electrons, positrons, Helium.

OPSOMMING

Effekte van terminasieskokversnelling op kosmiese strale in die heliosfeer

Die belangstelling in die rol van die heliosferiese terminasieskok (TS) en die helioskil in studies van die modulasie van kosmiese strale het opmerklik toegeneem met die nadering van die verwagte skok posisie deur die Voyager ruimtetuie. Vir hierdie werk word die modulasie van galaktiese protone, anti-protone, elektrone met 'n Jupiter bron, positrone, Helium, en anomale protone en Helium, sowel as die gevolglike ladingsafhanklikheid bestudeer deur gebruik te maak van 'n verbeterde en uitgebreide twee-dimensionele numeriese kosmiese straal modulasie model wat 'n TS met diffuse skokversnelling, 'n helioskil en dryf insluit. Die modulasie word bereken deur van verbeterde lokale interstellêre spektra (LIS) vir die meeste van die genoemde spesies, sowel as nuwe fundamenteel afgeleide diffusie koëffisiënte, wat op 'n aantal kosmiese straal spesies toegepas kan word, gebruik te maak vir beide die magneetveld polariteit siklusse van die Son. Die model laat ook vergelykings toe van oplossings met en sonder die TS, asook tussen sonminimum en gematigde sonmaksimum kondisies. Die modulasie van protone en Helium met hul onderskeie anomale komponente word ook gebruik om die gevolglike ladingsafhanklikheid by lae energie en die invloed op die berekende $\bar{p}/p$, e^-/p, and e^-/He te bepaal. Die hoeveelheid modulasie in die gesimuleerde helioskil sowel as die belangrikheid van hierdie modulasie 'obstruksie' en die TS vir die genoemde spesies word geïllustreer. Uit hierdie berekeninge is dit moontlik om die hoeveelheid modulasie wat in die helioskil plaasvind te vergelyk met die totale modulasie tussen die LIS en die Aarde vir die verskillende spesies. Hierdie helioskil modulasie hang af van die tipe deeltjies, die energie van die deeltjies, asook die polariteitsiklus en word verhoog deur die insluiting van die TS. Dit word ook aangetoon dat die berekende modulasie vir die verskillende spesies verbasend verskillend is en dat die helioskil belangrik is vir modulasie, alhoewel 'obstruksie' modulasie meer prominent was vir protone, anti-protons en Helium, terwyl die helioskil waarskynlik nie as 'n modulasie 'obstruksie' vir elektrone en positrone gesien kan word by energie hoër as $\sim$150 MeV nie. Die effekte van die TS op modulasie is meer prominent vir deeltjies wat primêr in die ekwatoriale gebiede van die heliosfeer langs die neutrale vlak na die Son dryf, bv. die A < 0 polariteitsiklus vir protone, positrone en Helium, en die A > 0 polariteitsiklus vir elektrone en anti-protone. Hierdie studie toon aan dat die proton en Helium LIS onbekend sal bly vir energie $\lesssim$ 200 MeV totdat 'n ruimtetuig die interstellêre ruimte binnedring as gevolg van die groot modulasie wat voorkom in die helioskil, die effekte van die TS en die teenwoordigheid van die onderskeie anomale komponente. Hierdie effekte is egter minder prominent vir anti-protone. Aangesien die LIS van positrone verskillend is van dié van die ander spesies, het positrone se gemoduleerde spektra in kontras met die ander spesies 'n baie gematigde energie afhanklikheid $\lesssim$ 300 MeV, selfs by die Aarde. Hierdie karakteristieke spektraaleienskappe kan van groot nut wees om tussen elektron en positron spektra te onderskei wat gemeet word by en in die omgewing van die Aarde. Hierdie simulasie kan gebruik word vir toekomstige sendings na die buitenste heliosfeer.

Sleutelwoorde: kosmiese strale, modulasie, heliosfeer, helioskil, terminasieskok, protone, anti-protone, elektrone, positrone, Helium.

NOMENCLATURE

ACRs	Anomalous component of Cosmic Rays
ADI	Alternating Direction Implicit
AU	Astronomical Unit = 1.49×10^8 km
CIR	Corotating Interaction Region
CME	Coronal Mass Ejection
COSPIN	Cosmic and Solar Particle Investigation
CR	Cosmic Ray
DSN	Deep Space Network
e^-	Electron
e^+	Positron
GCR	Galactic Cosmic Ray
GMIR	Global Merged Interaction Region
HD	Hydrodynamic
He	Helium
He^+	Anomalous Helium
He^{++}	Galactic Helium
HCS	Heliospheric Current Sheet
HMF	Heliospheric Magnetic Field
ISM	Interstellar Medium
KET	Kiel Electron Telescope
LIS	Local Interstellar Spectra
LISM	Local Interstellar Medium
LOD	Locally One-Dimensional
MHD	MagnetoHydroDynamic
MIR	Merged Interaction Region
p	Proton
$\overline{p}$	Anti-proton
PDE	Partial Differential Equation
QLT	Quasi-Linear Theory
SEP	Solar Energetic Particle
TPE	Transport Equation
TS	Termination Shock
WCS model	Current sheet approach of Hattingh (1993)
1D	One-dimensional
2D	Two-dimensional
3D	Three-dimensional

TABLE OF CONTENTS

Chapter 1
Introduction

The interaction between energetically charged particles and the interplanetary medium reduces the cosmic ray intensity below the level of the local interstellar spectrum of a given cosmic ray species: the process known as heliospheric modulation. The study of cosmic ray modulation is mainly concerned with the description of the transport of these energetic particles in the region of space influenced by the Sun, known as the heliosphere. The modulation of cosmic rays in the heliosphere is described by the Parker (1965) transport equation which contains all the relevant physical processes. This transport equation is solved numerically, as a two-dimensional shock acceleration modulation model which is referred to as the TS model, to calculate the cosmic ray distribution throughout the heliosphere. The importance of the solar wind termination shock and the modulation that may occur in the heliosheath have recently been emphasized by cosmic ray observations of the Voyager spacecraft in the distant heliosphere (e.g., McDonald et al., 2000; Webber et al., 2001). Studying the role of the termination shock and that of the heliosheath on cosmic ray modulation with numerical models have become particularly relevant since Voyager 1 is in the vicinity of the termination shock (Stone and Cummings, 2003) or may have even crossed it (Krimigis et al., 2003). The main objective of this work is therefore to study the effects of the solar wind termination shock on the modulation, propagation and distribution of galactic electrons, positrons, protons, anti-protons, Helium, Jovian electrons, and anomalous protons and Helium in the heliosphere. In particular the following topics are discussed:

(1) The role, and origin, of diffusive shock acceleration at the solar wind termination shock of energetic particles in the heliosphere.

(2) The modifications and improvements made to existing two-dimensional shock acceleration numerical modulation models in order to develop a numerically stable state-of-the-art TS model within the constraints of computer memory and time.

(3) The differences in the modulation of a variety of cosmic ray species, studied with the same modulation parameters.

(4) How the inclusion of a termination shock in the model alters this modulation and the consequent charge-sign dependence of cosmic rays.

(5) How the inclusion of anomalous particles alters the modulation for protons and Helium.

(6) The kind of modulation effects to be expected near the termination shock and in the heliosheath, and in particular the study of the so-called modulation 'barrier' in the outer heliosphere.

(7) The effects of increased solar activity on the modulation of a variety of cosmic ray species.

In this study the application of the TS model to anti-protons and positrons is new, and also the application of the same set of modulation parameters and diffusion coefficients to study the modulation for a variety of cosmic ray and anomalous species. These solutions of the TS model are compared to some major observations in the heliosphere for solar minimum and moderate solar maximum activity to test the generality and to confirm that the TS model can indeed reasonably reproduce the modulation in the heliosphere for a variety of galactic and anomalous cosmic ray species, even when considering detailed features for protons like the cross-over of solar minima spectra for the two polarity epochs and very moderate latitudinal gradients that become even smaller with

increasing solar activity. Although the aim of this work has not been a detailed study of the diffusion coefficients or fitting observations, it will be shown that the chosen set gives reasonable comparisons to the observations for solar minimum conditions but for extreme solar maximum activity modifications seem necessary. The difference between minimum and moderate maximum conditions in this model is contained in the change of the current sheet 'tilt angle' from 10° to 75° as well as a change in the solar wind and changes in the values of perpendicular diffusion, where the latter implies decreasing drift with increasing solar activity.

The structure of this thesis is as follows:

In **Chapter 2** an overview is given of the basic features of the heliosphere and the basic theory of cosmic ray transport in the heliosphere. It starts with a description of cosmic rays and the heliosphere, discusses the cosmic ray transport equation, and describes the fundamental modulation processes. It is meant as a summary of several of the well known aspects of modulation theory that are applicable to this work.

Galactic cosmic rays have to cross various boundaries and regions on their way to a point of observation in the heliosphere, which can be the Earth or one of the current fleet of spacecraft. Beyond the heliopause, the Sun's magnetic field and the solar wind can no longer influence cosmic rays. Within this modulation boundary, modulation of cosmic rays takes place. In **Chapter 3** a discussion of the transport processes and mechanisms as they occur in the transport equation is given, together with a short overview of modulation models and a detailed discussion of the two-dimensional TS model that will be used throughout this work. Understanding these physical mechanisms and their consequences are one of the most important areas in cosmic ray modulation studies. A short overview of existing knowledge will also be given, in particular the diffusion and drift processes, and a suitable diffusion tensor is constructed, based mainly on the work of Burger et al. (2000).

In **Chapter 4** the characteristics and features of the improved and extended TS modulation model are discussed. This model is an improvement of existing locally developed two-dimensional shock acceleration models (e.g., Steenkamp, 1995; le Roux et al., 1996; Haasbroek, 1997; Steenberg, 1998). For an approximation of the heliospheric current sheet, which is essentially a three-dimensional effect, the current sheet approach (WCS model) of Hattingh (1993) (see also Hattingh and Burger, 1995a) is used to simulate the HCS in a two-dimensional heliosphere. In this chapter this WCS approach is revisited and rederived to be valid for all 'tilt angles' in a more general approach which was then incorporated into the TS model and compared to the WCS approach. The effects of different transitions of the solar wind velocity across the termination shock on the spectra of galactic protons will also be discussed in this chapter, together with the effect of the injection energy and the form of the injected source spectrum at the termination shock on anomalous proton spectra. The characteristics and features of this modified TS model will be illustrated as comparisons to some major observations, as it has been mentioned earlier.

In **Chapter 5** the modulation of galactic protons in the outer heliosphere is studied. In particular, the effects of the termination shock and the heliosheath on proton modulation at different energies, manifesting as a 'barrier' effect, for the two magnetic field polarity cycles, and also as modulation changes from minimum to moderate maximum conditions.

This study is extended in **Chapter 6** to include the modulation of cosmic ray anti-protons and anomalous protons; in **Chapter 7** to include cosmic ray electrons, with a Jovian source, and positrons; and in **Chapter 8** to include galactic and anomalous cosmic ray Helium. The modulation of anomalous protons and Helium are included to establish the consequent charge-sign dependence of $\bar{p}/p$, e^-/p, and e^-/He at low energies. The following topics are addressed in more detail in these chapters: (1) The effects of the termination shock on the modulation of

these species, for both heliospheric magnetic field polarity cycles, and as solar activity changes from minimum to moderate maximum conditions. (2) A comparison of the modulation of these species with and without a termination shock. (3) The level of modulation in the simulated heliosheath and the importance of this 'barrier' modulation for the different species and how this affects the computed $\overline{\mathrm{p}}/\mathrm{p}$, e^-/e^+, e^-/p, and e^-/He and (4) to establish the consequent charge-sign dependent effects by means of the computed ratios in (3). The application of a shock acceleration model in these chapters to anti-protons and positrons is new. Different isotopes for galactic Helium, and anti-Helium, have not been considered for this study.

Extracts from this thesis have been published as seven refereed manuscripts: Langner et al. (2003a, 2003b), Langner and Potgieter (2003a, 2003b), and Potgieter and Langner (2003a, 2003b, 2003c).

Three articles were published in conference proceedings: Langner and Potgieter (2001a, 2001b), and Langner et al. (2001a).

Other publications in which the author has been involved during his studies are: Langner (2000), Langner et al. (2001b), Potgieter et al. (2001a, 2001b), Ferreira et al. (2001e, 2001f), and Moskalenko et al. (2001).

Chapter 2
Cosmic rays and the heliosphere

2.1. Introduction

This chapter gives an overview of the basic features of the heliosphere and the theory of cosmic ray transport in the heliosphere. It starts with a description of cosmic rays and the heliosphere, discusses the cosmic ray transport equation, and describes the fundamental modulation processes. It is meant as a summary of several of the well-known aspects of modulation theory that are applicable to this thesis.

2.2. Cosmic rays in the heliosphere

Cosmic rays (CRs) are energetic particles which, after being accelerated to very high velocities, propagate throughout the galaxy. These particles were discovered by Viktor Hess during the historic balloon flights in 1911 and 1912 (Hess, 1911, 1912) when it was shown that the origin of these particles was extraterrestial. These particles were called 'cosmic rays' by Millikan in 1925. By 1930 Compton and Clay had shown that these particles were electrically charged (for a review see e.g., Simpson, 1997). Galactic cosmic rays (GCRs), which are accelerated during supernova explosions, are distributed in energy from a few hundred keV to as high as 3×10^{21} eV in the form of a power law $j \propto E^{-\gamma}$ with $\gamma \approx 2.6$ the spectral index, E the kinetic energy in MeV.nuc^{-1} and j the differential intensity typically in units of particles.m^{-2}.s^{-1}.sr^{-1}.MeV^{-1} (e.g., Longair, 1990; Jokipii and Kóta, 1997; Baring, 1999). For $E > 10^{15}$ GeV the CR proton spectrum exhibits a break and becomes steeper with $\gamma \approx 3.1$. This break is known as the 'knee' of the spectrum. The reason for the occurrence of this 'knee' is believed to be a less efficient mechanism of galactic CR acceleration in supernova shocks. At these energies, a particle's gyroradius starts to exceed the thickness of the shock. These particles are generally referred to as GCRs, because of their origin outside the heliosphere. For $E < 20$ GeV, CRs measured at Earth have $\gamma \neq 2.6$ because of solar modulation effects in the heliosphere. Those particles that arrive at Earth are composed of ~98% nuclei, that have been stripped of all their orbital electrons, and ~2% electrons and positrons. In the energy range from 100 MeV (corresponding to a velocity for protons of ~43% of the speed of light) to 10 GeV (corresponding to a velocity for protons of ~99.6% of the speed of light), the nuclear component consists of ~87% Hydrogen, ~12% Helium and ~1% heavier nuclei (e.g., Simpson, 1992). CRs can generally be grouped into different populations, i.e.:

(1) GCRs originating from far outside our solar system. These particles are accelerated during supernova explosions, and it is generally believed that the subsequent blast wave is responsible for the acceleration (see a detailed review by Jones and Ellison, 1991). The supernova blast wave origin was first inferred by Axford et al. (1977), Bell (1978a, 1978b), Blandford and Ostriker (1978) and Krymski (1977). Experimental evidence of this was found by Koyama et al. (1995) and confirmed by Tanimori et al. (1998).

(2) Solar energetic particles (SEPs) originating from solar flares (e.g., Forbush, 1946). Coronal mass ejections (CMEs) and shocks in the interplanetary medium can also produce these energetic particles. SEPs may have energies up to several hundred MeV but are usually observed at Earth only for several hours when occurring. These particles are disregarded for the purpose of this study. For a review see Cliver (2000).

(3) The anomalous component of cosmic rays (ACRs). These particles are interstellar neutral atoms which get

singly ionized relatively close to the Sun. They are then transported to and accelerated at the solar wind termination shock through a process of first order Fermi acceleration, gaining energy by multiple crossings of the TS. This process was first discussed by Pesses et al. (1981). This population of the ACRs was first identified as an increased flux of He^+ (Helium) and O^+ (Oxygen) particles in spectra measured by the Pioneer 10 spacecraft by Garcia-Munoz et al. (1973a), while Fisk et al. (1974) first suggested their heliospheric origin. Some aspects of the modulation of these particles will be revisited in Chapters 4, 6 and 8. For a review see Fichtner (2001).

(4) The Jovian electrons. It was discovered with the Jupiter fly-by of the Pioneer 10 spacecraft in 1973 that the Jovian magnetosphere at ~5 AU (one astronomical unit = 1.49×10^8 km, the average distance between the Sun and Earth) in the equatorial region is a relatively strong source of electrons with energies up to at least ~30 MeV (Simpson et al., 1974; Teegarden et al., 1974; Chenette et al., 1974). These electrons, when released into the interplanetary medium, dominate these low energy electron intensities within the first ~10 AU and could even undergo diffusive shock acceleration at the TS to reach substantial higher energies (e.g., Jokipii and Kóta, 1991; Moraal et al., 1991 ; Haasbroek, 1997; Haasbroek et al., 1997a, 1997b; Ferreira et al., 2001e, 2001g; Ferreira, 2002; Potgieter and Langner, 2003c).

2.3. The Sun and solar activity

The Sun is a typical star of intermediate size and luminosity with radius $r_\odot \simeq 696\,000$ km (~0.005 AU). The Sun has a differential rotational period that increases with latitude from an average of 25 days at the equator up to even 32 days near the poles. This odd behavior is because the Sun is not a solid body like the Earth but rather a large 'sphere of plasma' that is gravitationally bound and compressed. This compression permits sustained high temperatures and densities in the core that allow a thermonuclear reaction to continue. Energy from the core radiates and convects out to the solar atmosphere where it escapes into space. The Sun is composed of mostly Hydrogen (~90 %) and Helium (~10%) with traces of heavier elements such as Carbon, Nitrogen and Oxygen. The visible solar surface over the convective zone is called the photosphere. Above the photosphere there are two transparent layers: The chromosphere, visible during eclipses, which extends some 10 000 km above the photosphere and the corona which is observable beyond the chromosphere for more than 10^6 km.

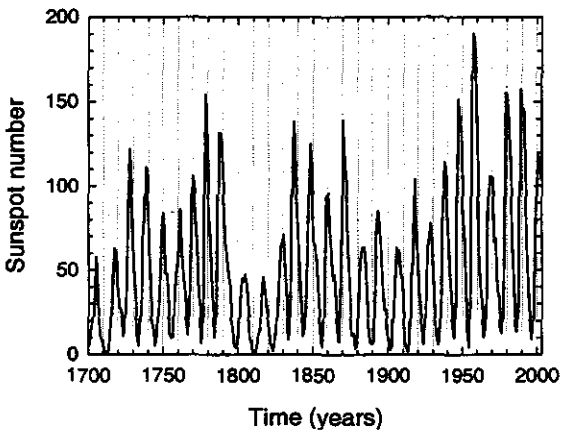

Figure 2.1. Yearly averaged sunspot number from the year 1700 up to 2003 (data from http://www.spaceweather.com).

Visible on the photosphere are sunspots as dark areas of irregular shape that are cooler than the rest of the surface. Strong magnetic fields are also associated with them. Detailed records of the sunspot numbers, which are direct indications of the level of solar activity, have been kept since 1749 and are shown in Figure 2.1 up to the end of 2003. From these observations of the yearly averaged values it is evident that the Sun has a quasi-periodic ~11 year cycle which is called a solar activity cycle. It is well established that CRs are modulated in anti-phase with solar activity. Every ~11 years the Sun moves through a period of fewer and smaller sunspots which is called 'solar minimum' followed by a period of larger and more sunspots which is called 'solar maximum' (Smith and Marsden, 2003).

The plasmatic atmosphere of the Sun constantly blows away from its surface to maintain equilibrium (Parker, 1958, 1963). This is possible because temperatures in the corona are so high that the solar material is not gravitationally bound to the Sun. The escaping hot coronal plasma from the Sun is called the solar wind and will be discussed in more detail in the following sections. Convective motions, along with solar rotation, create the Sun's magnetic field. The solar wind carries the solar magnetic field into interplanetary space, forming the heliospheric magnetic field (HMF) which is mostly responsible for the modulation of CRs in the heliosphere.

2.4. The geometry of the heliosphere

The region of space filled by the plasma originating from the Sun and transported outward through the solar wind is called the heliosphere. A simplistic understanding of the heliosphere is that the solar wind flows radially outward from the Sun and blows a spherical 'bubble' that continually expands. However, the interstellar space is not empty and contains matter in the form of the local interstellar medium (LISM). If there is a significant pressure in the LISM, the expansion of the solar wind must eventually stop, resulting is a quasi-static 'bubble' (for an overview see Fichtner and Scherer, 2000). The heliosphere can be seen as a giant laboratory, provided by nature where we can directly observe and measure physical parameters that reveal phenomena that cannot be scaled down to terrestrial laboratories.

A schematic representation of the heliosphere is shown in Figure 2.2 (adapted from Jokipii, 1989). It is a view of the heliospheric equatorial plane with respect to which the ecliptic plane, wherein most of the major planets rotate around the Sun, is tilted. As the heliosphere moves through the LISM, it forces the LISM to flow around it. The solar wind must merge with the LISM surrounding the heliosphere. At large radial distances the LISM pressure causes the supersonic solar wind plasma to decrease to subsonic speeds in order for the solar wind ram pressure to match the interstellar thermal pressure. A heliospheric shock is created, which is called the solar wind termination shock (TS), because the internal wave speed suddenly becomes larger than the plasma propagation speed as has first been suggested by Parker (1961). This TS is indicated by the dashed circle in Figure 2.2 and together with the heliosheath, the region between the TS and the outer boundary/heliopause, are prominent and interesting features of the heliosphere (e.g., Burlaga et al., 2003; Florinski et al., 2003). Therefore studying the role of the TS and that of the heliosheath on cosmic ray modulation with numerical models is the main topic of this study and has become most relevant since Voyager 1 is in the vicinity of the TS (Stone and Cummings, 2003) or may have even crossed it (Krimigis et al., 2003). Estimates for the position of the TS vary between ~70 AU and ~100 AU (e.g., Stone et al., 1996; Whang and Burlaga, 2000), but present consensus is that the TS should be between 80 AU and 90 AU (e.g., Stone and Cummings, 2001). The position of the outer boundary/heliopause is uncertain, probably at least 30-50 AU beyond the TS. The distance of the TS also varies over the solar cycle because of changes in the dynamic

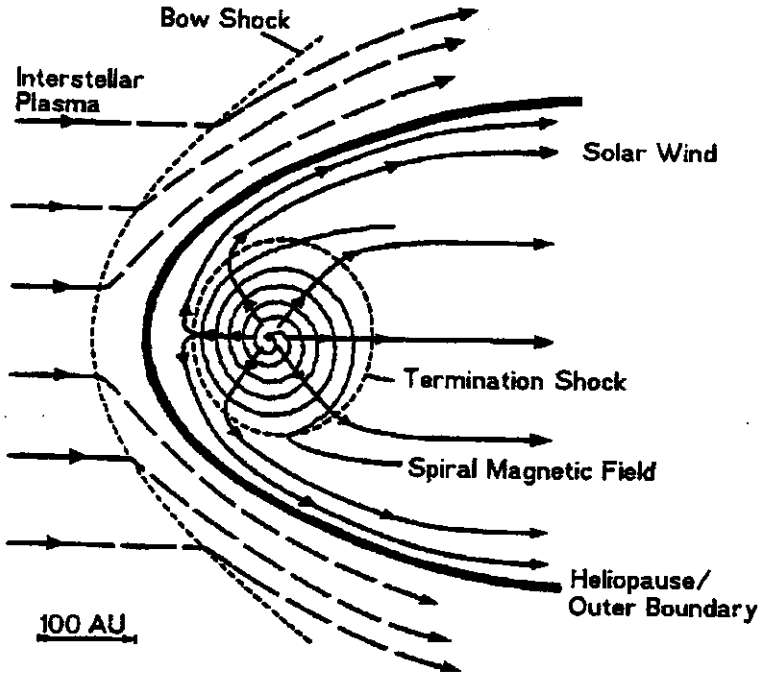

Figure 2.2. A representation of the heliosphere and its interaction with the local interstellar medium (adapted from Jokipii, 1989).

pressure of the solar wind, with the maximum distance predicted to occur near solar minimum (e.g., Whang and Burlaga, 2000). This distance has not yet been measured directly but is calculated using various methods that include: (1) Extrapolating observed CR gradients, (2) pressure balance calculations, (3) modulation models, (4) gas-dynamic models of the interaction of the solar wind and the LISM, (5) radio emissions from the heliopause triggered by the dissipation of large CR decreases in the heliopause, (6) comparing Lyman-α light scattering from neutral Hydrogen in the upwind and downwind direction, (7) solar wind velocity observations and (8) observations of the ACRs. In Table 2.1 (from Stone and Cummings, 2001) estimates of the location of the TS by various authors are shown. As is evident from this table and recent Voyager 1 observations (Stone and Cummings, 2003; Krimigis et al., 2003) the assumed TS location of $r_s = 90$ AU as is used in this work is a reasonable estimate.

Table 2.1: Estimates of the termination shock radius (r_s)

DynamicPressureBalance	r_s (AU)
Belcher et al. (1993)	78 - 105
Gloeckler et al. (1997)	$\leq$ 85
Pauls and Zank (1996, 1997)	88, 95
Linde et al. (1998)	80 ● 10
Exarhos and Moussas (2000)	88, 103
Radio Emissions	
Gurnett and Kurth (1996)	80 - 115
Zank et al. (2001)	$\leq$ 90
Hydrogen Ly-α Backscattering	
Hall et al. (1993)	70 - 105
Gradients of the ACRs	
Stone and Cummings (1999)	84 $\pm$ 5
Cosmic Ray Transients	
McDonald et al. (2000)	88.5 $\pm$ 7
Webber et al. (2001)	83 $\pm$ 1

Obviously the geometry of the TS, certainly that of the heliosphere, should be affected by the relative motion of the heliosphere through the LISM. Beyond the TS, the solar wind plasma flow direction is forced to change, causing the interstellar plasma and solar wind plasma flow directions to be equal. This is indicated in Figure 2.2 by the thick solid line which is considered by most researchers as the outer boundary/heliopause of the heliosphere. Beyond this boundary the Sun has no significant influence on CRs.

Current estimates for the distance from the Sun to the heliopause vary between ~90 AU to ~180 AU and are summarized in Table 2.2. In this study the position of the heliopause is assumed to be at 120 AU which seems a reasonable value. Larger values are most probable but available computer resources are then a serious limiting factor.

Table 2.2: Estimates of the outer boundary radius (r_b)

	r_b (AU)
Williams and Potgieter (1991)	> 90
Gurnett et al. (1993)	116 - 177
Czechowski and Grzedzielski (1993)	100 - 120
Krainev and Webber (1993)	> 120
Gurnett and Kurth (1995)	110 - 160
Lockwood and Webber (1995)	78 - 88
Pauls et al. (1995)	122
Whang et al. (1995)	150
Florinski et al. (2003)	165 - 255
Scherer and Fahr (2003)	100 - 139
Zank and Müller (2003) - 1 shock approach	110 ± 6
Zank and Müller (2003) - 2 shock approach	140 ± 5

Because of the heliosphere's motion through the LISM, a bow shock may also be formed outside the heliopause with the region between this shock and the heliopause known as the outer heliosheath (e.g., Ratkiewicz and Ben-Jaffel, 2002). In this study the heliosphere is assumed to be spherical. A modulation model with a more realistic non-spherical heliospheric boundary geometry (as indicated in Figure 2.2) was locally developed by Haasbroek and Potgieter (1998). They have found that the magnitude of the calculated CR intensity changes, when it is compared to a spherical boundary, which ranges between just 10% and 20% depending on the position in the heliosphere, indicating that the model solutions are not sensitive to this feature (see also Fichtner et al., 1996). A comprehensive review of the global properties of the heliosphere was given by e.g., Suess (1990).

2.5. Anomalous cosmic rays

The discovery of the anomalous component of cosmic rays by Garcia-Munoz et al. (1973a, 1973b, 1973c) has provided a powerful new tool with which the heliosphere can be probed. Soon thereafter, in addition to the Helium discovered by Garcia-Munoz, anomalous Oxygen (Hovestadt et al., 1973), Nitrogen (McDonald et al., 1974), and neon (von Rosenvinge and McDonald, 1975) were observed. Fisk et al. (1974) recognized that these elements all have high first ionization potentials and therefore they proposed that these elements enter the heliosphere as interstellar neutrals because of the movement of the heliosphere in its trajectory through interstellar space. These elements then penetrate deeply into the heliosphere before they become singly ionized by charge exchange with the solar wind ions, electron collisions, or photo-ionization.

These singly-ionized atoms are then picked up by the solar wind and convected outwards towards the outer heliosphere, where they undergo shock acceleration. Some of these accelerated charged particles may then diffuse

into the heliosphere, where they are modulated by the same processes as the galactic component, to form the anomalous component of cosmic rays.

Möbius et al. (1985) obtained the first conclusive evidence of the solar wind picking up singly-ionized interstellar Helium (He^+), using a time-of-flight spectrometer. According to Möbius (1986) the kinetic energies of these pick-up ions vary from basically zero to approximately four times the flow energy of the solar wind. Fisk (1986) reviewed a variety of acceleration mechanisms for these particles. However, the main problem with most of these mechanisms is that both the curvature cutoff and the acceleration time scale limit the acceleration efficiency. Pesses et al. (1981) proposed that the TS might accelerate these pick-up ions to sufficiently high energies. This remains the most plausible explanation for the source of the ACRs.

2.6. Heliospheric modulation of cosmic rays

CRs are subject to physical processes that change their distribution and intensity in position, energy, and time throughout the heliosphere. These major processes were combined by Parker (1965) into a time-dependent transport equation (TPE)

$$\frac{\partial f}{\partial t} = \nabla \cdot (\mathbf{K}_S \cdot \nabla f) - (\mathbf{V}^* + \mathbf{v}_d).\nabla f + \frac{1}{3}(\nabla \cdot \mathbf{V}^*)\frac{\partial f}{\partial \ln p} + \frac{1}{p^2}\frac{\partial}{\partial p}\left(p^2 D_{pp}\frac{\partial f}{\partial p}\right) + Q_{source}(\mathbf{r}, p, t), \tag{2.1}$$

to describe the transport and modulation of CRs in the heliosphere, by using a coordinate system rotating with the Sun. Here $f(\mathbf{r}, p, t)$ is the omnidirectional CR distribution function, with $\mathbf{r}$ the position and p the particle's momentum at time t, $\mathbf{V}^*$ the solar wind velocity in the corotating frame with $\mathbf{V}^* = \mathbf{V} - \mathbf{\Omega} \times \mathbf{r}$ where $\mathbf{\Omega}$ is the rotational velocity of the Sun, $\mathbf{K}_S$ the symmetric part of the diffusion tensor $\mathbf{K}$ and $Q_{source}(\mathbf{r}, p, t)$ a source function describing any CR source in the heliosphere. The most important modulation processes are convection by the solar wind (second term in Equation 2.1), and diffusion (first term in Equation 2.1) of CRs through scattering by irregularities in the HMF. The solar wind expands radially outward, causing the solar wind particle density, and therefore the density of the magnetic scattering centres, to decrease with radial distance from the Sun, so that CRs also undergo adiabatic cooling (deceleration) (fourth term in Equation 2.1). This fourth term of the TPE is also very important because shock acceleration at the TS appears implicitly through this term (Section 2.7.6). Since CRs are charged particles, they experience drift motions (third term in Equation 2.1) because of gradients in magnetic field magnitude, the curvature of the field or any abrupt changes in the field direction. For completeness, a term describing so-called second-order Fermi acceleration may also be added (fifth term in Equation 2.1). This describes diffusion in momentum space because of randomly moving magnetic irregularities, causing a net acceleration because particles have a slightly higher chance to collide with approaching scattering centres than with receding ones. The process is called second-order, because it can be shown that the average momentum gain per scattering is proportional to (plasma speed/particle speed)^2.

The averaged guiding center drift velocity for a near isotropic CR distribution is given by

$$\mathbf{v}_d = \nabla \times (\kappa_A \mathbf{e}_B), \tag{2.2}$$

with $\mathbf{e}_B = \mathbf{B}/B$ and B the magnitude of the modified background HMF and κ_A the 'drift coefficient'. The factor D_{pp} in the momentum diffusion term is given by

$$D_{pp} = \frac{p^2 V_A^2}{4\varsigma\kappa_{\|}}. \tag{2.3}$$

Here V_A is the Alfvèn velocity in the solar wind plasma, given by

$$V_A = \frac{B}{\sqrt{\mu_0 \rho}} \tag{2.4}$$

with $\varsigma \gtrsim 1$ (e.g. Gombosi et al., 1989), $\kappa_{\parallel}$ the diffusion coefficient parallel to the background HMF, ρ the density, and μ_0 the permeability of free space. This term is potentially important in CR transport, especially in regions with strong magnetic fields and small plasma densities, such as near the Sun or in the downstream region of a magnetohydrodynamic (MHD) shock. Even so, this term is quite small in comparison to the others and, therefore, it is usually omitted in most heliospheric CR transport models as in this study.

The distribution function $f(\mathbf{r}, p, t)$ is related to the differential intensity j_R, in units of particles.m^{-2}.s^{-1}.sr^{-1}.MeV^{-1} by $j_R = R^2 f$, where $R = pc/q$ is rigidity (in units of GV) with q the particle's charge and c the speed of light in space. The differential number density, $U_p(\mathbf{r}, p, t)$, is also related to $f(\mathbf{r}, p, t)$ by

$$f(\mathbf{r}, p, t) = \frac{U_p(\mathbf{r}, p, t)}{4\pi p^2}. \tag{2.5}$$

The diffusion tensor, $\mathbf{K}$, for a coordinate system with one axis parallel to the average magnetic field, $\mathbf{B} = B_0 \mathbf{e}_z$, and the other two perpendicular to it is

$$\begin{aligned} \mathbf{K} &= \begin{bmatrix} \kappa_{\parallel} & 0 & 0 \\ 0 & \kappa_{\perp,polar} & \kappa_A \\ 0 & -\kappa_A & \kappa_{\perp,radial} \end{bmatrix} \\ &= \mathbf{K}_S + \mathbf{K}_A \\ &= \begin{bmatrix} \kappa_{\parallel} & 0 & 0 \\ 0 & \kappa_{\perp,polar} & 0 \\ 0 & 0 & \kappa_{\perp,radial} \end{bmatrix} + \begin{bmatrix} 0 & 0 & 0 \\ 0 & 0 & \kappa_A \\ 0 & -\kappa_A & 0 \end{bmatrix} \end{aligned} \tag{2.6}$$

with $\kappa_{\perp,polar} = \kappa_{\perp\theta}$ and $\kappa_{\perp,radial} = \kappa_{\perp r}$ the diffusion coefficients describing the diffusion perpendicular to the average magnetic field in the polar and radial directions respectively, with $\mathbf{K}_S$ and $\mathbf{K}_A$ the symmetrical and anti-symmetrical parts, respectively.

Equation 2.1 contains all the relevant physics to describe CR transport and acceleration in the heliosphere. In this work it is solved numerically in two different modulation models, one with and one without a TS, to calculate the CR distribution throughout the heliosphere. These models will be discussed in the following chapters. Important aspects of Equation 2.1 and how they are incorporated into the modulation models are also discussed in the following sections. The relevant diffusion coefficients for CRs in the heliosphere and the numerical solving of Equation 2.1 to create a modulation model are discussed in the next chapter.

2.7. The solar wind

The solar wind (originally called the 'solar corpuscular radiation') was first proposed by Bierman (1951, 1961) to account for the behaviour of comet tails that always pointed directly away from the Sun regardless of the position of the comet. Biermann has found that the pressure of the solar radiation alone can not explain his observation and has suggested that the solar wind always exists and effects the formation of comet tails. Biermann's estimates of the solar wind speed, V, ranged between 400 - 1000 km.s^{-1} which was remarkably accurate. However, the name 'solar wind' was first introduced by Parker (1958). Parker (1963) showed that the atmosphere of the Sun could only be in equilibrium if the atmosphere was expanding at supersonic speeds. For a review see Marsch et al. (2003).

Observations over many years have revealed that $V = |\mathbf{V}|$ is not uniform over all latitudes and can be divided into the fast solar wind and the slow solar wind. The basic reason is that the Sun's magnetic field dominates the

original outflow of the solar wind (e.g., Smith, 2000). If the solar magnetic field is perpendicular to the radial outflow of the solar wind it can prevent the outflow. This is usually the case at low solar latitudes where the near Sun magnetic field lines are parallel to the Sun's surface. These field lines are in the form of loops which begin and end on the solar surface and stretch around the Sun to form the streamer belts. These streamers belts are regarded as the most plausible sources of the slow solar wind speed which have typical velocities of up to $V = 400$ km.s^{-1} (Schwenn, 1983; Marsch, 1991; Withroe et al., 1992). Other indications are that the slow solar wind speed may arise from the edges of large coronal holes or from smaller coronal holes (e.g., Hundhausen, 1977 and references therein).

In regions where the solar magnetic field is directed radially outward, such as at the solar polar regions, the magnetic field will assist rather than oppose the coronal outflow. The fast solar wind speed with characteristic velocities of up to $V = 800$ km.s^{-1} are associated with polar coronal holes which are located at the higher heliographic latitudes (Krieger et al., 1973; Zirker, 1977 and references therein). In these regions the magnetic field lines are carried off by the solar wind and their connection to the Sun at the one end of the field line is lost. It is these open magnetic field lines which affect the transport of CRs in the heliosphere. The fast solar wind from the polar regions can sometimes extend close to the equator and overtake the earlier emitted slow stream, resulting in a corotating interaction region (CIR); for a review see Odstrcil (2003).

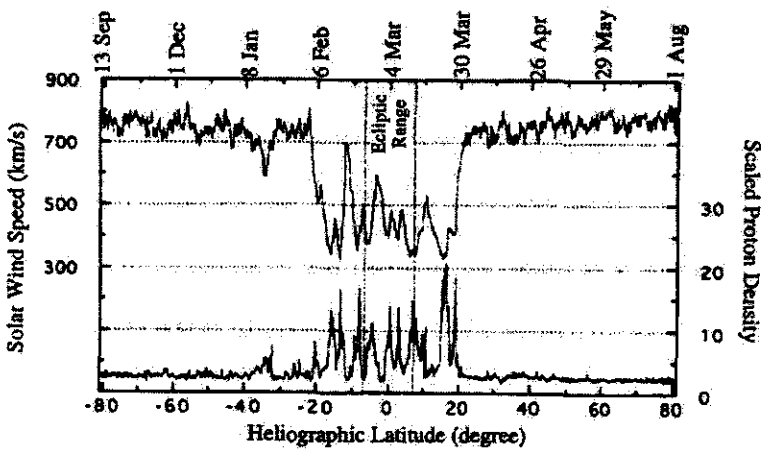

Figure 2.3. Six-hour average solar wind speed (top curve) for the pole-to-pole transit of Ulysses from the peak southerly latitude of -80.2° on 12 September 1994, to the corresponding northerly latitude on 31 July 1995. The proton density is shown by the bottom curve (adapted from Phillips et al., 1995).

The latitude dependence of V has been confirmed by Ulysses (e.g., Phillips et al., 1994; 1995) and is shown in Figure 2.3 as six hour averages during the fast pole to pole transit of Ulysses. Evident from Figure 2.3 is the significant variations of V with heliolatitude where Ulysses has observed a high solar wind speed, 700 - 800 km.s^{-1}, at $\gtrsim$ 20° S. In the ~20° S to the ~20° N band it observed medium to slow speeds, to increase again to a speed between 700 - 800 km.s^{-1} at $\gtrsim$ 20° N thus confirming the existence of the fast and slow solar wind streams during solar minima. For solar maxima no well-defined high speed solar wind is observed (e.g., Richardson et al., 2001).

The radial dependence of **V** between 0.1 AU and 1.0 AU was studied by e.g., Kojima et al. (1991) and Sheeley et al. (1997). They have found that both the low and high speed winds accelerate within 0.1 AU of the Sun and become a steady flow at 0.3 AU. Using measurements from e.g. Pioneer 10 and 11 and Voyagers 1 and 2, Gazis et

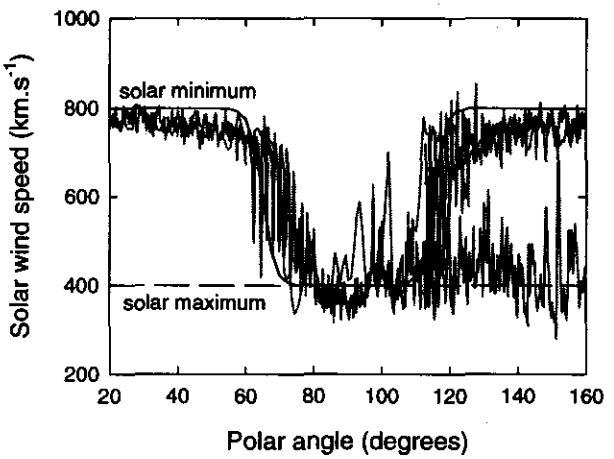

Figure 2.4. The modelled solar wind speed V as a function of polar angle for $r \geq 0.3$ AU for solar minimum (solid line) and solar maximum (dashed line). In comparison V as measured by Ulysses is shown (e.g., Phillips et al., 1995; McComas, 2000).

al. (1994) and Richardson et al. (2001) have found that the slow averaged solar wind speed does not vary with distance up to 50 AU. However, it does show a solar cycle dependence with values about 20% higher during solar minimum than during solar maximum. At solar maximum there is a mixture of high speed and low speed winds in the region of the equator (Gazis et al., 1991) so that the picture is not as clear.

To model the solar wind velocity $\mathbf{V}$ in the axially symmetric modulation model that is used in this work, it is assumed that

$$\mathbf{V}(r,\theta) = V(r,\theta)\mathbf{e}_r = [V(r)V(\theta)]\mathbf{e}_r \tag{2.7}$$

where r is the radial distance usually in AU, θ the polar angle and $\mathbf{e}_r$ the unit vector component in the radial direction. The latitude dependence $V(\theta)$ of the solar wind velocity during solar minimum conditions is similar to that which is given by e.g., Hattingh (1998), although some of the coefficients have been modified to give a better fit to the available observations and is given by

$$V(\theta) = 1.5 \mp 0.5 \tanh\left[16.0(\theta - \frac{\pi}{2} \pm \varphi)\right], \tag{2.8}$$

with all angles in radians in the northern (top signs) and southern (bottom signs) hemispheres respectively with $\varphi = \alpha + 15\pi/180$. Here, α is the angle between the Sun's rotation and magnetic axes known as the tilt angle. The effect of φ is to determine at which polar angle V start to increase from 400 km.s^{-1} towards 800 km.s^{-1}. In Figure 2.4 these solar wind speeds as given by Equation 2.8 for solar minimum and moderate solar maximum conditions are shown in comparison with V as measured by Ulysses (e.g., Phillips et al., 1995; McComas, 2000) for corresponding conditions. It follows from Figure 2.4 that for moderate solar maximum conditions no latitudinal dependence is assumed, so that $V(\theta) = 1.0$ under these conditions. Equation 2.8 therefore gives a realistic latitude dependence of the solar wind for both solar minimum and moderate solar maximum conditions. For solar minimum conditions the solar wind speed changes from ~400 km.s^{-1} in the equatorial plane ($\theta = 90°$) to ~800 km.s^{-1} in the polar regions ($\theta = 0°$). This increase of a factor of 2 is assumed to happen in the whole heliosphere for $120° \leq \theta \leq 60°$.

The radial dependence $V(r)$ of the solar wind is given as

$$V(r) = V_0\left\{1 - \exp\left[\frac{40}{3r_0}(r_\odot - r)\right]\right\}, \tag{2.9}$$

inside the shock, with $V_0 = 400$ km.s^{-1}, $r_\odot = 0.005$ AU, and $r_0 = 1$ AU. From this equation follows that the acceleration of the solar wind occurs rather rapidly close to the Sun and reaches V_0 at ~0.3 AU. For heliospheric modulation models without a shock Equation 2.9 has been used, but for a model with a TS, Equation 2.9 obviously needs to change which will be discussed in the following section.

2.8. The solar wind termination shock and shock acceleration

A supersonic flow cannot decelerate into a subsonic flow in a continuous way. Thus, the supersonic flow energy must be dissipated discontinuously. This discontinuity in supersonic flow to subsonic flow is called a shock.

Consider a household sink with a running tap. The stream of water coming from the tap hits the bottom of the sink and the water flows more or less radially away from that point. Practically all the kinetic and potential energy that the stream of water has when it comes from the tap is now converted into kinetic energy and this fluid flow on the sink bottom is faster than the spread of small amplitude waves on the water surface, i.e. 'supersonic'. This flow energy in the sink is now dissipated by cohesive and viscous frictional forces and the flow energy drops so low that the flow has to undergo a shock transition to become subsonic. The surplus flow energy is converted into turbulence beyond the shock (Jokipii and McDonald, 1995).

The solar wind presents us with a similar problem. The super sonic solar wind, originating on the Sun, must merge with the LISM surrounding the heliosphere. It must, however, first undergo a transition from a supersonic into a subsonic flow at the TS, in order for the solar wind ram pressure to match the interstellar thermal pressure. A shock is created because the internal wave speed suddenly becomes larger than the plasma propagation speed. As in the hydrodynamic equivalent, the surplus flow energy is converted into thermal energy and turbulence beyond the shock. The TS was first suggested by Parker (1961). At the lowest level of complexity the termination shock is expected to be a fast mode MHD shock which is attempting to propagate sunward against the solar wind flow. It is therefore a reverse shock, so that the upstream side is closest to the Sun and the downstream side is further from the Sun. Accordingly, the solar wind plasma should be compressed, heated, deflected, and slowed across the shock, while the magnetic field should increase. At a more complex level, the ACRs and GCRs may have sufficient energy density to modify the termination shock from being a primarily MHD shock to being a CR-modified shock, as has been suggested by the pressure of CRs being comparable to the pressure in magnetic turbulence, dust, and any other effects (Donohue and Zank, 1993; Zank et al., 1994; Zank, 1999). This might affect the detailed shock structure, including the compression ratio of the plasma density on both sides of the shock, and the locations of the shock and heliopause.

The process of acceleration of CRs at the TS is called diffusive shock acceleration (Axford et al., 1977; Bell 1978a, 1978b; Krymski, 1977). Because the HMF is not smooth but turbulent on both sides of the shock, there exist scattering points on both sides which may scatter particles various times across the shock until they reach substantial higher energies to escape. These scattering mechanisms will be discussed further below.

2.8.1. A hydrodynamic analysis

Astrophysical shocks have much in common with hydrodynamic shocks because of the fluid like models describing highly ionized plasmas. Many physical quantities and characteristics are therefore shared between these shocks. Thus, to define and derive the shock properties, it is instructive to start with an ordinary hydrodynamic shock. See e.g. Jones and Ellison (1991) for a more detailed discussion on this subject.

The velocity of a disturbance in a fluid is conveniently described by the Mach number

$$M = \frac{V}{c_s}, \tag{2.10}$$

with c_s the speed of longitudinal pressure waves which is given by

$$c_s = \sqrt{\frac{\gamma_g P}{\rho}}, \tag{2.11}$$

where $\gamma_g = C_P/C_V$, with C_P and C_V the heat capacity at a constant pressure and volume respectively, P the pressure of the solar wind plasma and ρ the mass density. Consider a coordinate system in one dimension where a shock is fixed at $x = 0$ in this frame. The upstream (unshocked - denoted by 1) flow at $x < 0$ goes into the shock with supersonic velocity V_1, or Mach number

$$M_1 = \frac{V_1}{c_s} > 1. \tag{2.12}$$

The downstream (shocked - denoted by 2) plasma, at $x > 0$, recedes with subsonic Mach number

$$M_2 = \frac{V_2}{c_s} < 1. \tag{2.13}$$

The mass, momentum, and energy flux across the shock must be conserved. These can be written as

$$\frac{\partial}{\partial x}(\rho V) = 0 \text{ mass flux}, \tag{2.14}$$

$$\frac{\partial}{\partial x}\left(\rho V^2 + P\right) = 0 \text{ momentum flux}, \tag{2.15}$$

and

$$\frac{\partial}{\partial x}\left(\frac{1}{2}\rho V^3 + \frac{\gamma_g}{\gamma_g - 1} V P\right) = 0 \text{ energy flux}, \tag{2.16}$$

respectively. If these equations are integrated across the shock, the so-called Rankine-Hugoniot conditions on the shock are obtained, namely

$$\rho_1 V_1 = \rho_2 V_2, \tag{2.17}$$

$$\rho_1 V_1^2 + P_1 = \rho_2 V_2^2 + P_2, \tag{2.18}$$

and

$$\frac{1}{2}V_1^2 + \frac{\gamma_g}{\gamma_g - 1}\frac{P}{\rho_1} = \frac{1}{2}V_2^2 + \frac{\gamma_g}{\gamma_g - 1}\frac{P}{\rho_2}. \tag{2.19}$$

The compression ratio or shock ratio of the shock for non-relativistic flows is now defined to be

$$s = \frac{\rho_2}{\rho_1} = \frac{V_1}{V_2}. \tag{2.20}$$

After a considerable amount of algebra with Equations 2.17, 2.18 and 2.19, the compression ratio and pressure may be written in terms of the upstream Mach number as (e.g., Ferraro and Plumpton, 1966)

$$s = \frac{\left(\gamma_g + 1\right) M_1^2}{\left(\gamma_g - 1\right) M_1^2 + 2}, \tag{2.21}$$

and

$$P_2 = P_1\left[1 + \gamma_g M_1^2\left(1 - \frac{1}{s}\right)\right]. \tag{2.22}$$

It is evident that for incoming flow speeds that are at the sound speed (i.e., $M_1 = 1$), $s = 1$ and $P_2 = P_1$; there is no shock. It would appear that for $M_1 < 1$ an expansion shock would be possible with $s < 1$ and $P_2 < P_1$, but such a transition would involve a decrease of entropy rather than an increase, therefore such transitions would be ruled out by the second law of thermodynamics. For a strong shock ($M_1 \longrightarrow \infty$) the compression ratio reduces to

$$s = \frac{\gamma_g + 1}{\gamma_g - 1}. \tag{2.23}$$

For monatomic, non-relativistic gases, such as the solar wind plasma, $\gamma = C_P/C_V = 5/3$ and, therefore, the compression ratio of a strong shock is $s = 4$.

2.8.2. Astrophysical MHD shocks

MHD shocks are defined as shocks in media that contain magnetic fields. In this case the relevant magnetic field pressure and energy terms must be added to Equations 2.18 and 2.19. Since an ionized gas or plasma has a high conductivity any magnetic field will be tied to the plasma (i.e., 'frozen in') and will, in general, contribute to the dynamics of the shock. When the magnetic field is parallel to the normal on the shock front and therefore in the same direction as the plasma flow, the MHD shock is called parallel. In this case the field is continuous across the shock and it has no effect on the shock structure. The field's only role is to support the Alfvèn waves that act as the 'glue' between the plasma and the energetic particles that are being accelerated. In oblique shocks (shocks with an angle between the upstream magnetic field and the shock normal greater than 0°), the magnetic field takes a more active role and influences both the shock jump conditions and particle acceleration. In this case the field also leads to modifications of the standard Rankine-Hugoniot conditions and the shock parameters (for details see Jones and Ellison, 1991).

In Astrophysics there are many examples of systems that project large amounts of plasma at supersonic velocities. Some of these are stellar and galactic winds, and the shell of matter projected by a supernova explosion. More locally, astrophysical shocks may be found in places such as the bow shock of Earth in the solar wind, and travelling interplanetary shocks at the leading and trailing edges of CIRs, merged interaction regions (MIRs) and global merged interaction regions (GMIRs). For a review see Jones and Ellison (1991).

2.8.3. First-order Fermi shock acceleration

Second-order Fermi acceleration cannot account for the effective acceleration of cosmic rays in the heliosphere since D_{pp}, as is given by Equation 2.3, is so small. However, if a MHD shock is present in a diffusive convective system, first-order Fermi acceleration does accelerate particles with great effectiveness, even if it does not appear explicitly in the transport equation that is given by Equation 2.1. This effect was discovered in 1977 (Axford et al., 1977; Bell, 1978a, 1978b; Blandford and Ostriker, 1978; Krymski, 1977), and the spectrum resulting from this acceleration is derived below (see also Steenkamp, 1995).

The fundamental starting point in such an analysis concerns the continuity properties of the density and streaming across the shock. Since particles have mobility across the shock, the first of these is that the differential CR number density or the omnidirectional distribution function of particles (Equation 2.5) must be continuous across the shock, i.e.

$$U_p^- = U_p^+ \tag{2.24}$$

or

$$f^- = f^+ \tag{2.25}$$

where the minus sign represents the upstream region and the plus sign the downstream region or

$$f^- = \lim_{r \to r_s} f(r) \tag{2.26}$$

and

$$f^+ = \lim_{r \leftarrow r_s} f(r). \tag{2.27}$$

Similarly, the condition on the streaming recorded by a stationary observer must be such that

$$\nabla.\mathbf{S}_p = Q, \tag{2.28}$$

where $\mathbf{S}_p$ is the differential particle current density, with

$$\begin{aligned} \mathbf{S}_p &= CVU_p - \mathbf{K}.\nabla U_p \\ &= -4\pi p^2 \left(\frac{\mathbf{V}}{3} \frac{\partial f}{\partial \ln p} + \mathbf{K}.\nabla f \right), \end{aligned} \tag{2.29}$$

where $\mathbf{K}$ is the diffusion tensor as is given by Equation 2.6, $\mathbf{V}$ the velocity of the scattering centres in the solar wind relative to a stationary observer and C the Compton-Getting factor (e.g., Gleeson and Axford, 1968), given by

$$\begin{aligned} C &= 1 - \frac{1}{3U_p} \frac{\partial}{\partial p}(pU_p) \\ &= -\frac{1}{3} \frac{\partial \ln f}{\partial \ln p}. \end{aligned} \tag{2.30}$$

Equation 2.28 states that the flux that diverges from the shock must have its origin at a source on the shock. In a one-dimensional case, or where the flux is perpendicular to the shock face, this second condition (Equation 2.28) simply reduces to

$$S^+ + S^- = \lim_{\varepsilon \to 0} \int_{r_s - \varepsilon}^{r_s + \varepsilon} Q dr. \tag{2.31}$$

Consider now an one-dimensional, steady-state plane MHD shock in the shock frame at $x = 0$, and assume that sufficient scattering centers exist on both sides of the shock to keep $f(\mathbf{r}, p, t)$ isotropic to the first order. Under sufficient simplifying assumptions, the TPE can be solved across this shock:

In one dimensional steady-state ($\partial f / \partial t = 0$), ignoring drifts, and for isotropic scattering, the TPE (Equation 2.1) reduces to

$$\frac{\partial}{\partial x} \left[Vf - K \frac{\partial f}{\partial x} \right] - \frac{1}{3p^2} \left(\frac{\partial V}{\partial x} \right) \frac{\partial}{\partial p} \left(p^3 f \right) = Q_f(x, p) \tag{2.32}$$

with K the diffusion coefficient in one dimension, while the streaming density is

$$S_p = -4\pi p^2 \left[\frac{Vp}{3} \frac{\partial f}{\partial p} + K \frac{\partial f}{\partial x} \right]. \tag{2.33}$$

If the upstream flow velocity and the diffusion coefficient are independent of x, the TPE becomes a simple linear differential equation,

$$\left(\frac{\partial^2}{\partial x^2} - \frac{V}{K} \frac{\partial}{\partial x} \right) f = \frac{Q_f(x, p)}{K}. \tag{2.34}$$

This equation has a simple solution which depends on how the source is treated. Assume that f is known far upstream of the shock, denoted by $f(-\infty, p)$, and that on the shock it is $f(0, p)$. Then, if the source is a delta function on the shock, i.e. $Q_f(x, p) = Q_*(p)\,\delta(x)$, the solution in the down stream medium is

$$f(x, p) = f(-\infty, p) + [f(0, p) - f(-\infty, p)] e^{Vx/K}. \tag{2.35}$$

If the source is distributed throughout the upstream medium, the solution is

$$\begin{aligned} f(x, p) &= f(-\infty, p) + [f(0, p) - f(-\infty, p)] e^{Vx/K} \\ &\quad + \frac{1}{V} \left[\left(1 - e^{Vx/K} \right) \int_x^{-\infty} Q_f dx - e^{Vx/K} \int_0^x Q_f \left(1 - e^{-Vx/K} \right) dx \right]. \end{aligned} \tag{2.36}$$

The shape of the spectrum on the shock, $f(0, p)$, is determined by the two continuity conditions given by Equations 2.25 and 2.28. For a delta function source on the shock, these conditions imply

$$\frac{V_1 p}{3} \frac{\partial f(0, p)}{\partial p} + K_1 \left(\frac{\partial f(0, p)}{\partial x} \right)^- = \frac{V_2 p}{3} \frac{\partial f(0, p)}{\partial p} + K_2 \left(\frac{\partial f(0, p)}{\partial x} \right)^+ + Q_*, \tag{2.37}$$

while for the distributed source at $x < 0$ it is

$$\frac{V_1 p}{3}\frac{\partial f(0,p)}{\partial p} + K_1\left(\frac{\partial f(0,p)}{\partial x}\right)^- = \frac{V_2 p}{3}\frac{\partial f(0,p)}{\partial p} + K_2\left(\frac{\partial f(0,p)}{\partial x}\right)^+. \tag{2.38}$$

To solve the problem analytically, one assumes a no-diffusion situation beyond the shock, or $K_2 = 0$. Under these circumstances the matching conditions become

$$\frac{V_1 - V_2}{3} p\frac{\partial f(0,p)}{\partial p} = -K_1\left(\frac{\partial f(0,p)}{\partial x}\right)^-. \tag{2.39}$$

From Equation 2.36 we can now calculate $\partial f(x,p)/\partial x$,

$$\frac{\partial f(x,p)}{\partial x} = \frac{V}{K}[f(0,p) - f(-\infty,p)]e^{Vx/K} - \frac{1}{K}e^{Vx/K}\left[\int_0^{-\infty} Q_f dx - \int_0^x e^{-Vx/K}Q_f dx\right]. \tag{2.40}$$

To obtain an expression for $(\partial f(0,p)/\partial x)^-$ take $K = K_1$ at $x < 0$,

$$\left(\frac{\partial f(0,p)}{\partial x}\right)^- = \frac{V}{K_1}[f(0,p) - f(-\infty,p)] - \frac{1}{K_1}\int_0^{-\infty} Q_f dx. \tag{2.41}$$

From Equation 2.39, we therefore have

$$\frac{V_1 - V_2}{3} p\frac{\partial f(0,p)}{\partial p} = -V_1[f(0,p) - f(-\infty,p)] + \int_0^{-\infty} Q_f dx. \tag{2.42}$$

If $s = V_1/V_2$ and $q = 3s/(s-1)$ then

$$\frac{\partial f(0,p)}{\partial p} + \frac{q}{p}f(0,p) = \frac{q}{p}\left[f(-\infty,p) + \frac{1}{V_1}\int_0^{-\infty} Q_f dx\right], \tag{2.43}$$

with the solution

$$f(0,p) = qp^{-q}\int_0^p \left[f(-\infty,p') + \frac{1}{V_1}\int_0^{-\infty} Q_f(x,p')dx\right] p'^{q-1}dp'. \tag{2.44}$$

Similarly, if one takes the simpler case of a source on the shock, Equations 2.35 and 2.37 give

$$f(0,p) = qp^{-q}\int_0^p \left[f(-\infty,p') + \frac{Q_*(p')}{V_1}\right] p'^{q-1}dp'. \tag{2.45}$$

Since Equation 2.34 is linear, Equations 2.44 and 2.45 may be added, or the problem may have been done in unison. The kernel of the combined expression is

$$f(-\infty,p') + \frac{1}{V_1}\left[\int_0^{-\infty} Q_f(x,p')dx + Q_*\right]. \tag{2.46}$$

This shows that a pre-existing spectrum far ahead of the shock, a source in the upstream medium (which has been produced for instance by travelling interplanetary shocks), or a source on the shock itself, will produce the same accelerated spectrum.

The spectrum in the downstream medium is homogeneous and equal to the spectrum on the shock, i.e. $f(x,p) = f(0,p), x > 0$. The spectrum infront of the shock falls off exponentially to the value of the spectrum at $x = -\infty$, i.e.

$$f(x,p) = \begin{cases} f(0,p) & \text{if } x \geq 0 \\ f(-\infty,p) + [f(0,p) - f(-\infty,p)]e^{V_1 x/K_1} & \text{if } x < 0 \end{cases} \tag{2.47}$$

Consider as an example a mono-energetic source function at the shock, i.e.

$$\frac{Q_*(p)}{V_1} = \frac{N_0}{4\pi p^2}\delta(p - p_0) \text{ and } f(-\infty,p) = 0.$$

If one keeps in mind that

$$\int_0^{\infty} 4\pi p^2 \frac{Q_*(p)}{V_1}dp = N_0,$$

the accelerated spectrum that is given by Equation 2.45 becomes

$$\begin{aligned} f(0,p) &= qp^{-q}\int_0^p \frac{N_0}{4\pi p'^2}\delta(p'-p_0)dp' \\ &= \frac{N_0}{4\pi p_0^3}q\left(\frac{p}{p_0}\right)^{-q}, \end{aligned} \tag{2.48}$$

i.e., a power law with the spectral index

$$q = \frac{3s}{s-1}. \tag{2.49}$$

Diffusive shock acceleration resulting from an infinite plane shock always gives rise to a power law spectrum with the spectral index given by Equation 2.49, that depends only on the compression ratio of the shock.

In practice, shocks are seldom plane or stationary. The power law 2.48 can only be achieved up to such a value of momentum as there is time for the particles to reach this momentum. From, e.g. Axford (1981), Drury (1983), and Lagage and Cësarsky (1983) it follows that the acceleration time that is needed for the establishment of the steady-state solution from momentum p_0 to p is given by

$$\tau_a = \frac{3}{V_1 - V_2}\int_{p_0}^{p}\left(\frac{K_1}{V_1}+\frac{K_2}{V_2}\right)\frac{dp'}{p'}. \tag{2.50}$$

Above that momentum the spectrum cuts off sharply. Similarly, in a curved shock there is a curvature cutoff in the spectrum. This occurs at the point where the diffusive length scale κ/V, becomes larger than the shock radius (r_s), or

$$\frac{K_1}{V_1}+\frac{K_2}{V_2} > r_s. \tag{2.51}$$

From Equation 2.48 it also follows that

$$f \propto p^{-q},$$

but

$$f \propto \frac{U_p}{p^2},$$

and

$$p \propto \sqrt{E}.$$

Thus

$$U_p \propto p^{-q+2} \propto E^{\frac{-q+2}{2}}. \tag{2.52}$$

Therefore, from Equation 2.49 and 2.52 it is evident that for a strong shock ($s = 4$) the differential intensity must be proportional to E^{-1}.

2.8.4. Geometry of the TS

A uniform and spherically symmetric solar wind, and a uniform interstellar gas pressure on all sides of the heliosphere, would result in a spherical symmetric shock at a constant radius around the Sun. Since the solar wind velocity rises towards the polar directions at solar minimum, the flow energy is larger in these regions (see Figure 2.4). Assuming a uniform interstellar gas pressure, this flow energy will not be dissipated as quickly as in the ecliptic plane. This will effectively destroy the spherical nature of the shock, turning it into something that can be better described by an ellipsoid with its major axis through the solar poles and its minor axis in the solar rotational plane (e.g., Suess, 1993; Pauls and Zank, 1997; Scherer and Fahr, 2003; Zank and Müller, 2003).

The localized high-velocity solar wind streams will cause localized bulges in the shock face where it reaches the termination shock, pushing the shock further back. This will give the shock an uneven character. In addition to this, the solar wind velocity is not constant with time, resulting in a structure which probably oscillates back and forth from almost spherically symmetric at solar maximum to an ellipsoid at solar minimum.

The motion of the heliosphere through the interstellar medium creates a larger ram pressure in the direction of motion and a smaller pressure in the opposite direction. This means that the flow energy of the solar wind will be dissipated faster in the direction of the motion than in the opposite direction, and thus the shock face will be nearer to the Sun in the direction of motion and further out on the other side. A spherical shock will thus be deformed into an ovoid (see e.g., Scherer and Fahr, 2003; Zank and Müller, 2003).

All these factors contribute to the possible asymmetric nature of the termination shock structure. Such asymmetries will, however, not be included in this thesis so that a purely spherical TS is assumed.

2.8.5. Structure of the solar wind at and beyond the TS

Parker (1963) showed that the solar wind must be accelerated to supersonic speeds very close to the Sun, while remaining independent of radial distance up to the point where it undergoes a shock transition to subsonic speeds. For the model which is developed in this thesis a TS is assumed at $r_s = 90$ AU with a compression ratio $s = 3.2$, and a shock precursor scale length of $L = 1.2$ AU. For the precursor scale length in front of the shock, V decreases, for example, in the equatorial plane from the upstream value of V_1 according to the relationship (le Roux et al., 1996)

$$V(r) = \frac{V_1(s+1)}{2s} - \frac{V_1(s-1)}{2s} \tanh\left(\frac{r - r_s}{L}\right). \tag{2.53}$$

This means that up to the shock, $V(r)$ decreases by $0.5s$ starting at L, then abruptly as a step function to the downstream value, in total to V_1/s, as has been shown in Figure 2.5. It was shown by Potgieter and Langner (2003a, 2003b) that s could be decreased in this model to explain the disappearance of the anomalous component at solar maximum activity. This is, however, beyond the scope of this work. In Chapter 5 to 8 it will be argued that a compression ratio of $s = 4$ is highly unlikely.

At the TS the solar wind plasma will be compressed, heated, deflected, and slowed across the shock, while the magnetic field will increase by a factor of s as is shown in the following section. This compression, or increase in pressure (P), implies the increase of the plasma density (ρ), i.e. $P = v^2\rho$ with v the speed of the particles. In the heliosheath the flow of the solar wind is also subsonic and therefore, together with the increase in density, it can be assumed to be incompressible, because $\partial\rho/\partial t \ll \rho\nabla \cdot \mathbf{V}$ to a first approximation. From the continuity equation for the plasma density, given by

$$\frac{\partial \rho}{\partial t} + \nabla \cdot (\rho \mathbf{V}) = 0, \tag{2.54}$$

it follows that

$$\begin{aligned} \frac{1}{r^2}\frac{\partial}{\partial r}\left(r^2 \rho V\right) &= 0 \Rightarrow \\ \frac{\rho}{r^2}\frac{\partial}{\partial r}\left(r^2 V\right) &= 0 \Rightarrow \\ r^2 V &= \text{constant} \end{aligned} \tag{2.55}$$

implying that $V(r)$ decreases further as

$$V(r) \propto 1/r^2 \tag{2.56}$$

to the outer boundary (see also le Roux et al., 1996). This means that a fully radial flow will be divergence free in the heliosheath region leading to interesting phenomena which will be discussed in more detail in Chapter 4. This divergence free $\mathbf{V}$ can obviously not continue to the heliospheric boundary because of changes in the direction of $\mathbf{V}$ near the boundary (see Figure 2.2), resulting in a flow that is not radial. This characteristic was however not incorporated into the present numerical TS modulation model so that Equation 2.56 was used as a first-order

approximation.

In the following chapter it will be shown that the TS model developed for this work can be used with a continuous, discontinuous, quasi-discontinuous (Figure 2.5) or constant (no shock) transition of the solar wind speed at the location of the TS. The effects of each of these transitions on the heliospheric modulation of CRs and the reasons for the chosen structure, the quasi-discontinuous transition, will also be illustrated and discussed in Chapter 4 together with the properties of the TS model.

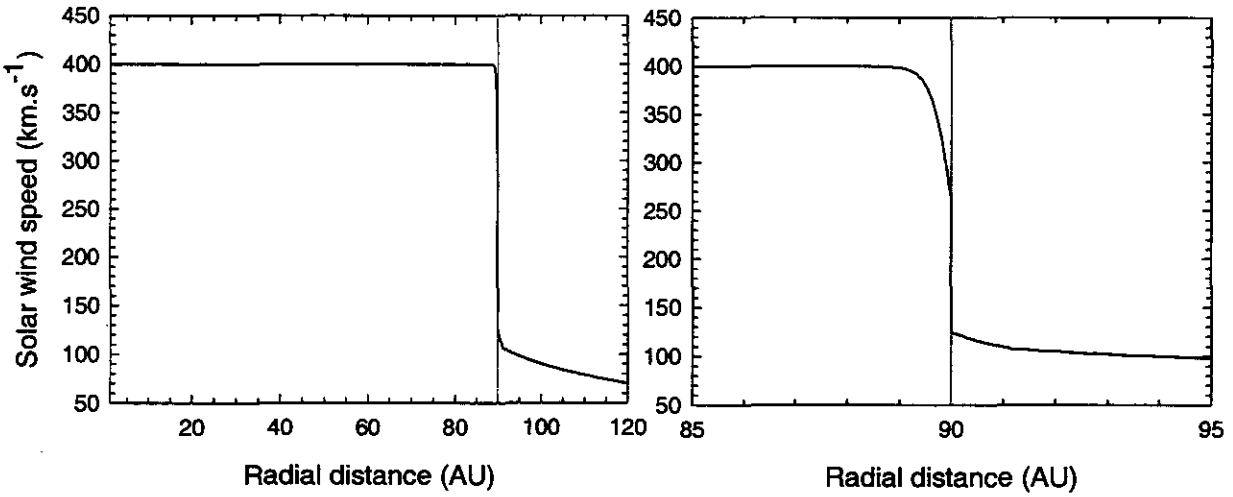

Figure 2.5. The slow solar wind speed as function of radial distance from Earth to the heliospheric boundary (left panel) and enlarged in the vicinity of the TS at $r_s = 90$ AU (right panel).

2.8.6. Divergence of the solar wind velocity

From the divergence and the structure of V given by Equations 2.9, 2.53, and 2.56 it is evident that the heliosphere can be divided into three regions, which are given by

$$\begin{aligned} \varrho &> 0 \text{ if } r < r_s \text{ (upstream region)}, \\ \varrho &< 0 \text{ if } r_s - L \leq r \leq r_s \text{ (shock region)}, \end{aligned}$$

and,

$$\varrho = 0 \text{ if } r > r_s \text{ (downstream region or heliosheath)}$$

if

$$\begin{aligned} \varrho &= \frac{1}{3}(\nabla \cdot \mathbf{V}) \\ &= \frac{1}{3}\left(\frac{\partial V(r,\theta)}{\partial r} + \frac{2}{r}V(r,\theta)\right), \end{aligned} \tag{2.57}$$

for the two-dimensional (2D) case. Equation 2.57 therefore implies different energy processes associated with these regions, i.e. adiabatic deceleration in the upstream region and shock acceleration in the shock region, while the assumed incompressibility of $\mathbf{V}$ in the heliosheath leads to the divergence free $\mathbf{V}$ in this region. Shock acceleration at the TS is therefore implicitly included in the TPE through the divergence of $\mathbf{V}$. This characteristic will be exploited further in the next chapter and throughout this work.

2.9. The heliospheric magnetic field

One of the most fundamental properties of the heliosphere is that its magnetic field is convected outward with the solar wind. The heliosphere is magnetodynamically embedded in the interstellar medium. This magnetic field determines the transport of energetic particles, such as CRs. For reasonably smooth fields, charged particles are compelled to follow the magnetic field lines. The net behavior of the many such particles in a plasma, therefore, depends upon the magnetic field line configuration. Every ~11 years, during maximum solar activity, the magnetic polarity of the Sun alternates to give rise to a ~22-year magnetic polarity cycle.

The heliosphere is dominated at solar minimum conditions by the influence of high speed solar wind originating from two well developed polar coronal holes on the Sun, with a relatively narrow streamer belt of low speed solar wind close to the equatorial regions. Most heliospheric magnetic field lines have their origin in the coronal holes and are swept out into the heliosphere by the solar wind (e.g., Balogh et al., 1995). The open magnetic field lines from the fast solar wind regions are descending to low latitudes above the current sheet (which will be discussed in the following section). Closed field lines in the streamer belts are lines which begin and end on the Sun. In this work we are interested in the global magnetic field of the Sun, typically the open magnetic field lines which are 'dragged' into the heliosphere by the solar wind and are called the heliospheric magnetic field. At a certain radial distance the open magnetic field lines become approximately radial. This distance is called the coronal source surface which lies at a heliocentric distance of about $2.5r_{\odot}$ (e.g., Wang and Sheeley, 1995).

2.9.1. The Parker magnetic field

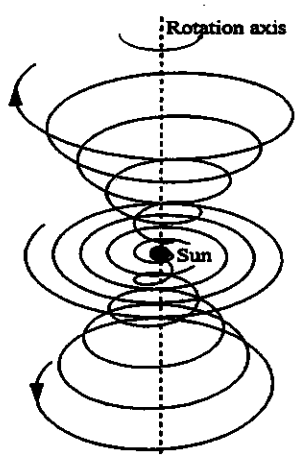

Figure 2.6. An idealized representation of the HMF spiral structure according to Parker (1958) with the Sun at the origin of the spirals. Spirals at 45°, 90° and 135° rotate around the polar axis. The equatorial plane is at 90° (adapted from Hattingh, 1998).

The solar rotation winds the HMF into a spiral in and away from the Sun's equatorial plane, which is called the Parker spiral. An analytical equation for the Parker spiral for $r \geq r_{\odot}$ as being first derived by Parker (1958) can be described by the expression

$$\mathbf{B} = B_0 \left(\frac{r_e}{r}\right)^2 (\mathbf{e}_r - \tan\psi \mathbf{e}_\phi) \left[1 - 2H(\theta - \theta')\right], \tag{2.58}$$

where $\mathbf{e}_r$ and $\mathbf{e}_\phi$ are unit vector components in the radial and azimuthal direction respectively, B_0 is a constant, $\left[1 - 2H(\theta - \theta')\right]$ determines the polarity of the magnetic field, $r_e = 1$ AU is the radial distance of Earth from the

Sun, θ' is the polar position of the heliospheric current sheet (HCS), H is the Heaviside step function, and ψ the spiral angle of the HMF with

$$\tan\psi = \frac{\Omega(r - r_\odot)\sin\theta}{V} = \Gamma. \tag{2.59}$$

Here $\Omega = 2.67\times10^{-6}$ rad.s^{-1} is the angular speed of the Sun. A three-dimensional representation of the Parker HMF is shown in Figure 2.6. The spirals in this figure rotate around the polar axis with $\theta = 45°, \theta = 90°$ and $\theta = 135°$.

The spiral angle ψ is the angle between the radial direction and the direction of the average HMF at a certain position. It gives an indication of how tightly wound the HMF spiral is. Typically $\psi = 45°$ at Earth and it increases with r to $\psi \approx 90°$ when $r \gtrsim 10$ AU in the equatorial plane. The value of B_0 is determined in such a way that the HMF has a magnitude of 5 nT at Earth. The Heaviside step function in Equation 2.58 is given by

$$H(\theta - \theta') = \begin{cases} 0, & \theta < \theta' \\ 1, & \theta > \theta' \end{cases}. \tag{2.60}$$

This function causes the HMF to change direction when crossing the HCS.

The magnitude of the Parker HMF throughout the heliosphere is given by

$$B = B_0 \left(\frac{r_e}{r}\right)^2 \sqrt{1+\Gamma^2}, \tag{2.61}$$

for a heliospheric modulation model without a TS. For a heliospheric modulation model containing the TS, the solar wind velocity is given by Equation 2.7, with Equation 2.9 in the upstream region, Equation 2.53 at the shock and Equation 2.56 in the down stream region, so that Equation 2.59 becomes

$$\tan\psi' = \frac{\Omega(r - r_\odot)\sin\theta}{V'} = \frac{s\Omega(r - r_\odot)\sin\theta}{V_0}\left(\frac{r}{r_s}\right)^2 = s\tan\psi\left(\frac{r}{r_s}\right)^2 = \Gamma' \tag{2.62}$$

in the downstream region, i.e., the field becomes even more tightly wound. In the upstream region Equation 2.59 does not change, because V is the same as for a model without a TS. The magnitude of the field in the downstream region is then

$$B' = B_0 \left(\frac{r_e}{r}\right)^2 \sqrt{1 + \left(s\tan\psi\left(\frac{r}{r_s}\right)^2\right)^2}. \tag{2.63}$$

Thus, at the poles where $\tan\psi \longrightarrow 0$ the field is continuous as required by Maxwell's equations and $B = B'$. While in the equatorial regions, where $\tan\psi \gg 1$ the field strength jumps by a factor s at the TS position.

Deviations from the Parker spiral, especially over the heliospheric poles, may occur (i.e., Forsyth et al., 1996). It therefore has become standard practise to use modulation models which modify the HMF in the polar regions of the heliosphere. The most important of these modifications are summarized below.

2.9.2. The Jokipii-Kóta modification

The radial field lines at the poles are in a state of unstable equilibrium. Therefore, the smallest perturbation can cause the collapsing of the field line. Jokipii and Kóta (1989) have argued that the solar surface, where the 'feet' of the field lines occur, is not a smooth surface, but a granular turbulent surface that keeps changing with time, especially in the polar regions. This turbulence may cause the 'footpoints' of the polar field lines to wander randomly, creating transverse components in the field, thus causing temporal deviations from the smooth Parker geometry. The net effect of this is a highly irregular and compressed field line. In other words, the magnitude of the mean magnetic field at the poles is greater than in the case of the smooth magnetic field of a pure Parker

spiral.

Jokipii and Kóta (1989) have therefore suggested that the Parker spiral field may be generalized by the introduction of a parameter, $\delta(\theta,\phi)$, which amplifies the field strength at large radial distances. With this modification the Parker spiral field, Equation 2.58, becomes

$$\mathbf{B} = B_0 \left(\frac{r_e}{r}\right)^2 (\mathbf{e}_r + \left(\frac{r\delta(\theta,\phi)}{r_\odot}\right) \mathbf{e}_\theta - \tan\psi \mathbf{e}_\phi) \left[1 - 2H(\theta - \theta')\right]. \tag{2.64}$$

The magnitude of this modified field is then given by

$$B = B_0 \left(\frac{r_e}{r}\right)^2 \sqrt{1 + \Gamma^2 + \left(\frac{r\delta(\theta,\phi)}{r_\odot}\right)^2}. \tag{2.65}$$

The effect of this modification is to increase the field in the polar regions in such a way that for large r it decreases as $1/r$ instead of $1/r^2$. In the ecliptic region of the outer heliosphere, where $1 + \tan^2\psi \gg 1$, this modification has little effect on the field and it becomes in essence a Parker spiral field. It should be noted, however, that this leaves the field divergence free ($\nabla \cdot \mathbf{B} = 0$) only if $\delta(\theta,\phi) \propto 1/\sin\theta$. The modification, $\delta(\theta,\phi)$, in this thesis is therefore given by

$$\delta(\theta,\phi) = \frac{\delta_m}{\sin\theta}, \tag{2.66}$$

with $\delta_m = 8.7 \times 10^{-5}$, so that $\delta(\theta,\phi) = 0.002$ near the poles (at $\theta = 2.5°$) and $\delta(\theta,\phi) \approx 0$ in the ecliptic plane. For this value of δ_m, the magnitude of the HMF changes significantly in the polar regions without altering the field noticeably in the equatorial plane.

Qualitatively this modification is supported by measurements made of the HMF in the polar regions of the heliosphere by Ulysses (e.g., Balogh et al., 1995). For applications and implications of a modification where $\delta(\theta,\phi)$ = 0.002 in the whole heliosphere, see e.g. Haasbroek and Potgieter (1995), Haasbroek et al. (1995a, 1995b), Jokipii et al. (1995), Kóta and Jokipii (1995), Potgieter (1996), Haasbroek (1997), Hattingh and Burger (1997), Hattingh (1998), Jokipii and Giacalone (1998), Potgieter and Ferreira (1999a, 1999b), Potgieter et al. (1999a, 1999b) and Potgieter (2000).

2.9.3. The Moraal modification

Moraal (1990) suggested that the Jokipii-Kóta modification could be modified by the introduction of an arbitrary function $\Theta(\theta)$ in the Parker field, to incorporate the same physical effects that their modification compensated for, thus giving

$$\mathbf{B} = B_0 \left(\frac{r_e}{r}\right)^2 \Theta(\theta)(\mathbf{e}_r - \tan\psi \mathbf{e}_\phi) \left[1 - 2H(\theta - \theta')\right], \tag{2.67}$$

for Equation 2.58. This function is chosen to be symmetric about $\theta = 90°$, with $\Theta(90°) = 1$, and increasing towards the poles. The magnitude of the Parker spiral field then becomes

$$B = B_0 \left(\frac{r_e}{r}\right)^2 \Theta(\theta)\sqrt{1 + \Gamma^2}. \tag{2.68}$$

This modification keeps the field divergence free for all forms of $\Theta(\theta)$. Note, however, that if $\Theta(\theta)$ is not a function of only θ, but also of r and ϕ, $\nabla \cdot \mathbf{B} \neq 0$.

2.9.4. The Smith-Bieber modification

Another modification was proposed by Smith and Bieber (1991) who based their modification on magnetic field observations. They have proposed that the magnetic field is not fully radial below the Alfvèn radius (below which

the magnetic field and the solar corona corotate in phase), taken to be in the order of 10 - 30 $r_\odot$. The modification is parameterized by the ratio of the tangential (azimuthal) component of the magnetic field to that of the radial component as is found at the Alfvèn radius, thus Equation 2.59 is given by

$$\tan\psi = \frac{\Omega(r-b)\sin\theta}{V(r)} - \frac{B_T(b)V(b)r}{B_R(b)V(r)b}, \tag{2.69}$$

where $b = 20r_\odot$ and $B_T(b)/B_R(b) \approx -0.02$ according to an estimate by Smith and Bieber. This modification also changes the geometry of the magnetic field and affects the field strength over the poles. For an implementation of their modification in a numerical model see Haasbroek (1993), Haasbroek et al. (1995a, 1995b), and Minnie (2002). Although this approach has particular merit, it is not further utilized in this study.

2.9.5. The Fisk magnetic field

For many decades the HMF has been considered, on average, to execute a simple Archimedian spiral. Through numerous observations of the HMF by spacecraft, the HMF seems to closely follow this spiral. However, Fisk (1996) has pointed out that a correction needs to be made to the Parker spiral model for the simple reason that the Sun does not rotate rigidly but differentially, with the solar poles rotating ~20 % slower than the solar equator (e.g., Snodgrass, 1983). The interplay between the differential rotation of the footprints of the HMF lines in the photosphere of the Sun, and the subsequent non radial expansion of the field lines with the solar wind from coronal holes, can result in excursions of the field lines with heliographic latitude. This effect can account for observations from the Ulysses spacecraft of recurrent energetic particle events at higher latitudes. In the Fisk model the magnetic field lines at high latitudes can be connected directly to corotating interaction regions in the solar wind at lower latitudes.

When the footpoint trajectories on the source surface can be approximated by circles offset from the solar rotation axis with an angle β_A, an analytical expression for the Fisk HMF is obtained (Zurbuchen et al., 1997):

$$\begin{aligned} B_r &= B_0\left(\frac{r_e}{r}\right)^2, \\ B_\theta &= B_r\frac{r}{V}\omega\sin\beta_A\sin\left(\phi+\frac{\Omega r}{V}\right), \\ B_\phi &= B_r\frac{r}{V}\left[\omega\sin\beta_A\cos\theta\cos\left(\phi+\frac{\Omega r}{V}\right)+\sin\theta(\omega\cos\beta_A-\Omega)\right] \end{aligned} \tag{2.70}$$

with ω the differential rotation rate. Equation 2.70 is referred to by Burger and Hattingh (2001) as the Fisk type I field. When compared to a Parker spiral HMF, the more complicated structure of the Fisk HMF is visible where these field lines can traverse different latitudes. Assuming $\beta_A = 90°$ in Equation 2.70 (e.g., Burger and Hattingh, 2001) leads to a Fisk type II field. The existence of such a HMF may be supported by a tilt angle varying in time which can cause a regular meridional component in the HMF (Kóta and Jokipii, 1997; Kóta and Jokipii, 1999).

A HMF with a meridional component, such as the Fisk field, leads to a more complicated form of the TPE than for the normal Parker field. It is inherently three dimensional and time dependent so that the increase of the number of mixed derivatives results in the numerical codes that are used to solve the TPE easily becoming unstable (e.g., Kóta and Jokipii, 1997; Kóta and Jokipii, 1999; Burger and Hattingh, 2001). The properties of this type of HMF have been studied extensively by e.g., Van Niekerk (2000), Burger and Hattingh (2001), and Burger et al. (2001), but because of the complexity of this field it is not incorporated in the numerical modulation model that is used in this work. Although the Jokipii-Kóta modification to the HMF is to some extent unsatisfactory, it is still well motivated and the most convenient to apply.

2.10. The heliospheric current sheet

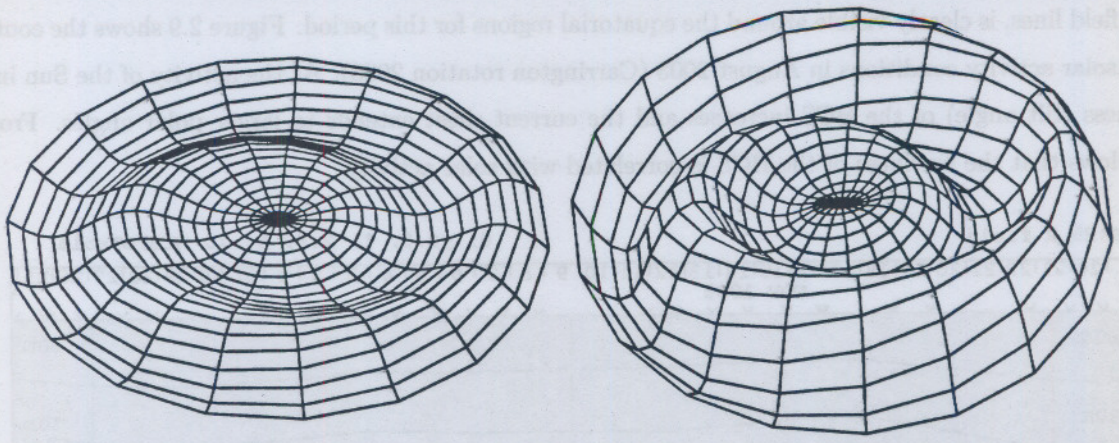

Figure 2.7. The wavy heliospheric current sheet to a radial distance of 10 AU with a tilt angle of $\alpha = 5°$ (low solar activity, left panel) and $\alpha = 20°$ (low to moderate activity, right panel). The Sun is at the centre (adapted from Haasbroek, 1997).

A major corotating structure in the heliosphere is the HCS which divides the HMF into hemispheres of opposite polarity. Every ~11 years the HMF changes sign across a neutral sheet, dividing the heliosphere into two halves: a hemisphere where the HMF is directed inward and a hemisphere where the HMF is directed outward. The transition between these hemispheres is necessarily made within a thin neutral sheet region, known as the heliospheric current sheet. The HCS has a wavy structure and is rooted in the coronal magnetic field. This is because of the fact that the magnetic equator of the Sun does not coincide with the heliographic equator, because the magnetic axis of the Sun is tilted relative to the rotational axis. This tilt angle is denoted by α. The waviness of the HCS is correlated to the solar activity of the Sun. During high levels of activity, the tilt angle increases to as much as $\alpha \approx 75°$. During times of low solar activity the axis of the magnetic equator and the heliographic equator become nearly aligned, causing relative small current sheet waviness with $\alpha \approx 5°$ to $10°$ (see Figures 2.7 and 2.10). The wavy structure of the HCS is carried, together with the HMF, radially outwards by the solar wind as is shown in Figure 2.7 (for a recent review see Smith, 2001). Here three-dimensional schematic representations of two HCS configurations for distances up to 10 AU are shown with the HCS evolving from a near flat sheet, $\alpha = 5°$, to one with $\alpha = 20°$. From these figures it follows that the increase from $\alpha = 10°$ to $\alpha = 20°$ causes a considerable increase in the waviness of the HCS. For periods of high levels of solar activity the dipole-like appearance of the Sun's magnetic field changes. The dipole configuration is replaced by quadrupole moments and therefore even multiple HCSs are possible (Crooker et al., 1993; Kóta and Jokipii, 2001). The discovery of the HCS is related to attempts in explaining the sector structure of the HMF. A surprising feature of the earliest HMF measurements in space was their organization into magnetic 'sectors' in which the fields alternated between inward and outward (Wilcox and Ness, 1965). It was Alfvèn (1977) who made the connection that the magnetic sectors were separated by a current sheet enclosing the Sun (see also Davis, 1972; Schulz, 1973; Levy, 1976).

Evidence of the HCS is shown in Figure 2.8 for the period of November 1995 (Carrington rotation 1902) which corresponds to solar minimum conditions. This figure shows the solar polar magnetic field strength as determined by Hoeksema (http://quake.stanford.edu/) for both the southern and northern hemisphere respectively. The contours

are on the solar source surface which is assumed to be present at $2.5r_\odot$. The different shades of grey correspond to different polarities of the magnetic field. The waviness of the HCS, which separates the outward from the inward magnetic field lines, is clearly visible around the equatorial regions for this period. Figure 2.9 shows the contours for increased solar activity conditions in August 2003 (Carrington rotation 2006). As the activity of the Sun increases, the waviness (tilt angle) of the HCS increases and the current sheet extends to larger polar angles. From these figures follows that the waviness of the HCS is correlated with solar activity.

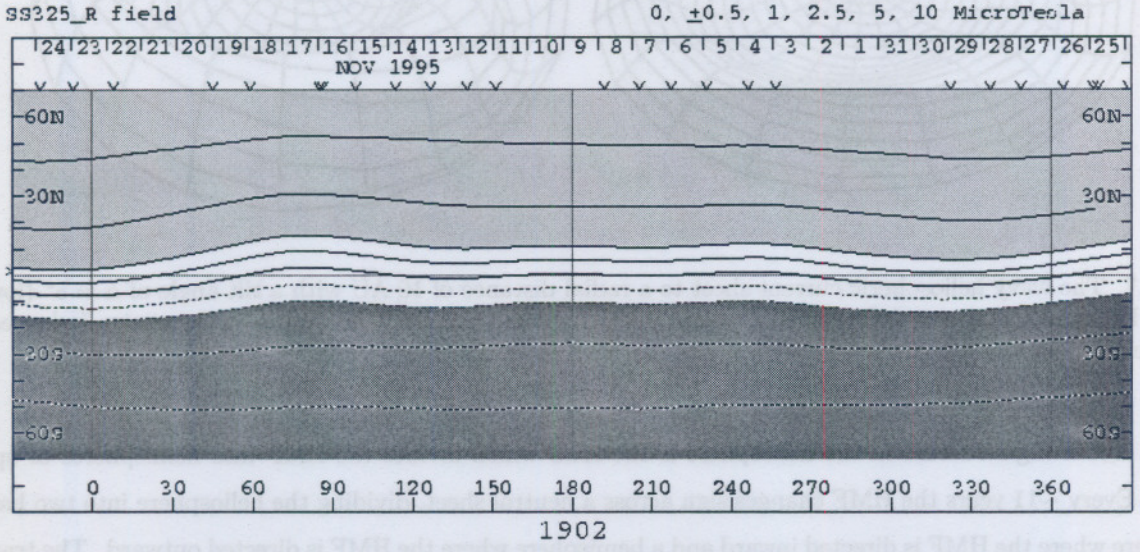

Figure 2.8. Computed source surface field map for solar minimum during November 1995 (Carrington rotation 1902) as determined by the Wilcox Solar Observatory (http://quake.stanford.edu/) for the southern and northern hemisphere respectively. The solar polar magnetic field strength is shown as contours for the solar source surface at $2.5r_\odot$ over 360°. The different shades of grey correspond to different polarities, with the transition the position of the HCS.

Because of the outblowing solar wind, the HCS is carried together with the HMF into the heliosphere, having been observed to be present in the most distant HMF observations of Pioneer 10 (Smith, 1989) and Voyager 1 and 2 (Burlaga and Ness, 1993). The wavy structure of the HCS, which has been first suggested by Thomas and Smith (1981), plays an important role in CR modulation affecting the drift motions. Because the HMF above and below the HCS is oppositely directed, CRs experience particle drifts along the HCS (a phenomenon which will be discussed in the next chapter). Fully three dimensional simulations of CR transport with a three-dimensional HCS and a two-dimensional approximation to the HCS have been done by e.g. Kóta and Jokipii (1983) and Hattingh and Burger (1995a, 1995b) and will be discussed in detail in the next chapter. For a constant and radial solar wind speed, the HCS according to Jokipii and Thomas (1981) is

$$\theta' = \frac{\pi}{2} + \sin^{-1}\left\{\sin\alpha \sin\left[\phi + \frac{\Omega(r - r_\odot)}{V}\right]\right\}. \tag{2.71}$$

This can be approximated by

$$\theta' = \frac{\pi}{2} + \alpha \sin\left[\phi + \frac{\Omega(r - r_\odot)}{V}\right] \tag{2.72}$$

for small α. In Chapter 4, the derivation for a HCS, done by Hattingh (1993), is revisited. This derivation was used to simulate the HCS in a 2D heliosphere for $\alpha \leq 25°$. An improved HCS model was thus derived in this work, in order to remove most of the assumptions and approximations made by Hattingh (1993) so that the axially

symmetric modulation models could be used for all α. The validity of the 2D-approximation of the HCS was discussed in detail by Hattingh (1993) and Hattingh and Burger (1995a).

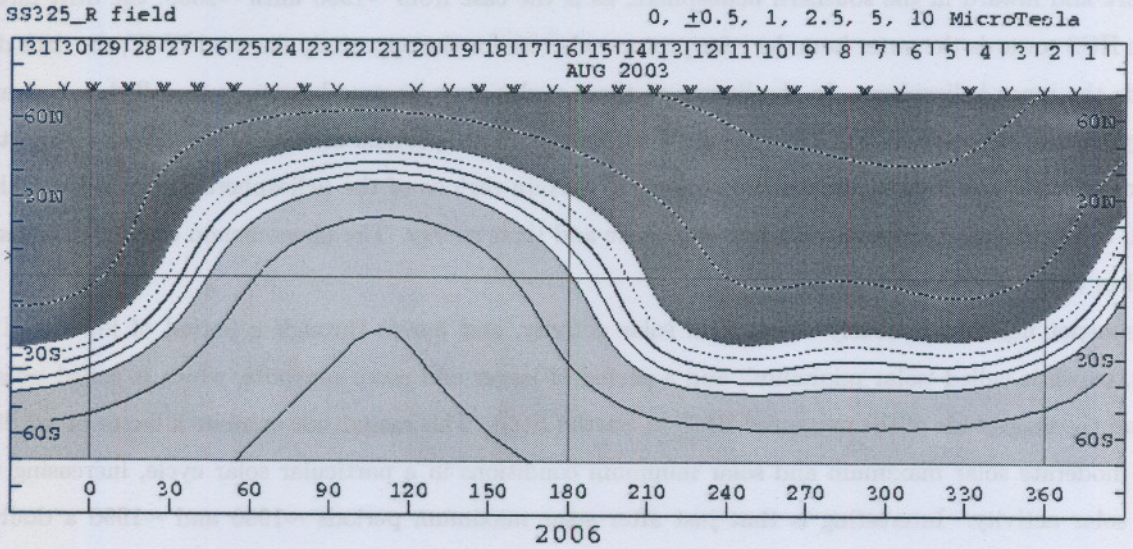

Figure 2.9. As in Figure 2.8, except for August 2003 (Carrington rotation 2006) which corresponds to increased solar activity conditions.

2.11. Solar cycle variations

Figure 2.10 shows the monthly averaged HCS tilt angles, α, until recently computed with the so-called 'new' model from 1976 (for details see Wilcox Solar Observatory with courtesy of J. T. Hoeksema: http://wso.stanford.edu). The 11-year cycles are clearly present. The relation between α and CR modulation has been studied in detail, see e.g. Potgieter (1984), le Roux (1990), Haasbroek (1997), and Ferreira (2002). It has been found that α is a good proxy for solar activity from a CR modulation point of view.

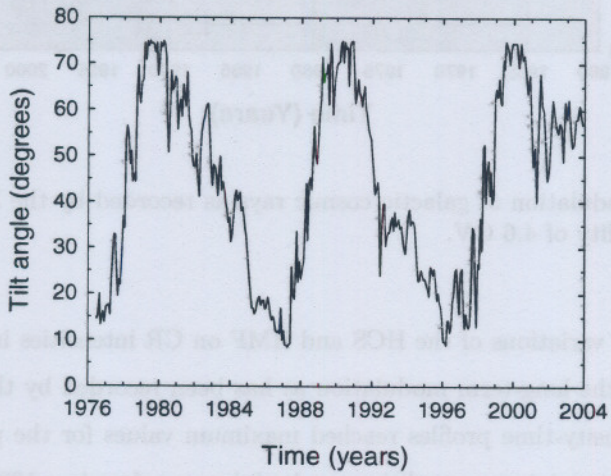

Figure 2.10. The monthly averaged tilt angles α from 1976 until recently computed with the so-called 'new' model (Wilcox Solar Observatory with courtesy of J. T. Hoeksema: http://wso.stanford.edu).

The HCS has important influences on the transport of CRs; because the HMF above and below the HCS is oppositely directed, particle drifts are caused along the HCS. When the HMF is directed outward in the northern hemisphere and inward in the southern hemisphere, as is the case from ~1990 until ~2000, the drift direction is along the HCS towards the outer boundary for protons whereas for the oppositely directed HMF, the drift direction is towards the inner heliosphere. In the literature these cycles have become known as so-called A > 0 and A < 0 polarity epochs, respectively. The level of HCS waviness and the particle drift direction play an important role in the extent with which a charged particle can reach certain regions of the heliosphere, depending on the HMF direction, the solar activity, the particle's charge state and their energy. The phenomenon of HCS drifts is further discussed in the next chapter.

The sunspot number obviously varies with solar activity, and moves through a period of fewer and smaller sunspots, which is called 'solar minimum'; and a period of larger and more sunspots, which is called 'solar maximum'; and the magnitude of the measured HMF at Earth ($B(t)$). This magnitude exhibits a factor of ~2 difference between moderate solar maximum and solar minimum conditions in a particular solar cycle, increasing with increasing solar activity. Interesting is that just after solar maximum periods ~1980 and ~1990 a double peak structure occurs (Gnevyshev Gap) in $B(t)$ which is also visible in CR measurements at Earth. Correlating with the sunspot numbers an ~11-year cycle also seems to be present in $B(t)$, with the largest values near the time of solar maximum conditions.

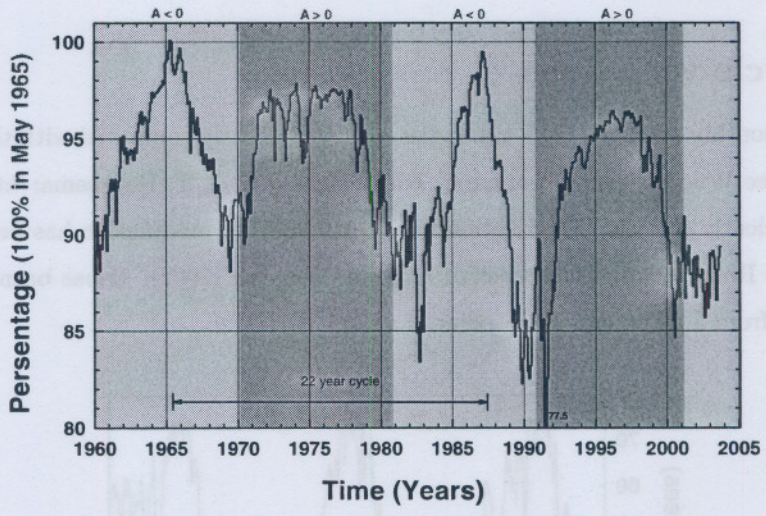

Figure 2.11. The long-term modulation of galactic cosmic rays as recorded by the Hermanus neutron monitor in South Africa with a cutoff rigidity of 4.6 GV.

The effect of the solar cycle variations of the HCS and HMF on CR intensities in the heliosphere is illustrated in Figure 2.11. It is shown as the long-term modulation as has been recorded by the Hermanus neutron monitor in South Africa. The CR intensity-time profiles reached maximum values for the periods of ~1975, ~1987, and ~1996, which correspond to solar minimum conditions and minimum values in ~1981, ~1991, and in ~2001 which correspond to solar maximum conditions. Obviously, the ~11-year solar activity cycle of the Sun leads to an ~11-year modulation cycle in the CR intensities. As discussed above, the source of the ~11-year modulation cycle is generally believed to be a combination of the effects of the solar cycle variations in the HCS and HMF, and global merged interaction regions. Apart from changes in the tilt angle and to some of the diffusion coefficients,

other causes of long-term modulation have not been considered for this work. For a recent review, see Ferreira and Potgieter (2002).

2.12. Spacecraft missions

One of the most important aspects in the study of the heliospheric modulation of CRs is the accumulation of data from in situ observations. In this section, the Ulysses, Voyager 1, Voyager 2, and Pioneer 10 spacecraft that have been used to accumulate CR data are briefly discussed. Descriptions of other methods and spacecraft, e.g. balloon experiments, neutron monitors and the Pioneer 11 spacecraft have been excluded for the purposes of this study.

2.12.1. The Ulysses Mission

The Ulysses mission is one of the most important missions to study several aspects of the heliosphere and in particular CR modulation (e.g., Rastoin, 1995; Heber, 2002). This is the first spacecraft to undertake measurements far from the ecliptic and over the polar regions of the Sun, thus obtaining first-hand knowledge concerning the high latitudes of the inner heliosphere. The Ulysses mission, together with the Kiel Electron Telescope (KET) which is part of the Ulysses Cosmic and Solar Particle Investigation (COSPIN), has been described by Simpson et al. (1992a, 1992b), Marsden (1993), Wenzel (1993), Ferrando et al. (1996) and Heber et al. (1997).

The Ulysses spacecraft was launched on 6 October 1990. From the launch the spacecraft moved close to the ecliptic plane to Jupiter (at ~5 AU) and from there it started to move to higher latitudes south of the ecliptic plane. In mid 1994 the highest southern latitude with $\theta \approx 170°$ was reached. From there Ulysses moved to the northern polar region which was reached in 1995 and returned to the ecliptic plane again in 1998. After ~1998 Ulysses started the second out of the ecliptic orbit moving into the southern heliospheric polar regions. It reached $\theta \approx 170°$ at the end of 2000 and crossed the equatorial plane in May 2001. On 5 February 2004, the spacecraft will again be close to the giant planet, Jupiter. Unlike the 1992 fly-by, however, this will be a distant 'encounter' (closest approach will be at 1684 Jovian radii from the planet's centre, compared with 6 Jovian radii in 1992). Another difference between the two flybys is that this time, the spacecraft will approach the planet from high northern latitudes. This difference had already become apparent in the radio data from the URAP experiment on board Ulysses, which in February and March 2003 detected intense radio emission from Jupiter at levels well above those seen in 1993 when Ulysses was at comparable distance from the planet (approximately 2.8 AU). Detail of the trajectory of the Ulysses spacecraft can be found on the Ulysses homepage: http://helio.estec.esa.nl/ulysses/.

Onboard Ulysses are nine scientific instruments of which the KET provides a wide range of e.g. electron fluxes from about 2.5 MeV to 6 GeV, which are used in Chapter 4, with observed latitudinal gradients between colatitudes 10° and 90° (Heber et al., 1996; Heber, 1997).

The Ulysses mission is highly successful and has contributed significantly to the current knowledge regarding the heliosphere. The mission is already in progress for 13 years and there is a possibility that it can continue after 2005. See the following publications for a review: Marsden (1995; 2001), Balogh et al. (2001).

2.12.2. The Pioneer 10 Mission

Launched on 2 March 1972, Pioneer 10 was the first spacecraft to travel through the asteroid belt, and the first spacecraft to obtain close-up observations and images of Jupiter. Famed as the most remote object ever made by Man, the heliocentric radial distance of Pioneer 10 had been greater than that of any other man-made object until 17 February 1998 when Voyager 1's heliocentric radial distance equalled that of Pioneer 10 at ~69 AU.

The spacecraft made valuable scientific investigations in the outer regions of our solar system until the end of its mission on 31 March 1997. The Pioneer 10's weak signal, however, continues to be tracked as part of a new advanced concept study of chaos theory. (See the Pioneer homepage at http://spaceprojects.arc.nasa.gov/).

The Pioneer 10 spacecraft stayed close to the equatorial regions with maximum latitude of 3.1°. The Pioneer 10 spacecraft, although terminated in March 1997, did reach a radial distance up to ~70 AU providing most valuable data. Both Ulysses and Pioneer 10, although launched almost 20 years apart, had almost the same trajectory up to Jupiter. While Ulysses returned to the inner heliosphere, Pioneer 10 set out to explore the outer heliosphere. Both these spacecraft made it to the Jovian magnetosphere in relatively high solar activity conditions.

In this work observed electrons in the energy range from 1.75 to 25.0 MeV by the University of Chicago instrument on the Pioneer 10 spacecraft are used. This telescope is discussed by Simpson et al. (1974, 1975). Low energy electrons are measured in the interval 2 - 7 MeV and 7 - 17 MeV with mean energies $< E > = 4$ MeV and $< E > = 16$ MeV, respectively (Eraker, 1982; Lopate, 1991; Lopate, 2001). See the review papers by Smith (1990).

2.12.3. The Voyager missions

Two of the important space probes for CR studies are the Voyager-1 and Voyager-2 spacecraft. For nearly 26 years the cosmic ray experiments onboard these spacecraft have been used to study the spatial and temporal variations of GCRs and ACRs at distances now extending beyond 90 AU (Voyager 1 was at ~90 AU on November 5, 2003) and 70 AU and to heliolatitudes from 35° N to 48° S for Voyager 1 and 2 respectively (http://voyager.jpl.nasa.gov/). Voyager 1 is escaping the solar system at a speed of about 3.6 AU per year, while Voyager 2 escapes at about 3.3 AU per year. Both Voyager spacecraft are so far away from the Earth that the largest of the Deep Space Network (DSN) antennas, the 70-meter, is needed to send command information to the Voyager spacecraft with the help of a 20 kilowatt transmitter. To provide some reference on how much power a 20 kilowatt transmitter produces, most AM and FM radio stations transmit their radio signals using 5 times that much power. The Voyager spacecraft have now reached such enormous distances from Earth that the smaller 34-meter antennas of the DSN can no longer provide enough command transmission power to successfully send sequenced instructions to either spacecraft. Their heliospheric positions in September 2003 are given in Table 2.3. Both are expected to keep functioning well into the century and dramatic discoveries may unfold as they cross the TS (e.g., Stone and Cummings, 2003; Krimigis et al., 2003).

In this study 175 MeV CR proton observations from these spacecraft are used in Chapters 4 and 5 for the 1987 and 1997-98 solar minimum periods and the 2000-01 solar maximum periods (Webber and Lockwood, 2001a, 2001b)

Table 2.3: Voyager spacecraft positions on 12 September 2003
(http://voyager.jpl.nasa.gov/mission/weekly-reports/index.htm)

Spacecraft	Day	Year	Distance from Sun (AU)	Velocity relative to Sun ($km.s^{-1}$)
Voyager 1	255	2003	89.8	17.2
Voyager 2	255	2003	71.5	15.7

2.13. Summary

In this chapter a brief overview was given of the major properties and the structure of the heliosphere. The Sun, being primarily responsible for the existence of the heliosphere, is a rotating magnetic star of which the plasmatic

atmosphere constantly blows radially away from its surface to form the solar wind. This solar wind speed can be divided into the fast solar wind and the slow solar wind, especially during solar minimum conditions. A fixed observer relatively close to the solar equatorial plane will observe successive fast and slow solar wind streams during much of the solar cycle because of the inclination of the Sun's rotation axis relative to the equatorial plane. The solar wind flows radially outward from the Sun and therefore blows a spherical bubble that continually expands. The region of space filled by the plasma originating from the Sun and transported outward through the solar wind, is called the heliosphere. At large radial distances the local interstellar medium pressure causes the supersonic solar wind plasma to decrease to subsonic speeds. A shock is created, which is called the solar wind termination shock. At this TS low energy particles are accelerated to higher energies by a process which is called first-order Fermi shock acceleration. The energy spectra of these accelerated particles give a characteristic power law spectrum with $U_p \propto E^{\frac{-q+2}{2}}$, where U_p is the differential cosmic ray number density and $q = 3s/(s-1)$, with s the compression ratio of the TS and E the kinetic energy of the particles. Estimates for the position of the TS vary between ~80 AU and ~100 AU. The distance beyond which the Sun has no significant influence is called the heliopause. Estimates for the distance from the Sun to the heliopause vary between ~90 AU to ~180 AU.

From observations of monthly average sunspot numbers it is evident that the Sun has a quasi-periodic ~11 year cycle which is called a solar activity cycle. Every ~11 years the Sun moves through a period of e.g. fewer and smaller sunspots which is called 'solar minimum' and periods of larger and more sunspots which are called 'solar maximum'. This ~11-year cycle is also present in the measured magnetic dipole angle of the Sun and the heliospheric magnetic field which are transported with the solar wind into space. During periods of solar maximum activity the HMF changes in sign.

The solar rotation winds the HMF into a spiral, which is called the Parker spiral. Deviations from the Parker spiral, especially away from the equatorial plane, may occur. In the equatorial regions of the heliosphere, a major three-dimensional corotating structure is present which is called the heliospheric current sheet. This structure divides the HMF into hemispheres of opposite polarity. Because the magnetic and rotation axis of the Sun are not aligned, the rotation of the Sun causes a warped or wavy current sheet. The angle between the magnetic and rotation axis of the Sun is known as the tilt angle and is commonly used as a proxy for solar activity.

The HMF determines the passage of CRs by changing the CR intensities with time as a function of energy and position, and reduces the CR intensities below the level of the local interstellar spectrum. This process is known as the modulation of CRs in the heliosphere and is described by the Parker transport equation as is given by Equation 2.1. In this work solutions of the TPE will be compared to observations from the Ulysses, Pioneer 10, and Voyager 1 and 2 missions.

What follows is an outline of the most important of these concepts as will be used in this study.

(1) The outer boundary (heliopause) of the heliosphere is assumed to be at $r_b = 120$ AU, while the location of the TS is assumed at $r_s = 90$ AU.

(2) The solar wind speed is assumed to change from 400 km.s^{-1} in the equatorial plane to 800 km.s^{-1} in the polar regions for solar minimum conditions, but to stay constant at 400 km.s^{-1} for moderate solar maximum conditions. Extreme solar maximum conditions are not considered.

(3) The HMF is assumed to be a Parker spiral, but was significantly modified in the heliospheric polar regions, as suggested by Jokipii and Kóta (1989).

(4) The heliosphere is divided into a northern and southern hemisphere with oppositely directed magnetic fields

that change polarity every ~11 years. These hemispheres are separated by the wavy HCS along which charged particles experience drifts effects.

(5) During the A > 0 polarity epoch, e.g. ~1990 to ~2000, the HMF is directed outward in the northern hemisphere. Electrons then drift primarily from the outer boundary of the heliosphere along the HCS towards the Sun. During the A < 0 polarity epoch, e.g. ~1980 to ~1990, the electrons drift from the heliospheric poles down into the equatorial regions, and then outwards along the HCS.

In the next chapter an overview will be given of the heliospheric transport processes, modulation theory and the numerical models that have been developed by the Potchefstroom CR group and for the present study.

Chapter 3
The transport equation, numerical models, and the diffusion tensor

3.1. Introduction

Galactic cosmic rays have to cross various boundaries and regions (see Figure 2.2) on their way to a point of observation in the heliosphere, which can be at the Earth or at one of the current fleet of spacecraft. Beyond the heliopause, the Sun's magnetic field and solar wind can no longer influence CRs. Within this modulation boundary, modulation takes place as CR intensities decrease relative to their interstellar values.

In this chapter a discussion of the heliospheric transport processes and mechanisms as they occur in the TPE is given, together with a short overview of modulation models and a detailed discussion of the 2D TS model that will be used in this work. Understanding these physical mechanisms and their consequences is one of the most important areas in CR modulation studies. A short overview of existing knowledge will also be given, in particular the diffusion and drift processes, and to construct a suitable diffusion tensor which will be used in this work. A fundamental study of the transport coefficients is beyond the scope of this work, instead, much of previous work have been used e.g., Palmer (1982), Bieber et al. (1994), Kóta and Jokipii (1995), Potgieter (1996), Zank et al. (1996), Zank et al. (1998), Burger and Hattingh (1998), Hattingh (1998), Giacalone (1998), Giacalone et al. (1999), Giacalone and Jokipii (1999), Ferreira et al. (2000), Burger et al. (2000), and Parhi et al. (2003).

3.2. The Parker transport equation

The modulation of CRs in the heliosphere is described by the TPE, see Equation 2.1, which has been developed by Parker (1965). To verify all the transport processes present, this equation has been rederived by Gleeson and Axford (1967) and it has been refined by Gleeson and Axford (1968) and Jokipii and Parker (1970). Rewriting Equation 2.1 in a spherical coordinate system rotating with the Sun (e.g., Kóta and Jokipii, 1983), gives

$$\begin{aligned}\frac{\partial f}{\partial t} &= \left[\frac{1}{r^2}\frac{\partial}{\partial r}(r^2 K_{rr}) + \frac{1}{r\sin\theta}\frac{\partial}{\partial\theta}(K_{\theta r}\sin\theta) + \frac{1}{r\sin\theta}\frac{\partial K_{\phi r}}{\partial\phi} - V\right]\frac{\partial f}{\partial r} \\ &+ \left[\frac{1}{r^2}\frac{\partial}{\partial r}(rK_{r\theta}) + \frac{1}{r^2\sin\theta}\frac{\partial}{\partial\theta}(K_{\theta\theta}\sin\theta) + \frac{1}{r^2\sin\theta}\frac{\partial K_{\phi\theta}}{\partial\phi}\right]\frac{\partial f}{\partial\theta} \\ &+ \left[\frac{1}{r^2\sin\theta}\frac{\partial}{\partial r}(rK_{r\phi}) + \frac{1}{r^2\sin\theta}\frac{\partial K_{\theta\phi}}{\partial\theta} + \frac{1}{r^2\sin^2\theta}\frac{\partial K_{\phi\phi}}{\partial\phi}\right]\frac{\partial f}{\partial\phi} \\ &+ K_{rr}\frac{\partial^2 f}{\partial r^2} + \frac{K_{\theta\theta}}{r^2}\frac{\partial^2 f}{\partial\theta^2} + \frac{K_{\phi\phi}}{r^2\sin^2\theta}\frac{\partial^2 f}{\partial\phi^2} + \frac{2K_{r\phi}}{r\sin\theta}\frac{\partial^2 f}{\partial r\partial\phi} \\ &+ \frac{1}{3r^2}\frac{\partial}{\partial r}(r^2 V)\frac{\partial f}{\partial\ln p} + Q_{source}(r,\theta,\phi,p,t), \end{aligned} \tag{3.1}$$

with a radial solar wind speed V (see Equations 2.7, 2.8, 2.9, 2.53, and 2.56) and where $K_{r\theta} = -K_{\theta r}$, $K_{\theta\phi} = -K_{\phi\theta}$, and $K_{r\phi} = K_{\phi r}$ (as will be discussed below). Here the coordinate system (see Figure 3.1) with one axis $\mathbf{e}_{\parallel}$ parallel to the averaged magnetic field in the $r\phi$-plane, the second axis $\mathbf{e}_1$ in the polar direction $\mathbf{e}_\theta$, and the third axis $\mathbf{e}_2$

also in the $r\phi$-plane, completing the system, is

$$\begin{aligned} \mathbf{e}_{\parallel} &= \cos\psi \mathbf{e}_r - \sin\psi \mathbf{e}_\phi, \\ \mathbf{e}_1 &= \mathbf{e}_\theta, \\ \mathbf{e}_2 &= \mathbf{e}_{\parallel} \times \mathbf{e}_1 \\ &= \sin\psi \mathbf{e}_r + \cos\psi \mathbf{e}_\phi, \end{aligned} \tag{3.2}$$

with ψ the spiral angle of the field. This coordinate system will be called the magnetic coordinate system. The transformation matrix from the magnetic coordinate system to the spherical coordinate system is

$$\mathbf{T} = \begin{bmatrix} \cos\psi & 0 & \sin\psi \\ 0 & 1 & 0 \\ -\sin\psi & 0 & \cos\psi \end{bmatrix} \tag{3.3}$$

so that the diffusion tensor $\mathbf{K}$ in spherical coordinates (r, θ, ϕ) is:

$$\begin{aligned} \begin{bmatrix} K_{rr} & K_{r\theta} & K_{r\phi} \\ K_{\theta r} & K_{\theta\theta} & K_{\theta\phi} \\ K_{\phi r} & K_{\phi\theta} & K_{\phi\phi} \end{bmatrix} &= \mathbf{T}\mathbf{K}\mathbf{T}^T \\ &= \begin{bmatrix} \cos\psi & 0 & \sin\psi \\ 0 & 1 & 0 \\ -\sin\psi & 0 & \cos\psi \end{bmatrix} \begin{bmatrix} \kappa_{\parallel} & 0 & 0 \\ 0 & \kappa_{\perp\theta} & \kappa_A \\ 0 & -\kappa_A & \kappa_{\perp r} \end{bmatrix} \begin{bmatrix} \cos\psi & 0 & -\sin\psi \\ 0 & 1 & 0 \\ \sin\psi & 0 & \cos\psi \end{bmatrix} \\ &= \begin{bmatrix} \kappa_{\parallel}\cos^2\psi + \kappa_{\perp r}\sin^2\psi & -\kappa_A \sin\psi & \left(\kappa_{\perp r} - \kappa_{\parallel}\right)\cos\psi\sin\psi \\ \kappa_A \sin\psi & \kappa_{\perp\theta} & \kappa_A \cos\psi \\ \left(\kappa_{\perp r} - \kappa_{\parallel}\right)\cos\psi\sin\psi & -\kappa_A\cos\psi & \kappa_{\parallel}\sin^2\psi + \kappa_{\perp r}\cos^2\psi \end{bmatrix}, \end{aligned} \tag{3.4}$$

where the superscript T denotes transpose.

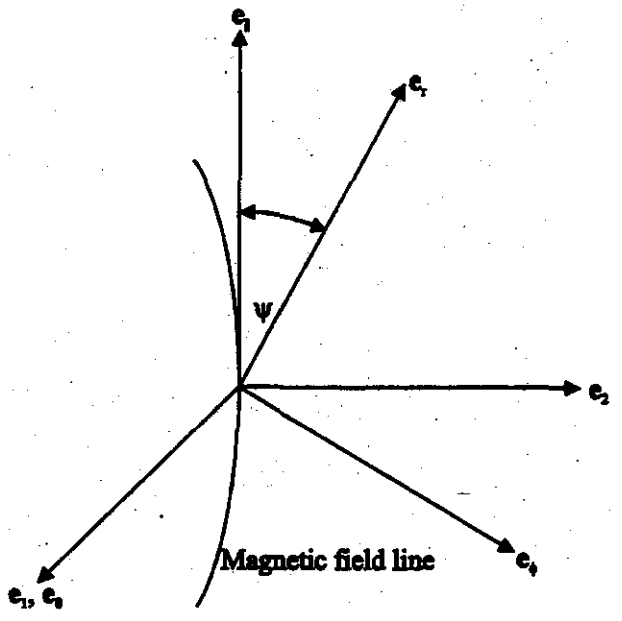

Figure 3.1. The magnetic coordinate system with one axis $\mathbf{e}_{\parallel}$ parallel to the averaged magnetic field in the $r\phi$-plane, the second axis $\mathbf{e}_1$ in the polar direction $\mathbf{e}_\theta$, and the third axis $\mathbf{e}_2$ also in the $r\phi$-plane, completing the system.

For clarity on the role of diffusion, drifts, convection, and adiabatic energy loss, the TPE 3.1 is written as

follows:

$$\begin{aligned}
\frac{\partial f}{\partial t} &= \overbrace{\left[\frac{1}{r^2}\frac{\partial}{\partial r}(r^2 K_{rr}) + \frac{1}{r\sin\theta}\frac{\partial K_{\phi r}}{\partial \phi}\right]\frac{\partial f}{\partial r} + \left[\frac{1}{r^2\sin\theta}\frac{\partial}{\partial\theta}(K_{\theta\theta}\sin\theta)\right]\frac{\partial f}{\partial\theta}}^{diffusion} \\
&\overbrace{+\left[\frac{1}{r^2\sin\theta}\frac{\partial}{\partial r}(rK_{r\phi}) + \frac{1}{r^2\sin^2\theta}\frac{\partial K_{\phi\phi}}{\partial\phi}\right]\frac{\partial f}{\partial\phi}}^{diffusion} \\
&\overbrace{+K_{rr}\frac{\partial^2 f}{\partial r^2} + \frac{K_{\theta\theta}}{r^2}\frac{\partial^2 f}{\partial\theta^2} + \frac{K_{\phi\phi}}{r^2\sin^2\theta}\frac{\partial^2 f}{\partial\phi^2} + \frac{2K_{r\phi}}{r\sin\theta}\frac{\partial^2 f}{\partial r\partial\phi}}^{diffusion} \\
&\overbrace{+\left[-\langle v_d\rangle_r\right]\frac{\partial f}{\partial r} + \left[-\frac{1}{r}\langle v_d\rangle_\theta\right]\frac{\partial f}{\partial\theta} + \left[-\frac{1}{r\sin\theta}\langle v_d\rangle_\phi\right]\frac{\partial f}{\partial\phi}}^{drift} \\
&\overbrace{-V\frac{\partial f}{\partial r}}^{convection}\ \overbrace{+\frac{1}{3r^2}\frac{\partial}{\partial r}(r^2 V)\frac{\partial f}{\partial \ln p}}^{adiabatic\ energy\ loss}\ \overbrace{+Q_{source}(r,\theta,\phi,p,t)}^{source}, \qquad (3.5)
\end{aligned}$$

with

$$\begin{aligned}
\langle v_d\rangle_r &= -\frac{A}{r\sin\theta}\frac{\partial}{\partial\theta}(\sin\theta K_{\theta r}), \\
\langle v_d\rangle_\theta &= -\frac{A}{r}\left[\frac{1}{\sin\theta}\frac{\partial}{\partial\phi}(K_{\phi\theta}) + \frac{\partial}{\partial r}(rK_{r\theta})\right], \\
\langle v_d\rangle_\phi &= -\frac{A}{r}\frac{\partial}{\partial\theta}(K_{\theta\phi}), \qquad (3.6)
\end{aligned}$$

the components of the gradient and curvature drifts $v_d = \nabla\times(\kappa_A e_B)$. Here $A = sign(Bq)$ determines the drifts direction of the charged particles in the heliosphere. The first three lines of Equation 3.5 are the terms describing the inward diffusion of particles, the fourth line contains the particle drifts, and the fifth line the outward convection which is caused by the solar wind, the adiabatic energy loss, and a source function. If we further assume azimuthal symmetry ($\partial/\partial\phi = 0$) and a radial solar wind (see Equation 2.7), Equation 3.1 becomes

$$\begin{aligned}
\frac{\partial f}{\partial t} &= \left[\frac{1}{r^2}\frac{\partial}{\partial r}(r^2 K_{rr}) + \frac{1}{r\sin\theta}\frac{\partial}{\partial\theta}(K_{\theta r}\sin\theta) - V\right]\frac{\partial f}{\partial r} \\
&+\left[\frac{1}{r^2}\frac{\partial}{\partial r}(rK_{r\theta}) + \frac{1}{r^2\sin\theta}\frac{\partial}{\partial\theta}(K_{\theta\theta}\sin\theta)\right]\frac{\partial f}{\partial\theta} \\
&+K_{rr}\frac{\partial^2 f}{\partial r^2} + \frac{K_{\theta\theta}}{r^2}\frac{\partial^2 f}{\partial\theta^2} + \frac{1}{3r^2}\frac{\partial}{\partial r}(r^2 V)\frac{\partial f}{\partial\ln p} + Q_{source}(r,\theta,p,t). \qquad (3.7)
\end{aligned}$$

In the following sections the numerical solution of Equation 3.7 with the Locally One-Dimensional (LOD) numerical method will be discussed, subject to the continuity condition 2.25 on the TS, together with

$$\left(\frac{\partial f}{\partial r}\right)^- = \frac{K_{rr}^+}{K_{rr}^-}\left(\frac{\partial f}{\partial r}\right)^+ - \frac{V^- - V^+}{3K_{rr}^-}\frac{\partial f}{\partial\ln p} - \frac{K_{r\theta}^- - K_{r\theta}^+}{r_s K_{rr}^-}\frac{\partial f}{\partial\theta} + \frac{Q_*}{K_{rr}^-}, \qquad (3.8)$$

which follows from Equation 2.31 if $Q_{source} = Q_*(p)\delta(r - r_s)$ is a delta function on the shock and where '$-$' again represents the upstream region and '$+$' the downstream region. The TPE, Equation 3.7, is then valid in the domain $r_\odot \le r < r_s$ and $r_s < r \le r_b$ $\forall\theta, R$ and the matching condition, Equation 3.8, is valid at the discontinuity $r = r_s$ $\forall\theta, R$. The source/sink function, $Q_{source} \neq 0$, in Equation 3.7 only if there exist sources/sinks away from the discontinuity. At the discontinuity it can have no effect, since the TPE, Equation 3.7, is not valid there. The part of the source/sink that is singular in the shock, Q_*, is found in Equation 3.8.

3.3. A brief review of numerical modulation models

Before the numerical solution of Equation 3.7 is discussed, it is appropriate to give a brief overview of current numerical modulation models, and to motivate why the 2D TS model used in this work has been developed and how it enhances modulation models that have previously been developed by the Potchefstroom modulation group. For detailed discussions on previous numerical models and the applicable numerical methods to obtain solutions of the TPE, see Potgieter (1984), le Roux (1990), Steenkamp (1995), Hattingh (1998), Ferreira (2002).

Fisk (1971) developed the first numerical solution of the TPE by assuming a steady-state and spherical symmetry, i.e. a one-dimensional (1D) model with the radial distance as the only spatial variable. Later the polar angle was included to form an axisymmetric (2D) steady-state model without drifts (Fisk, 1973). This model was improved by Moraal and Gleeson (1975), while Cecchini and Quenby (1975) also developed a 2D steady-state model. In 1979, Moraal et al. (1979) and Jokipii and Kopriva (1979) presented their separately developed 2D steady-state models including gradient and curvature drifts for a flat HCS. The first two 2D models to emulate the waviness of the HCS were developed by Potgieter (1984) and Burger (1987) (see also Potgieter and Moraal, 1985; Burger and Potgieter, 1989). This simulation has been improved by Hattingh (1993) and is referred to as the WCS-model (see also Hattingh and Burger, 1995a).

The first three-dimensional (3D) steady-state model including drifts and a full wavy HCS was developed by Kóta and Jokipii (1983) and later by Hattingh (1998) (see also Williams, 1990; Hattingh and Burger, 1995b) and more recently by Gil and Alania (2001). A comparison of the 2D and 3D steady-state models were done by Hattingh (1998) and Ferreira (1998) to show to what extent they agree. They have found that the agreement has been excellent and therefore the 2D models, which use less computer time and memory, can be used with great confidence. Fichtner et al. (2000) and Ferreira et al. (2001a) developed independently 3D steady-state models including the Jovian magnetosphere as a source of low-energy electrons. Ferreira (2002) has also showed that although the Jovian electron source must be a point source, it can be treated as a ring source in the 2D models, giving an upper limit on contributions of the Jovian electrons as long as distances beyond the Jupiter orbit are considered.

The first spherically symmetric time-dependent model was developed by Perko and Fisk (1983), and later extended to two spatial dimensions by le Roux (1990) enabling the study of long-term CR modulation effects and the effect of outwards propagating GMIRs at large radial distance (Potgieter and le Roux, 1994; le Roux and Potgieter, 1995). Fichtner et al. (2001) developed a 3D time-dependent model for electrons, but neglecting adiabatic cooling of electrons at lower energies by doing a momentum averaging of the Parker TPE.

The inclusion of the heliospheric TS was done by Jokipii (1986) who developed the first axisymmetric time-dependent diffusion shock acceleration model, which gave a natural explanation to several observed features of the anomalous component. Potgieter and Moraal (1988) demonstrated that it was possible to include shock acceleration in a steady-state spherically symmetric model by specifying the appropriate boundary conditions with regard to the CR streaming and spectra at the TS. This model was later expanded to 2D by Potgieter (1989). Kóta and Jokipii (1991) developed a 3D time-dependent model that could be used to study CIRs in the heliosphere. Later Steenkamp (1995) developed an independent 2D shock acceleration model with a discontinuous transition of the solar wind velocity across the TS to study the anomalous component (Steenkamp and Moraal, 1993). A similar model, but with a continuous transition of the solar wind velocity across the TS, was developed by le Roux et al. (1996). This model was originally developed in 2D, but only applied in 1D. This 2D model was expanded

by Haasbroek (1997) to include drifts. Steenberg (1998) improved the Steenkamp (1995) model and applied it extensively to the ACRs (see also Steenberg and Moraal, 1996). The Haasbroek (1997) model in its improved version had been applied extensively to study the TS effects on low-energy galactic and Jovian electrons (Ferreira, 2002).

Other types of modulation models include those by Fichtner et al. (1996), Haasbroek (1997), and Haasbroek and Potgieter (1998) studying the possible geometrical elongation of the heliosphere by assuming a non-spherical heliospheric boundary geometry. Yamada et al. (1999), Zhang (1999), and Gervasi et al. (1999) developed modulation models using stochastic approaches which did not include the effect of the TS and HCS as of yet. Although this work only concentrates on models that are based on the Parker (1965) transport equation, it must be noted that there are also several self-consistent, time-dependent hydrodynamic (HD) and MHD models of various complexity, e.g., Pauls and Zank (1996, 1997), le Roux and Fichtner (1997, 1999), Florinski and Jokipii (1999), Washimi and Tanaka (1999), Myasnikov et al. (2000), Rice and Zank (2000), Florinski et al. (2003), and Scherer and Fahr (2003).

The 2D steady-state WCS model (Hattingh, 1993), the 2D time-dependent shock acceleration models with continuous and discontinuous transitions of the solar wind (Steenkamp, 1995; le Roux et al., 1996; Haasbroek, 1997; Steenberg, 1998), and a Jovian model (Fichtner et al., 2000, 2001; Ferreira et al., 2001d) were used as basis for the 2D time-dependent TS model used in this study. The inclusion of more reliable local interstellar spectra and a fresh and more fundamental approach to diffusion coefficients in this model, and good observations closer to the TS, made it possible to study the modulation of GCRs in the outer heliosphere more quantitatively with this TS model. The anomalous component and Jovian electrons were also included in this study (see Chapters 5 to 8). The inclusion of a TS in the 2D models drastically increased the computer time needed to solve the TPE. For 3D time-dependent TS models the penalty that one must pay in terms of computer time and memory is still too high. The numerical codes also become drastically more complex when including a TS, so that practical utilization of a 3D time-dependent TS model is still beyond the capabilities of current desktop computers.

3.4. Numerical methods for solving the transport equation

From Equation 3.7 it is evident that the TPE is a partial differential equation (PDE) of the form

$$\frac{\partial f}{\partial t} = a_0 \frac{\partial^2 f}{\partial r^2} + b_0 \frac{\partial^2 f}{\partial^2 \theta} + c_0 \frac{\partial f}{\partial r} + d_0 \frac{\partial f}{\partial \theta} + e_0 \frac{\partial f}{\partial \ln p} + Q_{source}, \tag{3.9}$$

with coefficients

$$\begin{aligned} a_0 &= K_{rr} \\ b_0 &= \frac{K_{\theta\theta}}{r^2} \\ c_0 &= \frac{1}{r^2}\frac{\partial}{\partial r}(r^2 K_{rr}) + \frac{1}{r\sin\theta}\frac{\partial}{\partial \theta}(K_{\theta r}\sin\theta) - V \\ d_0 &= \frac{1}{r^2}\frac{\partial}{\partial r}(r K_{r\theta}) + \frac{1}{r^2\sin\theta}\frac{\partial}{\partial \theta}(K_{\theta\theta}\sin\theta) \\ e_0 &= \frac{1}{3r^2}\frac{\partial}{\partial r}(r^2 V). \end{aligned} \tag{3.10}$$

This TPE is a linear second-order parabolic PDE in four variables (two spatial variables r and θ, rigidity R, and time t). Various solutions of PDEs with finite difference methods were discussed in detail by Steenkamp (1995). In this section the LOD and Alternating Direction Implicit (ADI) methods which have been used extensively in

various numerical modulation models will be discussed briefly. Both these methods were tested against each other and it was found that they gave solutions that were qualitatively the same so that from a physics point of view they would therefore be considered equally good (see e.g., Lapidus and Pinder, 1982 for a comparison of the LOD and Peaceman-Rachford ADI algorithm). However, the LOD method is used for the TS model which has been developed in this work simply because the usage of computer memory and time has been less, which is still a major consideration. These aspects will be discussed in the following sections.

The starting point of any numerical solution of a PDE is the finite difference formulae and therefore it will be discussed next.

3.4.1. Finite difference formulae

Finite difference methods are discrete techniques that are used when the domain of interest is represented by a set of points or nodes, forming a structured grid with definite boundaries. Information between these nodes or points is then obtained by a Taylor series expansions. These expansions are used to approximate the PDE with a discrete difference equation. The transformation of the PDE into the discrete difference equation is frequently called the discretization of the PDE. In order to discretize a PDE, one must start by replacing the partial derivatives with discrete approximations, which are called finite difference formulae.

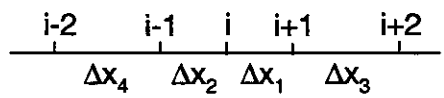

Figure 3.2. An uneven grid in one dimension using a general coordinate system.

In this section the finite difference approximations of first- and second-order derivatives will be given briefly for an uneven grid as is shown in Figure 3.2, where $\Delta x_1 \neq \Delta x_2 \neq \Delta x_3 \neq \Delta x_4$. Since the solution of the TPE may have steep gradients in certain regions of the heliosphere, e.g. at the TS, it is desirable to choose a fine mesh in those areas, in order to keep the numerical code stable. In other regions the gradients may change very slowly so that a fine mesh is unnecessary. For a complete derivation of these equations, see Steenkamp (1995).

The following conventions are used to denote the solutions at different grid points:

$$\begin{aligned} f(x-\Delta x_2-\Delta x_4) &= f_{i-2} \\ f(x-\Delta x_2) &= f_{i-1} \\ f(x) &= f_i \\ f(x+\Delta x_1) &= f_{i+1} \\ f(x+\Delta x_1+\Delta x_3) &= f_{i+2}. \end{aligned}$$

The central derivative formulae now yield the following expressions for the first

$$\frac{\partial f}{\partial x} = f' = \frac{-\Delta x_1}{\Delta x_2\,(\Delta x_1+\Delta x_2)} f_{i-1} + \frac{\Delta x_1-\Delta x_2}{\Delta x_1\,\Delta x_2} f_i + \frac{\Delta x_2}{\Delta x_1\,(\Delta x_1+\Delta x_2)} f_{i+1} \tag{3.11}$$

and second

$$\frac{\partial^2 f}{\partial x^2} = f'' = \frac{2}{\Delta x_2\,(\Delta x_1+\Delta x_2)} f_{i-1} - \frac{2}{\Delta x_1\,\Delta x_2} f_i + \frac{2}{\Delta x_1\,(\Delta x_1+\Delta x_2)} f_{i+1} \tag{3.12}$$

derivative, respectively. The second-order, one-sided differences yield

$$f' = -\frac{2\triangle x_1 + \triangle x_3}{\triangle x_1 (\triangle x_1 + \triangle x_3)} f_i + \frac{\triangle x_1 + \triangle x_3}{\triangle x_1 \triangle x_3} f_{i+1} - \frac{\triangle x_1}{\triangle x_3 (\triangle x_1 + \triangle x_3)} f_{i+2} \quad \text{(forward)} \tag{3.13}$$

and

$$f' = \frac{2\triangle x_2 + \triangle x_4}{\triangle x_2 (\triangle x_2 + \triangle x_4)} f_i - \frac{\triangle x_2 + \triangle x_4}{\triangle x_2 \triangle x_4} f_{i-1} + \frac{\triangle x_2}{\triangle x_4 (\triangle x_2 + \triangle x_4)} f_{i-2} \quad \text{(backward).} \tag{3.14}$$

In the case of an even grid, where $\triangle x_1 = \triangle x_2 = \triangle x_3 = \triangle x_4 = \triangle x$, Equations 3.11, 3.12, 3.13, and 3.14, respectively reduce to

$$f' = \frac{f_{i+1} - f_{i-1}}{2\triangle x} \quad \text{(centered)} \tag{3.15}$$

$$f'' = \frac{f_{i-1} - 2f_i + f_{i+1}}{(\triangle x)^2} \quad \text{(centered)} \tag{3.16}$$

$$f' = \frac{-3f_i + 4f_{i+1} - f_{i+2}}{2\triangle x} \quad \text{(forward)} \tag{3.17}$$

$$f' = \frac{3f_i - 4f_{i-1} + f_{i-2}}{2\triangle x}, \quad \text{(backward)} \tag{3.18}$$

which is their well known form.

3.4.2. The ADI method

Only a brief discussion will be given in this section on the ADI method. For detailed discussions see e.g., Potgieter (1984), Steenkamp (1995), and Hattingh (1998). ADI methods are extensions of the Crank-Nicolson implicit method that preserves the tridiagonal nature of the matrices to be inverted by employing an operator splitting technique that produces two or more (depending on the number of spatial dimensions) separate, but independent, difference equations. With these equations, a sequence of equations can be solved in each of the spatial dimensions. Douglas (1955) had initially developed this method to solve parabolic differential equations in terms of two spatial coordinates and time [e.g., (x, y, t) or (r, θ, t)]. The ADI-method was later modified by Douglas (1962) to include three spatial coordinates and a time coordinate (see also Potgieter, 1984). The ADI scheme for solving the TPE for two spatial dimensions and momentum was implemented in various numerical modulation models (e.g., Potgieter, 1984; Hattingh, 1993; Langner, 2000; Ferreira, 2002). In the Potchefstroom modulation group the numerical scheme for solving the TPE in three spatial dimensions (3D) and momentum was first developed by Williams (1990) for a flat HCS, and later by Hattingh (1998) for a 3D wavy HCS. The 3D numerical code was expanded by Ferreira (2002) to include a Jovian electron source.

To implement this method, i.e. for equations with two spatial dimensions and momentum (p), the first equation is used to solve implicitly in r for all θ in order to obtain a solution at a half momentum step forward, using the local interstellar spectrum (LIS) for each species as an initial condition. It is done by evaluating half of the difference equations in r at the present momentum step and half at a half momentum step forward (Douglas, 1962). A second solution is now obtained by solving implicitly in the θ for all r to get the solution at a full momentum step forward, by using the solution at the present momentum step and the previously calculated solution at half a momentum step forward. The result is a system of linear equations which can be solved using the Thomas algorithm (Steenkamp, 1995; Hattingh, 1998). This method has a local truncation error, e.g. $O\left[(\triangle t)^2 + (\triangle x)^2 + (\triangle y)^2\right]$ and is unconditionally stable (DuChateau and Zachmann, 1986; Lapidus and Pinder, 1982). Unfortunately the expansion to higher dimensions is not unconditionally stable (Lapidus and Pinder, 1982) so that the ADI method is less favourable.

3.4.3. The LOD method

The LOD and fractional splitting methods represent another approach to keep the matrices that have to be inverted tridiagonal. Fractional splitting methods are based on the fact that the differential operator in any parabolic PDE is a linear operator. For the equation

$$\frac{\partial u}{\partial t} = b_1 \frac{\partial^2 u}{\partial x^2} + b_2 \frac{\partial^2 u}{\partial y^2} \tag{3.19}$$

or

$$u_{tt} = b_1 u_{xx} + b_2 u_{yy}, \tag{3.20}$$

this linear differential operator is

$$L = b_1 \frac{\partial^2}{\partial x^2} + b_2 \frac{\partial^2}{\partial y^2}, \tag{3.21}$$

which is explicitly independent of t. Therefore Equation 3.19 may be written in terms of this linear differential operator (a linear transformation of the solution u) as

$$u_t = Lu. \tag{3.22}$$

Since L is a linear operator, it can be written as a linear combination of two other linear operators, $L = L_1 + L_2$, with $L_1 = b_1 \frac{\partial^2}{\partial x^2}$ and $L_2 = b_2 \frac{\partial^2}{\partial y^2}$ in the case of Equation 3.19.

With an expansion to more spatial dimensions the situation stays the same, and the linear differential operator may be written as $L = L_1 + L_2 + \cdots + L_n$, where n is the number of spatial dimensions (or physical processes). Now, a difference scheme was developed which replaces L with nL_1, nL_2, $\cdots$, nL_n, each operating for an interval $\Delta t/n$. In other words, the PDE may be split into a set of one-dimensional PDEs which can easily be solved by simpler one-dimensional methods. As may be anticipated, a PDE may be split in various ways. Some fractional splitting methods may even result in identical composite expressions that have been derived from the family of ADI approaches (see Lapidus and Pinder, 1982 for a comparison of the LOD and Peaceman-Rachford ADI algorithm).

A special case of the fractional splitting technique is the case where the PDE is split into a set of parabolic one-dimensional equations by splitting it with respect to its spatial variables. In this case Equation 3.19 becomes

$$\frac{1}{2} u_t = b_1 u_{xx} \tag{3.23}$$

and

$$\frac{1}{2} u_t = b_2 u_{yy}, \tag{3.24}$$

which can be solved individually with simpler one-dimensional methods (i.e., the Crank-Nicolson method), which are attractive because of increased stability and second order accuracy.

This method has a local truncation error $O\left[(\Delta t^2) + (\Delta x^2) + (\Delta y^2)\right]$ and is unconditionally stable (Lapidus and Pinder, 1982). Unfortunately, the LOD inherits all the problems of the Crank-Nicolson method and is therefore only accurate to second order in time for Equation 3.19 with $b_1 = b_2 = 1$. The LOD scheme implements in a way similar to the ADI, by first using the first equation (e.g., Equation 3.23) to calculate an intermediate solution and then using the second (e.g., Equation 3.24) to calculate a final solution for each time step. The major difference between the ADI and the LOD lies in the fact that the ADI calculates the final solution from the intermediate solution as well as the solution from the previous time step. Unlike the ADI, the extension of the LOD algorithm to more than three dimensions is almost trivial and stays unconditionally stable. This extension to three spatial variables, a momentum, and time variable, i.e. (r, θ, ϕ, p, t), can become very complex for the TPE because of the cross derivatives between the r and ϕ dimensions (see Equation 3.1) and is not used in this study although locally developed numerical codes already exist.

3.5. LOD solution of the time-dependent transport equation

In this section the implementation of the LOD method as has been discussed in the previous section will be shown for Equation 3.7. This application has been discussed in detail by Steenkamp (1995) and will therefore only briefly be repeated here. From Equation 3.9 with coefficients 3.10 and the theory of the LOD method, it is evident that the Parker TPE can be split into a system of three equations, each containing only derivatives in one dimension, giving

$$\frac{1}{3}\frac{\partial f}{\partial t} = a_0\frac{\partial^2 f}{\partial r^2} + c_0\frac{\partial f}{\partial r}, \tag{3.25}$$

$$\frac{1}{3}\frac{\partial f}{\partial t} = b_0\frac{\partial^2 f}{\partial \theta^2} + d_0\frac{\partial f}{\partial \theta}, \tag{3.26}$$

and

$$\frac{1}{3}\frac{\partial f}{\partial t} = e_0\frac{\partial f}{\partial \ln R} + Q_{source}. \tag{3.27}$$

Each of these equations is valid only on a third of the time step, i.e., Equation 3.25 (the radial equation) is valid on the interval $t' < t < t' + \Delta t/3$, Equation 3.26 (the polar equation) on $t' + \Delta t/3 < t < t' + 2\Delta t/3$, and Equation 3.27 (the energy equation) on $t' + 2\,\Delta\, t/3 < t < t' + \Delta t$. The radial and polar equations are of parabolic form and may therefore be solved with the Crank-Nicolson algorithm, but the energy equation is of first-order hyperbolic form and must be solved differently. The solution of the energy equation is constant along a set of characteristic curves (characteristics) in (R, t, f) space so that the method of characteristics is used to solve this equation, although different methods also exist, i.e., an explicit upwind method (e.g., Haasbroek, 1997). Each of the solutions is now obtained by specifying the LIS at the outer boundary, r_b, and starting with an empty heliosphere at time $t = 0$ and stepping in time until sufficient convergence (typically a steady-state) is reached.

Similarly, Equation 3.9 can also be split into a system of two equations:

$$\frac{1}{2}\frac{\partial f}{\partial t} = a_0\frac{\partial^2 f}{\partial r^2} + b_0\frac{\partial^2 f}{\partial \theta^2} + c_0\frac{\partial f}{\partial r} + d_0\frac{\partial f}{\partial \theta} \tag{3.28}$$

and

$$\frac{1}{2}\frac{\partial f}{\partial t} = e_0\frac{\partial f}{\partial \ln R} + Q_{source} \tag{3.29}$$

where Equation 3.28 can be solved by using the ADI method for two spatial dimensions and a time dimension (Haasbroek, 1997).

Successive time-dependent solutions can also be obtained, i.e. let the tilt angle vary from $\alpha = 10° \rightarrow 75°$ for the A > 0 cycle and back again from $\alpha = 75° \rightarrow 10°$ for the A < 0 cycle to complete a full $\sim$22 year cycle. Solutions for successive tilt angles are therefore obtained by using the solutions of the previous tilt angle as a starting point. This leads to solutions for the successive tilt angles that converge faster than when they are started with an empty heliosphere, as has been stated above.

3.6. LOD solution of the time-dependent transport equation with a discontinuity

The LOD solutions of Equations 3.25, 3.26, and 3.27 are sufficient to allow first order Fermi shock acceleration to be incorporated into the modulation model. Such a shock transition can now be modelled by letting the solar wind velocity (and other appropriate parameters) change continuously from the upstream to the downstream values over a series of grid points. This transition can be done sufficiently 'steep' by employing a transformed radial grid in the vicinity of the TS. However, this continuous transition of the solar wind velocity has caused an excess of

modulation at the TS, which will be illustrated and discussed in the next chapter. To avoid these problems a discontinuous transition of the solar wind velocity at the TS has been incorporated into the model to simulate the more realistic case where the flow velocity of the solar wind changes from supersonic to subsonic across a true infinitesimal distance. A complete description of this discontinuity at the TS and its incorporation into the numerical model is given by Steenkamp (1995) and partly by Steenberg (1998).

The handling of this discontinuity in the solution of the TPE, however, has presented a new problem. The radial streaming and the solution of the TPE, f , must stay continuous across the discontinuity (e.g., Equation 2.25). This yields the boundary condition that has been given in Equation 3.8, which is a first-order hyperbolic PDE in two variables, $\ln R$ and θ. Therefore, to solve the TPE with a discontinuous transition in the solar wind velocity, one must solve Equation 3.7 and Equation 3.8 simultaneously, where Equation 3.8 is in the general form

$$A_0 \left(\frac{\partial f}{\partial r}\right)^- = B_0 \left(\frac{\partial f}{\partial r}\right)^+ + C_0 \frac{\partial f}{\partial \ln R} + D_0 \frac{\partial f}{\partial \theta} + Q_0, \tag{3.30}$$

with coefficients

$$\begin{aligned} A_0 &= 1 \\ B_0 &= \frac{K_{rr}^+}{K_{rr}^-} \\ C_0 &= -\frac{V^- - V^+}{3K_{rr}^-} \\ D_0 &= -\frac{K_{r\theta}^- - K_{r\theta}^+}{r_s K_{rr}^-} \\ Q_0 &= \frac{Q_*}{K_{rr}^-}. \end{aligned} \tag{3.31}$$

The TPE is then valid in the domain $r_\odot \leq r < r_s$ and $r_s < r \leq r_b \; \forall \theta, R$ and the matching condition (Equation 3.30) is valid at $r = r_s \; \forall \theta, R$, with $r_\odot$ the radius of the Sun, $r_s = 90$ AU the TS location and $r_b = 120$ AU the outer boundary where the LIS is specified. As has been mentioned earlier, note that the source/sink function, $Q_{source} \neq 0$, in the TPE and Equation 3.27 only if there exist sources/sinks away from the discontinuity (e.g., a Jovian source). At the discontinuity it can have no effect since the TPE is not valid in the discontinuity. The part of the source/sink function that is singular in the shock, Q_*, is found in Equation 3.30. Equation 3.30 is a first order hyperbolic PDE in two variables (θ and $\ln R$) and may be solved with the second order accurate Wendroff's Implicit method (DuChateau and Zachmann, 1986; Steenkamp, 1995). To enhance the stability of this method, it is desirable to step the function in the direction in which drifts take place. Since drifts along the shock face change direction from one solar cycle to the next, this method must be used so that the function can step up or down the shock face depending on the drift cycle.

This model can therefore be used as a TS model with either a truly discontinuous transition or a continuous transition of the solar wind velocity at the TS by using the same method to find a solution. It is also 'downward compatible' in the sense that it can be used as a pure modulation model without acceleration at the TS by setting the compression ratio, $s = 1$ in Equation 2.53. This allows a constant solar wind velocity on both sides of the shock and the matching condition (Equation 3.30) therefore reduces to

$$\left(\frac{\partial f}{\partial r}\right)^- = \left(\frac{\partial f}{\partial r}\right)^+. \tag{3.32}$$

3.7. Boundary conditions, domains and initial values

To solve Equation 3.7 certain boundary conditions have to be used. In this section these boundary conditions, initial values and grid domains for the respective spatial, energy and time grids will be specified, as well as the values of the stepping parameters. These parameters and grid values are kept the same throughout this work except when it is stated otherwise. The influence of varying grids on model calculations will also be discussed below. The distribution function in terms of the numerical grid points is specified by

$$f(r_i, \theta_j, R_k, t_{st}) = f_{st,i,j,k}.$$

3.7.1. Time grid

The time grid is a simple linear relation which is generated by incrementing the time with an amount $\triangle t = 0.02$. The time grid is denoted by st and $st + 1/3$ represents a third time step ahead. The time starts at $t = 0$ and continues until sufficient convergence are reached, i.e. the difference between two successive solutions becomes sufficiently small. For galactic protons which are accelerated at the TS, 13 608 time steps are needed corresponding to a simulated time of ~3.2 years, however, for solutions where the acceleration at the TS is switched off, 7 293 time steps are needed corresponding to ~1.7 years. On an IBM 370 computer, 13 608 time steps in the TS model are done in ~2.5 hours real time.

3.7.2. Radial grid

Solutions were obtained on a radial grid ($i = 1 \rightarrow n$) with $n = 300$. The respective boundary positions are given by

$$\begin{aligned} r_1 &= \text{0.7 AU (the first grid point)}, \\ r_s &= \text{90 AU (TS position)}, \end{aligned}$$

and

$$r_n = r_b = \text{120 AU (outer boundary or LIS position)}.$$

The radial grid is transformed with uneven grid spacing, resulting in a fine grid in the inner heliosphere and on both sides of the shock, while large steps are given in the rest of the heliosphere where the grid increases exponentially. This is needed because mathematical limits are approximated at the TS with second-order difference formulae. This transformation is general and can be used for any value of n and boundary positions. It consists of four regions where the parameters have been chosen so that the r_i is continuous throughout the heliosphere. The transformation is given by

$$\begin{aligned} r_i &= \frac{r_s}{2}(\cos(\pi - a - \frac{ib\pi}{180}) + 1) \text{ if } i < \frac{2n}{3} - 0.15n, \text{ with } i_{tel1} = i_{tel1} + 1 \\ r_i &= \frac{r_s}{2}(\cos(\pi - a - \frac{b(i_{tel2}e + i_{tel1})\pi}{180}) + 1) \text{ if } \frac{2n}{3} - 0.15n \leq i < r_s, \text{ with } i_{tel2} = i_{tel2} + 1, \\ r_{2n/3} &= \text{90 AU}, \\ r_i &= r_s(\cos(\pi - g - \frac{\pi h(u_2 i_{tel3} + u_3 - 2n/3 - 0.05n)}{180}) + 2) \text{ if } r_s < i \leq 0.05n, \text{ with } i_{tel3} = i_{tel3} + 1 \\ r_i &= r_s(\cos(\pi - g - \frac{\pi h(i - 2n/3 - 0.05n)}{180}) + 2) \text{ if } r_s > 0.05n \end{aligned} \tag{3.34}$$

and

$$r_n = 120 \text{ AU}$$

with

$$\begin{aligned}
a &= -\arccos(\frac{2r_1}{r_s} - 1) + \pi, \\
b &= \frac{c-d}{\frac{2n}{3} - 0.15n}, \\
c &= -\frac{180}{\pi}\arccos(\frac{2(r_s-1)}{r_s} - 1) + 180, \\
d &= -\frac{180}{\pi}\arccos(\frac{2r_1}{r_s} - 1.0) + 180, \\
e &= \frac{f - (\frac{2n}{3} - 0.15n - 1)}{0.15n + 1}, \\
f &= \frac{180(\pi - a)}{b\pi}, \\
g &= -\arccos(\frac{r_s+1}{r_s} - 2) + \pi, \\
h &= \frac{u_1 - g}{n - 2n/3 - 0.05n}, \\
u_1 &= -\frac{180}{pi}(\arccos(\frac{r_n}{r_s} - 2) - \pi + g), \\
u_2 &= (2n/3 + 0.05n + 1 - u_3)/(0.05n + 1), \\
u_3 &= \frac{180g}{-h\pi} - 1 + 2n/3 + 0.05n + 1.
\end{aligned}$$

Note that i_{tel1}, i_{tel2}, and i_{tel3} start at 1 at $i = 1$ and are only valid in the regions where they are specified; all angles are specified in radians. In Figure 3.3 these transformed radial grid values, r_i, are shown as a function of the radial stepping parameter, i.

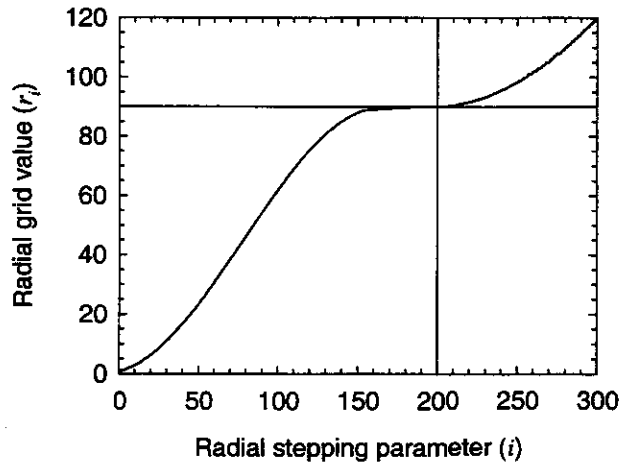

Figure 3.3. The transformed radial grid values, r_i, as a function of the radial stepping parameter, i. The reference lines denote the position of the TS.

Three boundary conditions are also specified on this grid:

(1) The heliosphere is taken to be spherical with an outer boundary at $r_b = 120$ AU where a relevant LIS ($f_g(R)$) is specified as input spectrum so that

$$f(r_b, \theta, R) = f_g(R) \tag{3.35}$$

for galactic CRs or a free escape boundary for the ACRs with

$$f(r_b, \theta, R) = 0 \tag{3.36}$$

or in expanded time-centered implicit form

$$f_{st+1/3,n,j,k} = f_g(R) \text{ or } 0 \tag{3.37}$$

for all values of θ and R, depending on whether the solutions have to include a galactic source or only an anomalous source. The relation between rigidity R and momentum p is given by $R = pc/q$, where c is the speed of light in space and q the charge of the particle. The different LIS for the different species and the source spectra for the ACRs will be discussed in Chapter 5 for protons, Chapter 6 for anti-protons, Chapter 7 for electrons and positrons and Chapter 8 for Helium.

(2) The boundary condition at the inner boundary, r_1, is assumed to be an absorbing boundary

$$\left.\frac{\partial f}{\partial r}\right|_{\lim r \to r_1^+} = \left.\frac{\partial f}{\partial r}\right|_{\lim r \to r_1^-}. \tag{3.38}$$

This implies that particles can enter (or leave) this boundary. If the radial grid is chosen so that $r_1 - r_0 = r_2 - r_1 = \triangle r$, with r_0 and r_2 the grid points just inside and just outside r_1, respectively, then Equation 3.38 becomes

$$f_{st+1/3,0,j,k} = 2f_{st+1/3,1,j,k} - f_{st+1/3,2,j,k} \tag{3.39}$$

in expanded time-centered implicit form.

A reflecting boundary, implying that no particles can enter or leave this boundary, can also be used where

$$\left.\frac{\partial f}{\partial r}\right|_{r=r_1} = 0. \tag{3.40a}$$

If the radial grid is again chosen so that $r_1 - r_0 = r_2 - r_1 = \triangle r$, then the derivative with respect to r can now be approximated by a central difference as

$$\frac{\partial f}{\partial r} = \frac{f_{st+1/3,2,j,k} - f_{st+1/3,0,j,k}}{2 \triangle r}. \tag{3.41}$$

This implies that in expanded time-centered implicit form

$$f_{st+1/3,0,j,k} = f_{st+1/3,2,j,k}. \tag{3.42}$$

Siluszyk and Alania (2001) showed that Equation 3.38 for an absorbing boundary could be a more appropriate boundary condition than Equation 3.40a for a reflecting boundary. However, comparisons between model calculations for these two different boundary conditions showed that this model was surprisingly insensitive to this feature and no effect was present further than 0.15 AU from r_1.

(3) At the TS (if present) the distribution function and the radial streaming are assumed to be related by $f^- = f^+$ and $S_r^+ - S_r^- = Q_*$. The boundary conditions at the TS in expanded time-centered implicit form approaching from the upstream medium then become

$$f^-_{st+1/3,n_s,j,k} = f^+_{st+1/3,n_s,j,k}, \tag{3.43}$$

where n_s denotes the position of the shock, and leaving the TS in the downstream region

$$\begin{aligned} f^+_{st+1/3,n_s,j,k} \;=\; & \frac{B_0^+}{D_{div}} f_{st+1/3,n_s+1,j,k} + \frac{B_0^{++}}{D_{div}} f_{st+1/3,n_s+2,j,k} - \frac{A_0^-}{D_{div}} f_{st+1/3,n_s-1,j,k} - \frac{A_0^{--}}{D_{div}} f_{st+1/3,n_s-2,j,k} \\ & + W\left(f_{st+1/3,n_s,j,k-1} - f_{st+1/3,n_s,j+\varsigma,k}\right) + \varsigma Z f_{st+1/3,n_s,j+\varsigma,k-1} + Q_0) \end{aligned} \tag{3.44}$$

with

$$D_{div} = A_0 - B_0 + \varsigma Z. \tag{3.45}$$

Here A_0, B_0, C_0, and D_0 represent the coefficients that have been given in Equation 3.30; A^-, A^{--}, B^+, and B^{++} are the coefficients of the second-order one-sided differences as have been given in Equations 3.13 and 3.14, and

$$W = -\varsigma \frac{1}{2}\left(\frac{D_0}{\triangle\theta} + \varsigma \frac{C_0}{\triangle \ln R}\right) \tag{3.46}$$

and

$$Z = \frac{1}{2}\left(\frac{D_0}{\triangle\theta} - \varsigma \frac{C_0}{\triangle \ln R}\right). \tag{3.47}$$

3.7.3. Polar grid

A polar grid ($j = 1 \rightarrow m$) with $j_1 = 0°$ and $m = 37$ or 73, respectively, can be used depending on whether the second polar boundary is specified at $j_m = 90°$ or 180°. Solutions for this linear grid were obtained in steps of $\triangle\theta = 2.5°$. The heliosphere is assumed to be symmetrical about the poles and the equatorial plane, which implies that

$$\left.\frac{\partial f}{\partial \theta}\right|_{\theta=0,\pi/2,\pi} = 0 \tag{3.48}$$

at these positions in the heliosphere. The polar grid can therefore be changed accordingly to obtain solutions for $\theta = 0° \rightarrow 90°$ or $\theta = 0° \rightarrow 180°$, without having an effect on the solutions, however, $j_m = 90°$ has been used for this work, because of computer time considerations. If the polar grid has been chosen so that $\theta_1 - \theta_0 = \theta_2 - \theta_1 = \triangle\theta$ and $\theta_{m+1} - \theta_m = \theta_m - \theta_{m-1} = \triangle\theta$, with θ_1 and θ_m the first and last grid points respectively, then

$$\frac{\partial f}{\partial \theta} = \frac{f_{st+1/3,i,2,k} - f_{st+1/3,i,0,k}}{2\triangle\theta} = 0 \tag{3.49}$$

or

$$f_{st+1/3,i,0,k} = f_{st+1/3,i,2,k} \tag{3.50}$$

at the first boundary ($j_1 = 0°$); At $j_m = 90°$ the boundary conditions are obtained in the same way and it gives

$$f_{st+1/3,i,m+1,k} = f_{st+1/3,i,m-1,k}. \tag{3.51}$$

3.7.4. Rigidity grid

The rigidity grid ($k = 1 \rightarrow nR$) is linear, i.e. $\triangle \ln R$ = constant, between a lower ($k_1 = R_{min}$) and upper ($k_{nP} = R_{max}$) boundary value. The lower boundary varied for the different species; for protons, anti-protons and Helium $R_{min} = 0.05$ GV, while for electrons and positrons $R_{min} = 0.001$ GV. The step length from R_{min} upwards is then given by $\triangle \ln R = 0.06$ for nR steps which is the same for all species, where nR has been adjusted accordingly so that the magnitude of $R_{max} \approx 20$ GV, corresponding to an energy of ~20 GeV for all species. At R_{max} no modulation is assumed.

3.7.5. Grid ratios and stability

The solutions were surprisingly stable for variations in the stepping parameters of the different grids. The variance between the spectra for a radial grid with $n = 300$ and $n = 420$ was less than 5 %. An even smaller value for n (down to ~ 180) could be chosen where solutions for only one tilt angle was required, but the value of $n = 300$ was chosen to be optimal for successive solutions in the tilt angle. For the polar grid, the variance between the spectra was even less with $\triangle\theta = 2.5°$ or $\triangle\theta = 3.0°$. However, the polar grid had to be chosen sufficiently small in

order for changes of the solar wind velocity to happen over more than one grid point. The value $\Delta \ln R = 0.06$ for the rigidity grid was also quite optimal and smaller values did not contribute substantially to the accuracy of the solutions, while larger values led to instabilities, especially at higher rigidities (see also Steenkamp, 1995).

The time grid is however the most important parameter, because too large values ($\Delta t > 0.04$) can lead to serious instabilities, especially at higher rigidities, while for too small values ($\Delta t < 0.02$) a heavy price is paid on computer time, because the runtime of the model is proportional to the number of time steps. These instabilities at large values of Δt arise from the method of characteristics as has been described in Steenkamp (1995). There also exists a relationship between the time and radial grids. This is similar to the stability criteria which have been imposed on explicit and some implicit methods to solve PDEs, which place restrictions on the ratio $\Delta t / \Delta x$, where Δx is a spatial grid spacing. le Roux (1990) and Steenkamp (1995) give this stability condition as

$$\left| (V + \langle \mathbf{v}_d \rangle_r) \frac{\Delta t}{\Delta r} \right| \leq 1. \tag{3.52}$$

This means that if the radial grid is refined by a certain amount, the time grid must also be refined by an equal amount, which can be quite inhibiting.

Another important condition for both stability and convergence has been the Courant condition

$$\frac{-\varrho \Delta t}{\Delta \ln R} < 1, \tag{3.53}$$

also known as the Courant-Friedrichs-Lewy stability criterion (Zwillinger, 1989), where ϱ is given by Equation 2.57. This condition implies that with $\Delta t > \Delta \ln R$ the solution cannot converge, but if the condition is satisfied the solution might converge.

In this model solutions for two consecutive time steps were tested and if

$$0.99999 \leq \frac{f_{st,i,j,k}}{f_{st-1,i,j,k}} \leq 1.00001, \tag{3.54}$$

where $f_{st,i,j,k}$ was the solution at the present time step and $f_{st-1,i,j,k}$ the solution at the previous time step, $f_{st,i,j,k}$ was considered as the final solution.

The stepping parameters for the different grids as described above were chosen to be optimal for this model, without losing the integrity of the model solutions or using too much computer resources.

3.8. The elements of the diffusion tensor

The diffusion coefficients of special interest for this study in Equation 3.7 are

$$K_{rr} = \kappa_{\parallel} \cos^2 \psi + \kappa_{\perp r} \sin^2 \psi, \tag{3.55}$$

$$K_{\theta\theta} = \kappa_{\perp \theta}, \tag{3.56}$$

with $\kappa_{\parallel}$ and $\kappa_{\perp}$ the diffusion coefficients parallel and perpendicular to the HMF respectively.

Figure 3.4 shows for illustrative purposes $\cos^2 \psi$ and $\sin^2 \psi$, see Equation 2.59, as a function of radial distance for the equatorial regions ($\theta = 90°$) and at the polar regions ($\theta = 10°$) and as a function of polar angle at $r = 1$ AU. From Equation 2.59 and Figure 3.4 follow that $\cos^2 \psi$ decreases with increasing radial distance for the polar regions and even more significantly for the equatorial regions. On the other hand, $\sin^2 \psi$ stays almost constant for most of the heliosphere, except for the inner heliosphere where it rapidly changes for both the polar and equatorial regions. This indicates that, although $\kappa_{\perp r}$ is usually $\leq 3\%$ of $\kappa_{\parallel}$, as will be discussed below, it dominates the term κ_{rr} in the outer heliospheric regions. On the other hand, $\kappa_{\parallel}$ dominates κ_{rr} in the inner heliosphere and in the

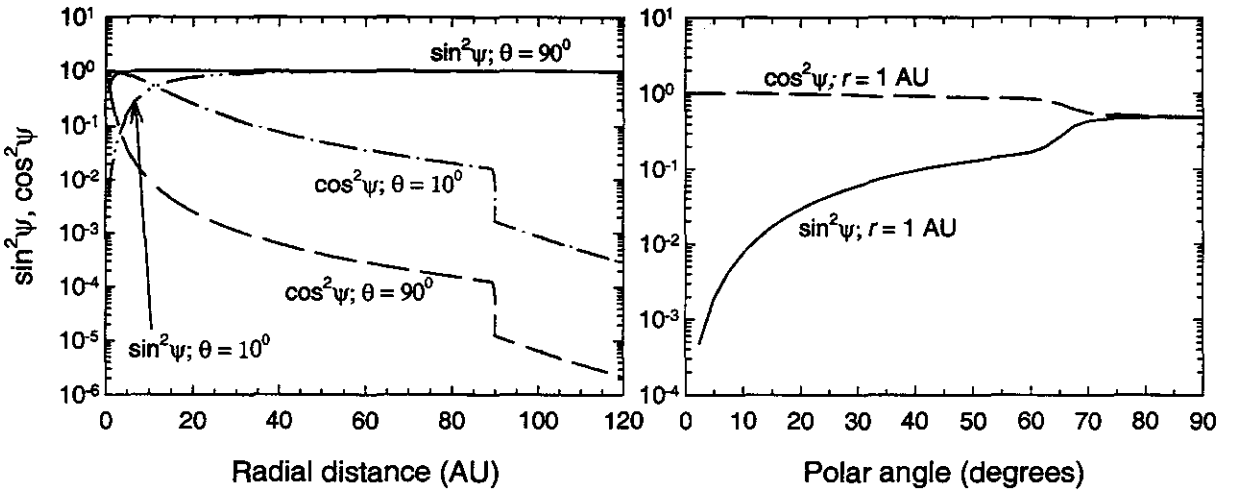

Figure 3.4. The values of $\cos^2\psi$ and $\sin^2\psi$ as a function of radial distance (left panel) in the equatorial plane ($\theta = 90°$) and for the polar regions ($\theta = 10°$) and as a function of polar angle at 1 AU (right panel). Here ψ is the spiral angle of the HMF as defined by Equation 2.59. The TS is at 90 AU.

polar regions.

Most of the recent work on the theory of diffusion coefficients has been done on perpendicular diffusion, because the theory behind parallel diffusion and drifts are thought to be in good shape (Teufel and Schlickeiser, 2002, 2003; Teufel et al., 2003; Stawicki, 2003). In this section a brief overview of the theory regarding diffusion coefficients in the heliosphere will be given, and a description of the diffusion coefficients to be used in this work. These diffusion coefficients are optimal for a numerical TS model without an azimuthal dependence and solar maximum effects e.g., global merged interaction regions. This set can also be used without additional changes for electrons, anti-protons, positrons, Helium, protons, and various anomalous sources to give reasonable fits to a variety of data sets (see Chapters 5 to 8) and is the same for both polarity cycles (Langner and Potgieter, 2003b; Langner et al., 2003b; Potgieter and Langner, 2003c).

3.8.1. Parallel diffusion

The basic physical process of diffusive propagation of CRs in the heliosphere is pitch angle scattering by fluctuations imposed by the HMF. This process can be described by weak turbulence quasi-linear theory (QLT). However, the interpretation of the fluctuations either as waves (e.g., Schlickeiser, 1988) or as dynamical turbulence (e.g., Bieber and Matthaeus, 1991) is still under discussion.

A long standing problem had been that the theoretical parallel mean free paths, $\lambda_{\parallel} = \kappa_{\parallel}\frac{3}{v}$ with v the speed of the particles, derived from the original QLT (Jokipii, 1966; Hasselmann and Wibberenz, 1968) were smaller than those from solar particle observations (Palmer, 1982). This is shown in Figure 3.5 where $\lambda_{\parallel}$ as has been predicted by standard QLT is shown as a function of rigidity. Filled and open symbols denote results derived from electron and proton observations, respectively. The shaded band is the observational consensus by Palmer (1982). The observations indicate a rigidity independent $\lambda_{\parallel}$ from 0.5 to 500 MV in contrast to QLT.

The $\lambda_{\parallel}$ as is predicted by standard QLT is given by

$$\lambda_{\parallel} = \frac{3v}{2}\int_0^1 \frac{(1-\mu^2)^2}{\Phi(\mu)}d\mu \tag{3.57}$$

with μ the cosine of the particle pitch angle and $\Phi(\mu)$ the Fokker-Planck coefficient for pitch-angle scattering

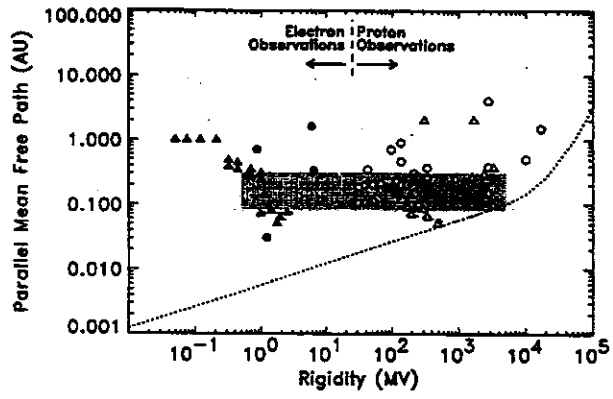

Figure 3.5. Parallel mean free path as a function of rigidity. Filled and open symbols denote results derived from electron and proton observations, respectively. The shaded band is the observational consensus by Palmer (1982). The dotted line represents the prediction of standard QLT (from Bieber et al., 1994).

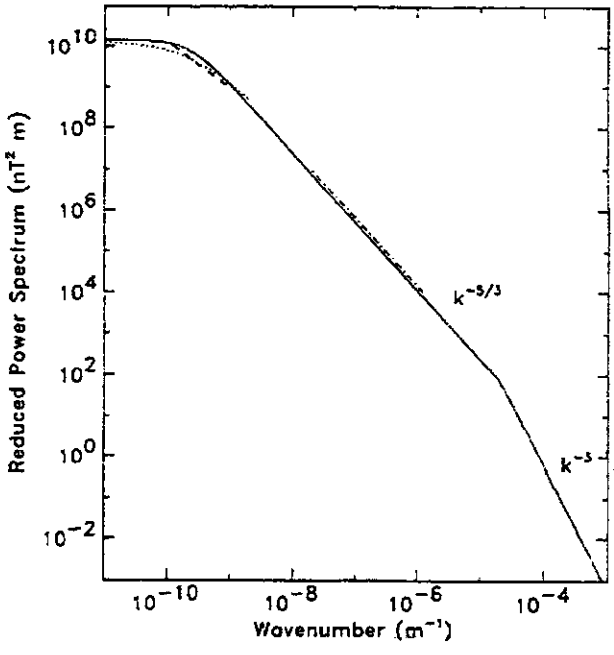

Figure 3.6. The power spectrum of the slab turbulence model (solid line) compared to observations (other lines). Note that the power spectrum can be divided into three ranges: The energy range where the power spectrum variation is independent of the wavenumber, k, the inertial range where it is proportional to $k^{-5/3}$, and the dissipation range where it is proportional to k^{-3} (from Bieber et al., 1994).

(Hasselmann and Wibberenz, 1970; Jokipii, 1971; Earl, 1974). To calculate $\Phi(\mu)$ a power spectrum of the magnetic field fluctuations is needed. Figure 3.6 shows an example of a power spectrum which can be divided in three ranges: The energy range where the power spectrum variation is independent of the wavenumber, k, the inertial range where it is proportional to $k^{-5/3}$, and the dissipation range where it is proportional to k^{-3}.

The dissipation range plays a significant role in the resonant scattering of low energy particles where the pitch angles of these particles approach 90°. In the original derivation of the $\lambda_{\|}$ the dissipation range was neglected (e.g., Jokipii, 1966; Fisk et al., 1974). However, it has become evident from magnetometer and plasma wave observations in the solar wind (e.g., Coroniti et al., 1982) that the magnetic fluctuation spectra typically exhibit a dissipation range. By neglecting the dissipation range, $\lambda_{\|}$ is too small at low rigidities, as is shown in Figure 3.5,

and has the wrong rigidity dependence (Bieber et al., 1994). However, this $\lambda_{\parallel}$ is applicable to proton modulation in the heliosphere because CR protons experience large adiabatic energy changes below ~300 MeV. At these lower energies the proton modulation is unaffected by changes in the $\lambda_{\parallel}$ (e.g., Potgieter, 1984). For electron modulation, the knowledge of the $\lambda_{\parallel}$ is vital because the CR electrons respond directly to changes in $\lambda_{\parallel}$, even for rigidities R < 100 MV.

Including the dissipation range, the original QLT predicts a $\lambda_{\parallel}$ which is infinite. This is because $\Phi(\mu)$ goes to zero more rapidly than without the dissipation range as the pitch angle approaches 90°. Figure 3.7 shows the Fokker-Planck coefficient for electrons that have been normalized to the particle's speed v as a function of the cosine of the pitch angle with and without the dissipation range. Values are shown at three different rigidities: 0.01 MV, 1 MV, and 100 MV. When $\Phi(\mu) \longrightarrow 0$ then from Equation 3.57 follows that $\lambda_{\parallel} \longrightarrow \infty$. A higher order theory is therefore needed.

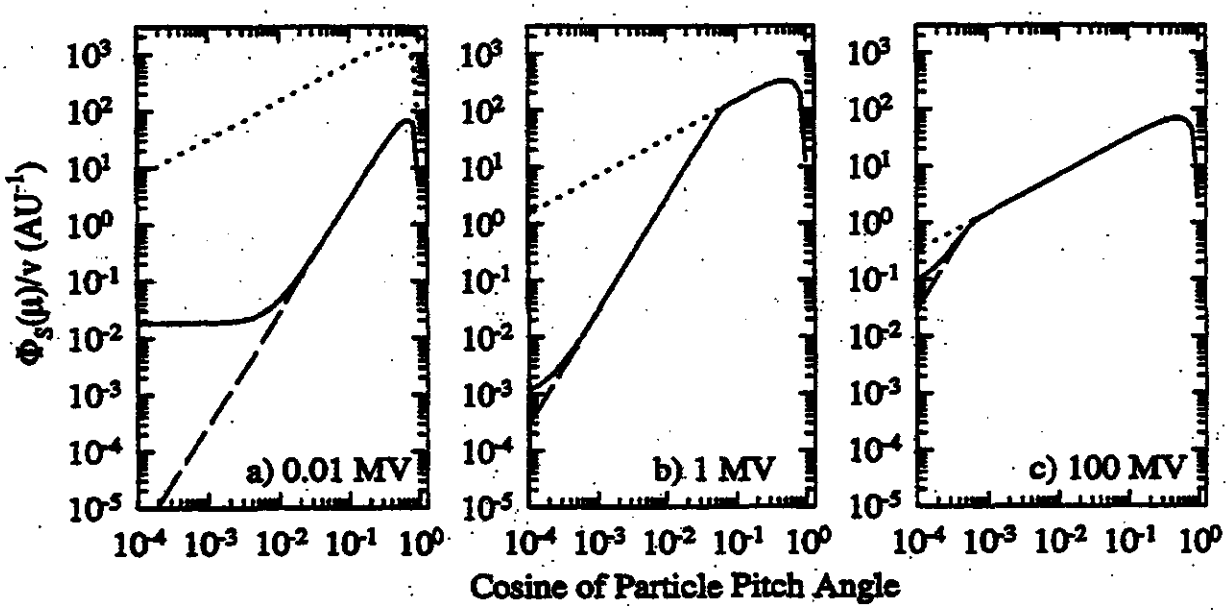

Figure 3.7. The Fokker-Planck coefficient for electrons normalized to the particle's speed (v) for slab geometry as a function of the cosine of the pitch angle calculated without the dissipation range (dotted lines) and with the dissipation range (dashed lines). The solid lines include the random sweeping model for dynamical turbulence. The coefficient is shown at three different rigidities (a) 0.01 MV (b) 1 MV and (c) 100 MV (from Hattingh, 1998).

Several mechanisms have been proposed to overcome this problem. Examples are mirroring by fluctuations of the magnetic field magnitude (Goldstein et al., 1975), a variety of nonlinear extensions of the theory of pitch angle scattering (e.g., Goldstein, 1976), wave propagation (Schlickeiser, 1988) and the effects of dynamical turbulence (Bieber and Matthaeus, 1991; Bieber et al., 1994). The latter introduced two dynamical turbulence models, namely the damping model and the random sweeping model. The inclusion of dynamical turbulence (in this case the random sweeping model) causes $\Phi(\mu)$ not to decrease to zero for small μ as is shown by the solid line in Figure 3.7 which leads to a finite $\lambda_{\parallel}$ at the lower energies (smaller μ).

Parallel mean free paths as have been predicted by the two models for dynamical turbulence (Bieber et al., 1994), namely the damping model and the random sweeping model, are shown in Figure 3.8 as a function of rigidity. The left panels show the predictions only for slab geometry, while the right panels show the predictions for slab

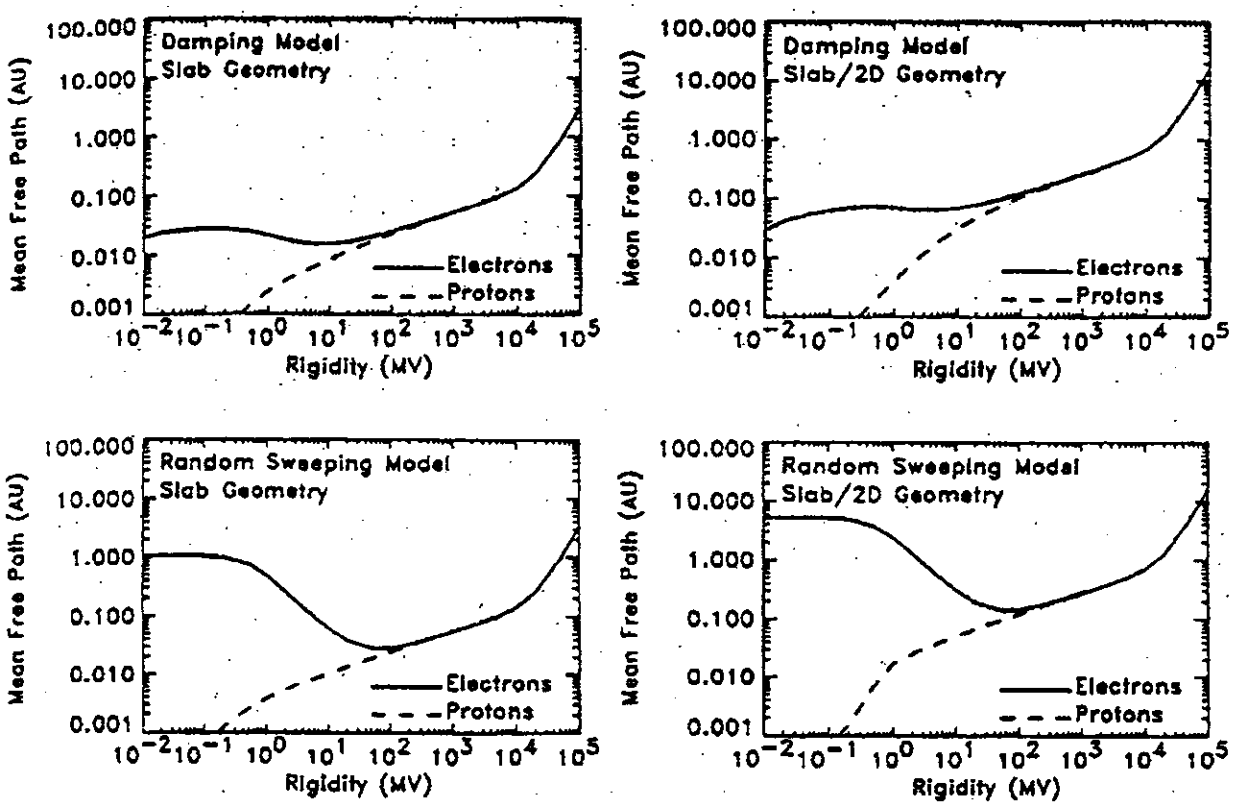

Figure 3.8. The parallel mean free path at Earth as predicted by the two models for dynamical turbulence (Bieber et al., 1994). The two top panels correspond to the damping model and the two bottom panels to the random sweeping model. The left panels show the predictions only for slab geometry and the two right panels for the composite slab/2D geometries (from Dröge, 2000).

and two dimensional (2D) geometry. In the slab magnetic turbulence geometry the perturbation wave vectors are aligned with the mean magnetic field of the Sun, while in the 2D geometry the wave vectors are perpendicular to the mean magnetic field.

The 2D geometry resulted from arguments from Bieber et al. (1994) who showed that on the basis of observed $\lambda_\parallel$ in the ecliptic plane, a purely slab model of interplanetary magnetic turbulence (Jokipii, 1966) is inappropriate. These authors instead suggested a composite model comprising a superposition of a dominant 2D component and a minor slab component. The two right panels in Figure 3.8 show the predictions for the composite slab/2D geometries where approximately 80% is 2D and the remainder in slab fluctuations. In both the inertial and energy ranges, the 2D component is effectively invisible (e.g., Zank et al., 1998). However, the reduction of the slab component to 20% leads to a larger $\lambda_\parallel$ at all energies. An interesting aspect from Figure 3.8 is that the proton and electron $\lambda_\parallel$ may be fundamentally different at low to intermediate rigidities (< 50 MeV) because of an explicit speed dependence of $\lambda_\parallel$ (see Equation 3.57).

The expressions for the diffusion coefficients $\kappa_\parallel$, $\kappa_\perp$, and κ_A which have been used in this work are similar to those that have been given by Burger et al. (2000) for a steady-state model, except for minor changes to their values that are caused by the introduction of the TS in this model (see also Langner et al., 2003b). These changes are insignificant for both polarity cycles at Earth but become more significant with increasing radial distance. They are based and motivated on diffusion (Burger and Hattingh, 1998) and turbulence theory (Zank et al., 1996), but have been adapted to reflect some of the results of numerical simulations by Giacalone and Jokipii (1999, 2001). For the diffusion parallel to the magnetic field QLT and a slab/2D geometry (20%/80%) for the turbulence is used.

The power spectrum for the magnetic fluctuations in terms of the wave number k is proportional to $k^{-5/3}$ in the inertial range and changes discontinuously from k^{-1} to k^0 in the energy range. The resonant rigidity R for which this change occurs varies with the spatial position. This is emphasized by assuming $\xi \propto R$. This leads to

$$\kappa_{||} = \kappa_{\parallel}^{0} \frac{9vB_0^{5/3}l_s^{2/3}}{28\pi^2 s_{slab} C_s} \left(\frac{R}{c}\right)^{1/3}, \tag{3.58}$$

if the quantity $D = cB_0 l_s/R \equiv l_s/r_L$ with r_L the Larmor radius, is > 1, while if it is < 1:

$$\kappa_{||} = \kappa_{\parallel}^{0} \begin{cases} \frac{v}{8\pi^2 s_{slab} C_s l_s} \left(\frac{R}{c}\right)^2 \left[\frac{\xi_0}{4\xi} + \left(2 + \frac{\xi}{2\xi_0}\right) D^2 - \frac{1}{12}\left(\frac{8}{7} + \frac{\xi^3}{\xi_0^3}\right) D^4\right] & \text{if } \xi D \leq 1 \\ \frac{vB_0}{4\pi^2 s_{slab} C_s} \left(\frac{R}{c}\right) \left[\frac{1}{3} + D - \frac{1}{12} D^3\right] & \text{if } \xi D > 1 \end{cases}. \tag{3.59}$$

In these expressions, $\kappa_{\parallel}^{0} = 0.9$ is a dimensionless constant for all tilt angles and both polarity cycles, B_0 is the magnitude of the average magnetic field, $l_s = 0.031(l/l_e)$ AU $= 4.55 \times 10^9 (l/l_e)$ m is the wavelength for slab turbulence at the break point between the energy and the inertial range of the magnetic field power spectrum, l is the correlation length of the magnetic field with $l_e = 0.023$ AU $= 3.41 \times 10^9$ m its value at Earth, s_{slab} is the fraction of slab turbulence, $C_s = 0.06(\delta B^2/B_0^2)$ nT^2 is the level of turbulence and δB^2 is the variance of the magnetic field. Here $\xi = 10.0R$ in units of GV and the range 0.2 GV $\leq \xi \leq$ 100.0 GV, is applicable for both polarity cycles, with $\xi_0 = 1$ GV. This quantity determines the transition from $\lambda_{\parallel} \propto R$ to $\lambda_{\parallel} \propto R^2$.

To construct a diffusion tensor applicable to the whole heliosphere, Burger et al. (2000) used the spatial variations of $\delta B^2/B_0^2$ and l/l_e. This was done by assuming the heliosphere to be divided into three distinct regions with different turbulence mechanisms dominating in each region. An ionization cavity is defined with radius $r = 10$ AU, inside the ionization cavity a so-called 'stream-interaction' approach dominates in the slow solar wind region centered on the equatorial plane. A different approach, namely the 'undriven' approach, dominates in the high speed high latitude region (Hattingh, 1998). Outside the ionization cavity the 'pickup ions' approach dominates. For the first two regions, expressions for $\delta B^2/B_0^2$ and l/l_e by Zank et al. (1996) were used, while for the third region Hattingh (1998) and Burger and Hattingh (1998) derived an analytical expression based on the results of Zank et al. (1996).

For both polarity cycles an additional adjustment had to be made to the radial dependence of $\kappa_{||}$ for all tilt angles (α) given here in radians, for both polarity cycles, and for all species given by

$$\kappa_{\parallel}^{*} = \kappa_{||} \left(45.0 - \frac{r}{r_e}\right)^{-0.218\alpha + 0.289} \tag{3.60}$$

when 0.1 AU $< r <$ 45.0 AU, in order to fit the measured proton radial intensities in the inner heliosphere and at Earth. Comparisons with observations will be shown in the following chapter. The effects of this modification given by Equation 3.60 in the equatorial plane for $\alpha = 10°$ and both polarity cycles on the proton spectra at Earth and the radial intensities at 0.2 GeV are shown in Figure 3.9. From this figure it is clear that the modification gives higher intensities for $r \lesssim 40$ AU for the A > 0 cycle and $r \lesssim 20$ AU for the A < 0 cycle. This modification is decreased to a value of ~1.0 for $\alpha = 75°$, at all radial distances.

Burger et al. (2000) calculated the diffusion coefficients in Equations 3.58 and 3.59 for protons, neglecting the dissipation range and limited the validity of the equations to particles with rigidity $R > 0.1$ GV. These equations for $\kappa_{||}$ had to be altered for electrons (e^-) and positrons (e^+) throughout the heliosphere for $R \leq 0.1$ GV to reflect a near constant rigidity dependence ($R^{0.1}$) at Earth in this rigidity region in accordance with the latest fundamental calculations (e.g., Teufel et al. 2002) and the damping model (Figure 3.8).

Assuming these expressions for the different turbulence models dominating in different sectors in the heliosphere

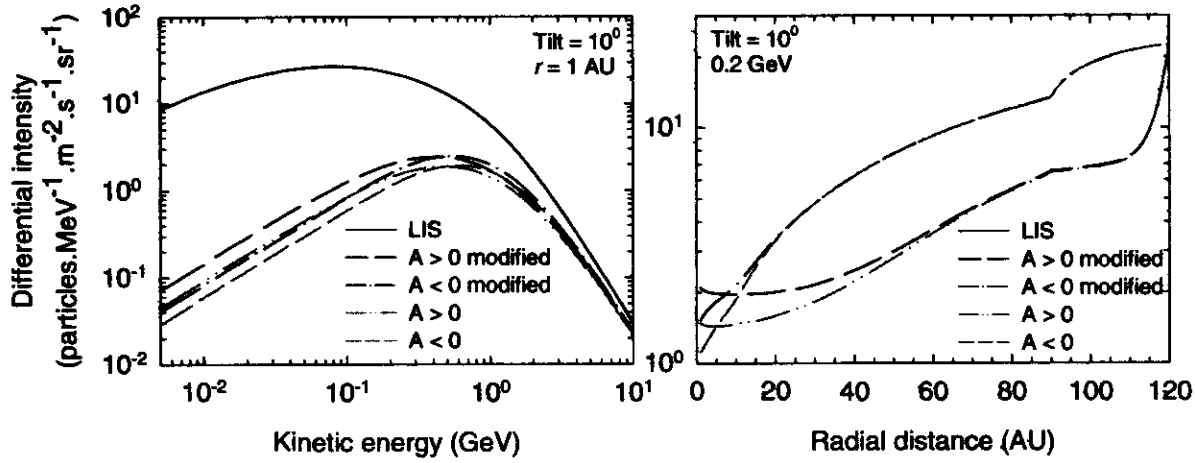

Figure 3.9. The effects of the modification given by Equation 3.60 in the equatorial plane for $\alpha = 10°$ and both polarity cycles on the proton spectra at Earth (left panels) and the radial intensities at 0.2 GeV (right panels). The black lines represent spectra with $\kappa_{\parallel}^{*}$, while the gray lines represent spectra with $\kappa_{\parallel}$.

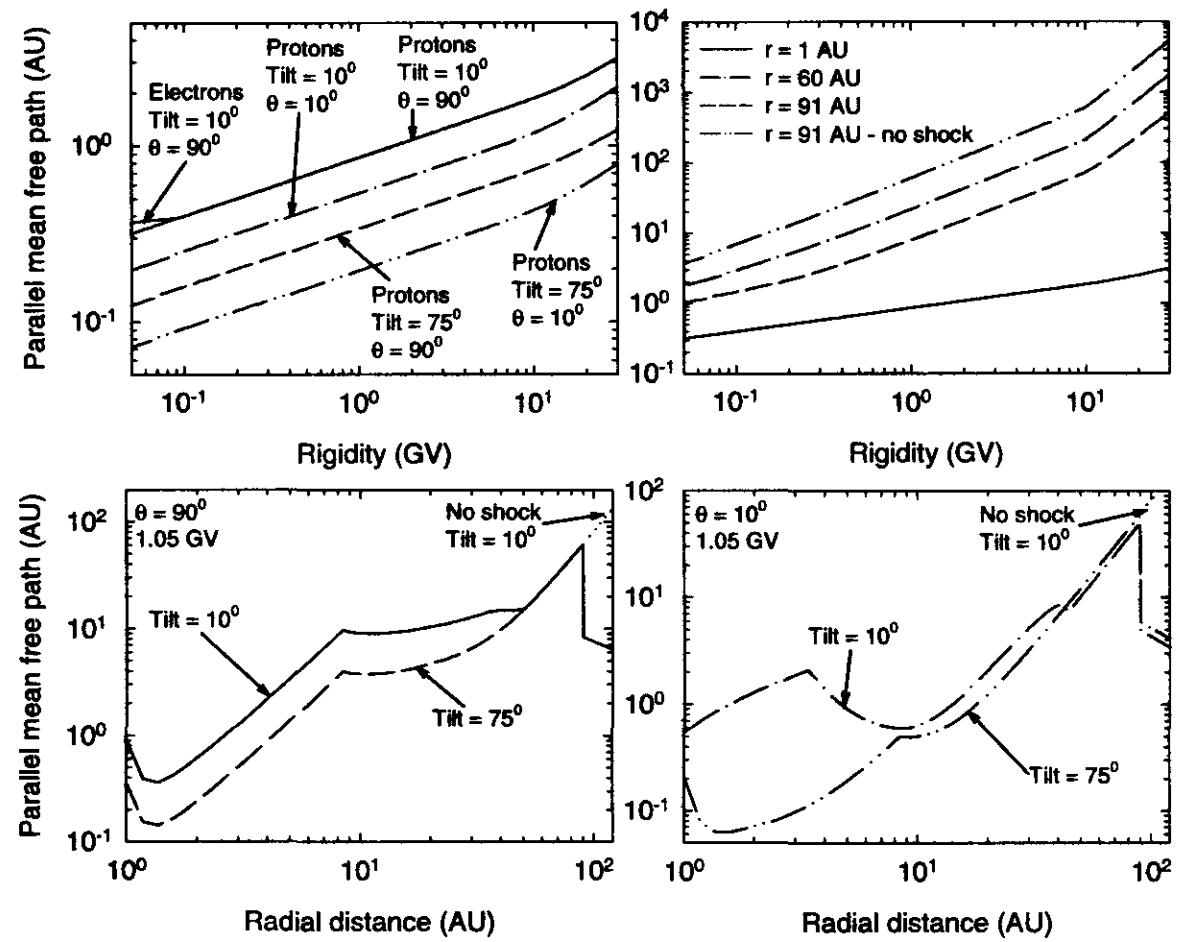

Figure 3.10. The parallel mean free path ($\lambda_{\parallel}$) as a function of rigidity (top panels) at 1 AU for the polar and equatorial regions and for solar minimum ($\alpha = 10°$) and moderate solar maximum ($\alpha = 75°$) activity (top left panel); also for radial distances of 1, 60 and 91 AU for a model with a TS and at 91 AU for a model without a TS in the equatorial plane (top right panel). In the bottom panels $\lambda_{\parallel}$ is shown as a function of radial distance for the equatorial plane (left panels) and the polar regions (right panels) for 1.05 GV particles, $\alpha = 10°$ and 75°, with and without a TS.

result in a $\lambda_{\parallel}$ with different spatial dependencies in different parts of the heliosphere. An example of the radial dependence of this $\lambda_{\parallel}$ is shown in Figure 3.10 at a rigidity of 1.05 GV in the equatorial plane and polar regions for $\alpha = 10°$ and 75°. Note the break in the radial dependence for the ionization cavity. Figure 3.10 also shows $\lambda_{\parallel}$ as a function of rigidity at 1 AU for the polar and equatorial regions with $\alpha = 10°$ and 75°, and for radial distances of 1, 60 and 91 AU for a model with a TS and at 91 AU for a model without a TS in the equatorial plane. It must be stressed again that the diffusion coefficients for the different CR particle species (except for e^- and e^+ at $R \leq 0.1$ GV) are the same for solar minimum activity for both polarity cycles, and the same for moderate solar maximum activity for both polarity cycles. Typical values as a function of rigidity for $\lambda_{\parallel}$ at Earth in the equatorial plane for protons in this model are between 0.07 AU - 1.5 AU, overall in good agreement with those values that have been given by Burger et al. (2000).

3.8.2. Perpendicular diffusion

Perpendicular scattering can be caused by two fundamental processes: (1) The gyrocentres of the particles are displaced transverse to the mean field because of scattering, and (2) the random walk of magnetic lines themselves. Both these processes which CRs experience are combined in the numerical models via a perpendicular diffusion coefficient $\kappa_{\perp}$. As has been mentioned above, $\kappa_{\perp}$ can be subdivided into two possibly independent coefficients, namely $\kappa_{\perp r}$ and $\kappa_{\perp \theta} = \kappa_{\theta\theta}$ which are perpendicular diffusion in the radial direction and in the polar direction, respectively. Because of its complexity, theoretical work on $\kappa_{\perp}$ was mostly neglected (see discussions by e.g., le Roux et al., 1999; Jokipii, 2001). As has been emphasized by Potgieter (1996) and Ferreira et al. (2000), who have studied the modulation of galactic electrons in the heliosphere, $\kappa_{\perp}$ is very important for CR modulation.

Because no exact theory exists as yet to adequately describe $\kappa_{\perp}$, it has become a standard and convenient practice when using modulation models to scale $\kappa_{\perp}$ as $\kappa_{\parallel}$ (e.g., Jokipii and Kóta, 1995; Potgieter, 1996; Ferreira et al., 2000; Burger et al., 2000; Ferreira et al., 2001a, 2001b). This assumption was largely vindicated by Giacalone and Jokipii (1999) who had found that $\kappa_{\perp}/\kappa_{\parallel}$ is in the range of 0.02 - 0.04 for rigidities between ~40 MV and ~1.7 GV. Earlier Giacalone (1998) found $\kappa_{\perp}/\kappa_{\parallel} = 0.02$ - 0.03 for rigidities between ~40 MV and ~2 GV. Unfortunately, owing to the geometry assumed in their calculations, no distinction was made between $\kappa_{\perp r}$ and $\kappa_{\perp \theta}$. However, studying the propagation of low-energy Jovian electrons, Ferrando (1997) found $\kappa_{\perp r}/\kappa_{\parallel} = 0.005$ and $\kappa_{\perp \theta}/\kappa_{\parallel} = 0.001$ at ~7 MeV.

Prior to the Ulysses mission, it was believed possible that CRs preferentially enter the heliosphere from above the Sun's poles in A < 0 HMF polarity cycles. However, observations with the Ulysses spacecraft in the inner heliosphere has shown that the latitude dependence of CR protons is significantly less than predicted by classical drift models (Potgieter and Haasbroek, 1993; Heber et al., 1996). Classical drift models predicted a large increase in intensity at high latitudes by a factor of ~3 for relatively low energies and ~1.6 for higher energies. However, the Ulysses observations showed essentially no change at low energies and an increase of about 30% at high energies.

This rather surprising result led Kóta and Jokipii (1995, 1997) to revive the concept that $\kappa_{\perp}$ might be anisotropic and that it should be larger in the polar direction than in the radial direction. This might arise naturally from the radial development of irregularities imposed by supergranulation at the surface of the Sun. It has since become standard practice to assume $\kappa_{\perp \theta} > \kappa_{\perp r}$ (e.g. Kóta and Jokipii, 1995; Potgieter, 1996; Burger et al., 2000; Ferreira et al., 2000; Ferreira et al., 2001a, 2001b) in modulation studies. Significant perpendicular diffusion not only results in more realistic latitudinal gradients of CRs, but can also explain the fact that CIR related increases and decreases

are observed at high latitudes without equivalent structures in the HMF (e.g., Jokipii et al., 1995; Kóta and Jokipii, 1998).

The effect of anisotropic perpendicular diffusion ($\kappa_{\perp\theta} > \kappa_{\perp r}$ in the off-equatorial regions) on CR electron modulation was studied in detail by Potgieter (1996), Ferreira (1998), and Ferreira et al. (2000). They found that when $\kappa_{\perp\theta}$ was increased from 5% to 15% of $\kappa_{\parallel}$, it resulted in a decrease of the radial dependence of the differential intensities at distances with large radial dependencies and an increase in the radial dependence of the differential intensities at distances with small radial dependencies. Similar effects are also visible for the A > 0 cycle. The increase in $\kappa_{\perp\theta}$ also resulted in the reduction of the latitudinal dependence of CR electron intensities at all radial distances.

It was shown by Potgieter (1997) and Potgieter et al. (1997) that, by assuming anisotropic perpendicular diffusion and by increasing $\kappa_{\perp\theta}$ relative to $\kappa_{\parallel}$ led to a remarkable reduction in drifts as experienced by CR protons. Increasing $\kappa_{\perp\theta}$ therefore smears out the signature of drifts. Potgieter (1996), Ferreira (1998), and Ferreira et al. (2000) found the same result for galactic CR electrons. Burger et al. (2000) illustrated that in order to produce the correct magnitude and rigidity dependence of the observed latitudinal CR proton density gradient by Ulysses, enhanced latitudinal transport was required (see also Potgieter et al., 1997).

Within the framework of QLT, employing the plasma wave approach, the diffusion along and perpendicular to the magnetic field have been considered at various levels of complexity by Shalchi (2003, pre-marital name: Teufel) and Stawicki (2003). Shalchi (2003) presented the first analytical calculation of the mean free path of energetic particles for different plasma turbulence models, in particular for the dynamic-magnetic slab turbulence. Semi-analytical results could be obtained for more complex scenarios, such as anisotropic turbulence. These studies were published in detail by Teufel and Schlickeiser (2002, 2003) and Teufel et al. (2003). Recent attempts to improve and understand the diffusion tensor based on turbulence theory and the theory of charged particle scattering were also made by Minnie (2002) and Parhi et al. (2003). They used the so-called 'ab initio' approach to modulation (see also Zank et al., 1998; Burger and Hattingh, 1998; Burger et al., 2000; Parhi et al., 2001, 2002). The development of an 'ab initio' theory faces at least three major challenges: Firstly, a satisfactory theory of diffusion perpendicular to the large scale magnetic field is non existent; secondly, perpendicular diffusion in two component slab/2D turbulence depends critically on an outer scale termed the 'ultrascale' about which very little observational information exists; and thirdly, the radial variation of both the perpendicular and parallel diffusion coefficients is strongly dependent on radial variations of the ordinary correlation length. However, variation of the correlation length is very poorly understood, in part owing to the uncertain impact of pickup ion-driven turbulence in the outer heliosphere (Zank et al., 1996; Zank et al., 1998; Smith et al., 2001) and in part owing to difficulties in measuring the correlation length in the relevant direction, namely, parallel to the magnetic field.

The diffusion perpendicular to the magnetic field in this work is also similar to that which is given in Burger et al. (2000) except for minor changes and it is assumed anisotropic, given by the two perpendicular diffusion coefficients:

$$\kappa_{\perp r} = \kappa_e^0 \frac{\delta B^2}{B_0^2} \kappa_{\parallel} \left(\frac{R}{R_0} \right)^{\gamma}, \tag{3.61}$$

and

$$\kappa_{\perp\theta} = g(\theta) \frac{\delta B^2}{B_0^2} \kappa_{\parallel} \left(\frac{R}{R_0} \right)^{\eta}, \tag{3.62}$$

with

$$g(\theta) = \frac{\kappa_p^0 + \kappa_e^0}{2} \mp \left(\frac{\kappa_p^0 - \kappa_e^0}{2} \right) \tanh \left[8 \left(\theta - \frac{\pi}{2} \pm \frac{25\pi}{180} \right) \right] \tag{3.63}$$

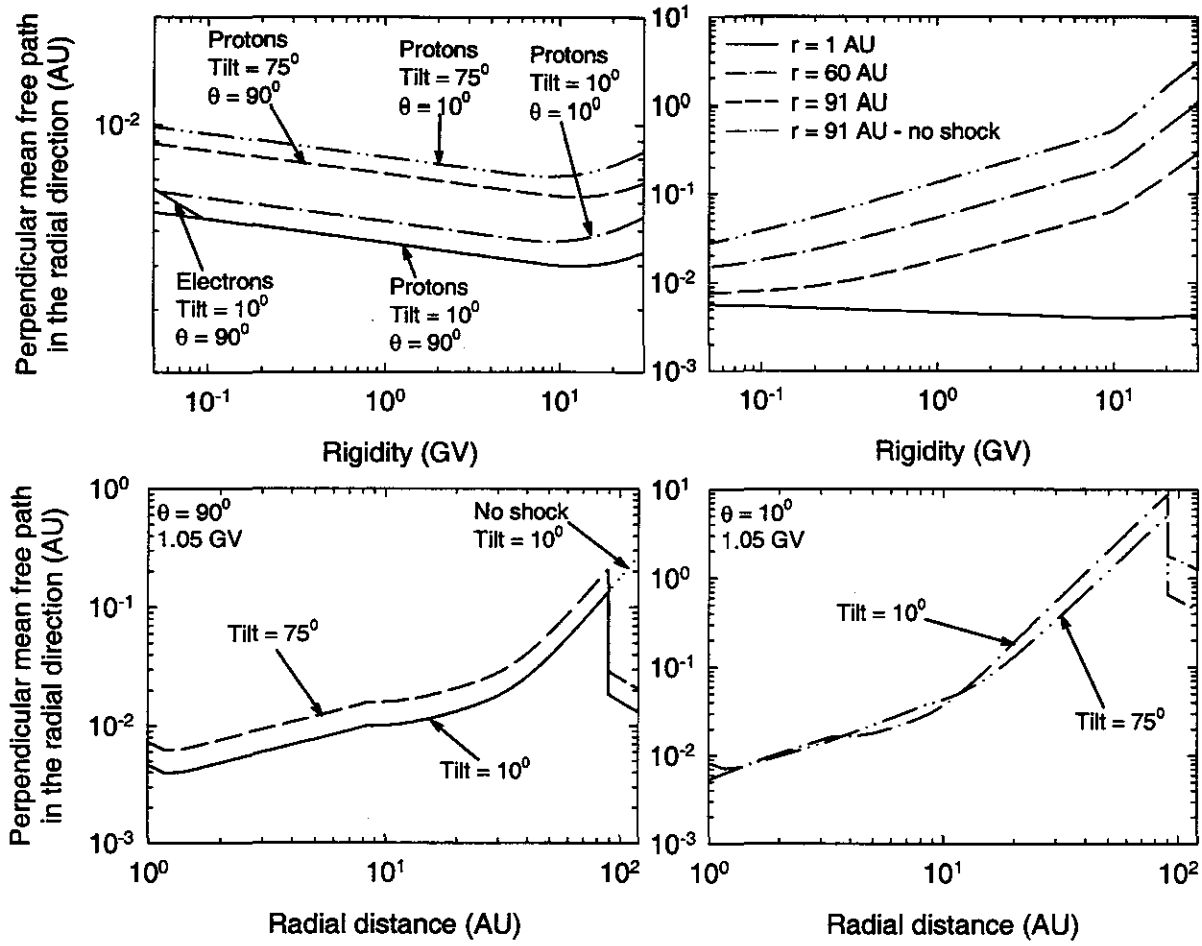

Figure 3.11. The perpendicular mean free path in the radial direction ($\lambda_{\perp r}$) as a function of rigidity (top panels) at 1 AU for the polar and equatorial regions and solar minimum ($\alpha = 10°$) and moderate solar maximum ($\alpha = 75°$) activity (top left panel) and also for radial distances of 1, 60 and 91 AU for a model with a TS and at 91 AU for a model without a TS in the equatorial plane (top right panel). In the bottom panels $\lambda_{\perp r}$ is shown as a function of radial distance for the equatorial plane (left panels) and the polar regions (right panels) for 1.05 GV particles and for $\alpha = 10°$ and 75°.

where θ the polar angle in radians and the top signs for $\theta \leq 90°$ and bottom signs for $\theta > 90°$ with $R_0 = 1$ GV. The quantities $\gamma = \eta = -0.4$ change the rigidity dependence of the perpendicular diffusion coefficients with respect to that of parallel diffusion. The quantities κ_p^0 and κ_e^0 are dimensionless. Diffusion perpendicular to the HMF is thus enhanced in the polar direction by assuming $\kappa_p^0 > \kappa_e^0$ according to Equation 3.63 (Kóta and Jokipii, 1995; Potgieter, 1996; Burger et al., 2000; Ferreira et al., 2000; Fichtner et al. 2000; Ferreira et al. 2001a, 2001b, 2001c). The quantities are $\kappa_p^0 = 0.185$ and $\kappa_e^0 = 0.026$ when $\alpha = 10°$. Increasing the tilt angle to $\alpha = 75°$ for moderate solar maximum conditions results in $\kappa_e^0 \rightarrow \sim 0.04$ and $\kappa_p^0 \rightarrow \sim 0.289$, respectively. This change for increasing α implies decreasing drifts with increasing activity as mentioned earlier. The magnitude of the enhancement towards the polar regions for $\kappa_{\perp\theta}$ is kept the same. A physical justification of this increase in $\kappa_{\perp\theta}$ toward the polar regions is given in Burger et al. (2000), basing their arguments on Ulysses measurements which have shown an increase in the variance of the components of the HMF, δB^2 in Equations 3.58 to 3.59, as it moved away from the equatorial plane to larger polar angles. The variance in the transverse and normal directions of the HMF increased more than in the radial direction resulting in larger diffusion in these directions. Furthermore, in a Fisk field (which is a more realistic HMF geometry at solar minimum, see Chapter 2) latitudinal transport is supposedly more effective than

in a Parker field and to account for this effect, $\kappa_{\perp\theta}$ is enhanced toward the polar regions when a Parker HMF is used.

An example of the radial dependence of $\lambda_{\perp r}$ and $\lambda_{\perp\theta}$ is shown in Figures 3.11 and 3.12, at a rigidity of 1.05 GV in the equatorial plane and polar regions for $\alpha = 10°$ and 75°. Figures 3.11 and 3.12 also show $\lambda_{\perp r}$ and $\lambda_{\perp\theta}$ as a function of rigidity at 1 AU, for the polar and equatorial regions with $\alpha = 10°$ and $\alpha = 75°$ and also for radial distances of 1, 60 and 91 AU for a model with and without a TS in the equatorial plane.

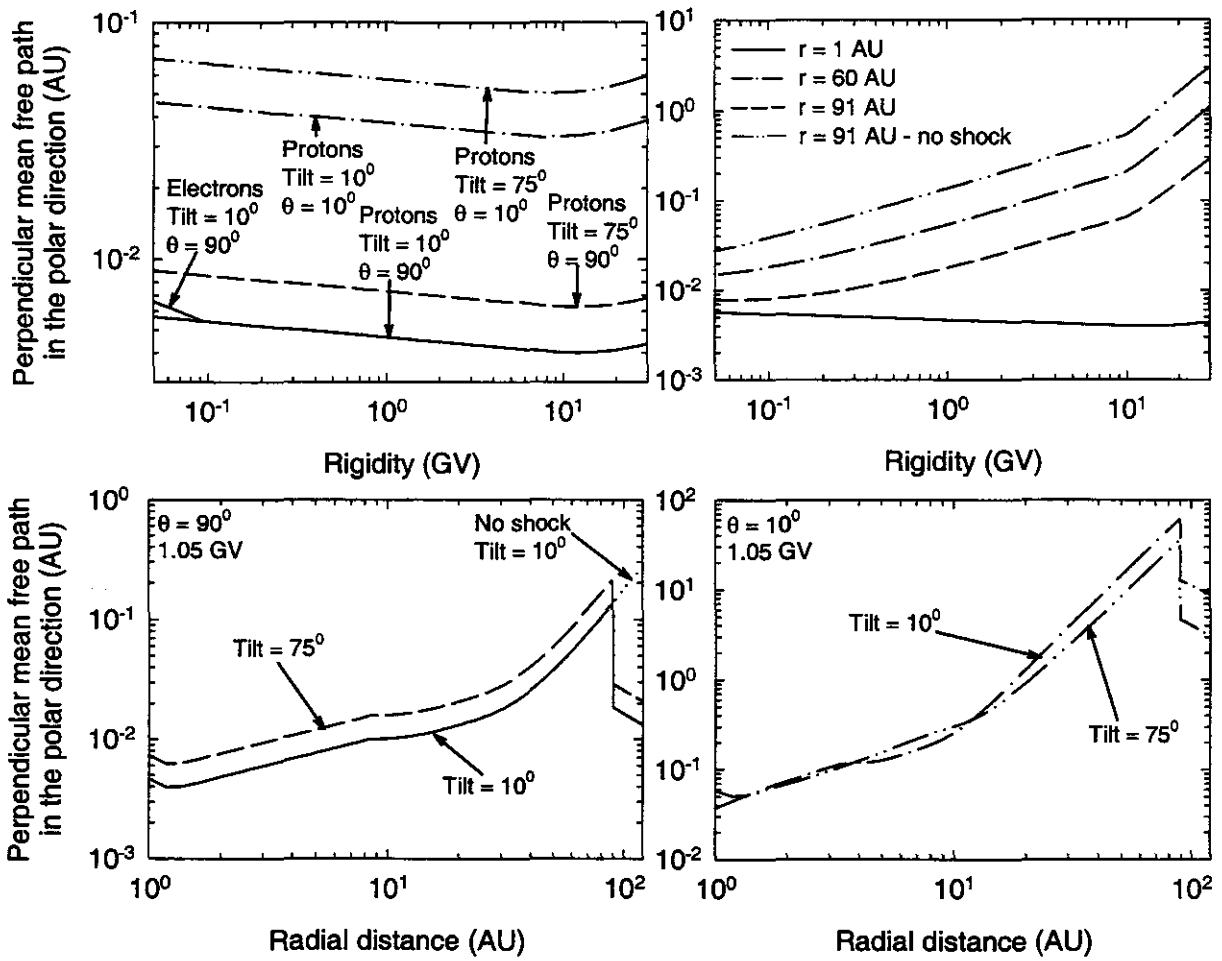

Figure 3.12. Similar to Figure 3.11, but for the perpendicular mean free path in the polar direction, $\lambda_{\perp\theta}$.

Typical values as a function of rigidity for $\lambda_{\perp r}/\lambda_{\parallel}$ at Earth for protons in this model are between 0.003 - 0.2 for 0.5 MV - 5.0 GV, as has been shown in Figure 3.13, overall in good agreement with those values which have been given by Burger et al. (2000), while the ratio $\lambda_{\perp r}/\lambda_{\perp\theta} \cong 1.0$ for these values.

3.8.3. Particle drifts

Although particle drifts were included in the original transport equation they had been neglected until Jokipii et al. (1977) pointed out that the inclusion of drifts could alter modulation, especially since drifts are sensitive to the polarity of the HMF leading to a charge asymmetry. The smooth global or background magnetic field affects the CR transport by contributing drift motions associated with the gradients in field magnitude, the curvature of the field and any abrupt changes in the field direction, such as the HCS. The components of the gradient, curvature

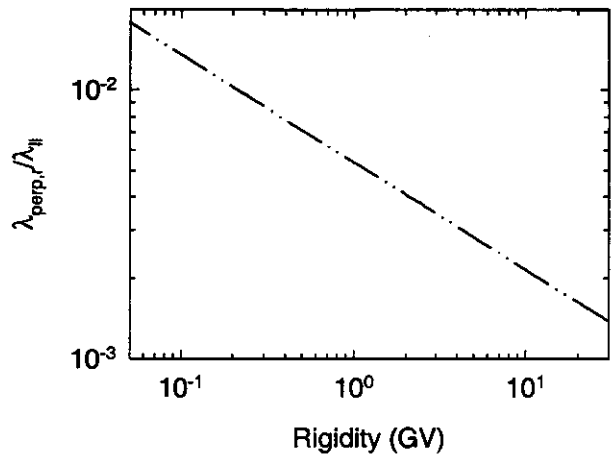

Figure 3.13. The ratio of $\lambda_{\perp r}/\lambda_{\parallel}$ at Earth as a function of rigidity for $\alpha = 10°$.

and current sheet drifts in Equation 3.1 are given in Equation 3.6 or alternatively by inserting the magnetic field, which is given by Equation 2.64 into Equation 2.2, thus

$$\begin{aligned} \mathbf{v}_d &= \boldsymbol{\nabla} \times \kappa_A \mathbf{e}_B \\ &= \left[\boldsymbol{\nabla} \times \left(\kappa_A \mathbf{e}_B^{'}\right)\right]\left[1 - 2H\left(\theta - \theta'\right)\right] + 2\delta\left(\theta - \theta'\right)\kappa_A \mathbf{e}_B^{'} \times \boldsymbol{\nabla}\left(\theta - \theta'\right) \\ &= \langle \mathbf{v}_d \rangle_m \left[1 - 2H\left(\theta - \theta'\right)\right] + \left(\mathbf{v}_{ns}\right)_m \delta\left(\theta - \theta'\right), \end{aligned} \tag{3.64}$$

with H the Heaviside function, and

$$\mathbf{e}_B = \left[1 - 2H\left(\theta - \theta'\right)\right]\mathbf{e}_B^{'}, \tag{3.65}$$

where

$$\mathbf{e}_B^{'} = \frac{\mathbf{B}}{B} = \frac{\mathbf{e}_r + \left(\frac{r\delta(\theta,\phi)}{r_\odot}\right)\mathbf{e}_\theta - \Gamma \mathbf{e}_\phi}{\sqrt{1 + \left(\frac{r\delta(\theta,\phi)}{r_\odot}\right)^2 + \Gamma^2}}, \tag{3.66}$$

and $\delta\left(\theta - \theta'\right)$ is the Dirac-function, as is given by

$$\delta\left(\theta - \theta'\right) = \begin{cases} 0 & \text{as } \theta \neq \theta' \\ \infty & \text{as } \theta = \theta' \end{cases}. \tag{3.67}$$

The first term in Equation 3.64 describes the gradient and curvature drifts which have been caused by the global magnetic field, and the second term describes drifts along the HCS.

In some of the 2D modulation models, such as the WCS model (Hattingh, 1993), the HCS is simulated by replacing the 3D drift velocity field by a 2D drift field. The 2D drifts are obtained by averaging Equation 3.64 over ϕ for one solar rotation to calculate the drifts along the HCS and the gradient and curvature drifts. The gradient and curvature drifts are then calculated by scaling the drifts in a region that is spanned by the current sheet from full drifts at the boundary of this region to zero at $\theta = \pi/2$ (Hattingh 1993; Hattingh and Burger 1995a; Burger and Hattingh 1995; Hattingh 1998). This scaling is caused by the simulated waviness of the current sheet. In the following chapter this WCS model is revisited in order to accommodate a magnetic field with a modification (Equation 2.64) as is used in this work and also to better approximate the WCS model for solutions with $\alpha > 40°$.

An example of gradient, curvature and current sheet drifts velocity directions are shown in Figure 3.14 for 2 GeV electrons and for both HMF polarity cycles. During A > 0 polarity epochs, e.g. ~1990 to ~2001, the HMF is directed outward in the northern hemisphere. Electrons then drift primarily from the equatorial boundary of the heliosphere along the HCS to the Sun. During A < 0 polarity epochs e.g. ~1980 to ~1990, the electrons drift

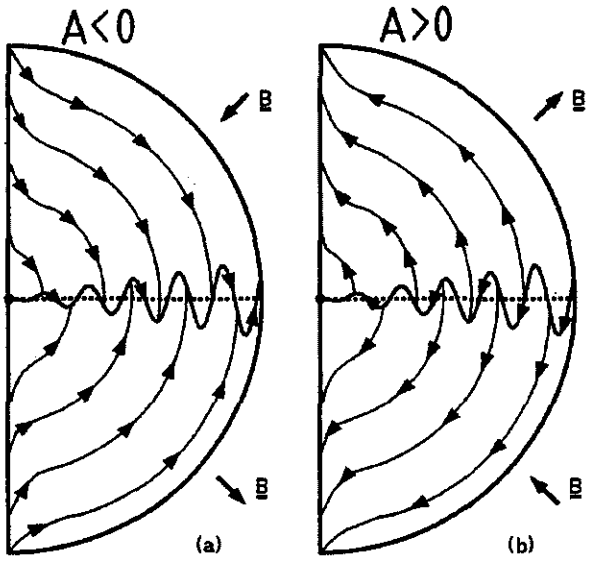

Figure 3.14. Gradient, curvature and current sheet drifts for electrons for (a) the A < 0 polarity cycle when the HMF, being depicted by **B**, is directed inward in the northern hemisphere and (b) the A > 0 polarity epoch when the HMF is directed outward in the norther hemisphere. See Jokipii and Thomas (1981) for proton drift directions.

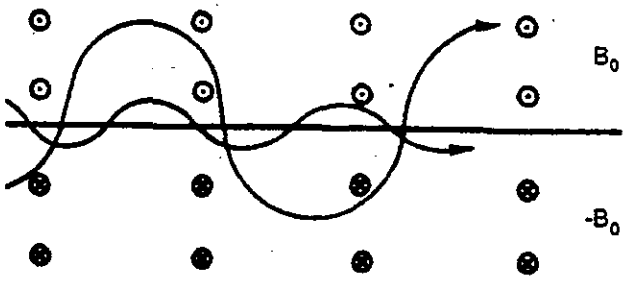

Figure 3.15. An illustration of drift trajectories of cosmic rays along a flat current sheet. Dots give an outward directed **B**, while crosses give an inward directed **B**. The wavy curves represent the drift trajectory of two sample positive particles (from Jokipii et al., 1977).

primarily from the poles down onto the equatorial regions and outwards along the HCS. The wavy curve represents drifts along the HCS which dominates the equatorial motion.

Figure 3.15 illustrates principally the drifts of CRs along a flat HCS. The magnetic field is outward above and inward below the HCS as has been indicated by the circles enclosing the dots and crosses. The wavy curves are trajectories of positively charged particles which gyrate around outward fields in a clockwise manner above the HCS and around inward fields in a counterclockwise sense below the HCS. The net effect is drifts along the HCS in the direction of the current flow (see Burger, 1987). As has been mentioned in the previous section, $\kappa_{\perp\theta}$ affects the drifts patterns of CRs. If $\kappa_{\perp\theta}$ becomes large, particles may not drift effectively, e.g. along the polar axis or current sheet, but will instead be spread in latitude, reducing the drifts effects on CR modulation.

The inclusion of drifts into the transport equation of CRs leads to the following modulation consequences (Jokipii and Thomas, 1981; Kóta and Jokipii, 1983; Potgieter and Moraal, 1985; Kóta, 1990; Potgieter, 1998):

(1) A polarity dependent ~11-year cycle with a peak-like maximum in A < 0 polarity cycles and a flat plateau maximum in the A > 0 polarity cycles (Kóta and Jokipii, 1983) for CR protons and vice versa for electrons. This is observed in neutron monitor data as shown in Figure 2.11. Because in A > 0 cycles, positively charged

particles drift inwards to the Sun through the polar regions, and are relatively insensitive to conditions in the equatorial region, like changes in the HCS, the plateau like pattern is observed. For the A < 0 polarity cycle, the positive charged particles drift in along the HCS and are sensitive to these changes resulting in a definite peak like shape of the intensity maxima. A good correlation with the tilt angle is therefore expected.

(2) Charge-sign dependent effects (will be discussed in Chapters 5 - 8).

(3) Different radial gradients for the two polarity cycles (e.g., Potgieter et al., 1989; Langner et al., 2003b; will be discussed in Chapters 5 - 8).

(4) The latitudinal gradients have opposite signs for different polarity cycles with the latitudinal gradients a maximum when the inclination of the HCS is smallest, which is evident from observations that have been reported by e.g., McKibben (1989), Cummings et al. (1990), and McDonald et al. (1992).

The 'drift coefficient' in Equation 3.64 under the assumption of weak scattering is given by:

$$(\kappa_A)_{traditional} = \kappa_A^0 \frac{vR}{3cB} \tag{3.68}$$

with κ_A^0 a dimensionless constant. With $(\kappa_A)_0 = 1.0$, 0.5, and 0.0 respectively, this equation describes what Potgieter et al. (1989) have called 100% (full drifts), 50% (half drifts) and no-drifts. This term was used previously by many authors e.g., Haasbroek (1997), Ferreira et al. (2000) and Potgieter (1996). The 'drift coefficient' as has been used by Burger et al. (2000) and in this work, differs slightly from the traditional form and is given by

$$\kappa_A = \kappa_A^0 \frac{vR}{3cB} \left(\frac{10R^2}{1+10R^2} \right). \tag{3.69}$$

Below ~1 GV, drifts are slightly reduced with respect to the weak scattering case for which $\kappa_A \propto R$, $\forall R$. This choice for the 'drift coefficient' is consistent with the numerical simulations of Giacalone et al. (1999), which show that in the case of weak scattering the 'standard' result as is given by Equation 3.68 is in fact appropriate. In this work $\kappa_A^0 = 0.5$ for all tilt angles and both polarity cycles which corresponds to 50% drifts. Without this assumption, the comparison between the computations and observations is very poor and it is clear that full drifts, $\kappa_A^0 = 1.0$, are not possible.

3.9. Summary

The distribution of cosmic rays in the heliosphere is the result of four different transport processes, namely diffusion, drifts, convection and adiabatic energy loss. The purpose of this chapter was to give a short overview of existing knowledge of numerical techniques for solving the Parker TPE and, in particular the diffusion process. A suitable diffusion tensor was also constructed applicable to modulation of a variety of particles (i.e., protons, anti-protons, electrons, positrons, Helium, and anomalous protons and Helium) in the heliosphere. It has been shown that in 2D modulation models three different diffusion coefficients are of particular interest, namely $\kappa_{\parallel}$, $\kappa_{\perp r}$, and $\kappa_{\perp \theta}$ the diffusion coefficients parallel and perpendicular to the HMF in the radial and polar directions, respectively. The 'drift coefficient' κ_A represents gradient, curvature and current sheet drifts.

In this work the LOD method was used for solving the TPE with a discontinuity at the assumed location of the TS. First the TPE was split into a system of three equations, each containing only derivatives in one dimension, as had been given by Equations 3.25, 3.26, and 3.27. The LOD scheme implements in a way similar to the ADI method, by first using the equation from the previous time step to calculate an intermediate solution and then using the intermediate solution to calculate a final solution for each time step. The major difference between the

ADI and the LOD lies in the fact that the ADI calculates the final solution from the intermediate solution as well as the solution from the previous time step. To solve the TPE with a discontinuous transition of the solar wind velocity at the TS, one must solve Equation 3.7 and Equation 3.8 simultaneously, where Equation 3.8 is in the general form given by Equation 3.30. This is solved by using the Wendroff's implicit method.

A $\kappa_{||}$ was constructed based on theoretical calculations without the dissipation range but with slab/2D turbulence (Burger et al., 2000) and extended to lower rigidities for electrons and positrons, $R \leq 100\,\mathrm{MV}$, to have a near constant rigidity dependence ($R^{0.1}$) as predicted by observations and models including dynamical turbulence, e.g., the damping model (see Figures 3.5 and 3.8). The corresponding $\lambda_{||}$ was shown in Figure 3.10 as a function of rigidity.

Because of the complexity of the perpendicular diffusion coefficient, not much theoretical work on $\kappa_{\perp}$ exists, although currently it is seriously researched (e.g., Minnie, 2002; Teufel and Schlickeiser, 2002; 2003; Teufel et al., 2003; Stawicki, 2003; Shalchi, 2003; Parhi et al., 2003), illustrating that it is realized that $\kappa_{\perp}$ is important for the better understanding of CR modulation. It has however become practice for authors using modulation models to scale $\kappa_{\perp}$ as $\kappa_{||}$. This scenario was largely confirmed by Giacalone and Jokipii (1999) where it was found that the value of $\kappa_{\perp}/\kappa_{||}$ is in the range of 0.02 - 0.04 for rigidities between ~0.04 and ~1.7 GV. Unfortunately, owing to the geometry assumed in their calculations, no distinction was made between $\kappa_{\perp r}$ and $\kappa_{\perp \theta}$. However, studying the propagation of low-energy Jovian electrons, Ferrando (1997) found $\kappa_{\perp r}/\kappa_{||} = 0.005$ at ~7 MeV. In this work it is assumed that $\kappa_{\perp} \propto \kappa_{||}$, and that $\lambda_{\perp r}/\lambda_{||} \cong \lambda_{\perp \theta}/\lambda_{||}$ between 0.003 - 0.2 for 0.5 MV - 5.0 GV (see Figure 3.13) at Earth.

Apart from the diffusive transport, CR particles also experience gradient, curvature and current sheet drift motions. The 'drift coefficient' which has been used in this work is the same as that which has been used by Burger et al. (2000) and is given by Equation 3.69. Below ~1 GV, drifts are slightly reduced with respect to the weak scattering case for which $\lambda_A \propto R$, $\forall R$. This choice for the 'drift coefficient' is consistent with the numerical simulations of Giacalone et al. (1999), which show that in the case of weak scattering the standard result as has been given by Equation 3.68 is in fact appropriate. In this work $\kappa_A^0 = 0.5$ for all tilt angles and both polarity cycles which corresponds to 50% drifts. Without this assumption, the comparison between the computations and observations is very poor and it is clear that full drifts, $\kappa_A^0 = 1.0$, are not possible as has been emphasized in many publications of the Potchefstroom group. The diffusion coefficients which had been shown in this chapter and used in the rest of this study were published by Langner et al. (2003b).

In the following chapter the WCS model of Hattingh (1993) is revisited in order to accommodate a magnetic field with a modification (see Equation 2.64) as is used in this work and also to better approximate the WCS model for solutions with $\alpha > 40°$. Refinements to changes of the solar wind velocity across the TS will also be shown, and the effects of all the different fundamental modulation processes and changes to the diffusion coefficients (which are discussed in Chapters 2 - 4) when it is applied to CR modulation in the heliosphere. This will be illustrated as a comparison of various observations for a variety of CR species.

Chapter 4
Characteristics and features of the TS model

4.1. Introduction

In this chapter the characteristics and features of the improved and extended 2D TS modulation model which is used for this study are discussed. This model is an improvement of existing locally developed 2D TS models (e.g., Steenkamp, 1995; Haasbroek, 1997; Steenberg, 1998). For an approximation of the HCS, which is essentially a 3D effect, the current sheet approach (WCS model) of Hattingh (1993) (see also Hattingh and Burger, 1995a) is used to simulate the HCS in a 2D heliosphere. This WCS approach was originally derived for $\alpha \leq 25°$ and a Parker HMF. In this section it will be revisited and rederived for $\alpha \leq 75°$ and for the HMF with the Jokipii-Kóta modification (Equation 2.64). This will be done by using the same method as Hattingh (1993), but attempting to remove most of the assumptions and approximations in order to obtain a more general approach to simulating the HCS in a 2D model. This general approach will then be incorporated into the TS model and will be compared to the WCS approach.

The TS model can be used for a variety of transitions of the solar wind velocity at the TS location. In this chapter the effects of each of these transitions on the spectra of galactic protons will be shown. These effects are qualitatively the same for the different species and will therefore not be repeated for other species. To illustrate the effect of the injection energy and the form of the injected source spectrum at the TS on spectra, anomalous protons have been used because this effect is better highlighted when the modulation is not dominated by the galactic component.

Finally, the characteristics and features of this modified TS model will be illustrated through comparisons to some major observations for a variety of CR species, which will be used as a starting point for the rest of this thesis. The LIS for the different species used in this chapter will be specified in the next chapters.

4.2. The WCS approach revisited

In the 2D WCS numerical modulation model (Hattingh, 1993; Hattingh and Burger, 1995a), the HCS given by Equation 2.71 and approximated by Equation 2.72, is simulated by replacing the 3D drift velocity field by a 2D drift field by averaging Equation 3.64 over one solar rotation. This averaging leads to gradient and curvature drifts that are scaled in the current sheet region, which is defined as the region swept by particles drifting along the HCS during one solar rotation, so that it is zero at $\theta = \pi/2$. The same method is followed in this section to derive a more general approach. Although these equations and the accompanying derivation for drifts in the HCS region have been meant for small tilt angles ($\alpha \leq 25°$) only (e.g., Jokipii et al., 1977; Jokipii and Thomas 1981; Hattingh, 1993; Hattingh and Burger, 1995a), it will be shown that acceptable results for larger tilt angles are obtained.

4.2.1. Drifts and the HCS

In Figure 4.1 two planes with radius r tilted at an angle of $\alpha = 35°$ relative to each other are shown. By using this figure an expression for the HCS can be derived (Burger, private communication). According to this figure $\tan\alpha$ can be written as

$$\tan\alpha = \frac{y}{x\sin\varphi^*} \Rightarrow \frac{y}{x} = \tan\alpha\sin\varphi^*, \tag{4.1}$$

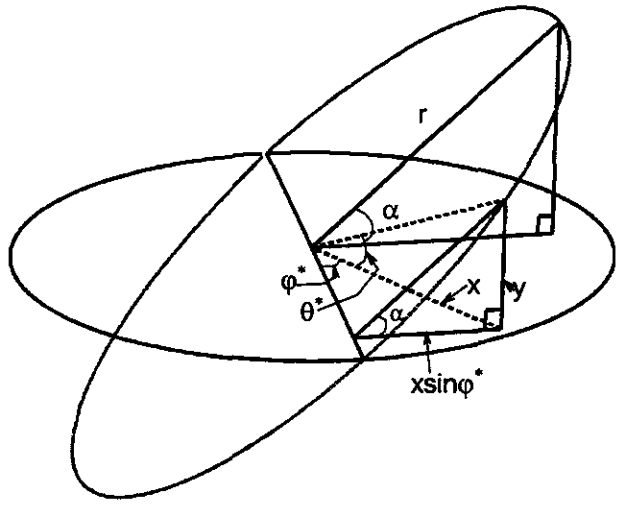

Figure 4.1. Two circular planes with a radius r tilted at an angle of $\alpha = 35°$ relative to each other (Burger, private communication).

and

$$\frac{y}{x} = \tan\theta^*. \tag{4.2}$$

Therefore

$$\tan\theta^* = \tan\alpha \sin\varphi^*. \tag{4.3}$$

Now, if the plane with φ^* is assumed to be at $\pi/2$, then the angle θ' is defined as $\theta' = \pi/2 - \theta^*$. Therefore

$$\cot\theta' = \tan\alpha \sin\varphi^* = \xi. \tag{4.4}$$

Let $\varphi^* = \phi + \Omega(r - r_\odot)/V$ and by using the identity $\tan^{-1}\xi + \cot^{-1}\xi = \pi/2$ it follows that for a constant and radial V the HCS satisfies the equation

$$\theta' = \frac{\pi}{2} - \tan^{-1}\left[\tan\alpha \sin\left(\phi + \frac{\Omega(r - r_\odot)}{V}\right)\right], \tag{4.5}$$

which is similar to Equation 2.71 which is derived by Jokipii and Thomas (1981). However, the approximation which has been given in Equation 2.72 for small α is not made. In Equation 4.5 the amplitude of the HCS is $\approx \alpha$, while the frequency of the HCS is determined by the angular velocity of the Sun, $\mathbf{\Omega}$, and V. The phase is given by ϕ and V is assumed to stay constant (typically 400 km.s^{-1}) for all tilt angles, because the slow solar wind region becomes larger if α is increased, as in Equation 2.8 and Figure 2.4, just as the amplitude of the HCS becomes larger with increasing α.

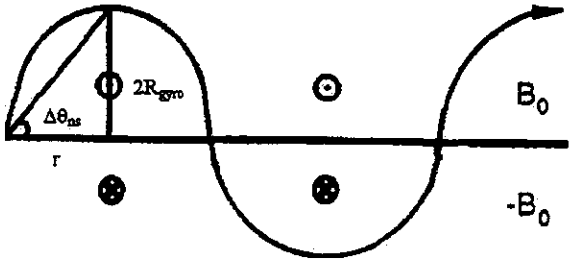

Figure 4.2. Drifts of a positive particle along a flat current sheet. The dots are for an outward directed HMF (above the current sheet), while the crosses are for an inward directed HMF (below the current sheet). Here $B_0 = |\mathbf{B}|$.

During one rotation of the Sun, the HCS fills a region lying between $\frac{\pi}{2} - \alpha \leq \theta \leq \frac{\pi}{2} + \alpha$. However, Burger and Potgieter (1989) has shown that charged particles in a region of two gyroradii above and below this region, will also partake in drifts along the HCS (see also Figures 3.15 and 4.2) if the particle gyrates about a magnetic field line that is a gyroradii above the HCS. Therefore the total extent of the current sheet region has a total angular width of $2(\alpha + \triangle\theta_{ns})$, where

$$\begin{aligned} \triangle\theta_{ns} &= \tan^{-1}\left(\frac{2R_{gyro}}{r}\right) \\ &\approx \frac{2R_{gyro}}{r} = \frac{2p}{rqB} = \frac{2R}{rcB} \\ &= \frac{2Rr}{cB_0 r_e^2\sqrt{1+\left(\frac{r\delta(\theta,\phi)}{r_\odot}\right)^2+\Gamma^2}}, \end{aligned} \tag{4.6}$$

from Figure 4.2 with R_{gyro} the gyroradius of a charged particle at a radial distance of r from the Sun, B is given by Equation 2.65, and with all angles in radians.

By using Equations 3.64 and 4.5, it can be shown that

$$\begin{aligned} \langle \mathbf{v}_d \rangle_m &= \boldsymbol{\nabla}\times\left(\kappa_A \mathbf{e}_B^{'}\right) \\ &= \frac{2pv r\Gamma}{3qA\left(1+\left(\frac{r\delta(\theta,\phi)}{r_\odot}\right)^2+\Gamma^2\right)^2}[-\cot\theta\left(1+2\left(\frac{r\delta(\theta,\phi)}{r_\odot}\right)^2\right)\mathbf{e}_r \\ &+ \left(2+\left(\frac{r\delta(\theta,\phi)}{r_\odot}\right)^2+\Gamma^2\right)\mathbf{e}_\theta \\ &+ \left(\frac{\left(\frac{r\delta(\theta,\phi)}{r_\odot}\right)}{\Gamma}\left(2+\left(\frac{r\delta(\theta,\phi)}{r_\odot}\right)^2+\Gamma^2-3\cot\theta\left(\frac{r\delta(\theta,\phi)}{r_\odot}\right)\right)+3\Gamma\cot\theta\right)\mathbf{e}_\phi], \end{aligned} \tag{4.7}$$

and

$$\begin{aligned} (\mathbf{v}_{ns})_m &= 2\kappa_A \mathbf{e}_B^{'}\times\boldsymbol{\nabla}\left(\theta-\theta'\right) \\ &= \frac{2pvr}{3qA\left(1+\left(\frac{r\delta(\theta,\phi)}{r_\odot}\right)^2+\Gamma^2\right)}[\left(\frac{-\left(\frac{r\delta(\theta,\phi)}{r_\odot}\right)G}{\sin\theta}+\Gamma\right)\mathbf{e}_r \\ &+ \left(\frac{\Omega\Gamma r G}{V}+\frac{G}{\sin\theta}\right)\mathbf{e}_\theta+\left(1+\frac{G\Omega\left(\frac{r\delta(\theta,\phi)}{r_\odot}\right)r}{V}\right)\mathbf{e}_\phi], \end{aligned} \tag{4.8}$$

where

$$G = \frac{\cos\left(\phi+\frac{\Omega(r-r_\odot)}{V}\right)\tan\alpha}{1+\tan^2\alpha\sin^2\left(\phi+\frac{\Omega(r-r_\odot)}{V}\right)}. \tag{4.9}$$

Here Equation 4.7 is the gradient and curvature drifts of charged particles. The direction in which the particles drift is determined by the direction of the magnetic field (A = $sign\,(Bq)$) and the charge of the particle (see Figure 3.14). Obviously, the particles drift in different directions above and below the HCS. The drift of charged particles along the HCS is given by Equation 4.8. Because of the change in sign of the HMF above and below the HCS, the direction in which particles drift along the HCS depends on the charge of the particle. The velocity field of the former term in Equation 3.64 is divergence free, because the divergence of the rotation of any vector is zero. The latter term of Equation 3.64 is mathematically infinite, because of the Dirac-function, and must be integrated to give physical meaning to it.

4.2.2. Modelling the HCS

Gradient and curvature drifts

The general expression for gradient and curvature drifts, and drift along the HCS are given by Equations 4.7 and 4.8, respectively. To keep the expressions for the drift velocities divergence free when expressing them two dimensionally, the averages over a solar rotation must be taken. Mathematically it is equivalent to take the average over ϕ from 0 to 2π, by integrating over ϕ.

The average of the gradient and curvature drifts over ϕ is thus (see also Hattingh, 1993)

$$\frac{\int_0^{2\pi} \langle v_d \rangle_m \left[1 - 2H\left(\theta - \theta'\right)\right] d\phi}{\int_0^{2\pi} d\phi} = \begin{cases} \langle v_d \rangle_m & \text{if } 0 \leq \theta \leq \frac{\pi}{2} - \alpha - \Delta\theta_{ns} \\ \langle v_d \rangle_m \frac{2}{\pi} \sin^{-1}\left(\frac{\tan\left(\frac{\pi}{2}-\theta\right)}{\tan(\alpha+\Delta\theta_{ns})}\right) & \text{if } \frac{\pi}{2} - \alpha - \Delta\theta_{ns} < \theta < \frac{\pi}{2} + \alpha + \Delta\theta_{ns} \\ -\langle v_d \rangle_m & \text{if } \frac{\pi}{2} + \alpha + \Delta\theta_{ns} \leq \theta \leq \pi \end{cases} . \tag{4.10}$$

Here the Heaviside step function is again given by Equation 2.60. From Equation 4.10 it follows that the average of the gradient and curvature drifts over ϕ has the physical effect of scaling the drift velocity in the 2D 'current sheet region' from a maximum value at the boundary of this region to a value of zero when $\theta = \pi/2$, so that the total flux in the θ-direction is zero in the equatorial plane.

Drifts along the HCS

To calculate the average of the drifts along the HCS, the average of the drift velocity over ϕ must also be taken for one solar rotation (first method). This, however, gives a drift velocity which is large at the edge of the 'current sheet region' and zero in the equatorial plane, which is numerically very difficult to handle. This problem is overcome by first taking the average of the drift velocity over θ and then over ϕ (second method). A θ-dependence is then given again to the drift velocity, so that the flux resulting from the velocity field stays the same. This ensures that the velocity field stays divergence free. The second method is numerically more friendly and easier to handle, but cannot be solved analytically for the integral over θ. The second method gives the same flux as the first method, which has been used by Hattingh (1993) to show that the drift velocity field is divergence free. Thereafter the second method is used because it is easier to handle numerically. These methods have been described in detail by Hattingh (1993) and therefore only the essential parts will be discussed here.

First method: The average of the drift velocity along the HCS over ϕ is given by

$$\frac{\int_0^{2\pi} (v_{ns})_m \delta\left(\theta - \theta'\right) d\phi}{\int_0^{2\pi} d\phi} = \frac{1}{2\pi} \int_{\theta'_{\min}}^{\theta'_{\max}} \frac{(v_{ns})_m \delta\left(\theta - \theta'\right) \csc^2\theta' d\theta'}{\sqrt{\tan^2\alpha - \cot^2\theta'}}, \tag{4.11}$$

if θ' is given by Equation 4.5.

If $\pi/2 - \alpha < \theta \leq \pi/2$ then $\theta = \theta'$ at two different values of ϕ, namely $\phi_a = \phi_a^* - \frac{\Omega(r-r_\odot)}{V}$ and $\phi_b = \phi_b^* - \frac{\Omega(r-r_\odot)}{V}$, with $\Omega(r - r_\odot)/V$ a phase constant (see Figure 4.3 (b)). The terms in Equation 4.8 at $\phi = \phi_a$ are

$$\begin{aligned} \cos\left(\phi_a + \frac{\Omega(r-r_\odot)}{V}\right) &= \cos\left(\pi - \sin^{-1}\left(\frac{\cot\theta}{-\tan\alpha}\right)\right) \\ &= -\cos\left(\sin^{-1}\left(\frac{\cot\theta}{-\tan\alpha}\right)\right), \end{aligned} \tag{4.12}$$

and

$$\begin{aligned} \sin\left(\phi_a + \frac{\Omega(r-r_\odot)}{V}\right) &= \sin\left(\pi - \sin^{-1}\left(\frac{\cot\theta}{-\tan\alpha}\right)\right) \\ &= \frac{\cot\theta}{-\tan\alpha}. \end{aligned} \tag{4.13}$$

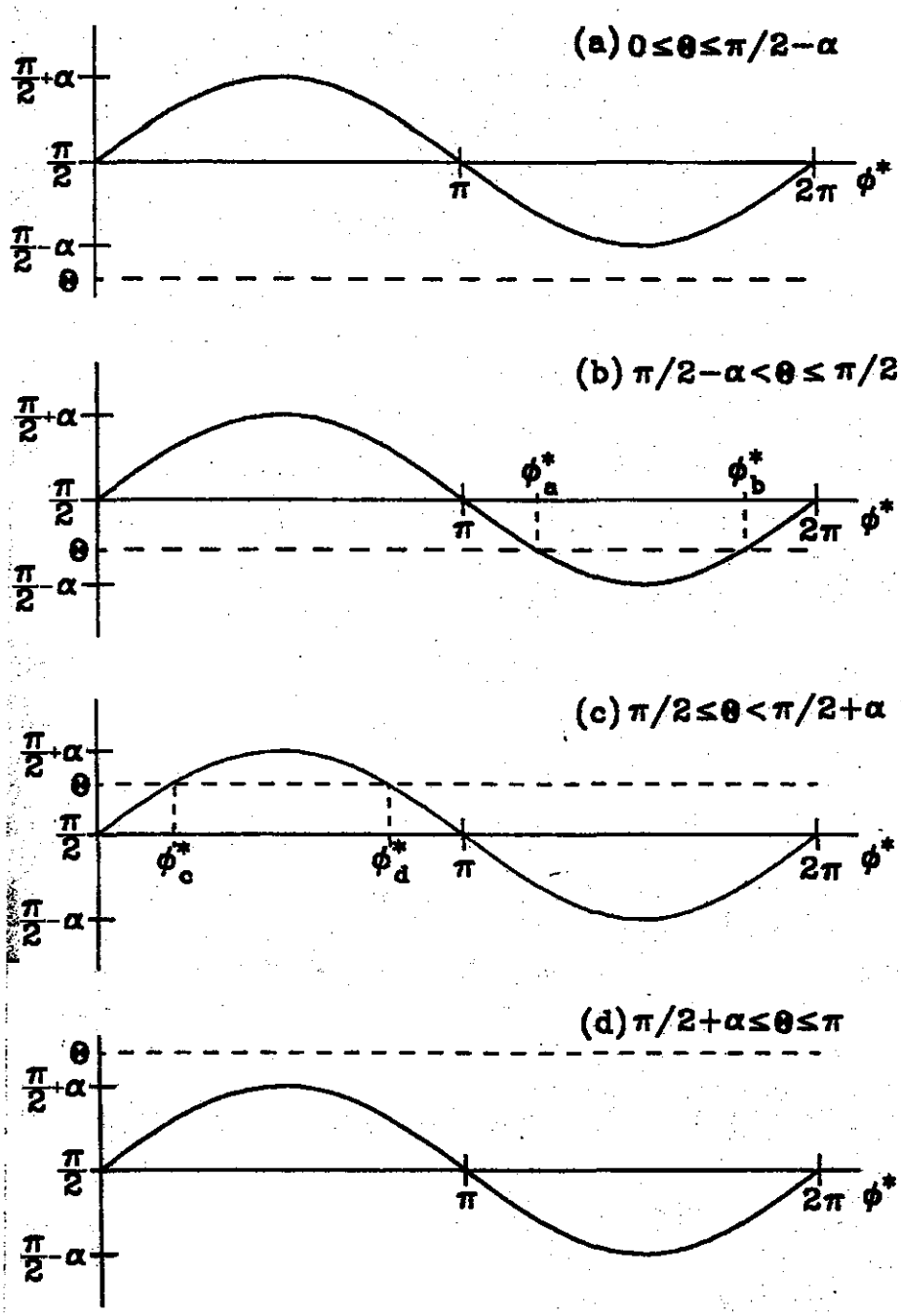

Figure 4.3. The neutral sheet (θ') as function of ϕ^*.

At $\phi = \phi_b$ the terms are

$$\begin{aligned} \cos\left(\phi_b + \frac{\Omega(r - r_\odot)}{V}\right) &= \cos\left(2\pi + \sin^{-1}\left(\frac{\cot\theta}{-\tan\alpha}\right)\right) \\ &= \cos\left(\sin^{-1}\left(\frac{\cot\theta}{-\tan\alpha}\right)\right), \end{aligned} \tag{4.14}$$

and

$$\begin{aligned} \sin\left(\phi_b + \frac{\Omega(r - r_\odot)}{V}\right) &= \sin\left(2\pi + \sin^{-1}\left(\frac{\cot\theta}{-\tan\alpha}\right)\right) \\ &= \frac{\cot\theta}{-\tan\alpha}. \end{aligned} \tag{4.15}$$

The drift velocity along the HCS for ϕ_a can now be calculated by using Equations 4.12, 4.13, and 4.8 and for ϕ_b

by using Equations 4.14, 4.15, and 4.8. Thus Equation 4.11 gives

$$\begin{aligned}\frac{\int_0^{2\pi}(\mathbf{v}_{ns})_m\,\delta\left(\theta-\theta'\right)d\phi}{\int_0^{2\pi}d\phi} &= \frac{1}{2\pi}\frac{\csc^2\theta}{\sqrt{\tan^2\alpha-\cot^2\theta}}\left[(\mathbf{v}_{ns})_m\mid_{\phi=\phi_a}+(\mathbf{v}_{ns})_m\mid_{\phi=\phi_b}\right]\\ &= \frac{1}{2\pi}\frac{\csc^2\theta}{\sqrt{\tan^2\alpha-\cot^2\theta}}\frac{4pvr\left(\Gamma\mathbf{e}_r+\mathbf{e}_\phi\right)}{3qA(1+\left(\frac{r\delta(\theta,\phi)}{r_\odot}\right)^2+\Gamma^2)}.\end{aligned} \tag{4.16}$$

When $\pi/2\le\theta<\pi/2+\alpha$, $\theta=\theta'$ at $\phi_c=\phi_c^*-\frac{\Omega(r-r_\odot)}{V}$ and $\phi_d=\phi_d^*-\frac{\Omega(r-r_\odot)}{V}$ as has been shown in Figure 4.3 (c). However, the same results are found for these values of ϕ as for ϕ_a and ϕ_b. For $0\le\theta\le\pi/2-\alpha$ (Figure 4.3 (a)) and $\pi/2+\alpha\le\theta\le\pi$ (Figure 4.3 (d)) there are no values for ϕ where $\theta=\theta'$. Thus the integral is zero for these values of θ. The 'current sheet region' is given by $\pi/2-\alpha-\triangle\theta_{ns}<\theta<\pi/2+\alpha+\triangle\theta_{ns}$, therefore the average value of the drift velocity along the current sheet over ϕ is given by

$$\frac{\int_0^{2\pi}(\mathbf{v}_{ns})_m\,\delta\left(\theta-\theta'\right)d\phi}{\int_0^{2\pi}d\phi}=\frac{1}{2\pi}\frac{\csc^2\theta}{\sqrt{\tan^2(\alpha+\triangle\theta_{ns})-\cot^2\theta}}\frac{4pvr\left(\Gamma\mathbf{e}_r+\mathbf{e}_\phi\right)}{3qA(1+\left(\frac{r\delta(\theta,\phi)}{r_\odot}\right)^2+\Gamma^2)}, \tag{4.17}$$

if $\pi/2-\alpha-\triangle\theta_{ns}<\theta<\pi/2+\alpha+\triangle\theta_{ns}$, and zero elsewhere.

Outside of the 'current sheet region' the velocity field is given by Equation 4.7 which is divergence free, because $\boldsymbol{\nabla}.\langle\mathbf{v}_d\rangle_m=\boldsymbol{\nabla}.\left[\boldsymbol{\nabla}\times\left(\kappa_A\mathbf{e}_B'\right)\right]=0$. Inside the 'current sheet region' the velocity field is given by Equations 4.10 and 4.17. Here the divergence is

$$\boldsymbol{\nabla}.\left[\langle\mathbf{v}_d\rangle_m\frac{2}{\pi}\sin^{-1}\left(\frac{\tan\left(\frac{\pi}{2}-\theta\right)}{\tan\left(\alpha+\triangle\theta_{ns}\right)}\right)+\frac{1}{2\pi}\frac{\csc^2\theta}{\sqrt{\tan^2(\alpha+\triangle\theta_{ns})-\cot^2\theta}}\frac{4pvr\left(\Gamma\mathbf{e}_r+\mathbf{e}_\phi\right)}{3qA(1+\left(\frac{r\delta(\theta,\phi)}{r_\odot}\right)^2+\Gamma^2)}\right]=0. \tag{4.18}$$

Second method: With this method, the average of the drift velocity field given by Equation 4.8 is first taken over θ for $\pi/2-\alpha-\triangle\theta_{ns}<\theta<\pi/2+\alpha+\triangle\theta_{ns}$ and then over ϕ for one solar rotation. With the help of Equation 4.5 the average over θ is given by

$$\begin{aligned}&\frac{\int_{\pi/2-\alpha-\triangle\theta_{ns}}^{\pi/2+\alpha+\triangle\theta_{ns}}(\mathbf{v}_{ns})_m\,\delta\left(\theta-\theta'\right)d\theta}{\int_{\pi/2-\alpha-\triangle\theta_{ns}}^{\pi/2+\alpha+\triangle\theta_{ns}}d\theta}\\ &= \frac{pvr}{3qA\left(1+M'^2+\Gamma'^2\right)\left(\alpha+\triangle\theta_{ns}\right)}[\left(\frac{-M'G}{\cos\left[\tan^{-1}\left(\tan\alpha\sin\phi^*\right)\right]}+\Gamma'\right)\mathbf{e}_r\\ &+\left(\frac{\Omega\Gamma'\tau G}{V}+\frac{G}{\cos\left[\tan^{-1}\left(\tan\alpha\sin\phi^*\right)\right]}\right)\mathbf{e}_\theta\\ &+\left(1+\frac{G\Omega M'r}{V}\right)\mathbf{e}_\phi],\end{aligned} \tag{4.19}$$

where $\phi^*=\phi+\Omega(r-r_\odot)/V$, G is given by Equation 4.9,

$$\Gamma'=\frac{\Omega(r-r_\odot)}{V}\cos\left[\tan^{-1}\left(\tan\alpha\sin\phi^*\right)\right], \tag{4.20}$$

and

$$M'=\frac{r\delta(\theta,\phi)}{r_\odot}=\frac{r\delta_m}{r_\odot\sin\theta}=\frac{r\delta_m}{r_\odot\cos\left[\tan^{-1}\left(\tan\alpha\sin\phi^*\right)\right]}. \tag{4.21}$$

The average over ϕ of the drift velocity given by Equation 4.19 is zero for the θ-component, because the resultant drift of particles along the HCS on both sides of the equatorial plane must be equal for an axisymmetrical heliosphere. The averages of the ϕ-component of the drift velocity given by Equation 4.17 and 4.19 are both independent of ϕ and therefore they do not contribute to the divergence of the drift velocity field. Thus only the radial component is of use. By evaluating the integrals of the radial components of Equation 4.17 over θ for $\pi/2-\alpha-\triangle\theta_{ns}<\theta<\pi/2+\alpha+\triangle\theta_{ns}$ (F_1) and Equation 4.19 over ϕ for one rotation (F_2) numerically, it is found

that $F_1 \approx F_2$ for all values of r and α (see also Hattingh, 1993). The second method to calculate the average of the drift velocity along the HCS will therefore also give a divergence free velocity field.

The average over ϕ of the drift velocity that is given by Equation 4.19 can only be calculated numerically. However, Equations 4.20, 4.21 and 4.9 can be approximated by calculating the root mean square of $\sin(\phi + \Omega(r - r_\odot)/V)$ and $\cos(\phi + \Omega(r - r_\odot)/V)$ over ϕ for one rotation, so that these equations become

$$\Gamma' = \frac{\Omega(r - r_\odot)}{V} \cos\left[\tan^{-1}\left(\frac{\tan\alpha}{\sqrt{2}}\right)\right], \tag{4.22}$$

$$M' = \frac{r\delta_m}{r_\odot \cos\left[\tan^{-1}\left(\frac{\tan\alpha}{\sqrt{2}}\right)\right]}, \tag{4.23}$$

and

$$G' = \frac{\tan\alpha\left(\frac{1}{\sqrt{2}}\right)}{1 + \tan^2\alpha\left(\frac{1}{\sqrt{2}}\right)^2}. \tag{4.24}$$

Thus the radial component of Equation 4.19 averaged over one solar rotation is

$$(\mathbf{v}_{ns})_r = \frac{pvr}{3qA\left(1 + M'^2 + \Gamma'^2\right)(\alpha + \Delta\theta_{ns})}\left(\frac{-M'G'}{\cos\left[\tan^{-1}\left(\frac{\tan\alpha}{\sqrt{2}}\right)\right]} + \Gamma'\right). \tag{4.25}$$

This result, the current sheet drift velocity, together with the gradient and curvature drifts (Equation 4.10), give the total drift velocity field of the 2D model which is used in this work.

The current sheet drift velocity (Equation 4.25) is a block function independent of θ, which is zero for $\theta < \pi/2 - \alpha - \Delta\theta_{ns}$. This, however, causes large gradients at some grid points in the numerical solution of the TPE. This problem is solved by multiplying the block function with a hyperbolic tangent function, so that the modified current sheet drift velocity is given by

$$(\mathbf{v}_{ns})_r^{'} = a\tanh\left[b\left(\theta + \alpha + \Delta\theta_{ns} - \frac{\pi}{2}\right)\right], \tag{4.26}$$

where $(\mathbf{v}_{ns})_r$ is contained in a, and b determines the ratio with which the function increases. The larger b, the closer the function will be to a block function. In this study the value of $b = 10$ is chosen so that the increase of the function goes over 5 grid points. To determine the value for a, the flux which is caused by Equation 4.26 over the current sheet region must be calculated, which must be the same as the flux that is given by Equation 4.25. The flux in the current sheet region in the radial direction which is caused by $(\mathbf{v}_{ns})_r$ is

$$\int_{\frac{\pi}{2}-\alpha-\Delta\theta_{ns}}^{\frac{\pi}{2}} (\mathbf{v}_{ns})_r\, 2\pi r^2 \sin(\theta) d\theta = (\mathbf{v}_{ns})_r\, 2\pi r^2 \sin(\alpha + \Delta\theta_{ns}). \tag{4.27}$$

The flux that is caused by $(\mathbf{v}_{ns})_r^{'}$ is

$$\int_{\frac{\pi}{2}-\alpha-\Delta\theta_{ns}}^{\frac{\pi}{2}} (\mathbf{v}_{ns})_r^{'}\, 2\pi r^2 \sin(\theta) d\theta = \int_{\frac{\pi}{2}-\alpha-\Delta\theta_{ns}}^{\frac{\pi}{2}} 2\pi r^2 a\tanh\left[b\left(\theta + \alpha + \Delta\theta_{ns} - \frac{\pi}{2}\right)\right]\sin\theta d\theta. \tag{4.28}$$

This integral can however not be solved analytically and is approximated by

$$\begin{aligned} &\int_{\frac{\pi}{2}-\alpha-\Delta\theta_{ns}}^{\frac{\pi}{2}} 2\pi r^2 a\tanh\left[b\left(\theta + \alpha + \Delta\theta_{ns} - \frac{\pi}{2}\right)\right] d\theta \\ &= \frac{2\pi r^2 a}{b}\ln\left|\cosh\left[b\left(\alpha + \Delta\theta_{ns}\right)\right]\right|, \end{aligned} \tag{4.29}$$

if $\alpha \leq 25°$, because then $\sin\theta \approx 1$ in the 'current sheet region' and

$$\int_{aa}^{\frac{\pi}{2}} 2\pi r^2 a \sin(\theta) d\theta + \int_{\frac{\pi}{2}-\alpha-\Delta\theta_{ns}}^{aa} 2\pi r^2 a \tanh\left[b\left(\theta + \alpha + \Delta\theta_{ns} - \frac{\pi}{2}\right)\right] d\theta$$

$$= 2\pi r^2 a \cos(aa) + \frac{2\pi r^2 a}{b} \ln\left|\cosh\left[b\left(aa + \alpha + \Delta\theta_{ns} - \frac{\pi}{2}\right)\right]\right|, \tag{4.30}$$

if $\alpha > 25°$, with aa the point where $\sin\theta = \tanh\left[b\left(\theta + \alpha + \Delta\theta_{ns} - \frac{\pi}{2}\right)\right]$. Using Equations 4.27 and 4.28 a is given by

$$a = \frac{b\left(\mathbf{v}_{ns}\right)_r \sin(\alpha + \Delta\theta_{ns})}{\ln\left|\cosh\left[b\left(\alpha + \Delta\theta_{ns}\right)\right]\right|} \tag{4.31}$$

for Equation 4.29 and

$$a = \frac{\left(\mathbf{v}_{ns}\right)_r \sin(\alpha + \Delta\theta_{ns})}{\cos(aa) + \frac{\ln\left|\cosh\left[b\left(aa+\alpha+\Delta\theta_{ns}-\frac{\pi}{2}\right)\right]\right|}{b}} \tag{4.32}$$

for Equation 4.30. Thus

$$\left(\mathbf{v}_{ns}\right)_r' = \frac{b\left(\mathbf{v}_{ns}\right)_r \sin(\alpha + \Delta\theta_{ns})}{\ln\left|\cosh\left[b\left(\alpha + \Delta\theta_{ns}\right)\right]\right|} \tanh\left[b\left(\theta + \alpha + \Delta\theta_{ns} - \frac{\pi}{2}\right)\right] \tag{4.33}$$

for $\alpha \leq 25°$, and

$$\left(\mathbf{v}_{ns}\right)_r' = \frac{\left(\mathbf{v}_{ns}\right)_r \sin(\alpha + \Delta\theta_{ns})}{\cos(aa) + \frac{\ln\left|\cosh\left[b\left(aa+\alpha+\Delta\theta_{ns}-\frac{\pi}{2}\right)\right]\right|}{b}} \tanh\left[b\left(\theta + \alpha + \Delta\theta_{ns} - \frac{\pi}{2}\right)\right] \tag{4.34}$$

for $\alpha > 25°$.

4.2.3. Application of the HCS approach

In this section the general HCS approach, derived above, and the WCS approach of Hattingh (1993) are compared. In Figure 4.4 calculated CR proton spectra for these approaches are shown in the equatorial plane for $\alpha = 75°$ at 1, 60, and 90 AU for the A > 0 polarity cycle. From this figure it is evident that the calculated intensities of the more general HCS approach is lower than that of the WCS approach for all radial distances with a maximum effect of ~20% at ~1 GeV at Earth. The difference between the two approaches is clearly decreasing with increasing radial distance, and is decreasing with decreasing tilt angles, with a difference of less than ~1% at $\alpha = 10°$, as has been expected. It is also evident that the WCS model of Hattingh (1993), which has been derived for a Parker spiral HMF and which is in principle only valid for $\alpha \leq 25°$, is a good approximation even at large tilt angles and can be used for qualitative studies, but the general HCS approach is recommended for quantitative studies.

4.2.4. The HCS and drifts beyond the TS

Across the TS the magnitude of the magnetic field increases by a factor of $\sim s$ (Equation 2.63 for the magnetic field as is given by Equation 2.64). Therefore the form of the HCS will also change in the heliosheath region as was shown by Hattingh (1993). The amplitude of the HCS in front and beyond of the TS stays the same, but the frequency changes, so that the HCS becomes more compressed beyond the TS. Equations 4.7 and 4.25 thus stay the same except for changing Equation 2.59 to Equation 2.62. The compression of the HCS causes the particles to drift for a longer time along the HCS to cover a given radial distance. The drifts will also decrease by a factor of $\sim s$ across the shock, although perpendicular diffusion, which inhibits drifts, also decreases by a similar factor, indirectly increasing the effects of drifts again in the heliosheath region. Therefore the effects of the drifts on CR modulation are still surprisingly large in the heliosheath as will be shown in Chapter 5. However, a detailed study of the structure of the HCS and the magnitude of drifts in the heliosheath region are beyond the scope of this work.

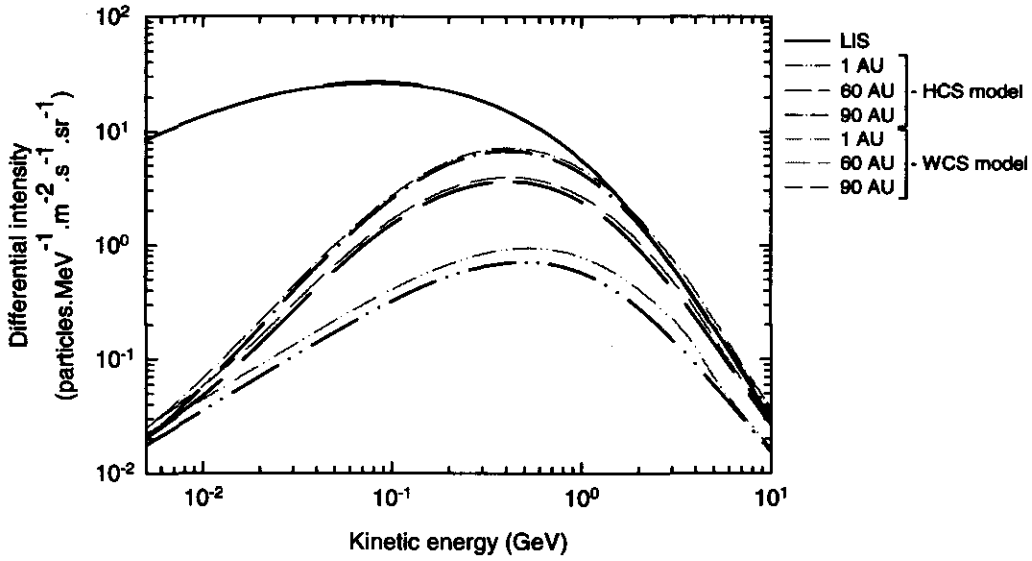

Figure 4.4. Proton spectra calculated for the general HCS approach (black curves) and for the WCS approach (grey curves) of Hattingh (1993) in the equatorial plane for $\alpha = 75°$ at 1, 60, and 90 AU for the A > 0 polarity cycle. The LIS will be specified in the next chapter.

4.3. Effects of different solar wind velocity transitions at the TS

In this section the effects on CR proton spectra of the continuous, discontinuous, and quasi-discontinuous transition functions for the solar wind speed at the TS are discussed. Figure 4.5 illustrates these transitions as a function of radial distance in the equatorial plane. Steenkamp (1995) and Steenberg (1998) used the discontinuous transition to study the modulation of the ACRs. The continuous transition was introduced by le Roux et al. (1996) and used by Haasbroek (1997) in a 2D TS model to escape the numerical difficulties that came with a discontinuous transition across the TS and was justified by the results of Donohue and Zank (1993). These quantitative results of Donohue and Zank (1993), concerning a CR mediated TS, showed that downstream of the TS the CR pressure was comparable to the plasma pressure which results in a gradual compression and deceleration of the solar wind, followed by a discontinuous jump to a downstream state which is dominated by the pressure contribution of the CRs. The radial distance over which the transition took place was calculated as $L \approx 1$ AU. Therefore the quasi-discontinuous transition is used in the present model and is considered the more realistic option.

In Figure 4.6 the effect of the transitions in Figure 4.5 on the spectra of CR protons in the equatorial plane for $\alpha = 10°$ and the A > 0 polarity cycle is shown. However, it has been found that the differences between the spectra that have been calculated for the discontinuous and quasi-discontinuous transitions are less than ~2%; the spectra for the discontinuous transition function are therefore not shown. The TS effects are larger for the discontinuous and quasi-discontinuous transitions of the solar wind speed, manifesting in the higher intensities at energies > 0.1 GeV. The effectiveness of the TS is therefore less for the continuous solar wind speed transition. However, note that the quasi-discontinuous and the continuous transitions are the same inside the TS, but not the discontinuous transition, while the quasi-discontinuous and the discontinuous transitions whose spectra differ very little, are the same in the downstream region, but not the continuous transition. This leads to the conclusion that the profile of the solar wind speed in the downstream region is the primary cause for the differences between the spectra shown in Figure 4.6 and that it can have a surprisingly significant effect on modulation. This is also shown from a different point of view in Figure 4.7.

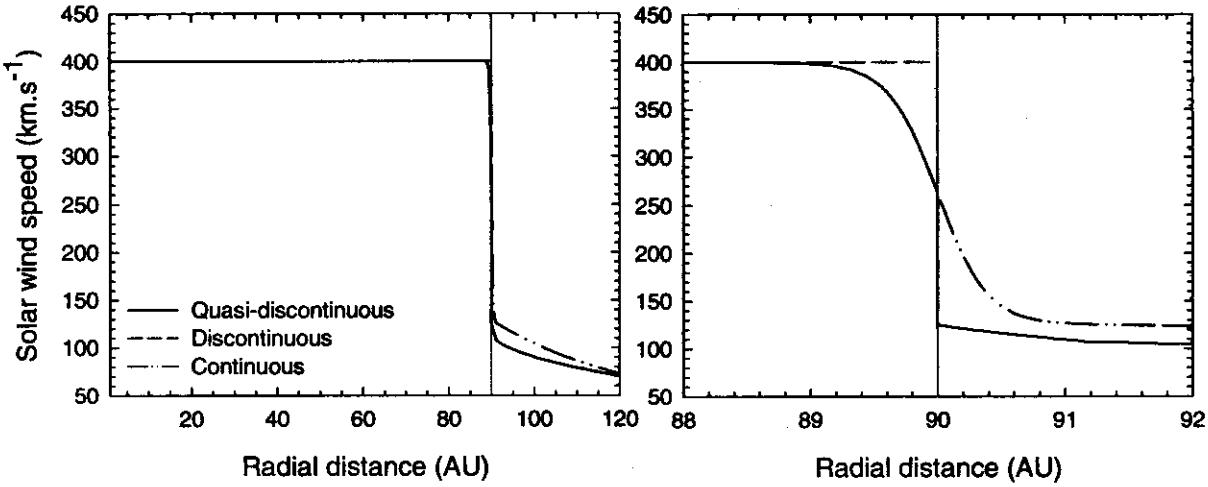

Figure 4.5. Different solar wind profiles for the transition of the solar wind speed at the TS (90 AU) as a function of radial distance in the equatorial plane. In the right panel the region of the TS is expanded for illustrative purposes. Note that the quasi-discontinuous and the continuous transitions are the same inside the TS, while the quasi-discontinuous and the discontinuous transitions are the same downstream of the TS. The quasi-discontinuous transition (solid line) is used in the present model.

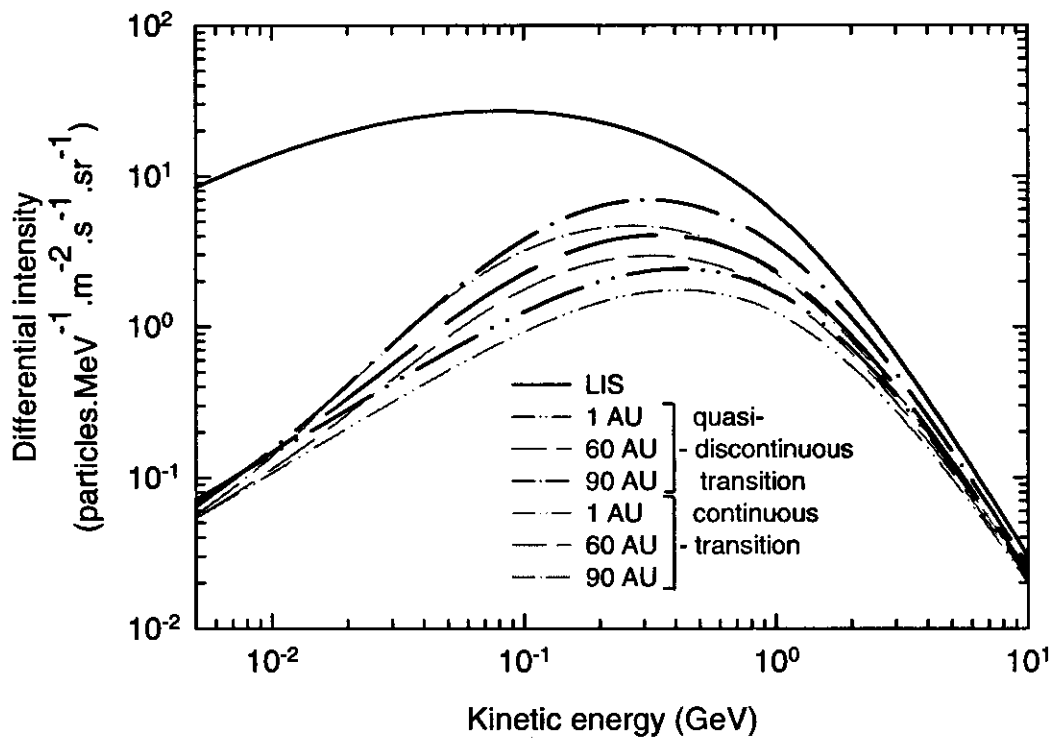

Figure 4.6. The effect of the quasi-discontinuous (black lines) and the continuous (grey lines) solar wind speed transitions in Figure 4.5 on the spectra of CR protons in the equatorial plane for $\alpha = 10°$ and the A > 0 polarity cycle. The results for the discontinuous transition differ within 2% from the quasi-discontinuous transition and are therefore not shown. The compression ratio $s = 3.2$.

In this work the quasi-discontinuous solar wind speed profile is used as are given by Equations 2.9, 2.53, and 2.56. It is clear that although the continuous profile of the solar wind speed is easier to handle numerically, it may underestimate the TS effect on GCRs.

4.4. The injection spectra and injection energy of anomalous protons

Modulation of the ACRs can also be studied with the TS model and will be added to spectra in Chapters 6 and 8. In this section the effects on the modulation and acceleration of the ACRs using different injection spectra and injection energies at the TS are discussed. In Figure 4.7 spectra of anomalous protons for the quasi-discontinuous solar wind speed transition are shown in the equatorial plane for $\alpha = 10°$ and for both polarity cycles at radial distances of 1 and 90 AU. Here, as in the remainder of this section, the spectra at 90 AU are compared to the theoretically expected $E^{-1.18}$ dependence, which is indicated by the straight grey line as a reference, as is given by Equation 2.52 for a compression ratio of $s = 3.2$, and is used throughout this work unless it is stated otherwise. Depending on heliolatitude, the shock spectra start to fall off rapidly beyond about 0.3 - 1.0 GeV, because of the well-known curvature (shock radius) effect when Vr/κ_{rr} becomes < 1 (Moraal and Axford, 1983; Drury, 1983). Another effect is noticeable on the spectrum at the TS; in the 10 - 300 MeV range it clearly deviates from the expected $E^{-1.18}$ dependence and has a concave profile for the A < 0 cycle, while it is almost absent in the A $>$ 0 cycle. This is mainly a drift effect and is described in detail by Steenkamp (1995) (see also Kóta and Jokipii, 1994), causing the shocked spectra in the A < 0 polarity cycle to be flatter than those of the A > 0 polarity cycle.

In Figure 4.9 spectra of anomalous protons are shown for the A < 0 polarity cycle in the equatorial plane at radial distances of 1 and 90 AU which are accelerated at the TS for two different injection energies of $R_{min} = 0.01$ GV and $R_{min} = 0.1$ GV, respectively. Preferably anomalous CRs of as low as possible energy should be injected at the TS, but it simply takes too much computer resources. Fortunately, the TS model is independent of this injection energy as is shown in Figure 4.9 where there is no significant difference between an anomalous source injected at different energies.

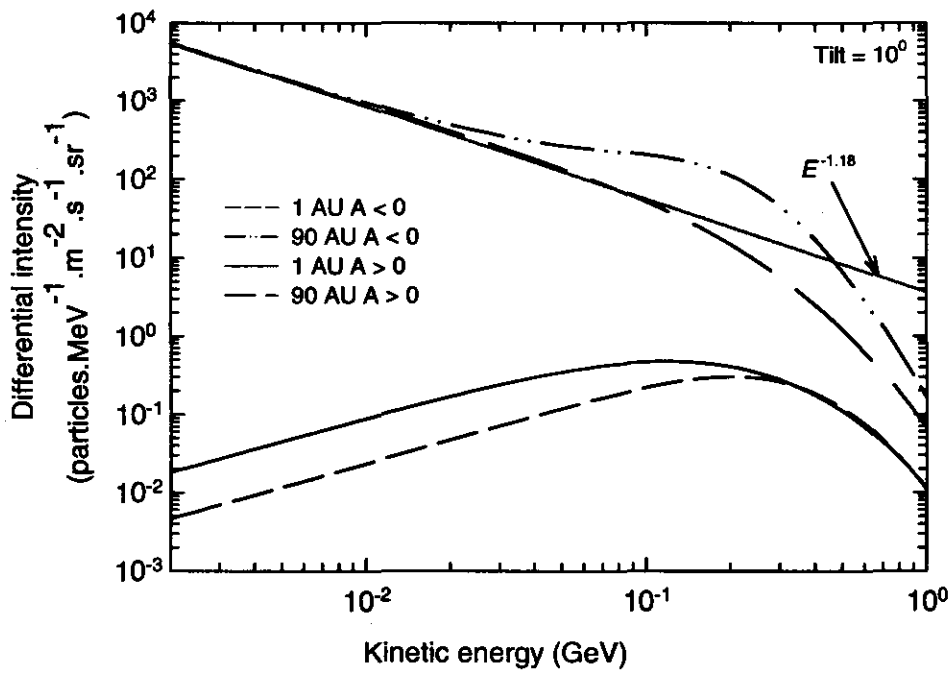

Figure 4.7. Spectra of anomalous protons for the quasi-discontinuous solar wind speed transition as is shown in Figure 4.5 in the equatorial plane for $\alpha = 10°$ and both polarity cycles at radial distances of 1 and 90 AU. The theoretically expected $E^{-1.18}$ dependence of the shocked spectrum, because of $s = 3.2$, is indicated by the straight grey line for comparative purposes.

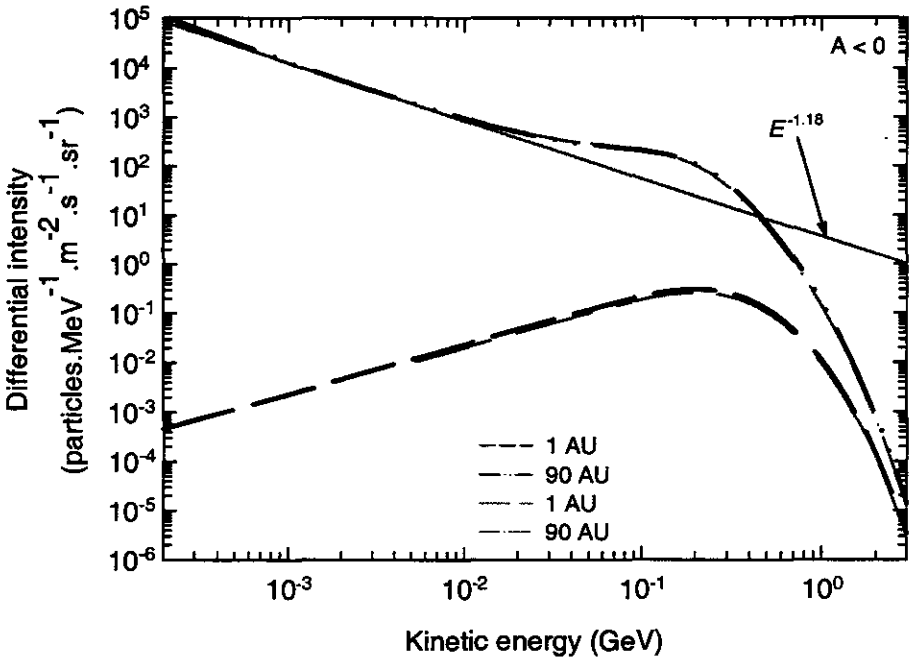

Figure 4.8. Spectra of anomalous cosmic ray protons for the A < 0 polarity cycle in the equatorial plane at radial distances of 1 and 90 AU accelerated at the TS for an injection energy with $R_{min} = 0.01$ GV (black curves) and $R_{min} = 0.1$ GV (grey curves). The straight grey line represents an $E^{-1.18}$ dependence. Spectra are normalised at 1 MeV. Since the two sets of curves coincide for all practical purposes, the injection energy has no significant effect on the acceleration process for this model.

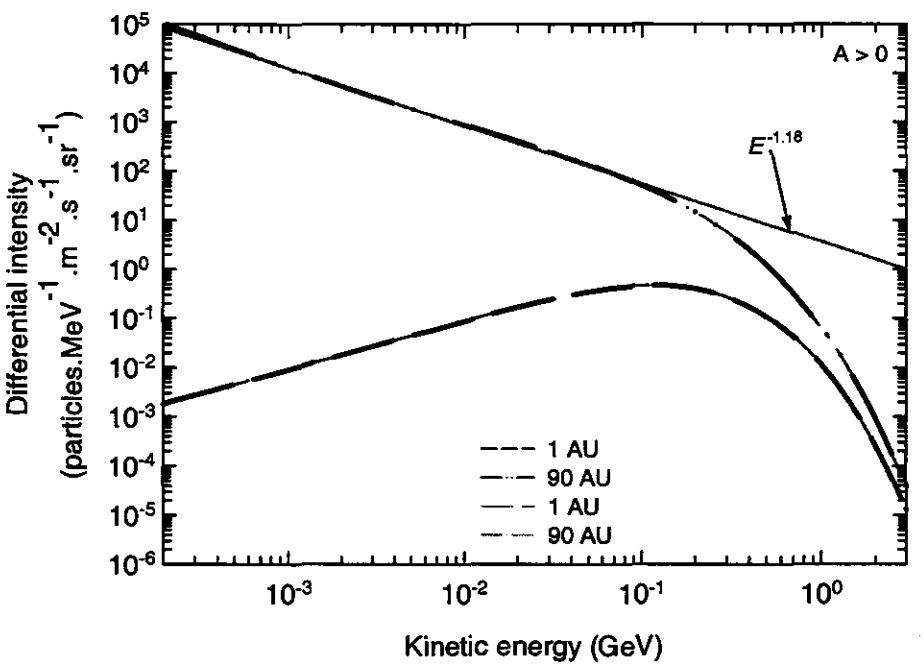

Figure 4.9. Spectra of anomalous cosmic ray protons for the A > 0 polarity cycle in the equatorial plane at radial distances of 1 and 90 AU accelerated at the TS for two different injected source spectral forms. The black lines represent a source injected at the TS position at all θ at an energy of ~86 keV as a delta function (see Q_0 in Equation 3.30), while the grey lines represent the second source injected at all θ, but as a function of energy given by E^{-5} for $E < 0.5$ MeV. The straight grey line represents an $E^{-1.18}$ dependence. Spectra are normalised at 1 MeV. Since the two sets of curves coincide for all practical purposes, the injected source function has no significant effect on the acceleration process for this model.

To test the effect of different injection spectra at the TS on the modulation and acceleration of the ACRs, two different spectra were injected at the TS. Firstly, an anomalous source was injected, as in the rest of this study, at all θ at an energy of ~86 keV as a delta function (see Q_0 in Equation 3.30), while the second source injected at all θ was a function of energy given by E^{-5} for $E < 0.5$ MeV. In Figure 4.8 the resulting spectra are shown for the A > 0 polarity cycle in the equatorial plane at radial distances of 1 and 90 AU. It is clear that the accelerated spectrum at the TS is independent of the form of the source spectrum, as long as the energy dependence is less than the expected theoretical energy dependence corresponding to the compression ratio. A source spectrum which is injected at the TS with an injection spectral form other than a delta function and one with a delta function result in the same shocked spectra, because in this model the acceleration efficiency only depends on the compression ratio and not on the injected distribution of particles in energy. These aspects of the TS model are consistent to the model described by Steenkamp (1995).

4.5. Tests and challenges for the TS model

One of the aims of this study was to develop a widely applicable numerical model including a TS by using the TPE. This newly developed model with all its fundamental modulation processes and fundamentally derived diffusion coefficients, as discussed in Chapter 2 to 4, is tested in this section by comparing it to observations of the main features of CR modulation. However, it must be noted that a quantitative fitting of the observations was not the purpose of this study. It was rather used as a tool to establish a set of diffusion coefficients that is not completely arbitrary but compatible to the basic observations made for a variety of CR species, especially 'fine-tuned' for a model with a TS for both polarity cycles and solar minimum and moderate maximum activity.

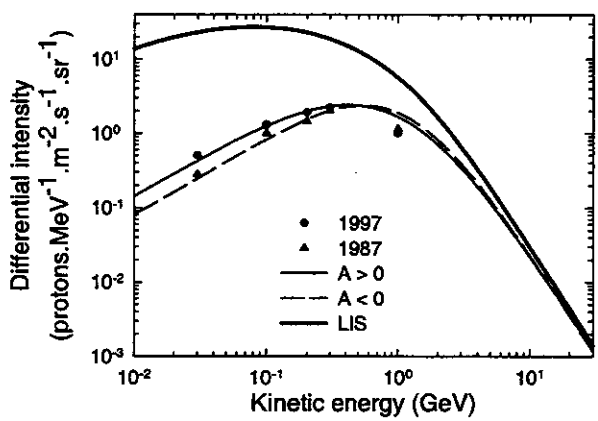

Figure 4.10. Computed differential intensities for galactic cosmic ray protons as a function of kinetic energy for both polarity cycles at Earth for $\alpha = 10°$ in comparison with solar minimum observations for 1987 (triangles) and 1997 (filled circles) (McDonald et al., 1998). The LIS is at 120 AU, with a TS at 90 AU.

In Figure 4.10 the computed modulation for galactic CR protons at Earth is shown as spectra with respect to the LIS at 120 AU, for both polarity cycles with $\alpha = 10°$, in comparison with observations for 1987 and 1997 at Earth (McDonald et al., 1998). Although it is easily done in principle, note that the A > 0 spectrum crosses the A < 0 spectrum as observations require, at ~500.0 MeV and again at ~5.0 GeV (see also Reinecke et al., 1997). Model results which are compared to more comprehensive data sets at Earth are shown in Figure 4.11 for protons, anti-protons, and protons with an anomalous component as function of kinetic energy for both polarity cycles with

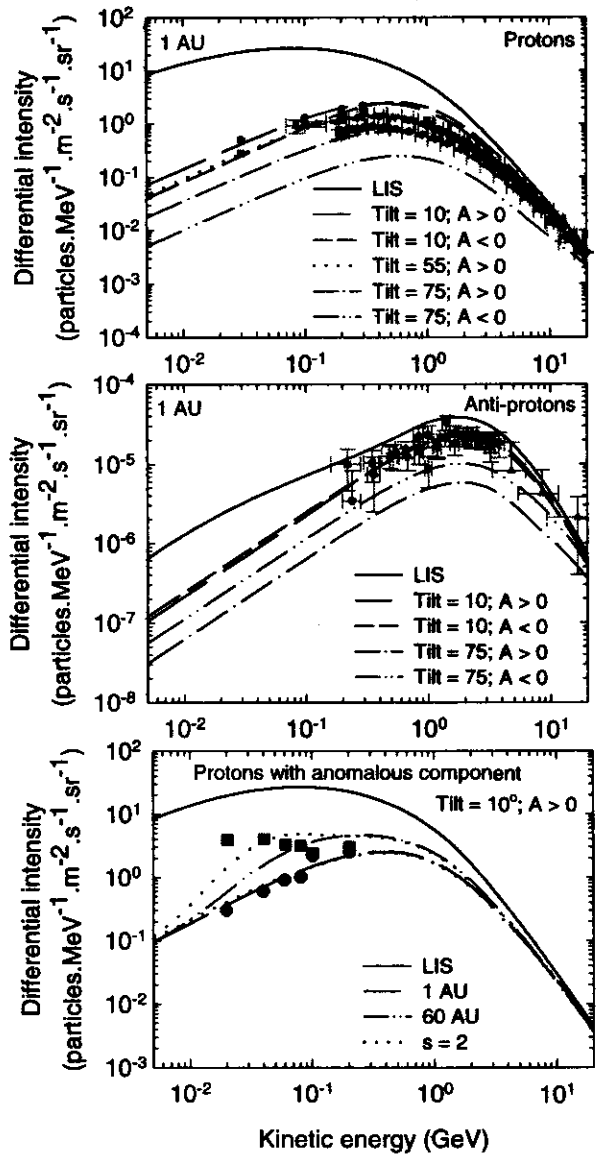

Figure 4.11. Computed modulated differential intensities for protons, anti-protons, and protons with an anomalous component as a function of kinetic energy for both polarity cycles with different tilt angles as indicated. Spectra are shown at Earth (top two panels), compared to observations from various experiments for protons and anti-protons which have been compiled by Moskalenko et al. (2001), and at 60 AU in the equatorial plane (bottom panel) in comparison with IMP (1 AU - filled circles) and Pioneer 10 (60 AU - filled squares) observations as have been compiled by Steenberg (1998). The TS is at 90 AU and the appropriate LIS at 120 AU. These LIS will be specified in the next chapters. In the bottom panel the computed spectra with compression ratios of $s = 3.2$ and $s = 2.0$ are compared to the observations.

different tilt angles as are indicated in the figures. The observations are from various experiments (e.g., BESS, IMAX, CAPRICE etc.) for protons and anti-protons and have been compiled by Moskalenko et al. (2001, 2002), while the observations for protons with an anomalous component (e.g., from Pioneer 10) have been compiled by Steenberg (1998). The model predicts that increasing α from 10° to 75° causes a drop in CR intensity, for example, by a factor of ~4.5 for the A > 0 period but a factor of ~9.0 for the A < 0 polarity cycle for energies $\lesssim$ 1.0 GeV. This behaviour is also a characteristic feature of steady-state drift models. To obtain the same reasonable compatibility with the anomalous protons at 60 AU, the compression ratio had to be decreased from $s = 3.2$ to $s = 2.0$ as illustrated in the bottom panel of Figure 4.11. The solutions in the inner heliosphere are insensitive to

this change. Decreasing s causes the peak in the modulated anomalous proton spectrum to shift to lower energies as the observations seem to require. These quantitative aspects of anomalous proton modulation were discussed in detail by Steenberg and Moraal (1996) and Potgieter and Langner (2003a, 2003b) and were not pursued further in this work. For our purpose any further 'fine-tuning' to the model parameters in order to achieve better compatibility with observations would not contribute significantly to the better understanding of modulation in the heliosphere.

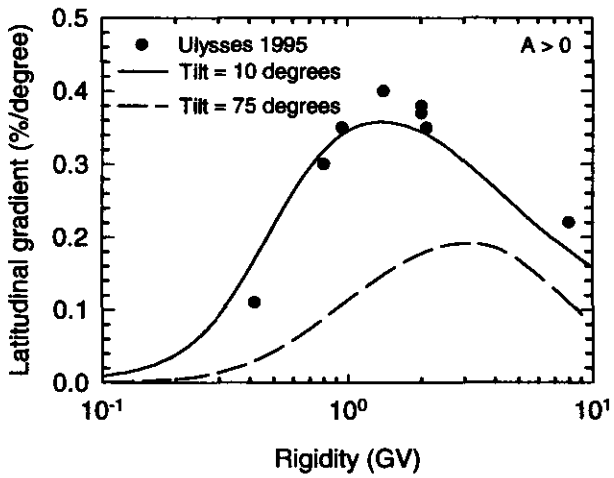

Figure 4.12. Computed latitudinal gradients, in %/degree, for the A > 0 polarity cycle at 3.0 AU for $\alpha = 10°$ and 75° between colatitudes 10° and 90°. Observations are from Ulysses in 1995 (see Heber et al., 1996; Heber, 1997; Burger et al., 2000).

In this model the latitudinal gradient between colatitudes θ_1 and θ_2 is calculated from

$$g_\theta = \ln\left(\frac{j_2}{j_1}\right)\left(\frac{100}{\theta_2 - \theta_1}\right) \text{ percent per degree} \tag{4.35}$$

with j_i the differential intensity at position (r, θ_i). Figure 4.12 shows the corresponding computed latitudinal gradients between colatitudes 10° and 90° at a fixed distance of 3.0 AU as a function of rigidity for $\alpha = 10°$ and 75° for the A > 0 polarity cycle. This is in comparison with observations by the Ulysses spacecraft which are based on the maximum intensities in 1995 (Heber et al., 1996; Heber, 1997). This observation is one of the most important cosmic ray observations that has been made by the Ulysses spacecraft and has become a required feature in any modulation modeling. The computations show that the latitudinal gradients become smaller with increasing solar activity as has been suggested by Ulysses observations. This observation, concerning both the value of the latitudinal gradient and its rigidity dependence, put severe constraints on the model and requires that $\kappa_\perp$ must be enhanced in the polar direction as described in the previous chapter. The computed latitudinal gradient with $\alpha = 75°$ could be made even smaller if $\kappa_\perp$ was further increased but then the compatibility to the radial gradients which had been shown in Figure 4.13 would be less reasonable.

Figure 4.13 shows the computed radial intensities for galactic protons for both polarity cycles in the equatorial plane at 0.2 GeV and for $\alpha = 10°$ and 75°. The observations are from IMP, Pioneer 10, Voyager 1 and 2 (Webber and Lockwood, 2001a, 2001b) for solar minimum and moderate maximum conditions (with α up to 75°). Observations showed a clear difference between A > 0 and A < 0, reproduced reasonably well by the TS model, with larger radial gradients predicted for A < 0 than for A > 0 in the inner heliosphere ($r \lesssim 40$ AU), but approximately the same values for 40 AU $\lesssim r \lesssim$ 90 AU, with $\alpha = 10°$ and 75°. The differences beyond the TS will be discussed in

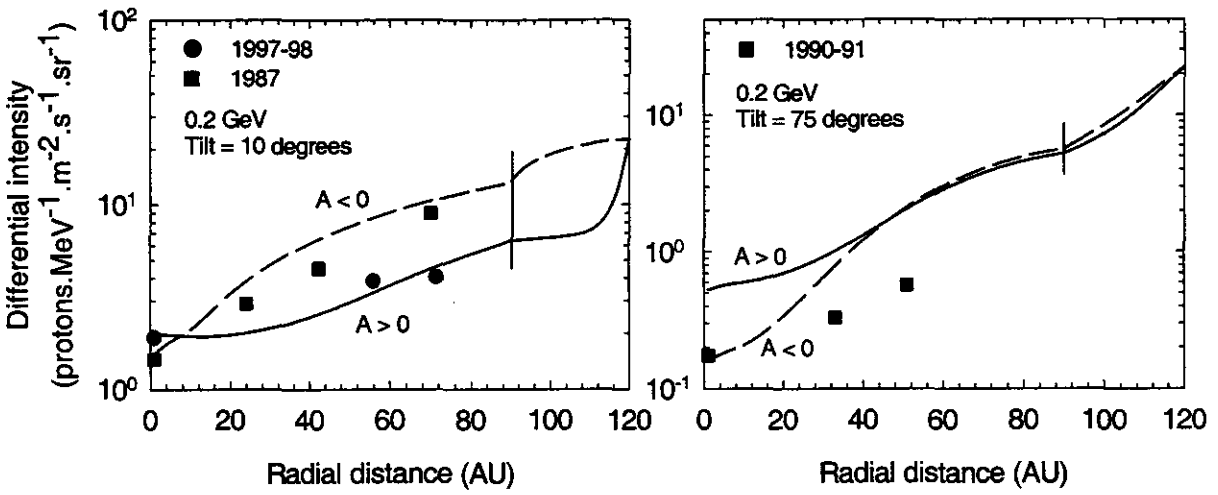

Figure 4.13. Computed radial intensities for CR protons for both polarity cycles in the equatorial plane at 0.2 GeV and for $\alpha = 10°$ (left panel) and 75° (right panel). Solid lines represent A > 0, while the dashed lines represent A < 0 as has been indicated. The filled circles represent A > 0 observations, the squares represent A < 0 observations of IMP, Pioneer 10, Voyager 1 and 2 (Webber and Lockwood, 2001a; 2001b) for solar minimum (left panel) and moderate maximum (right panel) conditions. Note the scale differences between the panels. The TS is indicated by the vertical lines.

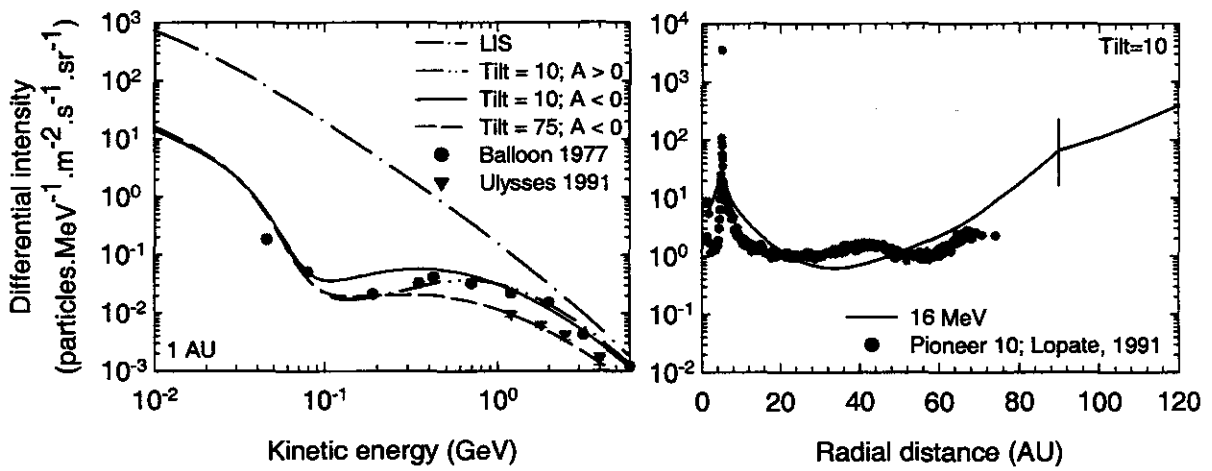

Figure 4.14. Left panel: Computed differential intensities for electrons at Earth as a function of kinetic energy for both polarity cycles, with $\alpha = 10°$ and 75° (only A < 0), compared to Ulysses spacecraft observations for solar maximum in 1991 (Potgieter et al., 1999b; Heber, 1997; Raviart, priv. comm.) and balloon measurements for solar minimum in 1977 (Evenson et al., 1983). Right panel: Differential intensities at 16 MeV as a function of radial distance for the A > 0 polarity cycle in the equatorial plane with $\alpha = 10°$, compared to 16 MeV electron observations from Pioneer 10 (Lopate, 1991; Ferreira et al., 2001g). The TS is indicated by the vertical line, while the LIS is specified at 120 AU.

the next chapter. For $\alpha = 75°$ the compatibility is less good with increasing radial distance, indicating that apart from changing α, the solar wind speed, and the values of perpendicular diffusion, where the last change implies decreasing drift with increasing solar activity, additional solar maximum modulation features, e.g. GMIRs, are required which have not been considered for this work.

Next, the TS model is applied to electron modulation and compared to electron spectra at Earth and as a function of radial distance. The observations are from the Ulysses spacecraft for solar minimum and solar maximum

(Heber, 1997; Potgieter et al., 1999b; Heber et al., 2001, 2002; Raviart, priv. comm.), balloon measurements (Evenson et al., 1983) and 16 MeV electron observations from Pioneer 10 (Lopate, 1991; Ferreira et al., 2001b) which are shown in Figure 4.14. In this figure the effect of the Jovian source in the inner heliosphere on the measured intensities is also illustrated. Evidently, the computed electron spectra are compatible with the observations. Although more detail fits are possible as has been illustrated for the radial dependence of the electrons by Ferreira et al. (2001b), any additional 'fine-tuning' will not contribute significantly to the better understanding of global heliospheric modulation as has been mentioned earlier.

The comparisons between the model and observations which have been shown in this section confirm that the TS model that is used in this work can indeed reasonably reproduce the modulation between the outer boundary and Earth for a variety of GCRs, anomalous components of CRs and Jovian electrons, even when considering detailed features for protons like the cross-over of solar minima spectra for the two polarity epochs and very moderate latitudinal gradients that become even smaller with increasing solar activity.

4.6. Summary

In this chapter characteristics and features of the improved and extended 2D TS modulation model developed and used for this study were shown. This model is an improvement of existing locally developed 2D TS modulation models (e.g., Steenkamp, 1995; Haasbroek, 1997; Steenberg, 1998), but with a more general approach to handling the HCS in a 2D model and the manner in which the solar wind speed transition at the TS is treated numerically. For an approximation of the HCS, which is essentially a 3D effect, the WCS model of Hattingh (1993) has been used as a starting point. Firstly, a more general HCS approach has been derived in this chapter, in order to remove most of the assumptions and approximations made by Hattingh (1993) so that the 2D TS model can be valid for all α. It was found that the calculated intensities of the general HCS approach were lower than that of the WCS model for all radial distances with a maximum effect at $\sim$1 GeV at Earth of $\sim$20%. The difference between the two models is also decreasing with increasing radial distance and with decreasing tilt angles, with a difference of $\lesssim$ 1% at $\alpha = 10°$. The 'simpler' WCS model of Hattingh (1993), which has been derived for a Parker spiral magnetic field and is valid only for $\alpha \leq 25°$, is however still a good approximation and can be used for qualitative studies when detail modulation aspects are not required.

The effects of continuous, discontinuous, and quasi-discontinuous transitions of the solar wind speed at the TS on the numerical solutions were also studied. It has been found that the spectra which have been calculated for the continuous transition function of the solar wind speed differ from that of the discontinuous and quasi-discontinuous transitions. It has become clear that although the continuous profile of the solar wind speed is easier to handle numerically, care has to be taken because the acceleration and modulation effects may be underestimated. In this work the quasi-discontinuous solar wind speed transition function is used as is given by Equations 2.9, 2.53, and 2.56, with a compression ratio of $s = 3.2$ and a scale length of $L = 1.2$ AU inside of the TS. The deviation from the theoretically expected $E^{-1.18}$ dependence of the shocked spectra for the ACRs for the quasi-discontinuous transition could clearly be seen in the 10 - 300 MeV range. This drift effect is prominent for the A < 0 cycle, while it is almost absent in the A > 0 cycle and is similar to the effect which has been discussed by Steenkamp (1995) (see also Kóta and Jokipii, 1994), which causes the the ACRs spectra in the A < 0 polarity cycle to be flatter than that of the A > 0 polarity cycle.

It was also shown that the TS model solutions were independent of the ACRs injection energy. Another

interesting feature of the model for the ACRs is that the accelerated spectrum at the TS is independent of the spectral form of the injected source spectrum, as long as the energy dependence is less than the expected energy dependence corresponding to the compression ratio used. For this model a delta function was injected at the TS with an arbitrary value which could be normalised by comparing the resulting spectra to observations. These aspects of the TS model are consistent to that of the Steenkamp (1995) model.

Finally the effects of all these fundamental modulation processes and changes to the diffusion coefficients (discussed in Chapters 2 to 4) when applied to CR modulation in the heliosphere were shown. This was illustrated by comparing solutions to some major observations, which was used as departing point for the rest of this thesis. These comparisons confirm that the TS model that is used in this work can indeed reasonably reproduce the modulation in the heliosphere for a variety of galactic, anomalous and Jovian CR species, even when considering very detailed features for protons like the cross-over of solar minima spectra for the two polarity epochs and very moderate latitudinal gradients that become even smaller with increasing solar activity. Although the aim of this work is not to study the diffusion coefficients, it is evident that the chosen set gives reasonable comparisons to the observations for solar minimum, but for extreme solar maximum activity modification seems necessary e.g., by introducing transient 'barriers' like GMIRs into the model to reproduce the observed radial gradients.

In the following chapters this TS model will be applied to the study of the modulation of protons, anti-protons, electrons, positrons, Helium, anomalous protons and Helium, and Jovian electrons in the heliosphere. The model parameters as have been described in Chapters 2 to 4 will be used for the rest of the work, except when it is stated otherwise.

Chapter 5
Modulation of cosmic ray protons in the heliosheath

5.1. Introduction

The solar wind termination shock and the heliosheath are prominent and interesting features of the heliosphere. Studying the role of the TS and that of the heliosheath on cosmic ray modulation with numerical models have become most relevant since Voyager 1 is in the vicinity of the TS (Stone and Cummings, 2003) or may have even crossed it (Krimigis et al., 2003). Voyager 1 and Pioneer 10 spacecraft observations over 22 years and out to ~82 AU have also shown markedly different behaviour for minimum modulation conditions between the radial intensity profiles for periods of opposite magnetic polarities and that most of the residual modulation for these periods took place in the outer heliosphere, near and beyond where the termination shock is expected to be. If the heliosheath is several tens of AU, it should have a noticeable effect on the modulation of GCRs in the heliosphere.

With more reliable LIS (e.g., Moskalenko et al., 2001, 2002), a fresh and more fundamental approach to diffusion coefficients (e.g., Burger et al., 2000; Giacalone and Jokipii, 2001) and good observations closer to the TS, the modulation of GCRs in the outer heliosphere can be studied more quantitatively with the TS model. In this chapter the TS model, with parameters as described in Chapters 2, 3, and 4, is used to illustrate the effects of the TS and the heliosheath on proton (p) modulation at different energies, for the two magnetic field polarity cycles, and also as modulation changes from minimum to moderate maximum conditions. Because the emphasis is on what happens at and beyond the TS, the difference between minimum and moderate maximum conditions in this model is contained in the change of the tilt angle from 10° to 75°, the change in the solar wind speed as has been indicated in Chapter 2, and changes in the values of perpendicular diffusion as has been indicated in Chapter 3, where the last change implies decreasing drifts with increasing solar activity.

The content of this chapter was published by Langner et al. (2003b).

5.2. The 'barrier' effect in the heliosheath

A contemporary numerical model including a solar wind termination shock, a heliosheath and drifts is used to study the features of CR proton modulation in the outer heliosphere. Present modulation models based on the solution of Parker's (1965) transport equation to explain solar modulation of GCRs include four major mechanisms: convection, diffusion, drifts, and adiabatic energy losses. Individually these mechanisms are well understood, but how they combine to produce modulation, especially at solar maximum, is still a very active field of research. In the same context, the importance of the TS and the heliosheath have been realized but relatively few studies have been done to appreciate and to establish the role of the TS and heliosheath on the modulation of GCRs. The possibility of significantly large modulation in the very distant heliosphere was first addressed from an experimental point of view by Webber and Lockwood (1987). The importance of modulation beyond the TS was discussed by e.g., Quenby et al. (1990) and some numerical models included calculations of this modulation (e.g., Potgieter and le Roux, 1989a, 1989b), and more comprehensively by Jokipii et al. (1993). Recently, the interest in heliosheath modulation has leaped forward when it has become apparent, particularly from the Voyager and Pioneer spacecraft

observations in the outer heliosphere, that the global modulation was significantly different in the positive solar magnetic field cycle (A > 0) in 1997 than in the negative magnetic cycle (A < 0) in 1987 (Webber and Lockwood, 1995, 1997, 1998; McDonald, 1998; McDonald et al., 1998). The question of what happens beyond the TS has followed and several observational publications address the issue of heliosheath modulation (McDonald et al., 2000, 2002; Webber and Lockwood, 2001a, 2001b; Webber et al., 2001). Webber and Lockwood (2001a, 2001b) used IMP, Voyager and Pioneer observations to derive radial intensity profiles of GCRs out to ~70 AU at several energies during the minimum modulation periods in 1987 and 1997, followed by a similar study for solar maximum conditions in 1990-1991. They have concluded, as do the other authors, that modulation in the outer heliosphere dominates the overall residual modulation at low energies, even at solar minimum, and that there is a clear difference between the modulation for the A > 0 and A < 0 polarity cycles, with the heliosheath 'barrier' being more pronounced and effective during A > 0 periods. For the purpose of this chapter the anomalous protons are neglected, but will be shown in the following chapter.

5.3. LIS for protons

Protons and Helium are the most abundant species in cosmic radiation and knowledge of their absolute abundance and the exact shape of their energy spectra are of particular astrophysical importance. Their spectral shapes are sensitive indicators of the processes of particle acceleration in the galaxy (Gaisser, 1990) and their fluxes are the primary measure of the energy density of CRs in the interstellar medium (ISM). These spectra also serve as important input to calculations which aim to predict the γ-ray flux in the ISM because of π^0 decay or the secondary interstellar anti-proton ($\overline{\mathrm{p}}$) or positron fluxes, all results of high energy interactions of p and Helium nuclei with the interstellar gas.

Despite the importance of these most abundant CR species, neither their absolute fluxes nor their spectral shape in the LISM are known with adequate precision (e.g., Menn et al., 2000). The low-energy LIS for CR protons and $\overline{\mathrm{p}}$ cannot be measured directly deep inside the heliosphere because of modulation, especially the large adiabatic energy losses that these particles experience during their inward propagation. Currently, many proposed LIS for the different species exist, using various different techniques to calculate these spectra (e.g., Langner, 2000). For this work the proton LIS of Moskalenko et al. (2002) was used. They use complex propagation models of particles through the galaxy to derive these spectra, treating the calculations in a self-consistent manner so that the spectra for different species are linked and derived simultaneously. In Moskalenko et al. (2002) it has been shown that the LIS for p and $\overline{\mathrm{p}}$ that are used in this work give the most reasonable heliospheric modulation results and are believed to be the best current LIS for these species.

The LIS for a given CR species is specified at the heliospheric outer boundary (r_b) as an initial condition for the numerical model. The proton LIS of Moskalenko et al. (2002) is given by

$$j_{LIS} = \begin{cases} \exp\left(4.64 - 0.08\,(\ln E)^2 - 2.91\sqrt{E}\right) & \text{if } E < 1.0 \text{ GeV} \\ \exp\left(3.22 - 2.86\,(\ln E) - \frac{1.50}{E}\right) & \text{if } E \geq 1.0 \text{ GeV} \end{cases}, \tag{5.1}$$

with E the kinetic energy in GeV, $j_{LIS} = R^2 f$ the differential intensity in particles.m^{-2}.s^{-1}.sr^{-1}.MeV^{-1} and $R = pc/q$ the rigidity in GV, and where p is the particle momentum, c the speed of light in space, q the particle charge and f the CR distribution function.

5.4. Effects on proton spectra

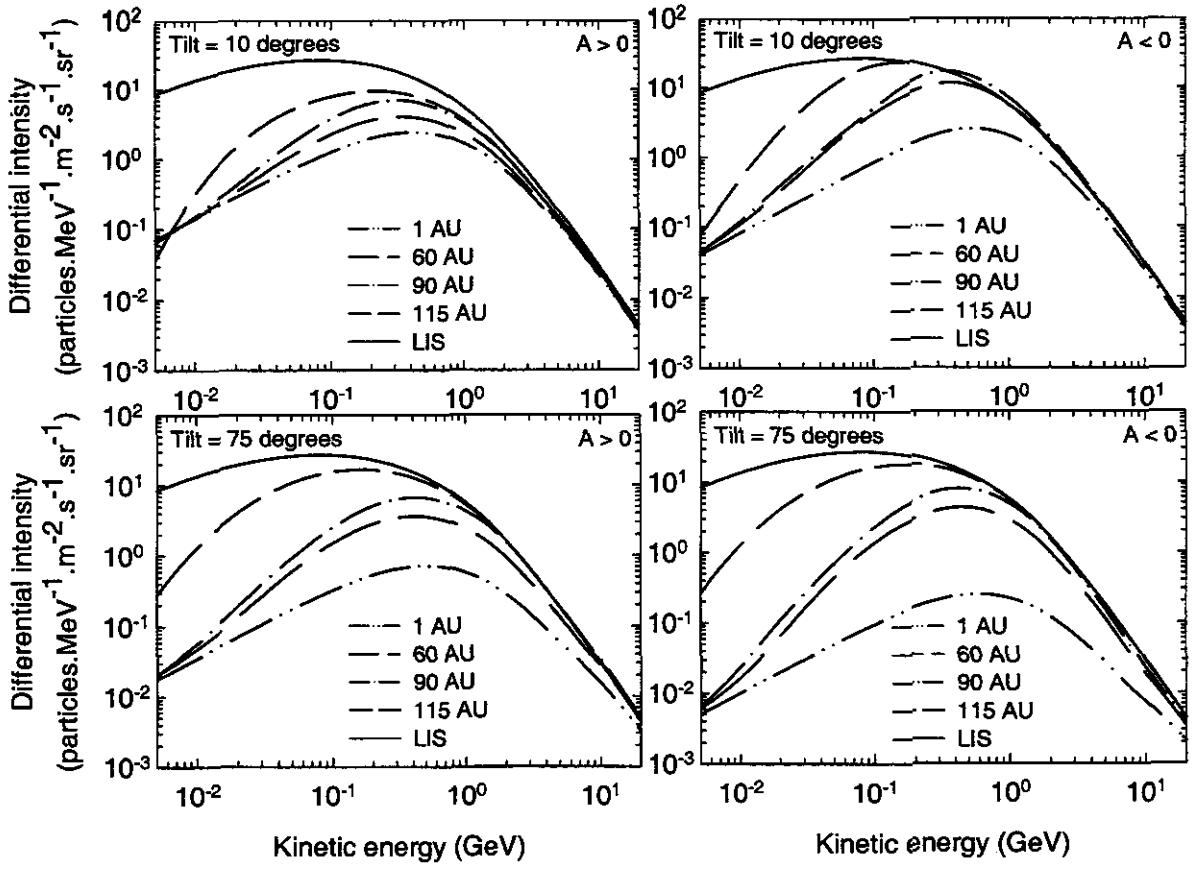

Figure 5.1. Computed differential intensities for protons as a function of kinetic energy for the A > 0 polarity cycle (left panel) and the A < 0 polarity cycle (right panel) in the equatorial plane for $\alpha = 10°$ (top panels) and $\alpha = 75°$ (bottom panels), respectively and at radial distances of 1, 60, 90 and 115 AU (bottom to top). The LIS is at 120 AU, with a TS at 90 AU.

In Figure 5.1 the computed modulation for galactic protons in the equatorial plane at radial distances of 1, 60, 90 and 115 AU, respectively, are shown as spectra with respect to the LIS at 120 AU for the A > 0 (left panel) and A < 0 (right panel) polarity cycles at solar minimum (top panel) and moderate maximum (bottom panel) conditions with $\alpha = 10°$ and $\alpha = 75°$, respectively. Here the effects of the TS, which is situated at 90 AU, are illustrated with emphasis on the differences in modulation for the two polarity epochs. The TS effect is most pronounced for the A < 0 polarity cycle when $\alpha = 10°$ in the sense that the modulated spectra exceed the LIS value at energies above several hundreds of MeV. This is because of the acceleration of low energy particles to higher energies. The drift along the shock for the A < 0 cycle is also in the same direction as the diffusion which is caused by $\kappa_{\theta\theta}$ and this could enhance the effect in this cycle because particles can spend more time closer to the shock front. In the case with $\alpha = 75°$ the shock effects are about equally pronounced for both cycles because the A < 0 cycle responds faster to changes in the tilt angle than the A > 0 cycle. These characteristics will be discussed in greater detail in the next chapter. The radial dependence of the spectra also clearly differs for the two polarity cycles and will be discussed in greater detail below. Note that at 1 AU the spectra assume the well-known 'adiabatic slope' at low energies ($\lesssim$ 200-300 MeV) but progressively deviate with increasing radial distances (see also e.g., Reinecke

and Moraal, 1992). Beyond the TS and at energies < 10 MeV, the slope of the spectra becomes much steeper than the adiabatic slope because the energy change term in the TPE becomes zero beyond the shock as required by the divergence free solar wind velocity ($1/r^2$ dependence). These low energy particles obviously experience large modulation, which is probably caused by $\kappa_{\perp r} \propto R^{1/3}$ as the dominating diffusion coefficient at large radial distances. This effect shifts to very low energies (< 10 MeV) for the A < 0 cycle and also as solar activity increases. This implies that the proton LIS will in principal not be known at these low energies until a spacecraft approaches the outer boundary. These effects are also illustrated from a different point of view in Figures 5.2 and 5.3.

5.5. Effects on radial intensities for protons

Figure 5.2 depicts the computed radial intensities for galactic protons in the equatorial plane, for both polarity cycles, with $\alpha = 10°$, and at six chosen energies: 0.016, 0.05, 0.2, 0.5, 1.0 and 5.0 GeV, respectively. The filled circles represent A > 0 observations and the squares represent A < 0 observations from IMP, Pioneer 10, Voyager 1 and 2 for solar minimum conditions (Webber and Lockwood, 2001a). The modulation effects of the TS, the heliosheath and the differences between the two polarity cycles are illustrated as a function of radial distance. At low energies (0.016 and 0.05 GeV) the difference in modulation between the two cycles is relatively weak but the strong modulation in the heliosheath is quite evident and is the main reason why this feature is also called the 'barrier' effect. Generally, these effects diminish with increasing energy to the extent that the 'barrier' remains prominent only for A > 0 cycles. The differences between the two cycles, however, increase up to ~1.0 GeV where it again diminishes with increasing energy.

At 0.016 and 0.05 GeV the model also gives negative radial gradients (g_r) in the heliosheath for the A > 0 cycle if $\alpha = 10°$ and for 85 AU < r < r_s in both cycles. (Here $g_r = \ln(j_2/j_1)/(r_2 - r_1)$ with j_i the differential intensity at position (r_i, θ).) This is because of the slope of the spectra that becomes steeper than the adiabatic slope if $r > r_s$, as has been mentioned in the previous section. This effect is seen at energies of up to ~0.05 GeV, but this depends on the solar cycle. This negative g_r for $r < r_s$ is caused when the steeper spectra are forced into the lower adiabatic slope in this region and the recovery distance can be as large as ~6 AU at low energies. In the heliosheath at energies $\lesssim$ 16 MeV this g_r becomes even steeper as the distance increases from the shock upto ~10 AU infront of the LIS where it suddenly increase to the LIS value, thus enhancing the 'barrier' effect at these energies. This effect is not as prominent for the A < 0 cycle and as solar activity increases.

The model and observations at 0.2 GeV are most reasonably compatible, illustrating that the model represents the observed g_r for both polarity cycles, with g_r for the A > 0 always less than for the A < 0 cycles for r < 40 AU at energies $\gtrsim$ 0.05 GeV but almost the same for r between 40 and 90 AU. For the A > 0 cycles the intensity at the TS is always less than for the LIS at 120 AU, and give significant modulation beyond the TS, which is decreasing with increasing energy. For the A < 0 polarity cycle, a more gradual increase in the radial intensities occur up to the TS - a characteristic of any drift model - with the intensity higher at the TS than at 120 AU for energies larger than several hundreds of MeV. At energies around 200 MeV the modulation is conspicuously different beyond the TS when it is compared to the other energies, an interesting feature also evident in Figure 5.1. From Figure 5.2 the cross-over between the A > 0 and A < 0 intensities can also be seen for $E \lesssim 0.4$ GeV. For $E > 0.5$ GeV this cross-over does not occur and intensities in the A < 0 cycle always stay above intensities in the A > 0 cycle. This cross-over migrates towards higher radial distances as the energy decreases and occurs at ~100 AU at 16 MeV.

In Figure 5.3 the solutions for moderate solar maximum conditions are illustrated. It shows the radial intensities

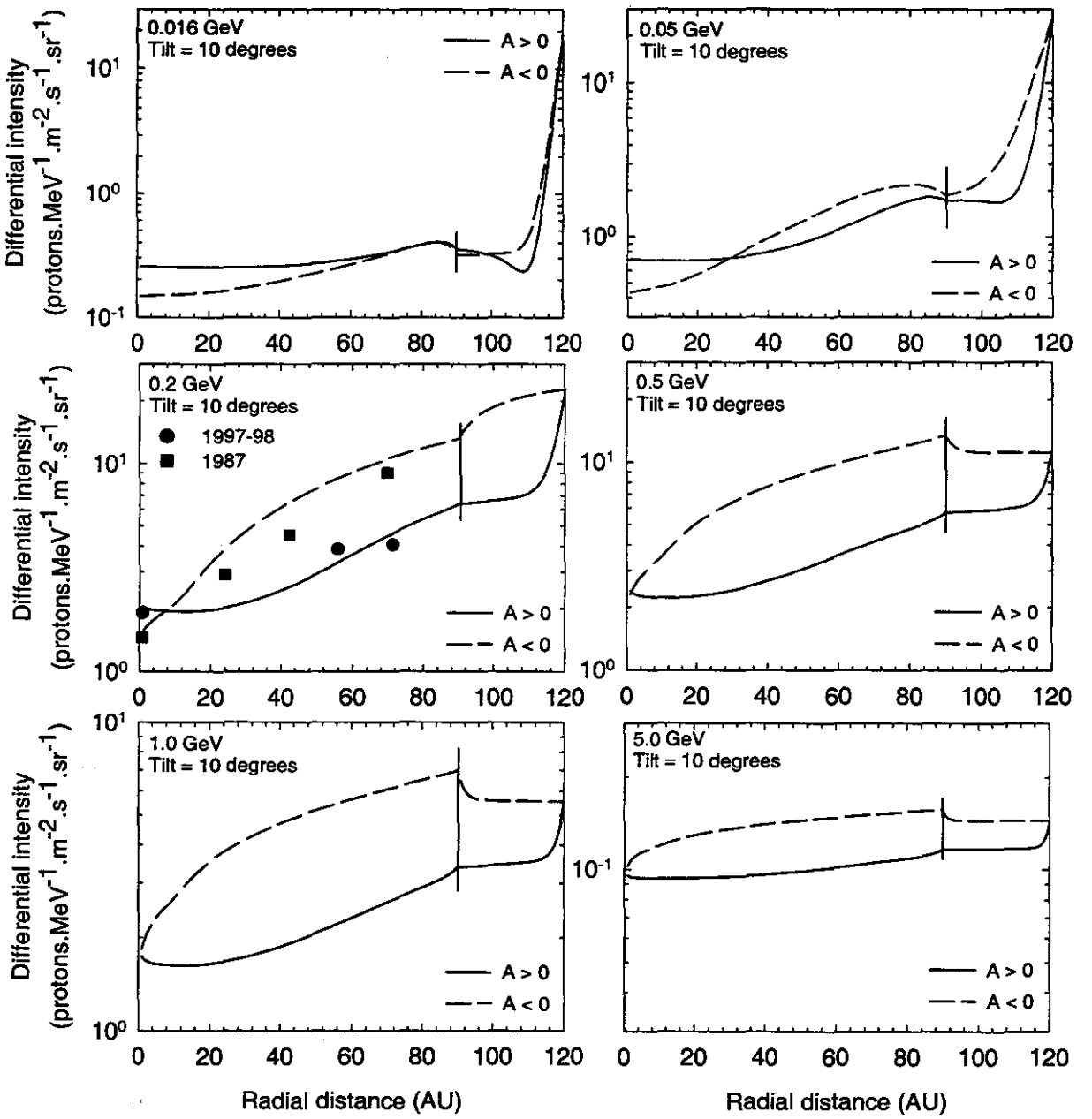

Figure 5.2. Computed radial intensities for GCR protons for both polarity cycles in the equatorial plane at 0.016, 0.05, 0.2, 0.5, 1.0 and 5.0 GeV, respectively, and for $\alpha = 10°$. Solid lines represent A > 0, while the dashed lines represent A < 0 as indicated. The LIS is specified at 120 AU. In the 0.2 GeV panel, the filled circles represent A > 0 observations, the squares represent A < 0 observations of IMP, Pioneer 10, Voyager 1 and 2 (Webber and Lockwood, 2001a) for solar minimum conditions. The reference line denotes the position of the TS. Note the scale differences between the panels.

for protons for both polarity cycles in the equatorial plane at 0.016, 0.05, 0.2, 0.5, 1.0 and 5.0 GeV, respectively, but now for $\alpha = 75°$, with the the appropriate change in the diffusion coefficients as is explained in Chapter 3. The three data points are from IMP, Pioneer 10, and Voyager 2 for solar maximum conditions in 1990-1991 (Webber and Lockwood, 2001b). The compatibility with the observations is obviously not as good as for solar minimum conditions, as expected, indicating that additional solar maximum modulation effects are required e.g., global merged interaction regions and time-dependent diffusion coefficients (Potgieter and Langner, 2003c). Similar to

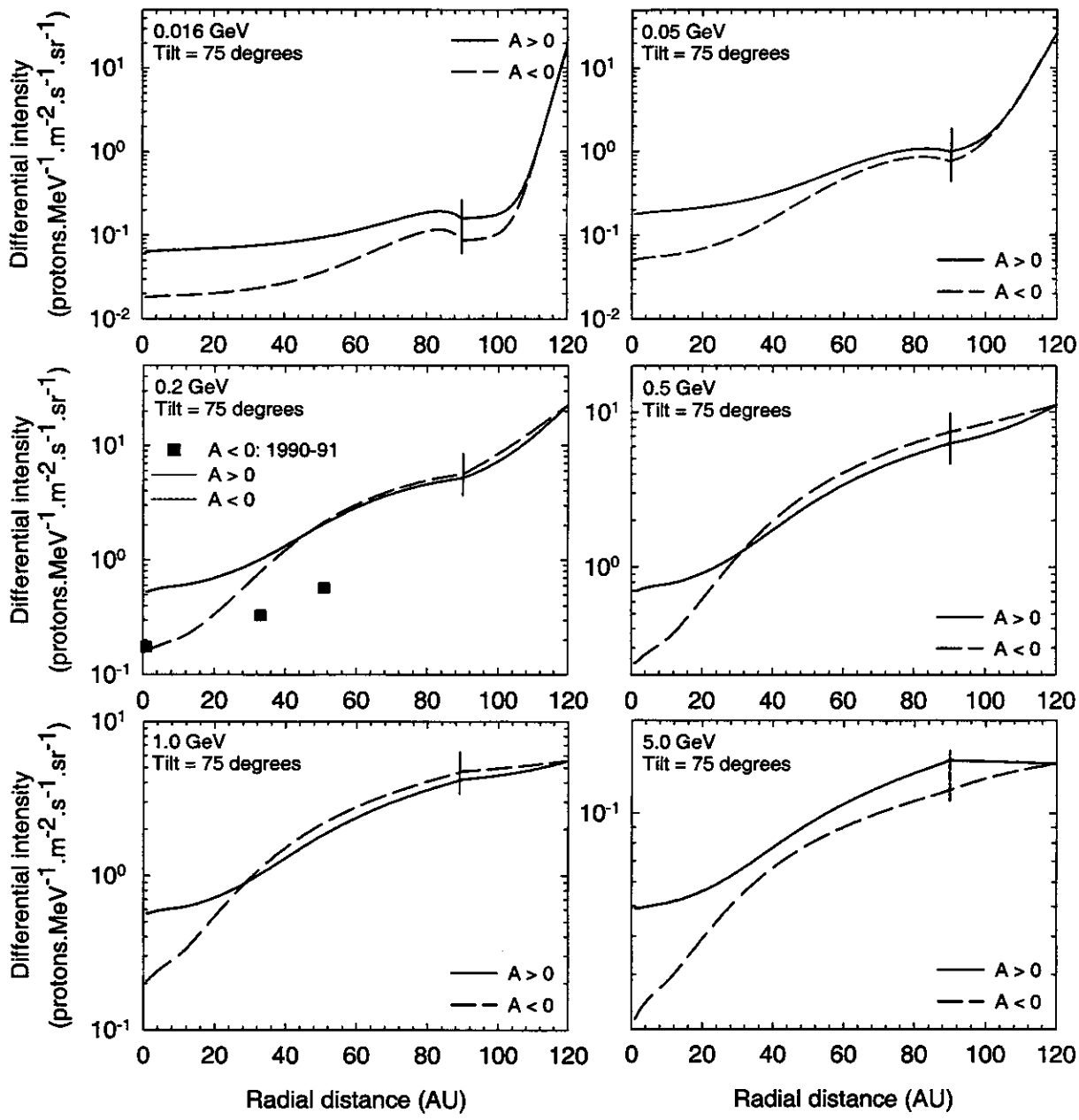

Figure 5.3. Radial intensities for protons for both polarity cycles in the equatorial plane at 0.016, 0.05, 0.2, 0.5, 1.0 and 5.0 GeV respectively, for $\alpha = 75°$ as function of radial distance. Solid lines represent A > 0, while the dashed lines represent A < 0 as is indicated. In the 0.2 GeV panel the squares represent A < 0 observations of IMP, Pioneer 10, and Voyager 2 (see Webber and Lockwood, 2001b) for solar maximum conditions, 1990-1991. The reference line denotes the position of the TS. Note the scale differences between the panels.

solar minimum conditions, the modulation inside the TS is different for A > 0 and A < 0 cycles but these differences diminish with increasing energy. The reason is that the A < 0 intensities respond more significantly to changes in the tilt angle (α). The 'barrier' effect is still strongly present at 16 MeV for both polarity cycles although g_r is different than before. The modulation difference beyond the TS between A > 0 and A < 0 is insignificant at all energies larger than a few tens of MeV, in contrast to solar minimum. This indicates that drifts are already almost negligible in this region for moderate solar maximum. At 0.5 GeV the 'barrier' effect is barely visible and for energies $\gtrsim$ 1.0 GeV, its effect takes a different radial dependence not evident in the solar minimum solutions;

in this case without the large increases close to the outer boundary for the A > 0 cycle. This is because of the reduced drifts in the heliosheath as will be shown in the next section. However, the modulation beyond the TS is still substantial for 0.2 GeV but becomes less significant with increasing energy compared to the amount of modulation inside the TS. From Figure 5.3 the cross-over between the A > 0 and A < 0 intensities can also be seen for moderate solar maximum conditions. Here the cross-over occurs for almost all energies of interest, which is not the case for solar minimum conditions (see Figure 5.2). This cross-over also migrates towards higher radial distances as the energy decreases as for solar minimum conditions and occurs at ~110 AU at 16 MeV.

5.6. Non-drift solutions in the heliosheath

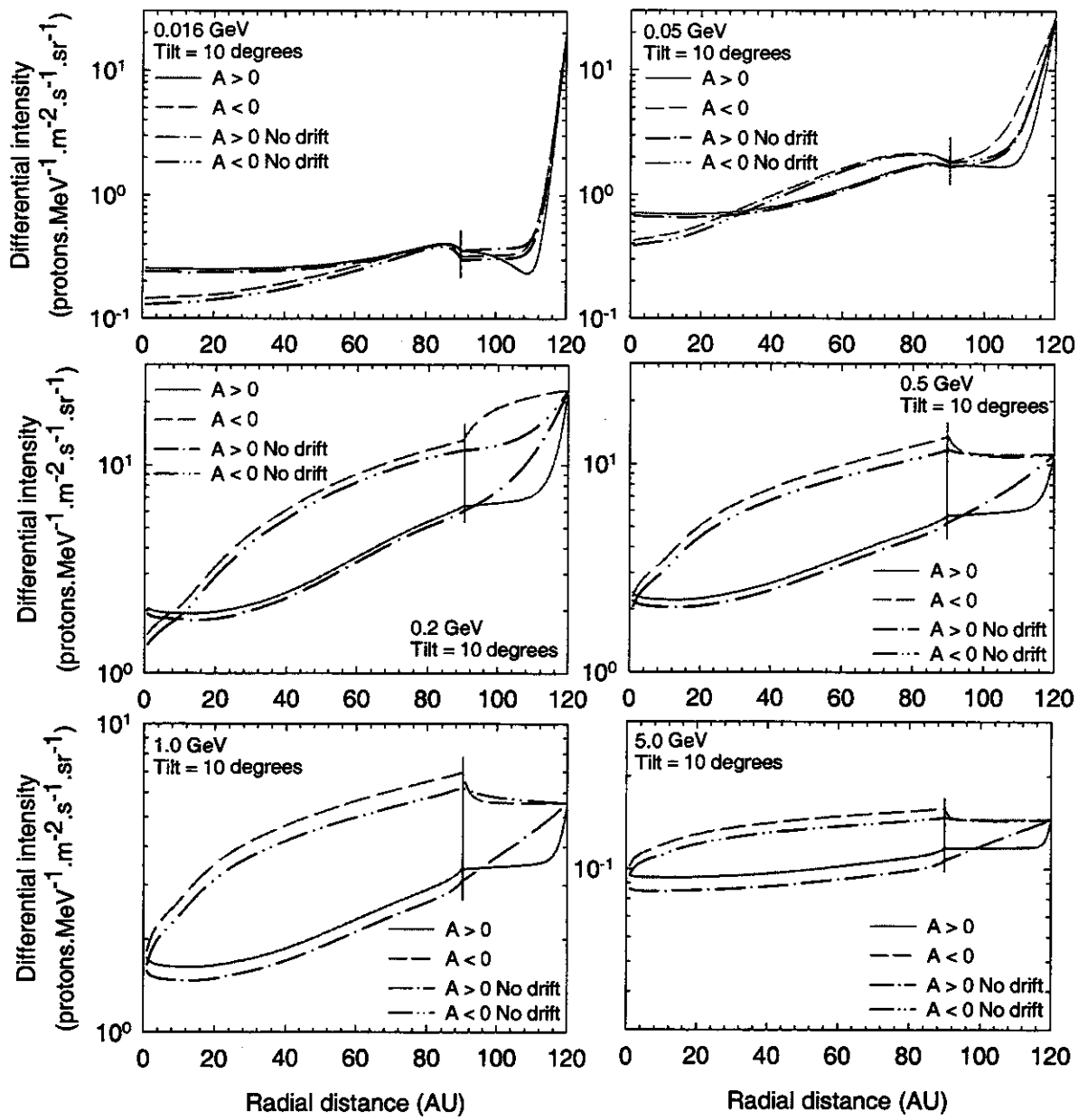

Figure 5.4. Computed radial intensities for GCR protons without drifts but only if $r > 90$ AU (dark lines) for both polarity cycles in the equatorial plane at 0.016, 0.05, 0.2, 0.5, 1.0 and 5.0 GeV, respectively, and for $\alpha = 10°$. Solutions with drifts if $r > 90$ AU are shown as grey lines as a reference.

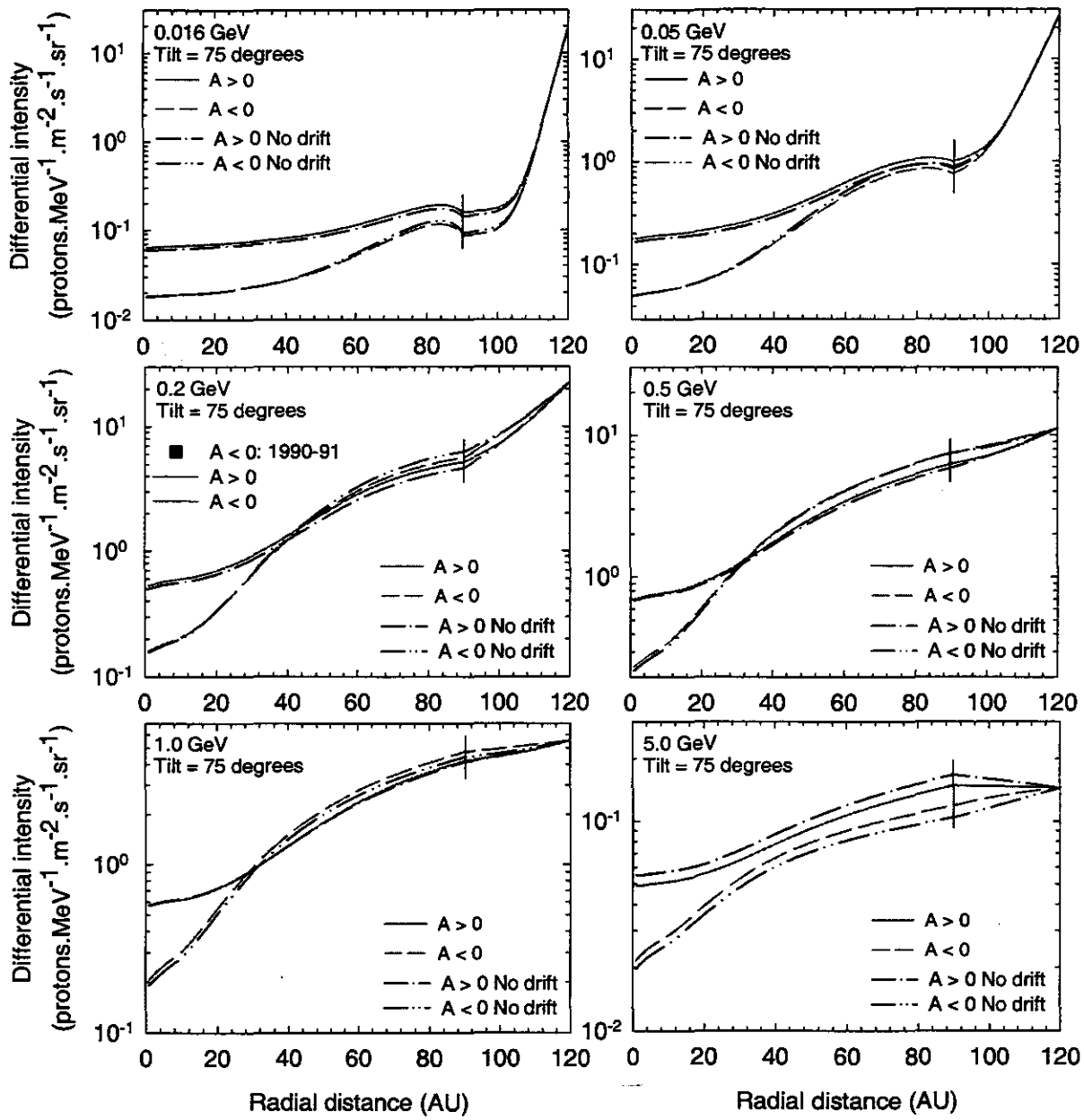

Figure 5.5. Similar to Figure 5.4 but for moderate solar maximum conditions with $\alpha = 75°$. Note the scale differences between the panels.

It is generally assumed that increasing turbulence and a less ordered HMF should occur beyond the TS which will reduce drifts. To illustrate to what extent particle drifts play a role in the heliosheath, solutions are repeated for the case where there are no drifts beyond the TS instead of just reducing drifts by a factor of s as in the previous cases. Figure 5.4 depicts the computed radial intensities for galactic protons for this case in the equatorial plane, for both polarity cycles, with $\alpha = 10°$, and at six chosen energies: 0.016, 0.05, 0.2, 0.5, 1.0 and 5.0 GeV, respectively. This is also shown for $\alpha = 75°$ in Figure 5.5 in contrast to the solutions with drifts in the heliosheath. From these figures it follows that the sudden changes at the TS clearly make way for more gradual increases in the non-drift case. The drifts effect which is given by the model is still surprisingly large inside the heliosheath and is increasing with energy despite the reduction by a factor of s. Although the spectral slopes at distances r > 90 AU also become steeper than the adiabatic slope, it happens at much lower energies. Consequently, there

is no negative g_r as in Figure 5.2 for A > 0 when $\alpha = 10°$. The modulation in the heliosheath can become quite different for the two cases, especially for A > 0 if $\alpha = 10°$.

For moderate maximum conditions with $\alpha = 75°$, the differences are almost negligible because of the decrease in drifts by a factor of s at and beyond the shock and the enhancement of $\kappa_{\theta\theta}$ as has been described in Chapter 3. Obviously, how much drifts really occur in the heliosheath and how important it is for modulation in the outer heliosphere will have to be investigated further and more fundamentally than what is presented in this work. The situation will also be more clear if spacecraft enter the heliosheath region. From this study, however, it follows that by allowing drifts beyond the TS, the 'barrier' effect is enhanced.

5.7. Heliosheath modulation vs total modulation

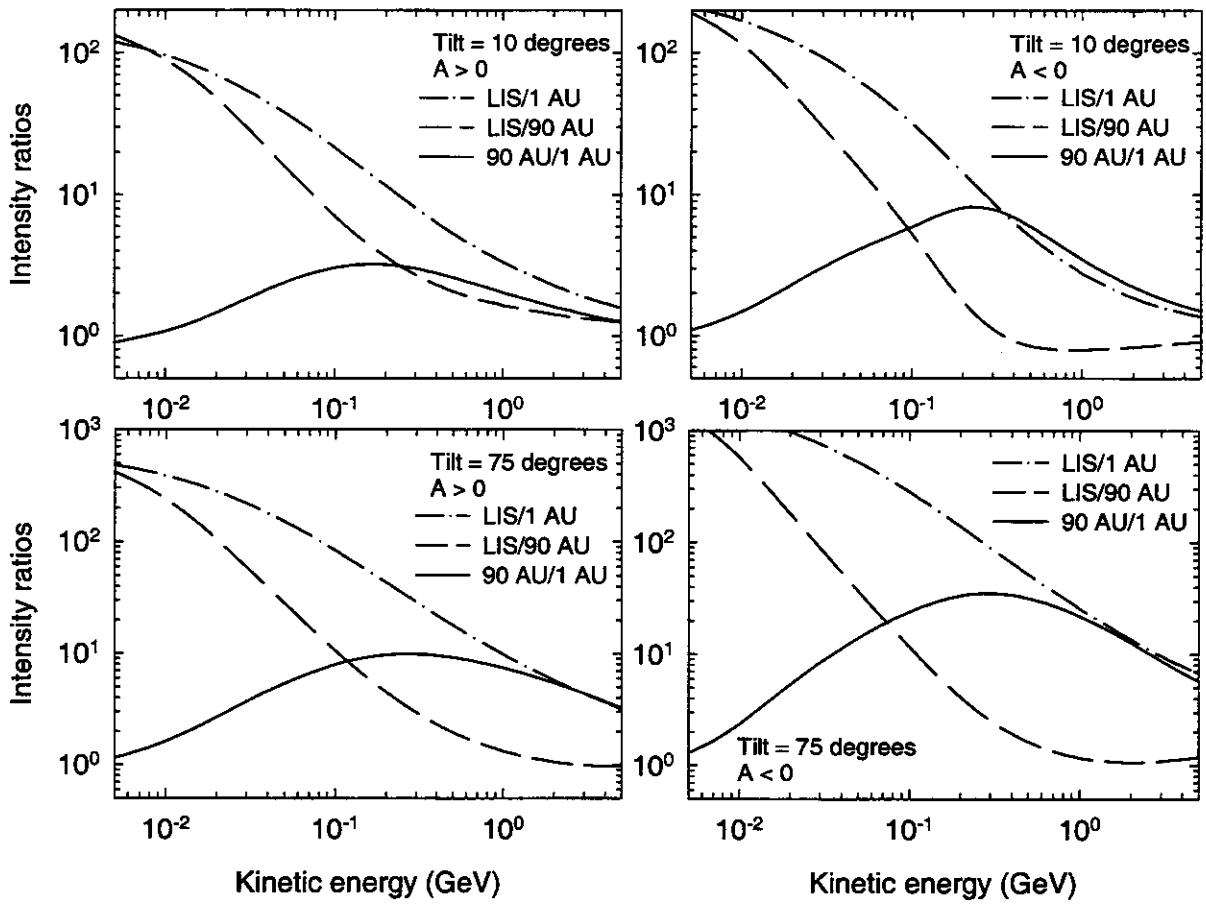

Figure 5.6. Intensity ratios j_{LIS}/j_1, j_{LIS}/j_{90} and j_{90}/j_1 (120 to 1 AU, 120 to 90 AU and 90 to 1 AU) for protons as a function of kinetic energy in the equatorial plane with $\alpha = 10°$ (top panels) and 75° (bottom panels); left panels: for A > 0, right panels: for A < 0. The LIS is at 120 AU and the TS at 90 AU.

Next, the modulation which is computed to take place in the heliosheath, between r_b and r_s (LIS to TS), is compared to what happens between r_b and 1 AU (LIS to Earth) and between r_s and 1 AU (TS to Earth). This comparison is emphasized by showing in Figure 5.6 the intensity ratios j_{LIS}/j_1, j_{LIS}/j_{90} and j_{90}/j_1 for protons as a function of kinetic energy in the equatorial plane for both polarity cycles with $\alpha = 10°$ and 75°, respectively. Note that for a few cases the ratios become less than unity.

According to this figure a significant level of modulation occurs in the heliosheath for p when A > 0 with $E \lesssim$ 200 MeV. This is also true for the A < 0 cycle if $\alpha = 10°$ and both cycles if $\alpha = 75°$, but at a somewhat lower energy. When A < 0 and $\alpha = 10°$, j_{LIS}/j_{90} drops below unity because the intensity at the TS becomes larger than the LIS value. The 'barrier' effect is clearly the most prominent for the A > 0 cycle if $\alpha = 10°$. Obviously, these ratios all converge at a high enough energy where no modulation is present (not shown).

5.8. Summary and conclusions

The TS and the heliosheath are prominent and interesting features of the heliosphere. The inclusion of a TS in the modulation model for protons and for solar minimum conditions causes abrupt changes in the CR radial gradients, g_r, at the TS, at almost all energies of interest to modulation studies. For A > 0 cycles, g_r becomes typically very large (positive) inside the TS but almost zero at energies > 1.0 GeV beyond the TS, to increase again significantly close to the outer boundary. At lower energies, g_r progressively becomes larger positive behind the TS. The CR proton intensity is lower at the TS than the value of the assumed LIS at 120 AU for all energies that have been considered here.

For the A < 0 cycle, the abrupt changes at the TS in g_r are qualitatively similar, but they differ quantitatively, especially at low energies. For these cycles the intensity at the TS at energies $\gtrsim$ 0.5 GeV can be higher than the corresponding value of the LIS, so that g_r may even be negative beyond the TS. At energies $\lesssim$ 0.2 GeV, g_r is very similar to that for the A > 0 cycle. Beyond the TS at energies < 10 MeV the slope of the spectra becomes much steeper than the adiabatic slope because the energy change term in the TPE becomes negligible beyond the shock caused by the assumed divergence free solar wind. These low energy particles obviously experience large modulation which is probably caused by $\kappa_{\perp r} \propto R^{1/3}$. This implies that the LIS for protons will in principle not be known at these low energies until a spacecraft approaches the outer boundary.

For increased solar activity, the modulation in the heliosheath is quite different from minimum activity. The heliosheath no longer plays the role of a distinguished 'barrier', although abrupt changes in g_r at the TS may still occur, especially for A > 0 cycles, surprising more so for higher energies. The role of drifts manifests itself in the clear differences between the polarity cycles. Drifts in the heliosheath region have the effect to enhance the 'barrier' effect, while no drifts cause more gradual increases in the radial intensities. The spectral form of the LIS is not primarily important but the value of the LIS at a given energy may change the total 'barrier' effect. This of course is not true for energies $\lesssim$ 0.4 GeV in the inner most heliosphere because of adiabatic 'cooling'. Qualitatively, our results are consistent to those of Jokipii et al. (1993) but there are quantitatively marked differences.

Can the heliosheath be considered a distinguishable modulation 'barrier'? The answer is a reserved 'yes' as has been illustrated in Figure 5.6. The overall effect is clearly energy, solar polarity cycle and solar activity dependent. At low energies (E < 100 MeV) most of the modulation happens in the heliosheath for solar minimum and moderate maximum activity. At moderate maximum modulation conditions the 'barrier' effect above ~1 GeV is surprisingly less significant than for solar minimum conditions. Incorporating huge transient 'barriers' in the model may alter these conclusions in the sense that an accumulation of these 'barriers' may enhance or diminish the heliosheath effect depending on the polarity cycle and the phase of solar activity.

In the following chapter the TS model is expanded to include the heliospheric modulation of anti-protons and protons with an anomalous component.

Chapter 6
Heliospheric modulation of protons and anti-protons

6.1. Introduction

The interest in the role of the TS and the heliosheath in CR modulation studies have increased significantly as the Voyager 1 and 2 spacecraft approach the estimated position of the TS. Observations near the predicted location of the TS (e.g., McDonald et al., 2000) have made it possible to study CR modulation in the outer heliosphere in more detail, especially the effects of the TS and what level of modulation may occur in the heliosheath. Modulation of protons and anti-protons inside the heliosphere also hides the value of their different local interstellar spectra, especially below a few GeV. However, improved calculations for the proton and in particular the anti-proton LIS based on sophisticated models for the propagation of cosmic rays in the Galaxy were published by Moskalenko et al. (2002).

In the previous chapter the 'barrier' effect for galactic protons was discussed. In this chapter it is expanded to include the modulation of cosmic ray anti-protons, and anomalous protons. The modulation of anomalous protons is included to establish the consequent charge-sign dependence in $\overline{p}/p$ at low energies. The following topics are addressed in more detail: (1) The effects of the TS on the modulation of protons, with and without an anomalous component, and for the first time also for anti-protons, for both HMF polarity cycles, and as solar activity changes from minimum to moderate maximum conditions. (2) A comparison of the modulation of these species with and without a TS. (3) The level of modulation in the simulated heliosheath and the importance of this 'barrier' modulation for the different species and how this affect the computed $\overline{p}/p$, and (4) to establish the consequent charge-sign dependent effects by means of the modulated $\overline{p}/p$. The TS model in this chapter will be used with the parameters which have been described in Chapters 2, 3, and 4. The content of this chapter was published by Langner and Potgieter (2003b).

6.2. LIS for anti-protons and the anomalous proton source

The proton LIS and the parameterisation used were described in detail in the previous chapter (see Equation 5.1).

6.2.1. LIS for anti-protons

The main process producing $\overline{p}$ is collisions of high energy cosmic p with the interstellar gas. The energy spectrum of these secondary $\overline{p}$ thus produced can be computed with reasonable confidence and therefore a good a priori knowledge is assumed of the input spectrum for heliospheric modulation. The distinct maximum of the $\overline{p}$ production spectrum around 2 GeV is because of the high energy threshold for $\overline{p}$ production in collisions. Moskalenko et al. (2002) argued that their anti-proton LIS might be too low despite the large error bars of the $\overline{p}$ observations, causing peculiar little modulation for $\overline{p}$ inside the heliosphere (see also Langner and Potgieter, 2003b).

The galactic propagation models designed by Moskalenko et al. (2002, 2003) to match the secondary/primary nuclei ratios seem to produce too few anti-protons. They argue that there may exist a source of primary $\overline{p}$ at low energies that may increase the LIS. However, this is still unclear and therefore the anti-proton LIS of Moskalenko

et al. (2002) is used, with a parametrization given by

$$j_{LIS} = \begin{cases} \exp\left(-9.60 - 0.10\ln(E)^2 - 1.91\exp(-E)\right) & \text{if } E < 0.94 \text{ GeV} \\ \left(2.42 \times 10^{-3} E^{-2.81}\right) / \left(0.81 + 7.74 E^{-1.81}\right)^2 & \text{if } E \geq 0.94 \text{ GeV} \end{cases}, \quad (6.1)$$

with E the kinetic energy in GeV.

6.2.2. The anomalous proton source

For protons with an anomalous component a source was injected at the TS position for all θ at an energy of ~86 keV as a delta function with a magnitude set to give reasonable fits to anomalous proton observations at 60 AU and to proton observations at Earth (see also Steenberg, 1998; Steenberg and Moraal, 1996). The solutions are independent of this injection energy as long as it is lower than the cutoff energy for anomalous protons as has been discussed in Chapter 4. Since the mass-to-charge ratios, $A/Z = 1$, are the same for galactic and anomalous protons, the model can give simultaneous solutions for these species if the spectra of protons with an anomalous proton component are required.

6.3. Comparison of the modulation of protons, anti-protons, and anomalous protons

The results that will be shown in the following sections concentrate on five aspects of heliospheric modulation for p and $\overline{\text{p}}$: (1) The difference in the modulation of p and $\overline{\text{p}}$, given the vastly different LIS. (2) How the inclusion of a TS in the model alters the modulation of p and $\overline{\text{p}}$ and the subsequent effects on charge-sign dependence. (3) The nature of modulation effects to be expected near the TS and in the heliosheath. (4) The effects of increased solar activity and tilt angle dependence. (5) How the inclusion of an anomalous proton source affects the modulation and charge-sign dependence.

The left panels of Figures 6.1, 6.3 and 6.5 show the modulation obtained with the TS model with respect to the LIS for galactic p, $\overline{\text{p}}$, and for p with an anomalous component, as a function of kinetic energy, respectively. This is done at 1, 60, 90 and 115 AU in the equatorial plane for the A > 0 and A < 0 polarity cycles with $\alpha = 10°$ and $\alpha = 75°$, respectively. The right panels of Figures 6.1 and 6.3 show the corresponding differential intensities at 0.016, 0.2 and 1.0 GeV as function of radial distance in the equatorial plane, respectively for solutions with a TS and without a TS. In Figure 6.5 the right panels also show the corresponding differential intensities at 0.016, 0.2 and 1.0 GeV as function of radial distance in the equatorial plane, respectively but for solutions with $s = 3.2$ and $s = 2.0$. The solutions without a TS corresponding with the left panels of Figures 6.1 and 6.3 are shown in Figures 6.2 and 6.4.

In Figure 6.5 the p solutions are repeated with an anomalous component with $s = 3.2$, as the rest but also with $s = 2.0$. This decrease in the compression ratio was necessary to obtain reasonable compatibility with the anomalous proton observations at 60 AU as was shown in Chapter 4. The solutions in the inner heliosphere ($r \lesssim$ 40 AU) are largely insensitive to this change. Decreasing s causes the peak in the modulated anomalous proton spectrum to shift to lower energies as the observations seem to require and can be caused by a decreasing shock strength with increasing solar activity. These quantitative aspects of anomalous proton modulation were discussed in detail by Steenberg and Moraal (1996) and Potgieter and Langner (2003a, 2003b) and are not pursued further in this work.

From Figures 6.1 and 6.3 it follows that the modulation is significantly different for galactic p and $\overline{\text{p}}$, primarily

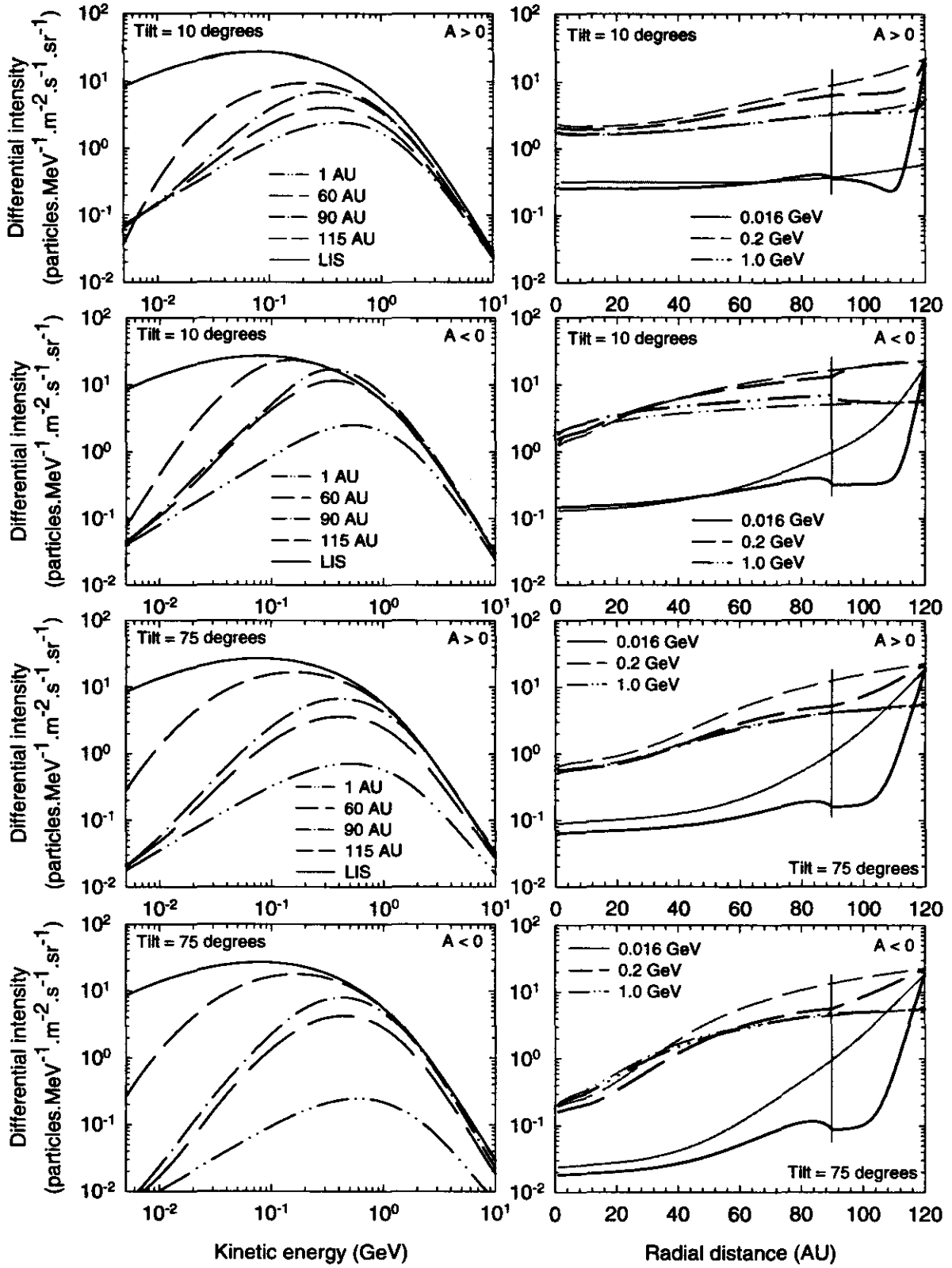

Figure 6.1. Left panels: Computed differential intensities for galactic protons as a function of kinetic energy for both polarity cycles and solar minimum and moderate maximum conditions, at radial distances of 1, 60, 90 and 115 AU (bottom to top) in the equatorial plane. Right panels: Corresponding differential intensities as function of radial distance for 0.016, 0.2 and 1.0 GeV, respectively. Solutions without a TS are given here as thin grey lines. In all panels the TS is at 90 AU, as indicated, and the LIS is specified at 120 AU.

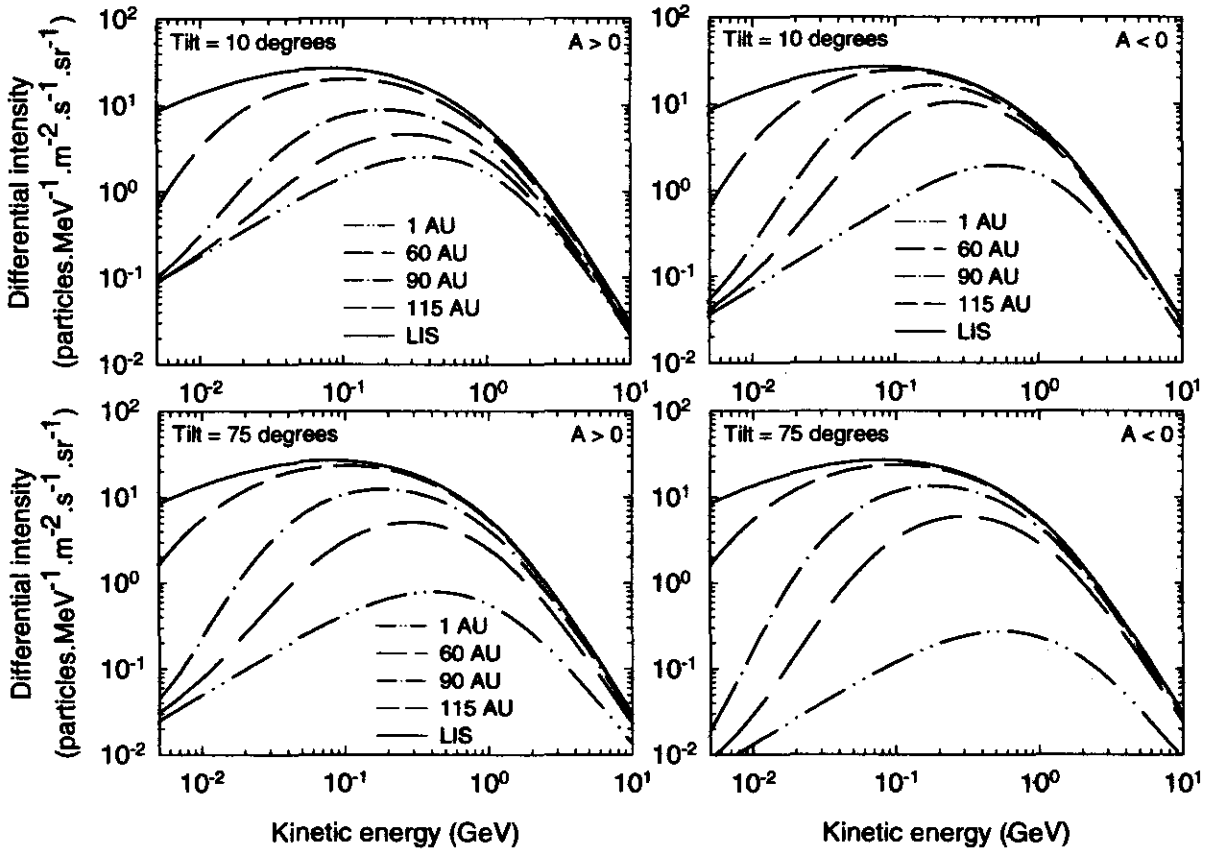

Figure 6.2. Differential intensities computed without a TS for galactic protons as a function of kinetic energy for both polarity cycles and solar minimum (top panels) and moderate maximum (bottom panels) conditions, at radial distances of 1, 60, 90 and 115 AU (bottom to top) in the equatorial plane.

caused by differences between the two LIS below 2 GeV. A remarkable feature with the TS is that the modulated p spectra at large radial distances for the A < 0 cycle can actually exceed the corresponding LIS between ~200 MeV and a few GeV, which cannot happen without a TS, as is shown in Figures 6.2 and 6.4. This effect is not as pronounced for $\bar{p}$, seems absent for larger α's and clearly depends on the drifts direction.

The energy spectra in Figures 6.1 and 6.3 also depict how the slopes of the modulated $\bar{p}$ spectra obtain the characteristic spectral index (energy slope) which is caused by adiabatic 'cooling' at higher energies than for protons. The reason is that the anti-proton LIS at $E < 1$ GeV already has an almost E^1 dependence, with E the kinetic energy. This causes much larger modulation with respect to the relevant LIS for p than for $\bar{p}$ at energies below ~1 GeV, but the level clearly depends on the polarity cycle. Beyond the TS ($r > r_s$), the spectra obtain a much steeper energy slope and can cause rather strong negative radial gradients at very low energies as is evident from the top left panel of Figure 6.1. As has been discussed in Chapter 5, this is caused by the assumed divergence free solar wind speed in the heliosheath ($V \propto 1/r^2$). This implies that the proton LIS may not be known at these low energies until a spacecraft actually approaches the heliopause. This feature is not present in the solutions without a TS, as has been expected. Differences between the models with and without a TS will be discussed in detail in the next section.

The modulation in the heliosheath is clearly an important part of the total modulation for p and $\bar{p}$ as is shown in the right panels of Figures 6.1, 6.3 and 6.5. The TS in this regard plays a prominent role. For both species its effect

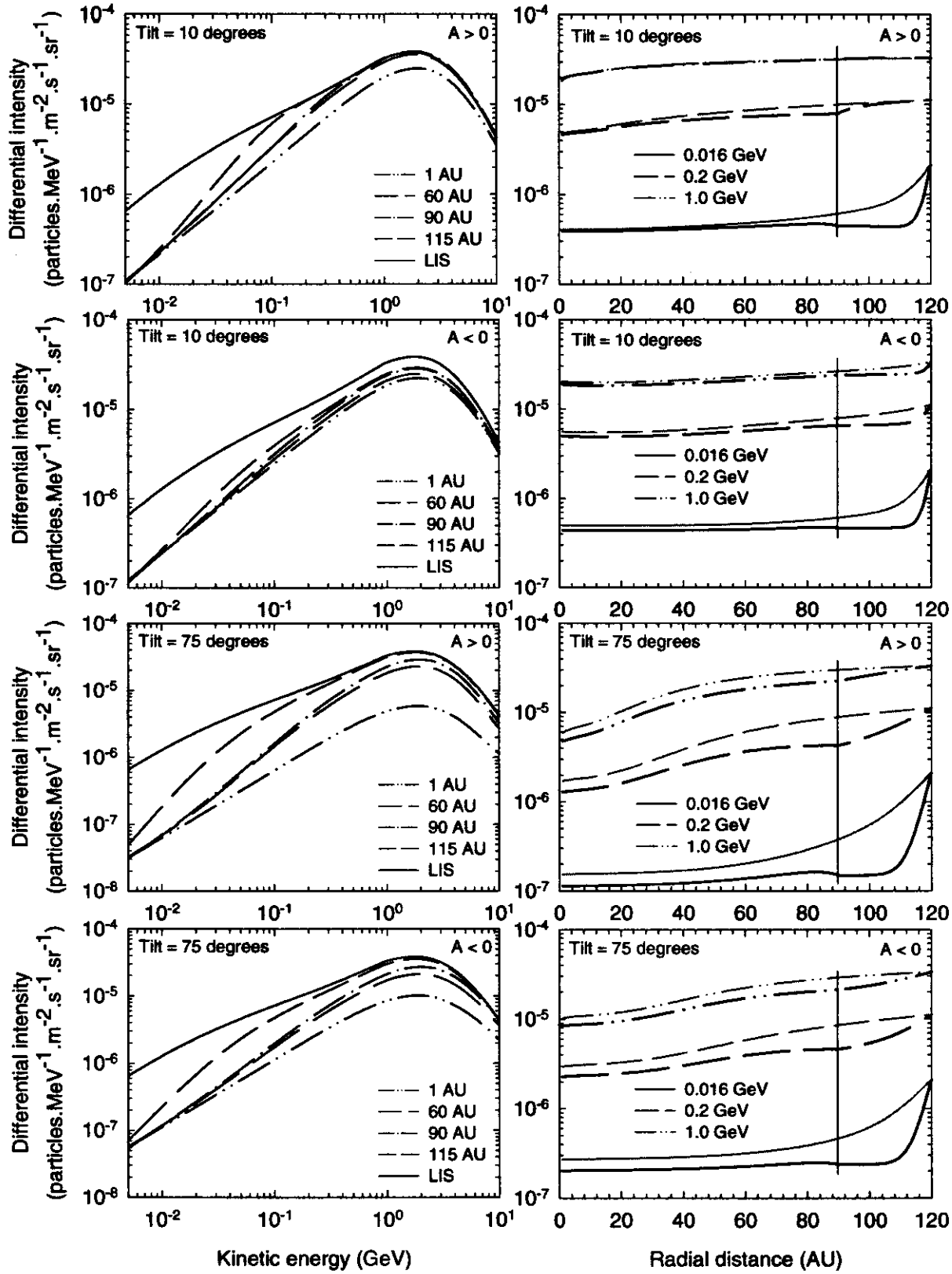

Figure 6.3. Similar to Figure 6.1, but for anti-protons. Note the scale differences between the panels.

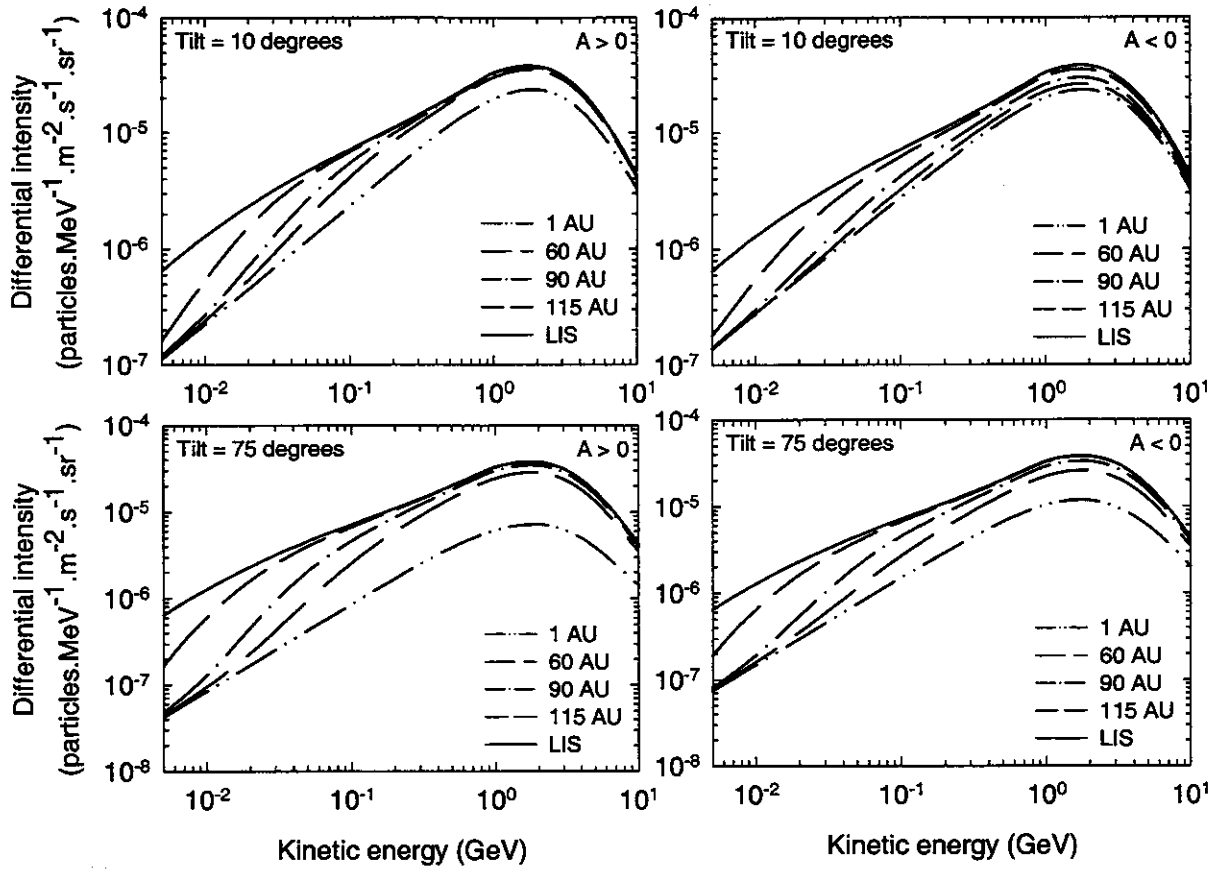

Figure 6.4. Similar to Figure 6.2, but for anti-protons. Note the scale differences between the panels.

becomes more pronounced the lower the energy. At higher energies, the 'barrier' effect progressively diminishes; the radial dependence beyond the shock may vanish or may even become negative to create a conspicuous shock effect on the radial intensity profiles. This effect is strongly dependent on the HMF polarity cycles, and also on the level of drifts that have been allowed beyond the TS e.g., the peculiar radial dependence for 200 MeV p in the A < 0 cycle and $\overline{\text{p}}$ in the A > 0 cycle for $\alpha = 10°$. For an elaborate discussion on these effects for protons, see the previous chapter (see also Langner et al., 2003b).

The radial dependence for $\overline{\text{p}}$ is noteworthy because it is very weak except for $E < 300$ MeV where it becomes somewhat stronger. The shock effects (the abrupt changes in the radial intensities) above this energy are almost negligible. Despite the large error bars of the observations (see Chapter 4), the modelling also indicates that the computed LIS may be too low, causing peculiar little modulation but with interesting consequences, e.g., that measurements in the inner heliosphere below 1 GeV may already indicate the spectral shape of the LIS in sharp contrast to protons.

For protons with an anomalous component, as is shown in Figure 6.5, the intensities at the TS where the anomalous source is injected follow the characteristic $E^{-1.2}$ spectrum with $s = 3.2$ and $E^{-2.0}$ with $s = 2.0$ (see Equations 2.49 and 2.52), which is dictated by the acceleration of the anomalous protons at the TS with $E \lesssim$ 100 MeV. The inclusion of an anomalous proton component has a profound effect on the proton intensities at larger radial distances ($r \gtrsim 60$ AU) at $E \lesssim 100$ MeV, but an almost negligible effect on the intensities at Earth. Near the TS the spectrum is of course substantially different because of the injected anomalous source. The radial

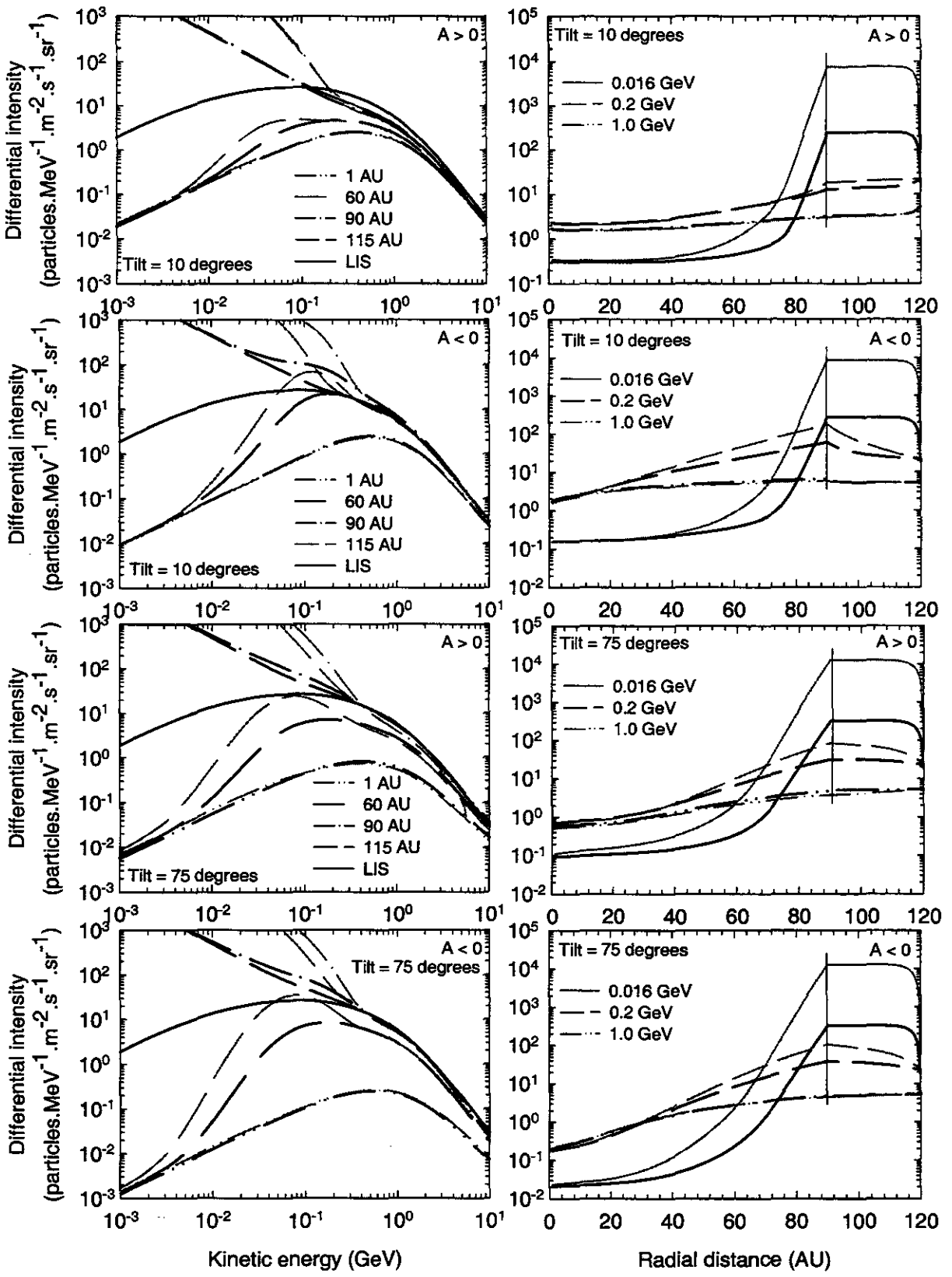

Figure 6.5. Similar to Figure 6.1 but for protons with an anomalous component. Here the thin gray lines represent solutions with $s = 2.0$, while the black lines represent solutions with $s = 3.2$.

dependence of the 16 MeV intensity is consequently significantly different, but at the higher energies the effect diminishes as the acceleration cut-off is approached. The 'barrier' for this component at 16 MeV occurs inside the TS. This implicates that at these low energies a spacecraft may begin to observe a significant increase from ~10 AU infront of the TS. These aspects will be shown more quantitatively later in the chapter. Our results indicate that a s between 3.2 and 2.0 is preferred when anomalous protons are also considered, in fact, this ratio cannot be determined effectively using only galactic p and $\overline{\text{p}}$ spectra. Clearly, a strong shock with $s = 4$ is most unlikely (see also Potgieter and Langner, 2003a, 2003b).

6.4. Differences in modulation with and without a TS

In this section the differences in modulation with and without a TS are shown for p and $\overline{\text{p}}$. In Figure 6.6 the effects of the TS on p and $\overline{\text{p}}$ modulation are illustrated by depicting the ratio of intensities obtained with and without a TS as a function of kinetic energy at radial distances of 1, 60, 90 and 115 AU, and as a function of radial distance at energies of 0.016, 0.2 and 1.0 GeV, respectively, in the equatorial plane for both polarity cycles when $\alpha = 10°$. This is also shown for $\alpha = 75°$ in Figure 6.7. The parameters of the two models were kept the same for these calculations in order to quantify the effects of the TS on the modulation of p and $\overline{\text{p}}$. The ratios as a function of energy converge naturally at $E \gtrsim 10$ GeV because the TS has progressively less modulation effects the higher the energy. The ratios as function of radial distance approach unity at 120 AU where the LIS are specified. These computed ratios indicate quantitatively how much the computed modulation for p and $\overline{\text{p}}$ changes when a TS is present.

The effect of the TS on the modulation of p and $\overline{\text{p}}$ with respect to the relevant LIS is profound, it decreases the intensities at lower energies (e.g., at 100 MeV) but increases it at higher energies (e.g., at 1 GeV) as the lower energy particles are being accelerated to higher energies. This effect is also indicated by the ratios in Figures 6.6 and 6.7 which become larger than 1 for high energies. The differences between the two models can be significant, especially with $E <$ 100-300 MeV and $r \gtrsim 60$ AU for both $\alpha = 10°$ and 75°. For $\alpha = 10°$ the ratios in Figure 6.6 are always the smallest at 115 AU for A > 0 for p and A < 0 for $\overline{\text{p}}$ at all energies, which indicate that the effect of the TS model is the most at these larger distances. This is partly because of the assumed divergence free solar wind in the heliosheath region, causing the characteristic spectral slope which is caused by adiabatic 'cooling' to be steeper for the TS model if $r \geq 90$ AU. The ratios at the different radial distances also seem to have a minimum at a certain energy which becomes smaller as the radial distance increases. This is also because of the adiabatic 'cooling' that these particles experience, which will tend to let the ratios converge to a constant value at low energies. These two effects cause shifts in the minima of the ratios, e.g., for A < 0 for p and A > 0 for $\overline{\text{p}}$ and if $\alpha = 75°$ for both species the minima seem to become smaller if $r > 90$ AU and to cross for $r = 90$ AU and 115 AU.

The effect of the TS at Earth is not as pronounced as for larger distances, although the inclusion of the TS in the model can evidently influence the modulation of p and $\overline{\text{p}}$ even at Earth at low energies. The intensities can become less at Earth at low energies for the TS than without a TS. This is because of the acceleration of these low energy particles to higher energies, as has been mentioned earlier.

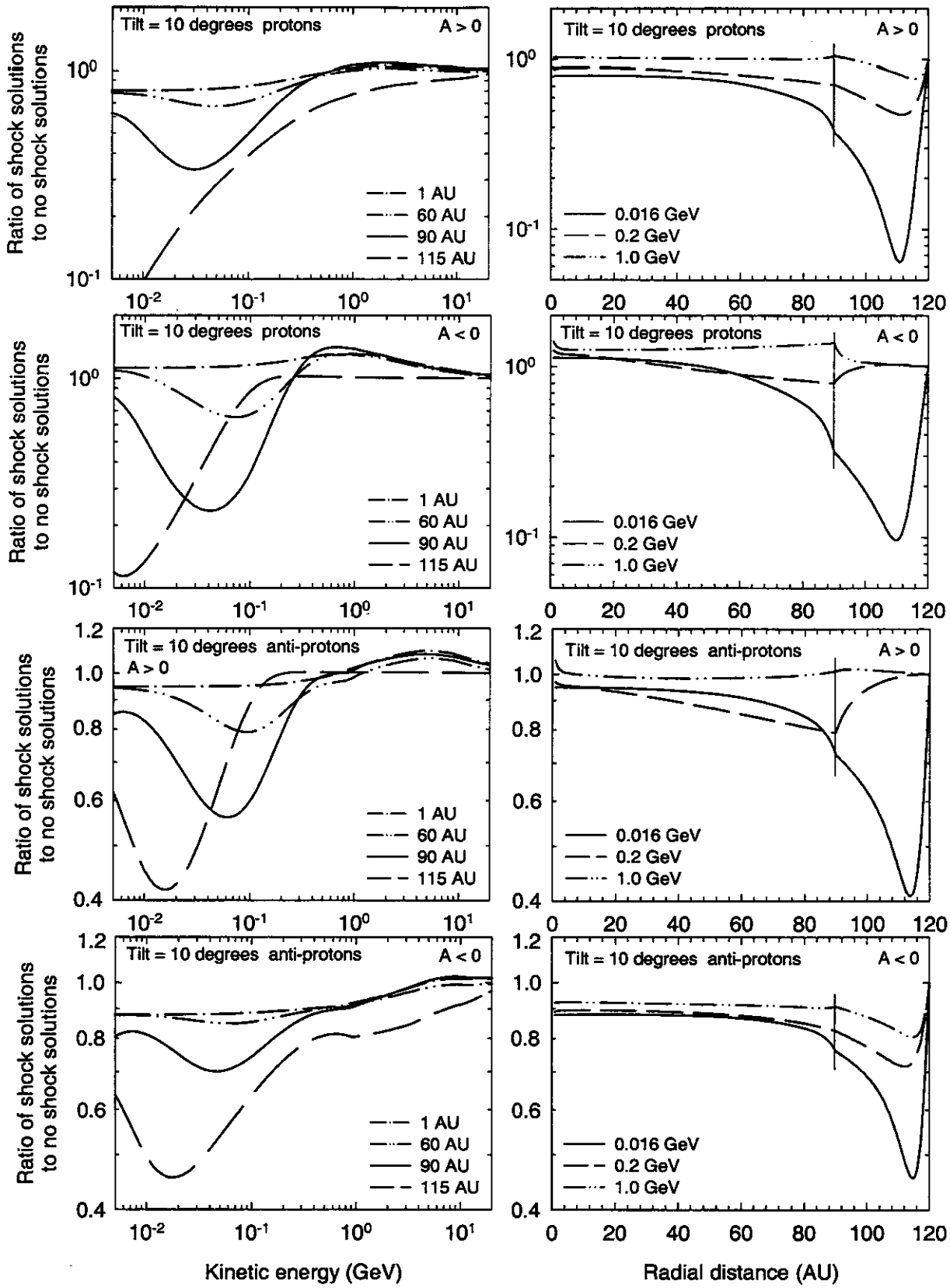

Figure 6.6. Intensity ratios of solutions with a TS compared to those without a TS as a function of kinetic energy (left panels) at radial distances of 1, 60, 90 and 115 AU and as function of radial distance (right panels) at energies of 0.016, 0.2 and 1.0 GeV for both polarity cycles in the equatorial plane. Top four panels are for protons and bottom four for anti-protons, all with $\alpha = 10°$. Note the scale differences between the panels.

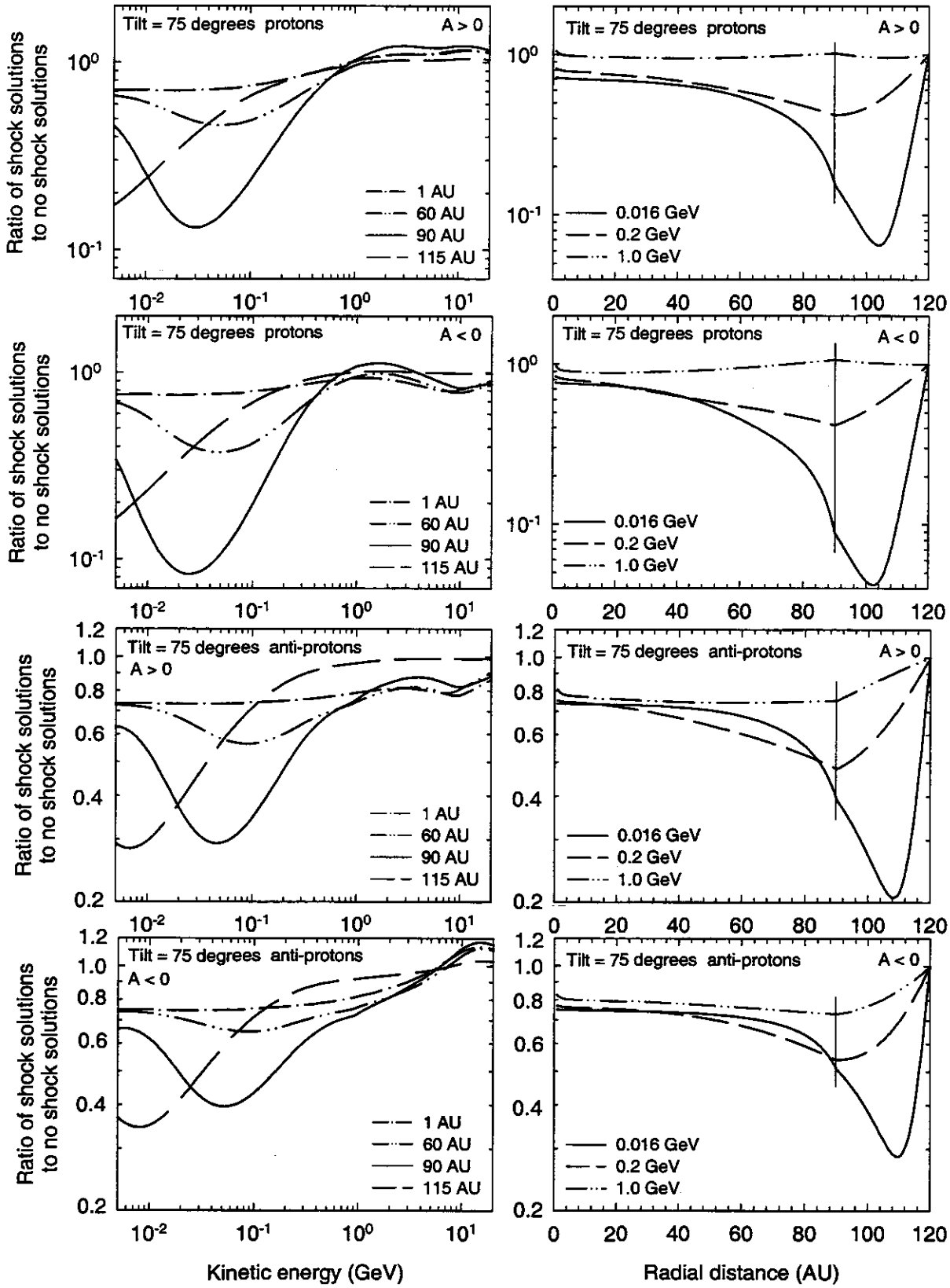

Figure 6.7. Similar to Figure 6.6, but for $\alpha = 75°$. Note the scale differences between the panels.

6.5. Charge-sign dependence for protons and anti-protons

6.5.1. Tilt angle dependence of protons, anti-protons and protons with an anomalous component

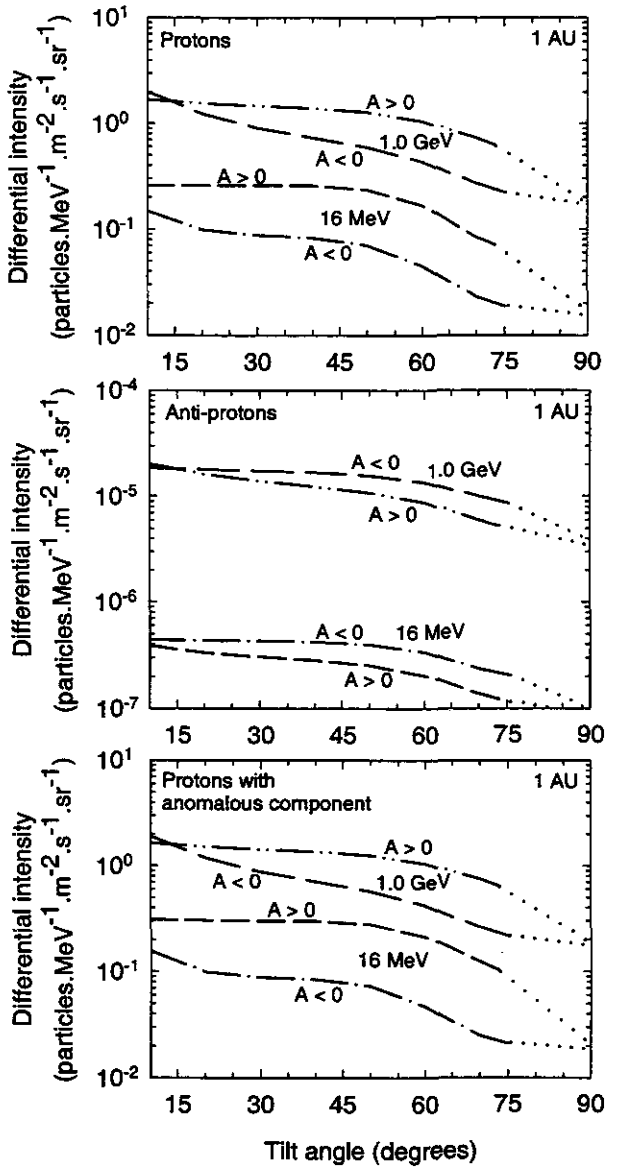

Figure 6.8. Differential intensities for protons, anti-protons and protons with an anomalous component, as a function of the tilt angle at Earth for both polarity cycles at energies of 0.016 and 1.0 GeV. Dotted lines are extrapolations to $\alpha = 90°$ where no drifts are assumed. Note the scale differences between the panels.

Figure 6.8 shows differential intensities for p, $\overline{\text{p}}$ and p with an anomalous component, as a function of the tilt angle at Earth for both polarity cycles at energies of 0.016 and 1.0 GeV. It is evident that this model predicts a flatter tilt angle dependence for the A > 0 cycle than for the A < 0 cycle for $\alpha \lesssim 50°$ but a somewhat steeper decrease for higher tilt angles than for the A < 0 cycle. For the A < 0 cycle a more gradual decrease with the tilt angle (almost linear) is predicted. This is in contrast with earlier drift models which have predicted a more gradual increase for the A > 0 cycle and an almost hyperbolic decrease for the A < 0 cycle (e.g., Potgieter et al., 2001c). These

differences between the present and earlier models are caused by the decreasing drifts with increasing tilt angles, which tend to let the differential intensities for the two polarity cycles converge with increasing solar activity if no drifts are assumed for extreme maximum conditions, as are indicated by the dotted lines in Figure 6.8 which are extrapolations to $\alpha = 90°$ (see also Ferreira et al., 2002). At $\alpha = 0°$ (not shown) the intensities for the A < 0 (A > 0) cycle will be higher than that of the A > 0 (A < 0) cycle for p ($\overline{\text{p}}$) at $E = 1.0$ GeV. This effect disappears for decreasing energy causing the intensities for the A > 0 (A < 0) cycle to be always larger than those for the A < 0 (A > 0) cycle for p ($\overline{\text{p}}$) at low energies. This effect obviously reverses for $\overline{\text{p}}$ as is required by drift models and is shown for the first time for this species with its recently computed LIS.

From Figure 6.8 it is evident that the decrease in intensities from $\alpha = 10°$ to 90° for p and p with an anomalous component at Earth is a factor of ~10 at 1 GeV, while it is only a factor of ~5 for anti-protons, because of the slope of the anti-proton LIS. For 16 MeV the factor decreases are approximately the same for protons and anomalous protons because of the effects of adiabatic 'cooling' at this energy.

6.5.2. Energy dependence of $\overline{\text{p}}$/p and $\overline{\text{p}}$/p with an anomalous component

In Figure 6.9 the modulation differences between p and $\overline{\text{p}}$ are emphasized by plotting $\overline{\text{p}}$/p, and $\overline{\text{p}}$/p with an anomalous proton component, as a function of kinetic energy for both polarity cycles in the equatorial plane at 1 AU and 90 AU, with $\alpha = 10°$ and $\alpha = 75°$, respectively. As a reference, all the modulated ratios are compared to the corresponding (unmodulated) LIS ratios. From Figure 6.8 it is evident that the intensities of $\overline{\text{p}}$ at 1.0 GeV at Earth are approximately a factor of $\sim 10^{-6}$ less than those of protons, while the intensities of protons and protons with an anomalous component are approximately the same. This will have a clear effect on the computed ratios.

The TS combined with charge-sign dependent effects caused by drifts should have clear observable effects on cosmic ray modulation. The computed charge-sign dependence of p and $\overline{\text{p}}$ becomes more significant in the outer heliosphere, manifesting at higher energies, than at 1 AU and more pronounced with $\alpha = 75°$. As the modulation processes become dominated by adiabatic energy losses in the inner heliosphere, $\overline{\text{p}}$/p reaches steady values with $E < 100$ MeV, but somewhat depending on the polarity cycle. At $r_s = 90$ AU this also happens but at lower energies. These steady values are significantly different when $\alpha = 75°$. For p with an anomalous component, the $\overline{\text{p}}$/p exhibits similar behaviour at 1 AU, but differs significantly at r_s, as has been expected. The $\overline{\text{p}}$/p curves as a function of energy also crosses for the A > 0 and A < 0 cycles, at 1 AU at a much higher energy than at r_s, and the effect seems to move to higher energies with increasing solar activity. For the no shock ratios at r_s this cross-over still occurs but at much lower energies, indicating that it is strongly imbedded in the drifts modulation and cannot easily be overwhelmed by TS effects.

6.5.3. Tilt angle dependence of $\overline{\text{p}}$/p and $\overline{\text{p}}$/p with an anomalous component

In Figure 6.10 the $\overline{\text{p}}$/p, and $\overline{\text{p}}$/p with an anomalous proton component, as a function of the tilt angle at 1 AU and 90 AU for both polarity cycles in the equatorial plane are shown at energies of 0.016, 0.2, 0.5, and 1.0 GeV. The characteristic 'Λ' and 'V' shapes for the A > 0 and A < 0 cycles, respectively are clearly recognizable for 1 AU and become more pronounced for decreasing energy. The tilt angle dependence increases for the A > 0 cycle at 90 AU and therefore the 'Λ' shape is more clearly recognizable (note the scale difference). The tilt angle dependence for A < 0 becomes weaker with increasing radial distance. At 90 AU for the A < 0 cycle this characteristic 'V' shape even disappears for the A < 0 cycle at $E \lesssim 0.1$ GeV. At 1 AU the difference in the ratios with $\alpha = 10°$ and with $\alpha = 75°$ is larger for the A < 0 cycle than for the A > 0 cycle, because of the stronger tilt angle dependence

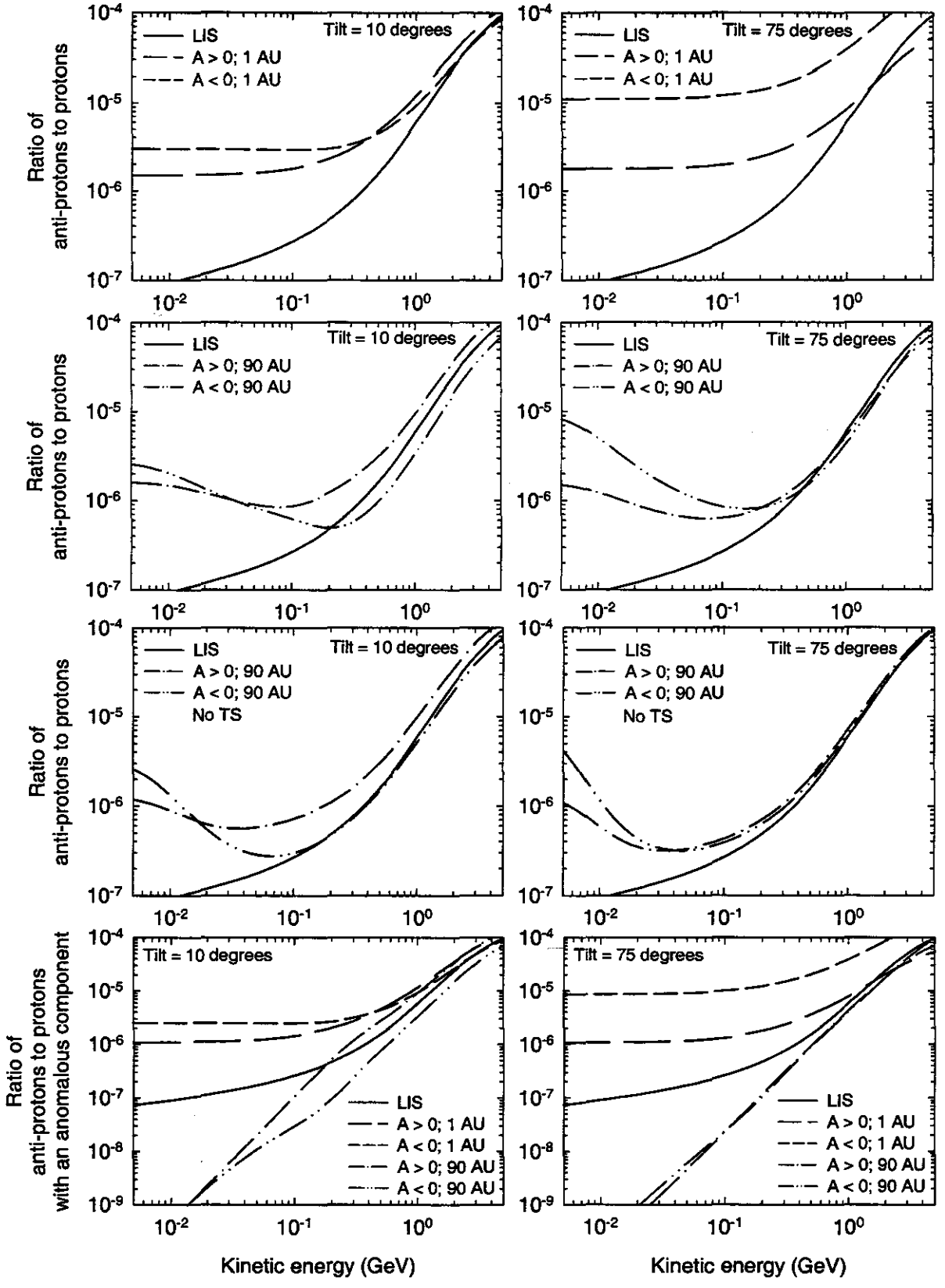

Figure 6.9. Ratios $\overline{p}/p$, and $\overline{p}/p$ with an anomalous proton component (bottom panels), as a function of kinetic energy in the equatorial plane at 1 AU (top panels) and at the TS (r_s = 90 AU) for both polarity cycles with $\alpha = 10°$ (left panels) and $\alpha = 75°$ (right panels), respectively. All ratios are compared to the LIS $\overline{p}/p$ ratio (at 120 AU) as a reference. The ratios without a TS are shown only in the third row panels at 90 AU.

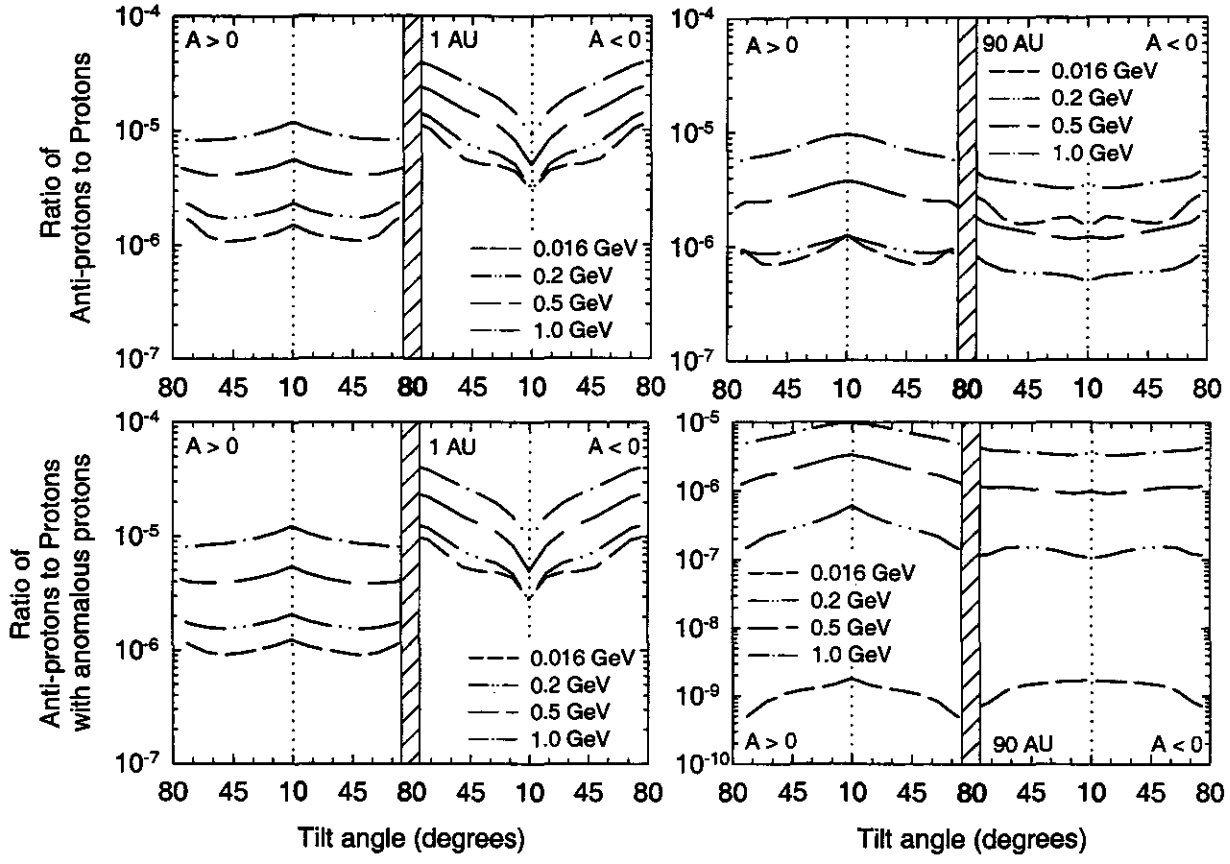

Figure 6.10. Ratios $\overline{p}/p$, and $\overline{p}/p$ with an anomalous proton component, as a function of tilt angle in the equatorial plane at 1 AU (left panels) and at the TS ($r_s = 90$ AU) (right panels) for both polarity cycles at energies of 0.016, 0.2, 0.5, and 1.0 GeV. Note the scale differences in the panels.

of p modulation in the A < 0 cycle than for the A > 0 cycle. This was also shown from a different point of view in Figure 6.8, i.e., for 16 MeV protons the difference in the intensities at 1 AU with $\alpha = 10°$ compared to $\alpha = 75°$ is a factor of ~10 for the A < 0 cycle, while for the A > 0 cycle it is a factor of ~5.

The transition from A > 0 to A < 0 at $\alpha = 75°$ is also much smoother at 90 AU than the drastic increases/decreases at 1 AU. This is because of drifts decreasing with a factor of $s = 3.2$ at the TS, and further indicates that drifts must dissipate completely at extreme solar maximum conditions ($\alpha \rightarrow 90°$) for all radial distances. This was already implicated for e^- by the work of Ferreira et al. (2001a, 2002, 2003) on time dependent electron modulation.

6.6. Heliosheath modulation

Next, the modulation computed to take place in the heliosheath, between r_b and r_s, is compared to what happens between r_b and 1 AU (LIS to Earth) and between r_s and 1 AU (TS to Earth). This comparison is emphasized by showing in Figures 6.11 and 6.12 the intensity ratios j_{LIS}/j_1, j_{LIS}/j_{90} and j_{90}/j_1 for the three species under consideration as a function of kinetic energy in the equatorial plane for both polarity cycles with $\alpha = 10°$ and 75°, respectively. Note that for a few cases the ratios become less than unity, because of the acceleration of particles at the TS which can increase the intensities to values larger than the LIS intensities, as has been mentioned before.

According to Figures 6.11 and 6.12 a significant level of modulation occurs in the heliosheath for galactic protons

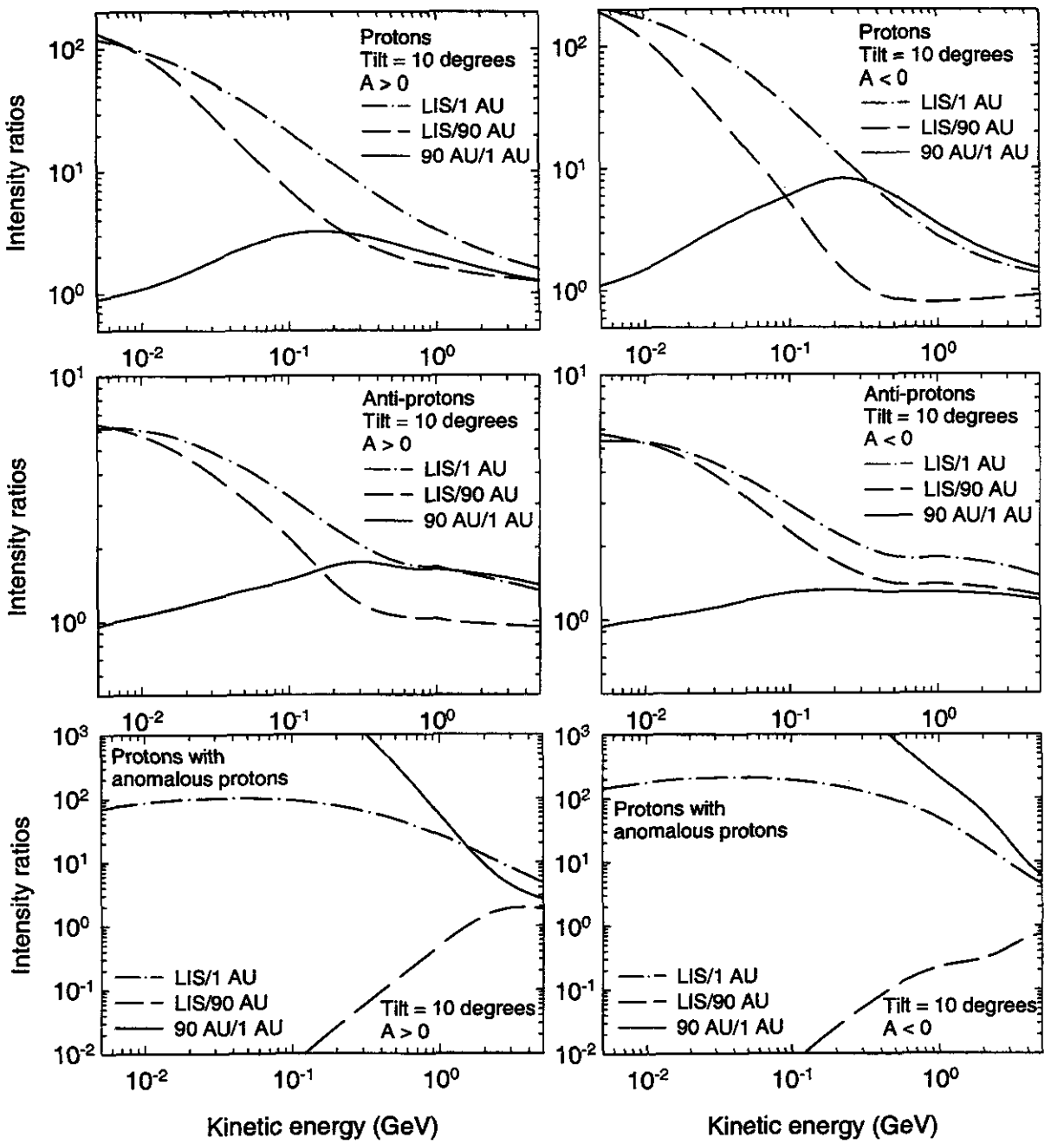

Figure 6.11. Intensity ratios j_{LIS}/j_1, j_{LIS}/j_{90} and j_{90}/j_1 (120 to 1 AU, 120 to 90 AU and 90 to 1 AU) for protons, anti-protons, and for protons with an anomalous component as a function of kinetic energy in the equatorial plane with $\alpha = 10°$; left panels: for A > 0, right panels: for A < 0. Note the scale differences between the panels.

when A > 0 with $E \lesssim 200$ MeV for solar minimum ($\alpha = 10°$) and for moderate solar maximum ($\alpha = 75°$) conditions. This is also true for A < 0 but at a somewhat lower energy, as has been discussed in the previous chapter. For $\bar{p}$ the equivalent happens in the A > 0 cycle although clearly not as pronounced as for galactic protons, e.g., at 10 MeV the heliosheath (barrier) modulation for galactic protons is a factor of ~100 but a factor of only ~7 for $\bar{p}$. For moderate solar maximum conditions the level of modulation in the heliosheath decreases significantly for $E >$ 200 MeV in contrast with that of j_{90}/j_1. This is also true for solar minimum conditions, but to a lesser extent. Obviously, these ratios all converge at a high enough energy where no modulation is present. The addition of the anomalous protons changes the ratios significantly for energies up to 1-2 GeV; j_{LIS}/j_1 is only slightly changed as

has been expected. Evidently, at lower energies the presence of anomalous protons in the outer heliosphere will make observations of true heliosheath modulation difficult.

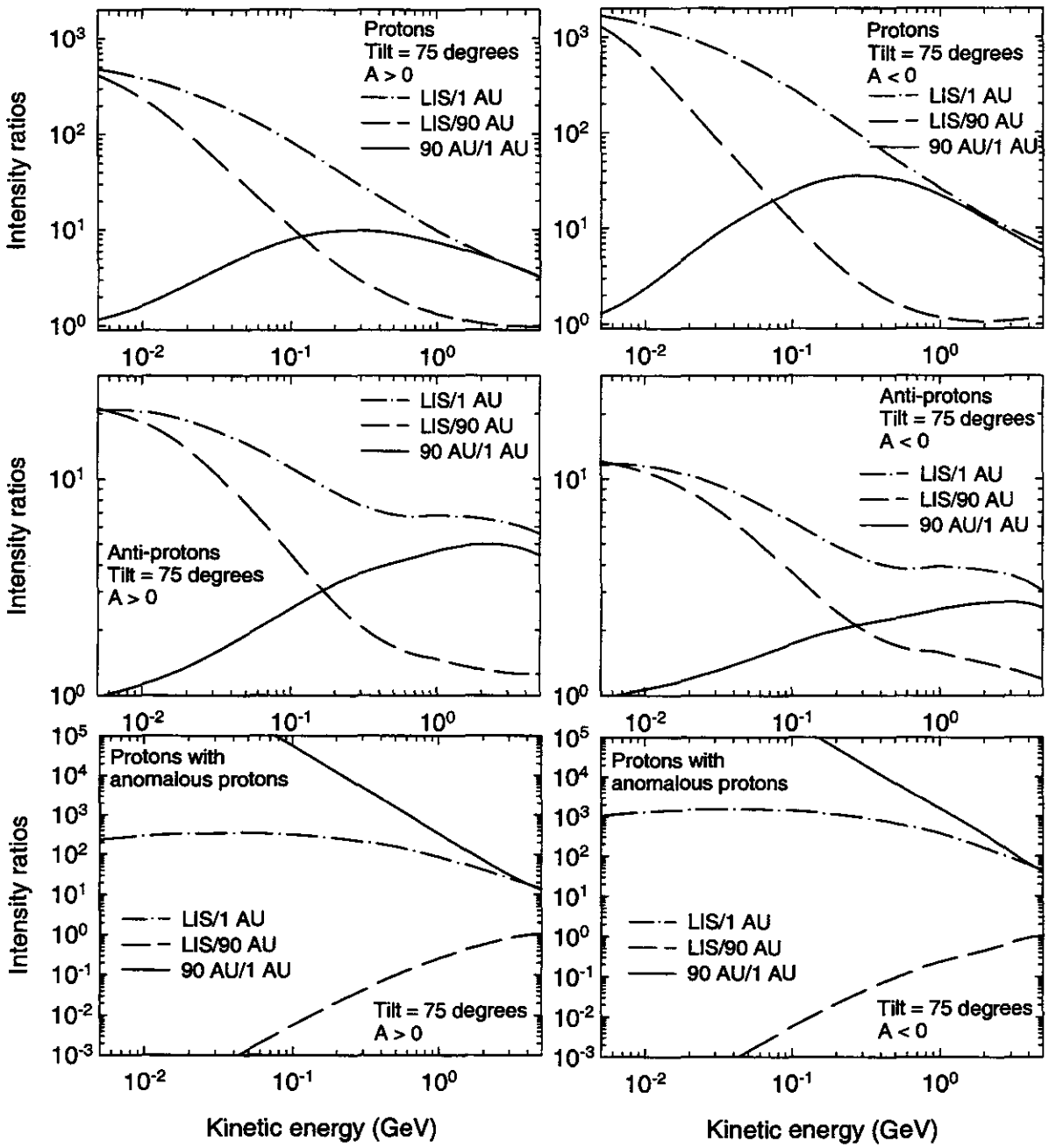

Figure 6.12. Similar to Figure 6.11 but for $\alpha = 75°$.

6.7. Summary and conclusions

In this chapter five aspects of heliospheric modulation were highlighted: (1) The differences in the modulation of galactic protons and anti-protons. (2) How the inclusion of a TS in the model altered this modulation and the consequent charge-sign dependence. (3) How the inclusion of anomalous protons changed the modulation for protons. (4) The kind of modulation effects to be expected near the TS and in the heliosheath and (5) The effects

of increased solar activity. Qualitatively, these results for p are consistent to those of Jokipii et al. (1993) but there are quantitatively marked differences (see also Langner et al., 2003b). The TS modulation results for $\overline{\text{p}}$ and the effects of the TS on charge-sign dependent modulation are new. The results confirm that this numerical model with a TS can reasonably reproduce the modulation between the outer boundary and Earth for protons, and anomalous protons. This will also be illustrated for electrons, positrons and Helium in the following chapters. Although these results are most reasonable it seems unavoidable that the diffusion coefficients should change time-dependently, together with the 'tilt angle' and parameters like the compression ratio (see also Potgieter and Langner, 2003a, 2003b). These results indicate that a TS compression ration between 3.2 and 2.0 is preferred when anomalous protons are also considered, in fact, this ratio cannot be determined effectively using only galactic p and $\overline{\text{p}}$ spectra. A strong shock with $s = 4$ is most unlikely.

The modulation produced by a model with and without a TS can differ significantly, depending on the species and HMF polarity. These differences increase towards lower energies and larger radial distances. The $\overline{\text{p}}$/p approaches a steady value at all radial distances for lower energies which is a manifestation of the adiabatic 'cooling' these species experience in the heliosphere and is independent of the shape of the LIS. Strong charge-sign dependent effects occur for p and $\overline{\text{p}}$ enhanced by the vastly different LIS and the different effect the TS has on these CR particles.

The heliosheath can be considered a distinguishable modulation 'barrier' for both p and $\overline{\text{p}}$ with the overall effect clearly energy, polarity cycle and solar activity dependent, e.g., for galactic protons most of the modulation may occur in the heliosheath for $E \lesssim 200$ MeV at solar minimum during A < 0 cycles. For $\overline{\text{p}}$ the equivalent happens in the A > 0 cycle but not as pronounced as for p e.g., at 10 MeV the heliosheath (barrier) modulation for galactic p is a factor of $\sim$100 but a factor of only $\sim$7 for $\overline{\text{p}}$. This aspect can make it easier to detect in the inner heliosphere any additional galactic anti-proton component (Moskalenko et al., 2003) given that the LIS for $\overline{\text{p}}$ indeed has the illustrated spectral form at lower energies and that the chosen energy is not too low.

These results indicate that the proton LIS may not be known at $E \lesssim 200$ MeV until a spacecraft actually approaches the heliopause because of the strong modulation that occurs in the heliosheath, the effect of the TS and the presence of anomalous protons. For $\overline{\text{p}}$, in contrast, these effects are less pronounced.

In the following chapter the TS model is expanded to include the heliospheric modulation of electrons and positrons.

Chapter 7
Heliospheric modulation of electrons and positrons

7.1. Introduction

In this chapter the TS model, which has been applied to p and $\bar{p}$ in the previous chapter, is expanded to include the heliospheric modulation of electrons (e^-) and positrons (e^+). Concerning modulation mechanisms, large-scale gradient, curvature and current sheet drifts that charged particles experience in the global HMF are most prominent, if not the dominating aspect. Drift models predict a clear charge-sign dependence for the modulation of cosmic ray e^- and e^+. For example, e^- will drift inward primarily through the polar regions of the heliosphere during so-called $A < 0$ polarity cycles, that is when the HMF is directed towards the Sun in the northern hemisphere. On the other hand, e^+ will then drift inward primarily through the equatorial regions of the heliosphere, encountering the HCS in the process. The modulation of low energy e^- was also comprehensively studied by Ferreira et al. (2001a, 2001b, 2001c). The effect of the TS on charge-sign dependent modulation as is experienced by e^- and e^+ is the main topic of this chapter.

Modulation of e^- and e^+ inside the heliosphere hides the true value of the LIS below a few GeV and makes it difficult to derive the values from modulation studies alone because the heliospheric diffusion coefficients are poorly known. The e^-/e^+ and e^-/p ratios at different energies and positions in the heliosphere could be computed in detail if the LIS of the different cosmic ray species were better known. Fortunately, new calculations have been made of the LIS for cosmic ray e^- and e^+, which are based on sophisticated models for the propagation of CRs in the Galaxy, and on comparisons with a variety of data sets, including radio synchrotron indices and γ-rays (e.g., Peterson et al., 1999; Strong et al., 2000; Langner et al., 2001b).

For e^- and e^+ modulation the following topics are addressed in detail: (1) The effects of the TS on the modulation of galactic cosmic ray e^-, including a Jovian e^- source, and e^+ in a simulated heliosphere for both magnetic field polarity cycles using these new LIS, and also as modulation changes from minimum to moderate maximum conditions. (2) The differences between a model with and without a TS. (3) The level and the importance of modulation in the simulated heliosheath for the two species, and (4) to establish the consequent charge-sign dependence and the effects of the TS on the modulated e^-/e^+ and e^-/p. The application to cosmic ray e^+ are new.

Preliminary reports of the results in this chapter were made by Potgieter et al. (2001a, 2001b) and Langner and Potgieter (2001b). The content of this chapter was published by Potgieter and Langner (2003c).

7.2. LIS for electrons, positrons and the Jovian electron source

7.2.1. LIS for electrons

Cosmic ray e^- differ from the nuclear component in the sense that, apart from γ-rays and radio synchrotron photons, e^- interactions in the ISM do not produce secondary particles that can be used to infer the characteristics of the propagation of electrons. The situation is further complicated by the fact that other physical processes in the ISM also produce γ-rays and radio wavelength photons in the same energy and wavelength ranges as that which are produced from CR electrons. The diffuse continuum γ-ray emission from the galactic plane at MeV

energies is believed to originate mainly in bremsstrahlung interactions of cosmic ray e^- with interstellar gas, but is still subject to considerable uncertainties. While the main γ-ray production mechanisms are agreed to be inverse Compton scattering, π^0-production and bremsstrahlung, their individual contributions depend on many details such as interstellar e^- and nucleon spectra, interstellar radiation and magnetic fields, gas distribution etc. (Strong et al., 2000). At energies above ~1 GeV the dominant physical mechanism is yet to be established and the situation below ~30 MeV is even more unclear. Diffuse gamma ray observations appear to be 'contaminated' by Crab-like point sources, so that it is difficult to derive a consistent LIS for e^- in the 1 to 30 MeV range (Strong and Moskalenko, 1998). Measurement of the γ-ray spectrum at low energies therefore provides important constraints on the spectrum and propagation of CR electrons. This information is complementary to direct measurements and estimates which are based on radio synchrotron radiation.

Large energy losses in the ISM because of ionisation cause low energy e^- to be especially sensitive to galactic propagation effects (Strong et al., 1994). Energy losses are related to the gas distribution at low energies (ionisation and bremsstrahlung) and to magnetic fields and radiation density (synchrotron and inverse compton emission) at high energies; it follows that the electron spectrum is sensitive to the spatial properties of the propagation process. Since the bremsstrahlung spectrum could not be directly deconvolved to obtain the corresponding e^- spectrum, plausible model spectra were computed based on propagation/energy loss models and the resulting bremsstrahlung emission was compared with the observations (Strong et al., 1994).

Below ~10 GeV solar modulation effects become increasingly important, making it impossible to determine a realistic LIS from observed modulated e^- spectra at Earth because the heliospheric diffusion coefficients are simply not known well enough (Potgieter, 1996; Ferreira et al., 1999; Langner, 2000). Therefore indirect methods using galactic propagation models of CRs through the ISM and Monte Carlo simulation models are used (e.g., Strong et al., 2000; Higbie et al., 1999).

Fortunately, cosmic ray e^- do not experience large adiabatic energy losses inside the heliosphere; this only becomes important below ~1 MeV. For implications of different LIS on heliospheric modulation of CRs, see Langner (2000) and Ferreira and Potgieter (2002). For this study the galactic electron LIS of Langner et al. (2001b) were used. The parameterisation of this LIS is given by

$$j_{LIS} = \begin{cases} \frac{214.32+3.32\ln(R)}{1+0.26\ln(R)+0.02(\ln(R))^2} & \text{if } R < 0.0026 \text{ GV} \\ 1.7\left(\frac{52.55+23.01R}{1+148.62R}\right)^2 & \text{if } 0.0026 \text{ GV} \leq R < 0.1 \text{ GV} \\ \frac{1555.89+17.36R-3.4\times10^{-3}R^2+5.13\times10^{-7}R^3}{1-11.22R+7532.93R^2+2405.01R^3+103.87R^4} & \text{if } 0.1 \text{ GV} \leq R \leq 10.0 \text{ GV} \\ 1.7\exp\left(-0.89-3.22\ln(R)\right) & \text{if } R > 10.0 \text{ GV} \end{cases}, \quad (7.1)$$

with j_{LIS} the differential intensity in particles.m^{-2}.s^{-1}.sr^{-1}.MeV^{-1} and R rigidity in units of GV.

7.2.2. LIS for positrons

Secondary CR particles are created in collisions of primary CR particles with the diffuse interstellar gas and include a small fraction of antimatter particles, i.e., e^+ and $\overline{\text{p}}$. In addition, e^+ and $\overline{\text{p}}$ may also come from unusual sources and possibly provide insight into new physics. For instance, the annihilation of heavy supersymmetric dark matter particles within the galactic halo could lead to e^+ and $\overline{\text{p}}$ with distinctive energy signatures. Primary e^+ can also arise when e^+e^- pairs are created by electromagnetic processes, i.e., through the conversion of high energy γ rays in the polar cap region of galactic radio pulsars and various other proposed processes (Harding and Ramaty, 1987). The uncertainties in the existing models and data for e^+ are such that none of these models can yet be ruled out. Measurements show that there can be sources of primary e^+ above 7 GeV, but that the contribution of primary e^+

at $E < 100$ MeV is most probably negligible (Harding and Ramaty, 1987; Coutu et al., 1999). Unfortunately, there are only a few measurements in the < 50 MeV energy range. This contribution was thus neglected for the purpose of this study. Strong et al. (2000) considered their computed positron LIS more reliable than their electron LIS, because of more accurate measurements for e^+ in the 1-10 GeV range (see also Moskalenko and Strong, 1998).

As for CR electrons, adiabatic energy losses for e^+ in the heliosphere become important only below $\sim$1 MeV. For galactic positrons the LIS of Strong et al. (2000) was used. The parameterisation of this LIS is given by

$$j_{LIS} = \begin{cases} \exp\left(\frac{-11.46-3907.68R+1921926.98R^2}{1+8664.02R+478789.20R^2+85019405.88R^3}\right) & \text{if } R < 0.003 \text{ GV} \\ \frac{-0.06+353.58R-253.99R^2}{1+59.72R+126.13R^2+3775.65R^3} & \text{if } 0.003 \text{ GV} \leq R < 0.8 \text{ GV} \\ \frac{-0.02+1.53\times10^{-4}R-8.13\times10^{-7}R^2}{1-4.45R+6.39R^2-3.72R^3} & \text{if } R \geq 0.8 \text{ GV} \end{cases} . \quad (7.2)$$

7.2.3. The Jovian electron source

In 1973 the Pioneer 10 spacecraft facilitated the discovery that the Jovian magnetosphere at $\sim$5 AU in the ecliptic plane is a relatively strong source of e^- with energies up to at least $\sim$30 MeV (e.g., Simpson et al., 1974; Teegarden et al., 1974; Chenette et al., 1974). This was anticipated by McDonald et al. (1972) who observed e^- flux variations at Earth at these energies. These Jovian e^- propagate along and across the heliospheric magnetic field and are observed inward to and at Earth, and outward to $\sim$30 AU (e.g., Hamilton and Simpson, 1979; Eraker and Simpson, 1979; Eraker, 1982; Ferrando et al., 1993a, 1993b, 1999).

Several attempts were made to calculate the Jovian contribution to the total e^- intensity in the equatorial regions of the inner-heliosphere. The growth of the observational basis, however, was not accompanied by any comparable progress with the modelling of the propagation of Jovian electrons. The few existing models suffer from the restriction that they are valid either only close to or far away from the source region. Being motivated by this situation, Fichtner et al. (2000), have developed a new 3D model of the propagation of both Jovian and galactic electrons. Although this model is limited to a steady-state and does not explicitly contain the TS, it allows one to simultaneously study both the propagation of Jovian e^- from a localized source and cosmic ray e^- entering the 3D heliosphere from interstellar space. Fichtner et al. (2000) have found that the Jovian e^- distribution in the inner heliosphere is determined by the spiral pattern of the HMF. This implies that the perpendicular spatial diffusion is not efficient enough to erase the spiral pattern that is imposed by the HMF. They also have found that the Jovian e^- source is dominant inside 10 - 15 AU in and near the equatorial plane ($\theta = 90°$) depending on the modulation parameters. These truely 3D effects cannot be studied with a 2D model.

Another 3D model for the propagation of Jovian e^- and the effects and implications of Jovian modulation is described in detail in the Ph.D. thesis of Ferreira (2002) and accompanying publications (Ferreira et al., 2001a, 2001d, 2002). For this study the source function of Ferreira et al. (2001a) is used for the Jovian e^- source injected at 5 AU in the equatorial plane, which is given by

$$Q_{source} = 0.5\left(\frac{c_Q j_{1.5} d_Q j_{6.0}}{c_Q j_{1.5} + d_Q j_{6.0}}\right); \quad (7.3)$$

with $j_{1.5} = 5 \times 10^3 E^{-1.5}$; $j_{6.0} = 10^{10} E^{-6.0}$; $c_Q = 0.6$ and $d_Q = 5.0$. Here E is in MeV. This function is a combination of $j \propto E^{-1.5}$ and $j \propto E^{-6.0}$ spectra and is compatible to the normalized ISEE 3 (ICE) spectra (Moses, 1987) and Pioneer 10 observations (Lopate, 1991; Lopate, priv. comm., 2000). In the 2D model this point source is by implication a ring source, which means that the contribution of Jovian electrons in the inner heliosphere is overestimated, but by assuring compatibility to observed low energy electrons, the effect is minimized (see also Haasbroek, 1997).

7.3. Comparison of the modulation of electrons and positrons

The left panels of Figures 7.1 and 7.3 respectively show the e^- spectra including a Jovian source and the e^+ spectra with respect to the corresponding LIS, as a function of kinetic energy for 1, 60, 90 and 115 AU in the equatorial plane with a TS, while Figures 7.2 and 7.4 show similar spectra but without a TS. This is done for the A > 0 and A < 0 polarity cycles with $\alpha = 10°$ and 75°, respectively. The right panels of Figures 7.1 and 7.3 show the corresponding differential intensities as a function of radial distance in the equatorial plane at 0.016, 0.20 and 1.00 GeV, respectively with a TS. Again the spectra without a TS are shown by Figure 7.2 and 7.4. The effect of the Jovian e^- source is clearly visible at low energies. These results are consistent with the e^- simulations of Ferreira and Potgieter (2002). Comparing the energy spectra and radial dependence of the intensities for the chosen energies, one can see how: (1) The modulation differs from solar minimum to moderate solar maximum for e^- and e^+. (2) The effect of switching the HMF polarity from A > 0 to A < 0. (3) The vast differences between e^- and e^+ modulation and how it is affected by incorporating a TS; and (4) The heliosheath modulation for e^- and e^+. At 1 AU the solutions without a TS coincide with the TS solutions for e^- but not for e^+ as is evident from the figures.

The interesting general feature in Figures 7.1 and 7.3 is that under certain conditions the modulated spectra at r_s exceed the corresponding LIS with the kinetic energy $E \gtrsim 200$ MeV because of the TS acceleration, which has been noted before for protons. This effect is not equally pronounced for all species and depends on the drift direction. It becomes less evident when particles drift in over the heliospheric poles towards the equatorial regions (A > 0 for e^+ and A < 0 for e^-) when $\alpha = 10°$; with $\alpha = 75°$ it is still present but less pronounced. This effect is not present in Figures 7.2 and 7.4 as has been expected.

It is well-known that for e^- and e^+ the adiabatic energy losses are not significant down to ~1 MeV. For this reason the modulated spectral slopes of these particles retain the slope of the LIS at low energies as long as the diffusion coefficients also have a constant rigidity at these low energies. Consequently, the modulated spectra for e^- at lower energies are increasing with decreasing energy, in sharp contrast to p and $\overline{\text{p}}$ (see previous chapter). For e^+, with a completely different shape LIS, this causes modulated spectra to have a rather mild energy dependence below ~300 MeV, almost independent of energy, as is shown in the two bottom left panels of Figure 7.3, a feature not possible for protons and anti-protons. These kind of characteristic spectral features can be most helpful to distinguish between e^- and e^+ when measured at Earth, and to determine the rigidity dependence of the various diffusion coefficients at these low energies for the two species, again this is unachievable for protons.

The modulation in the heliosheath is also clearly noticeable in the right panels of Figures 7.1, 7.2, 7.3, and 7.4. The extent of the modulation in this region depends on the particle species, is strongly dependent on the polarity cycle, and is enhanced by the inclusion of the TS. This modulation is not similar as a function of energy for e^- and e^+ primarily because of the differently shaped LIS. The Jovian e^- source conspicuously dominates the 16 MeV intensities in the inner heliosphere - for a detailed discussion see Ferreira et al. (2001a).

7.4. Differences in modulation with and without a TS

A general effect of the inclusion of the TS is to decrease the intensities at lower energies somewhat while increasing it at mid-energy ranges. This general feature is also evident from the radial intensity profiles that are shown in the right panels of Figures 7.1, 7.2, 7.3, and 7.4. The e^- intensities are consistently larger at the TS than without a shock, associated with the increasing LIS for e^- at these energies, enabling a large population of e^- to

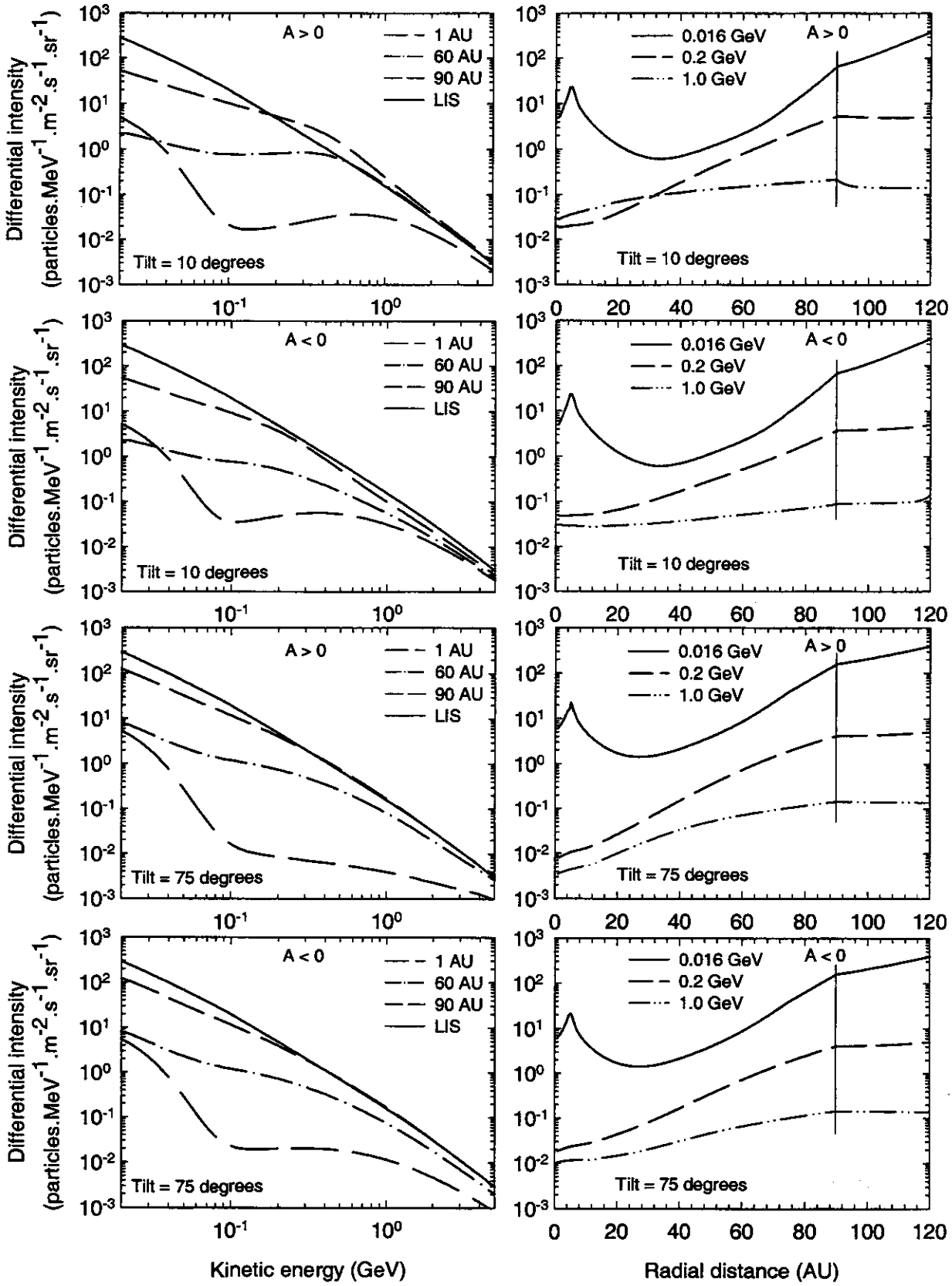

Figure 7.1. Left panels: Electron spectra with a TS and including a Jovian source, for both polarity cycles with $\alpha = 10°$ and 75°, respectively, for 1, 60, and 90 AU (bottom to top graphs) in the equatorial plane. Right panels: Corresponding differential intensities as a function of radial distance for 0.016, 0.2 and 1.0 GeV for solutions with a TS. The LIS is at 120 AU, and the TS at 90 AU.

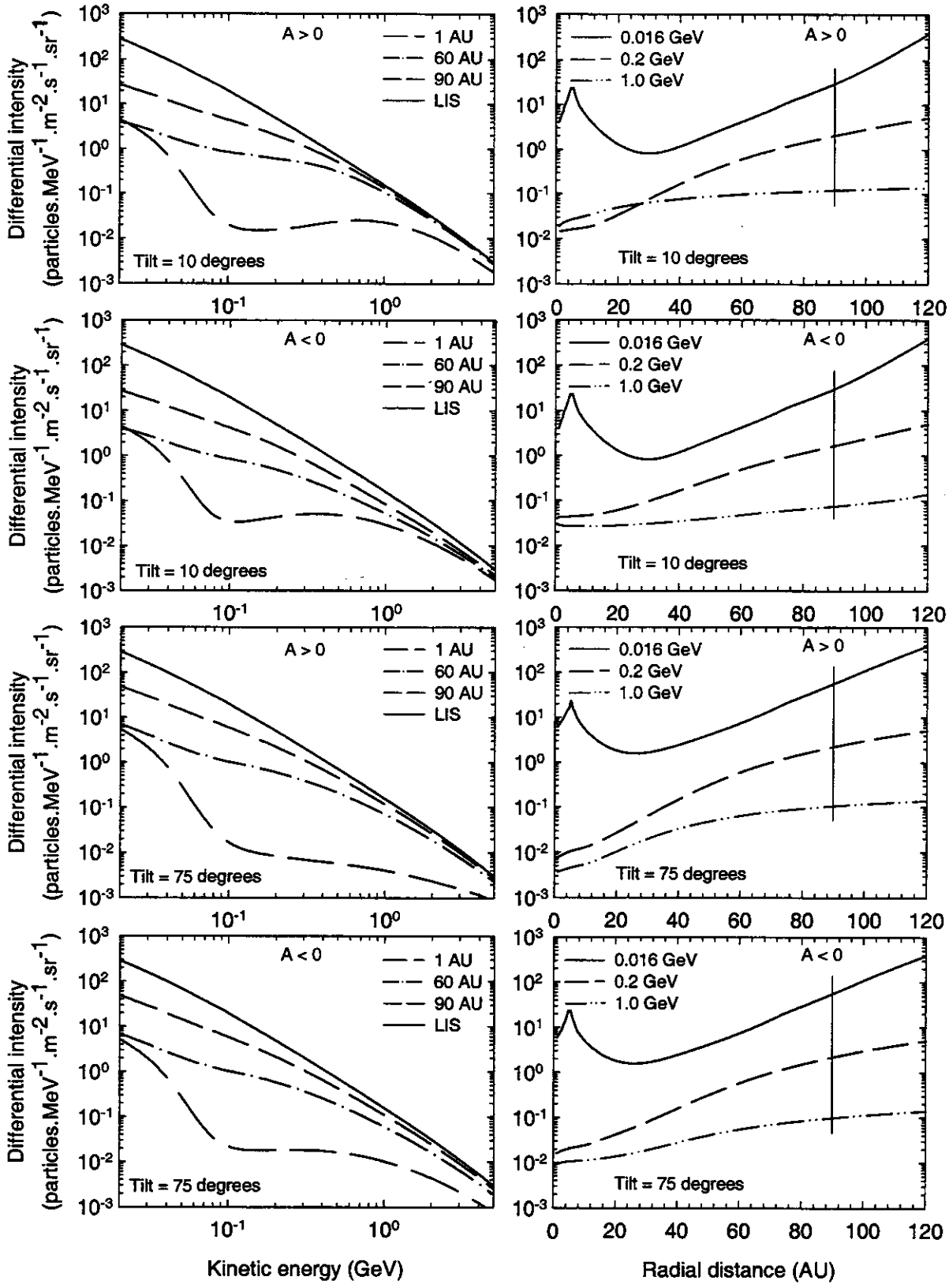

Figure 7.2. Similar to Figure 7.1, but without a TS.

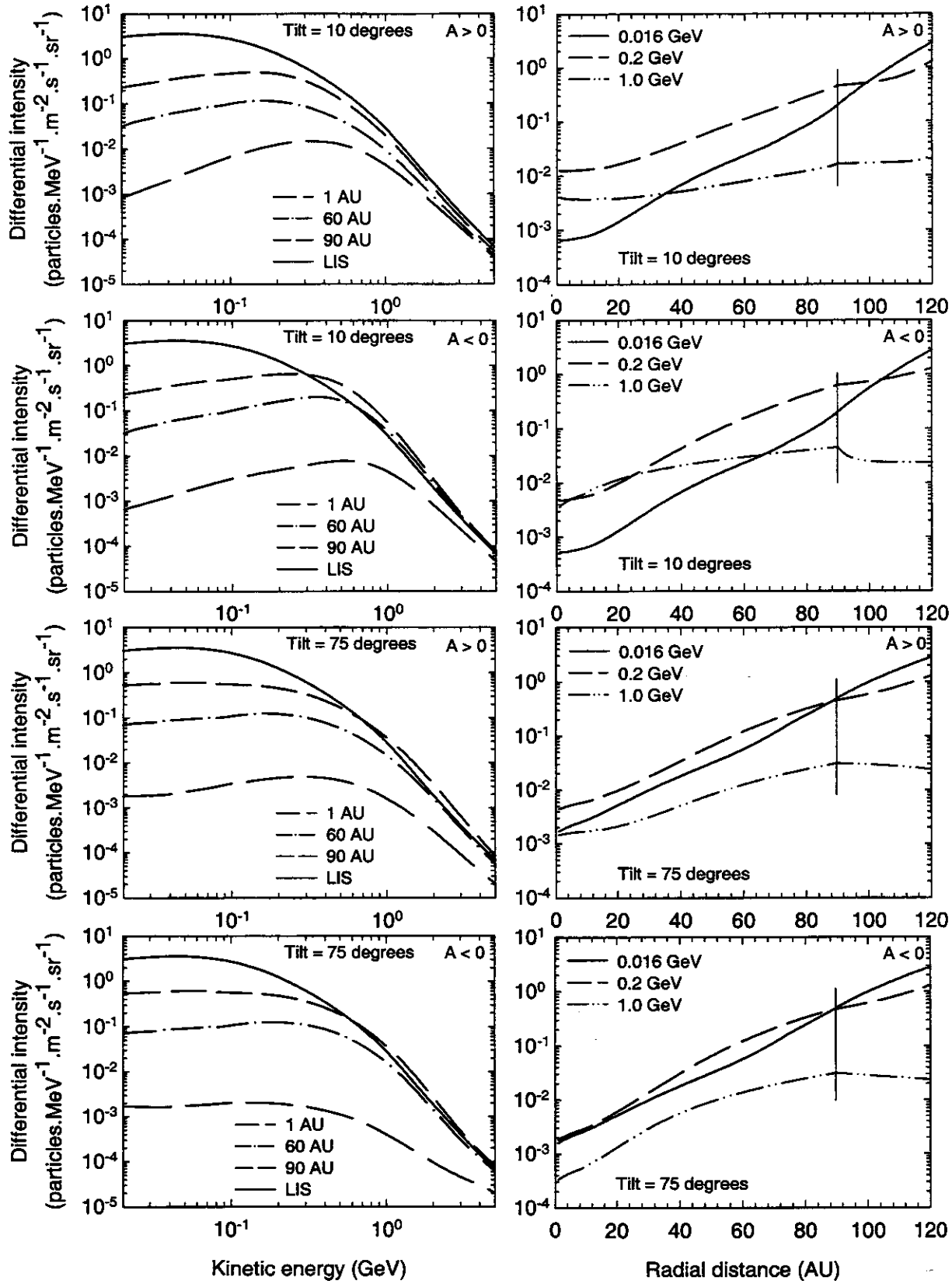

Figure 7.3. Similar to Figure 7.1 but for positrons. Note the relatively weak energy dependence of the spectra below ~300 MeV, in contrast to the electron, proton, and anti-proton spectra.

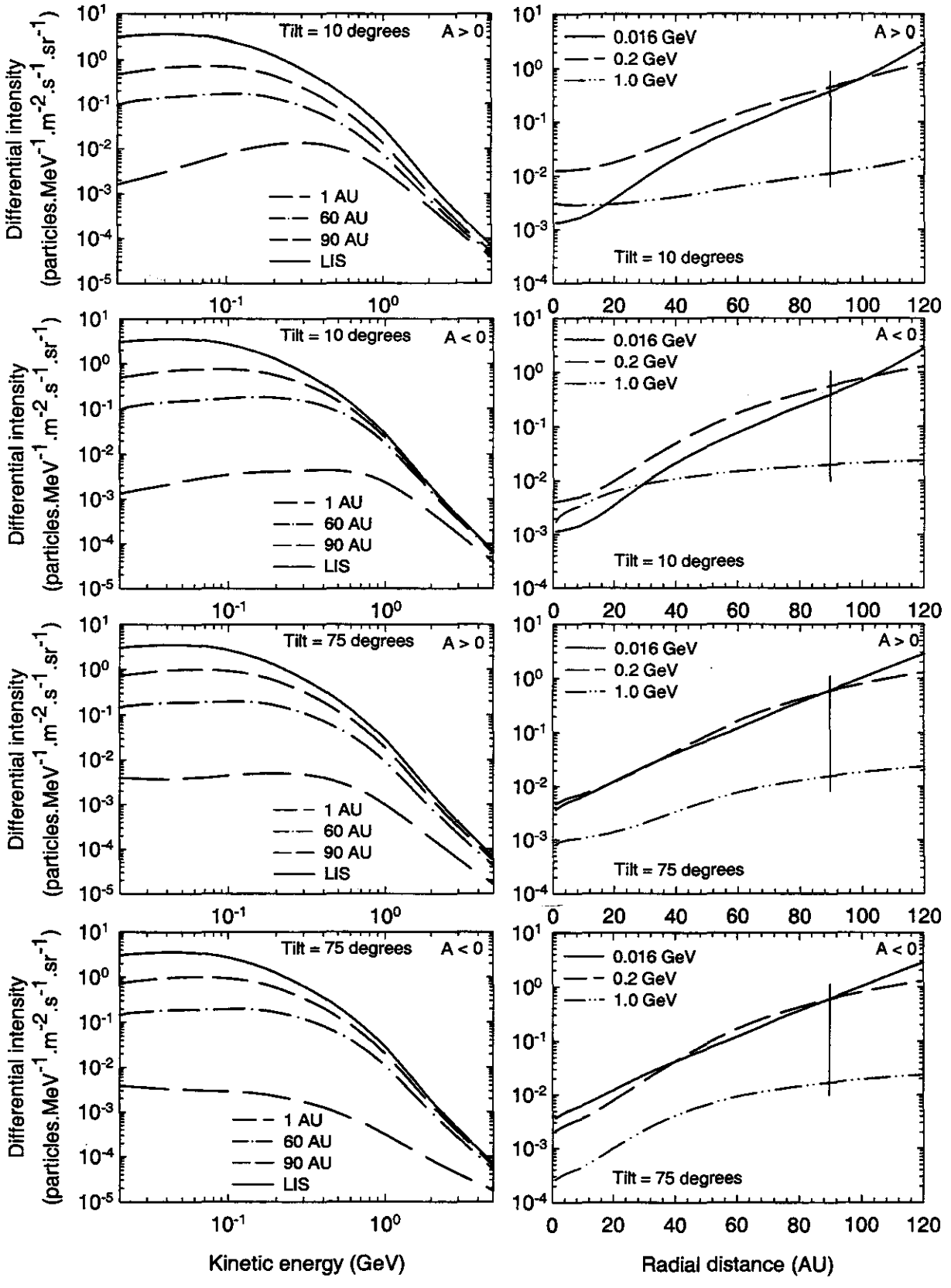

Figure 7.4. Similar to Figure 7.2, but for positrons.

be accelerated. The lower the energy the more distinct the changes in the radial gradients become near and at the TS for e^- but this tendency is not similar for e^+, i.e., the TS has little effect on the 16 MeV e^+. For them the intensities with and without the TS are almost equal for 100-300 MeV depending on the radial distance; below ~100-300 MeV the intensities are lower, but larger for higher energies.

Figures 7.5 and 7.6 show the ratio of intensities with and without a TS for e^- and e^+ as a function of kinetic energy at 1, 60, and 90 AU and as a function of radial distance at 0.016, 0.2 and 1.0 GeV for both polarity cycles in the equatorial plane for solar minimum with $\alpha = 10°$ and 75°, respectively. Obviously the solutions must converge at high energies ($E > 10$ GeV) because the TS has progressively less effect with increasing energy primarily being caused by the acceleration cutoff effect (e.g., Steenberg and Moraal, 1996). It is clear that the differences between the TS solutions and solutions without a TS can be substantial for both species, especially at lower energies and at larger radial distances. In Figures 7.5 and 7.6 the deviation from unity illustrates the effect of the TS in more detail. As has been expected the largest effect occurs at or near the TS. Intensities between 0.1 and 1.0 GeV are most affected and can be up to ~3 times higher at 90 AU than without a TS. When A > 0, the TS effect is the largest for e^- but the smallest for e^+. Qualitatively, these ratios show the same tendency, i.e. to obtain a maximum value between 100 MeV and 1 GeV, although clearly at different energies for e^- and e^+. With the ratio < 1, the TS intensities are less than those without a shock. This is usually the case at lower energies as is expected, especially for e^+. Intensities are affected by the presence of the TS in the inner heliosphere, even at Earth, in contrast to what have been found for p and $\overline{\text{p}}$ (Langner and Potgieter, 2003a, 2003b); however, e^+ intensities are clearly more affected at Earth than e^- below ~80 MeV but for another reason, the e^- intensities are dominated by the Jovian e^- source so that the ratios do not become < 1, as they do for example at 60 AU.

7.5. Charge-sign dependence for electrons and positrons

7.5.1. Tilt angle dependence of electrons and positrons

Figure 7.7 shows differential intensities for e^- and e^+ as a function of the tilt angle in the equatorial plane at 1 AU for both polarity cycles at an energy of 1.0 GeV. There is no difference between the differential intensities for the two polarity cycles at 16 MeV (not shown), because drifts become negligible at $E \lesssim 100$ MeV for e^- and e^+. It is evident that this model predicts a more gradual decrease with the tilt angle (almost linear) for the A > 0 cycle for e^-, which is in contrast with predictions from earlier drift models (e.g., Burger and Potgieter, 1989; Potgieter and Burger, 1990). Those models predicted an almost parabolic shape for the e^- intensities as a function of the tilt angle for the A > 0 cycle and an extrodinary insensitivity for e^- intensities in the A < 0 cycle to changes in the current sheet waviness leading to a flat intensity-time profile. The latter characteristic is also different in this model, because the e^- differential intensities stay more or less constant between $\alpha = 0°$ and 50°, thereafter it decreases sharply towards larger α's. The differences between this and earlier models are caused by the decreasing drifts with increasing tilt angles, which tend to let the differential intensities for the two polarity cycles converge with increasing solar activity. As has been discussed for protons in Chapter 6, the differential intensities at $\alpha = 90°$ converge when zero drifts are assumed during extreme solar maximum activity. At $\alpha = 0°$ (not shown) the intensities for the A > 0 (A < 0) cycle will be higher than that of the A < 0 (A > 0) cycle for e^- (e^+). This effect obviously reverses for e^+ as is required by drift models and is shown for the first time for this species with its recently computed LIS.

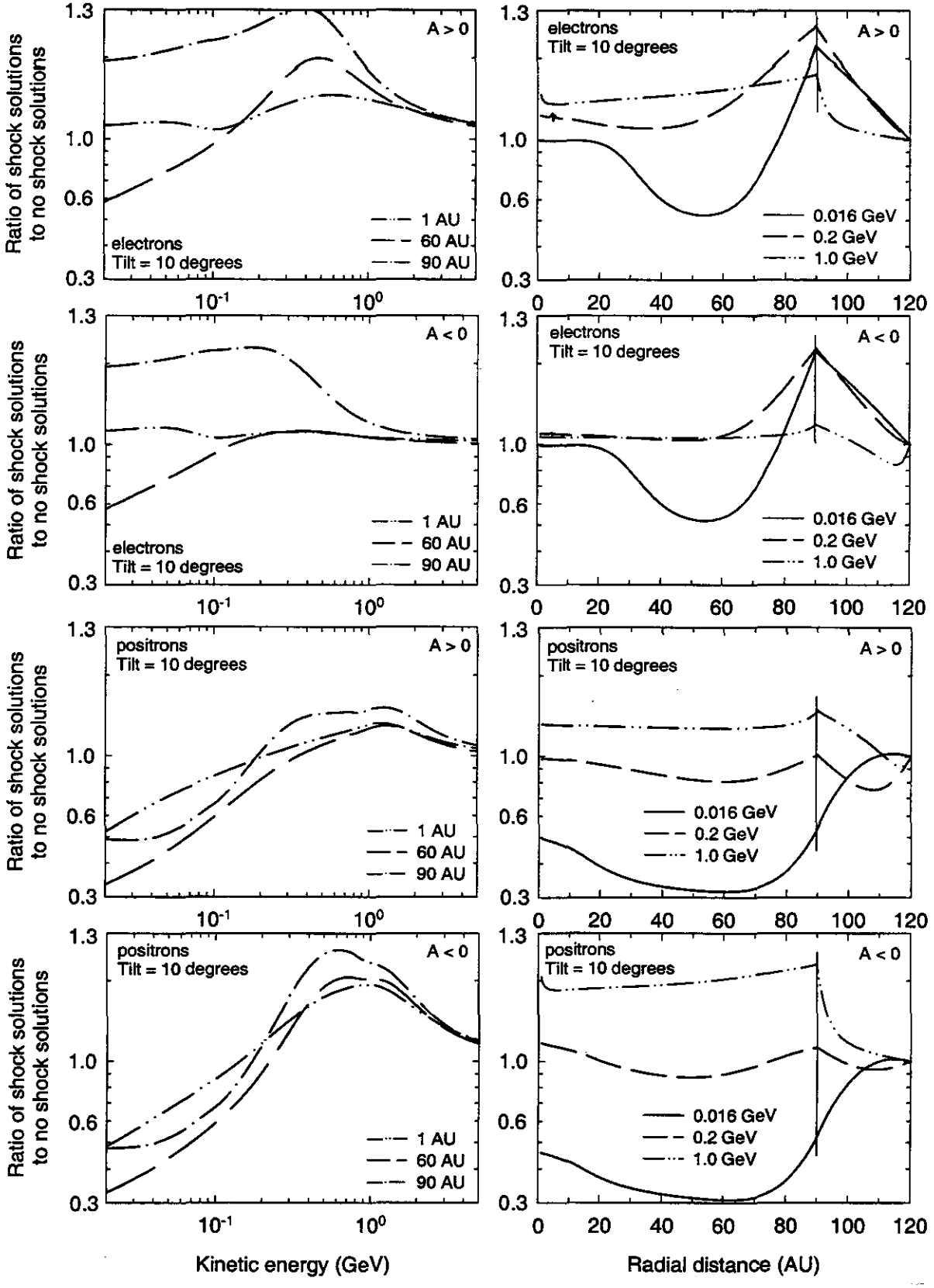

Figure 7.5. Intensity ratios with a TS to without a TS as a function of kinetic energy at radial distances of 1, 60 and 90 AU (left panels) and as a function of radial distance at energies of 0.016, 0.2 and 1.0 GeV (right panels) for both polarity cycles in the equatorial plane. Top four panels are for electrons and bottom four for positrons, all with $\alpha = 10°$.

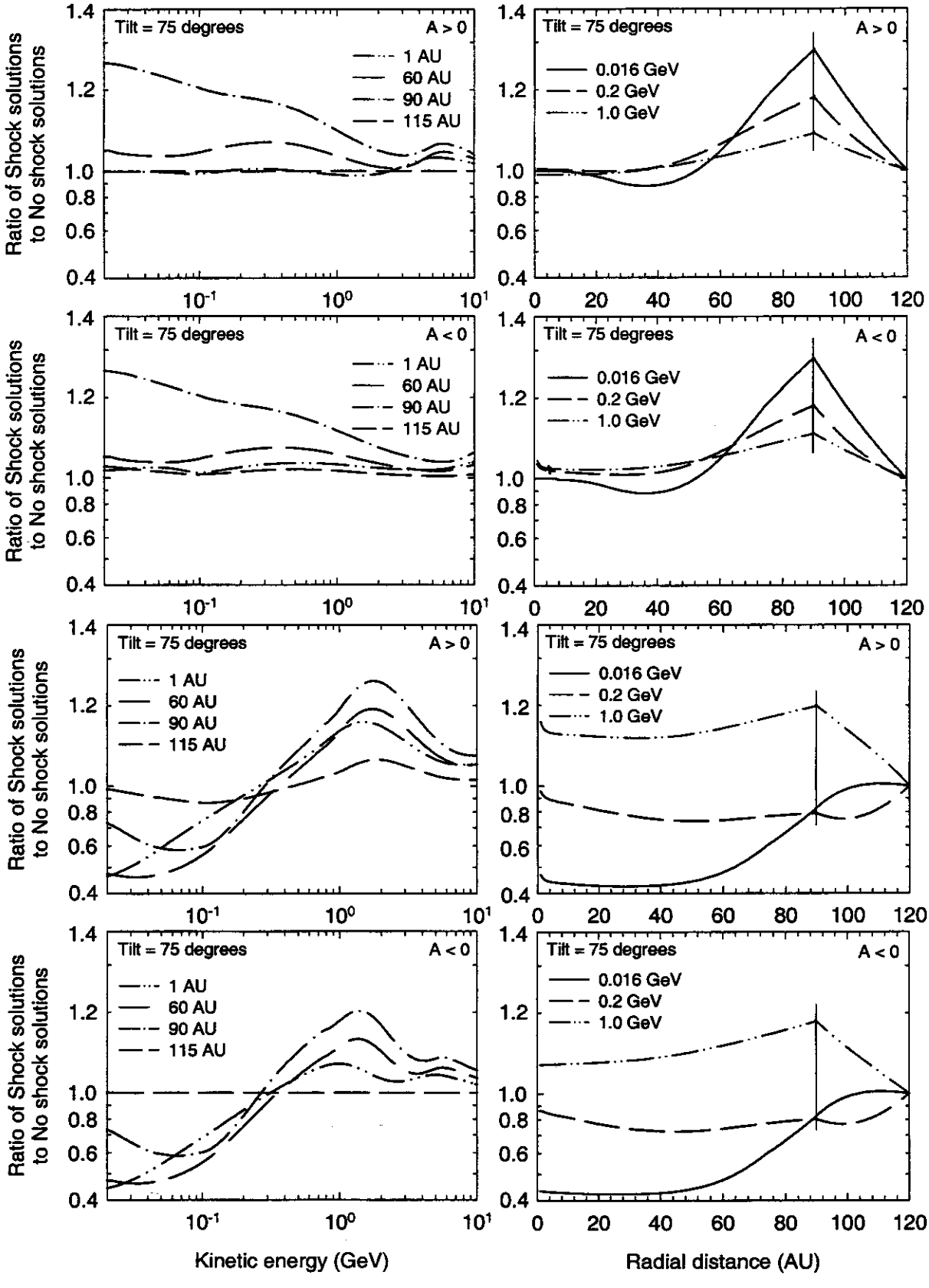

Figure 7.6. Similar to Figure 7.5 but for $\alpha = 75°$.

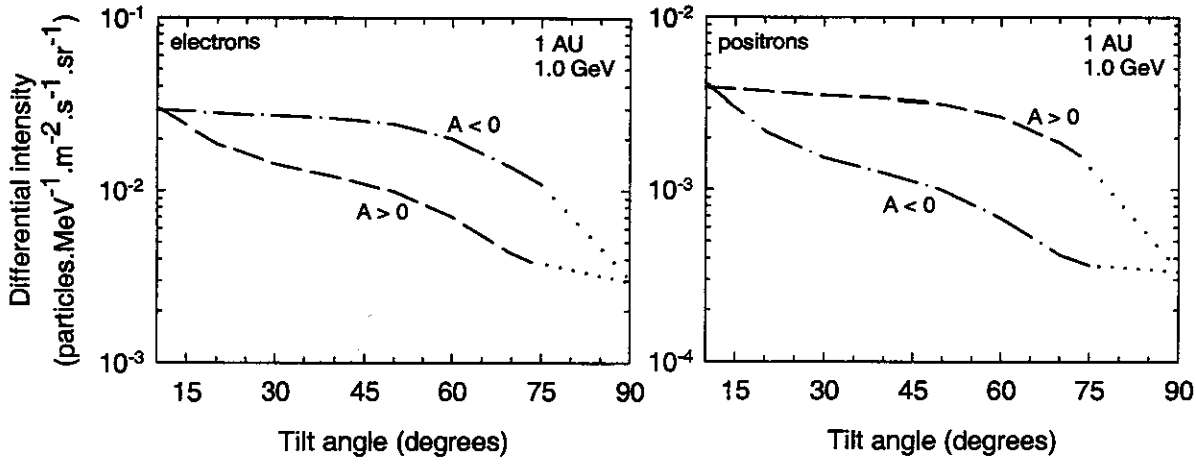

Figure 7.7. Differential intensities for electrons and positrons as a function of the tilt angle at Earth for both polarity cycles at 1.0 GeV.

7.5.2. Energy dependence of e^-/e^+, e^-/p, and e^-/p with an anomalous proton component

In Figures 7.8 and 7.9, the intensity ratios of e^- (with a Jovian source) to e^+ (e^-/e^+) are shown as a function of kinetic energy, also e^-/p, and e^-/p with an anomalous proton source, as a function of rigidity in the equatorial plane at 1 AU and 90 AU, respectively for both polarity cycles with $\alpha = 10°$ and $\alpha = 75°$. The p intensities are taken from the previous chapter (see also Langner and Potgieter, 2003a, 2003b). As a reference, these ratios are compared to the corresponding LIS ratios at 120 AU. For a review of the modelling of the e^-/p over 22-years without a TS and observations with the Ulysses spacecraft, see Ferreira et al. (2003) and Heber et al. (2002, 2003), respectively. Figures 7.8 and 7.9 are similar and illustrate the dependence of charge-sign-dependent modulation on energy (or rigidity) for e^-, e^+, and p, except that these intensity ratios are shown at 1 AU in the former and at the TS ($r_s = 90$ AU) in the latter figure. Ratios for the corresponding solutions without a TS are also shown to emphasize the TS contribution to modulation. From Figure 7.7 it is evident that the intensities of e^+ are approximately a factor of ~10 less than those of e^- at 1.0 GeV. The total contribution of e^+ to the sum of $e^- + e^+$ at 1.0 GeV at Earth will therefore be in the order of ~10% according to this model.

The first result to be emphasized is that at low energies (< 20 MeV) the e^-/e^+ is converging for the two polarity cycles because they become progressively independent of drifts, while adiabatic energy changes are still insignificant. Secondly, with decreasing energy this ratio will obtain the same slope as the LIS ratio, but only where the Jovian electrons become less dominating, typically with r > 10-15 AU. For p this is not possible, as has been mentioned previously. Above ~80 MeV the effect of drifts complicates this type of calculation. Between ~80 MeV and ~1 GeV the e^-/e^+ at 1 AU differs markedly for the two polarity cycles, even more with $\alpha = 75°$. From Figure 7.9 follows that at 90 AU this diverging starts at a higher energy; the e^-/e^+ deviates more from the LIS ratios when the TS is taken into account. The difference between the two polarity cycles is also less for the no shock solutions.

For the intensity ratios, e^-/p, and the e^-/p with anomalous protons, one can expect to see a combination of the main features of the energy dependence of the $\overline{\text{p}}$/p as has been described in the previous chapter and the e^-/e^+ as has been discussed above. For example, p experience large adiabatic energy losses at low energies while

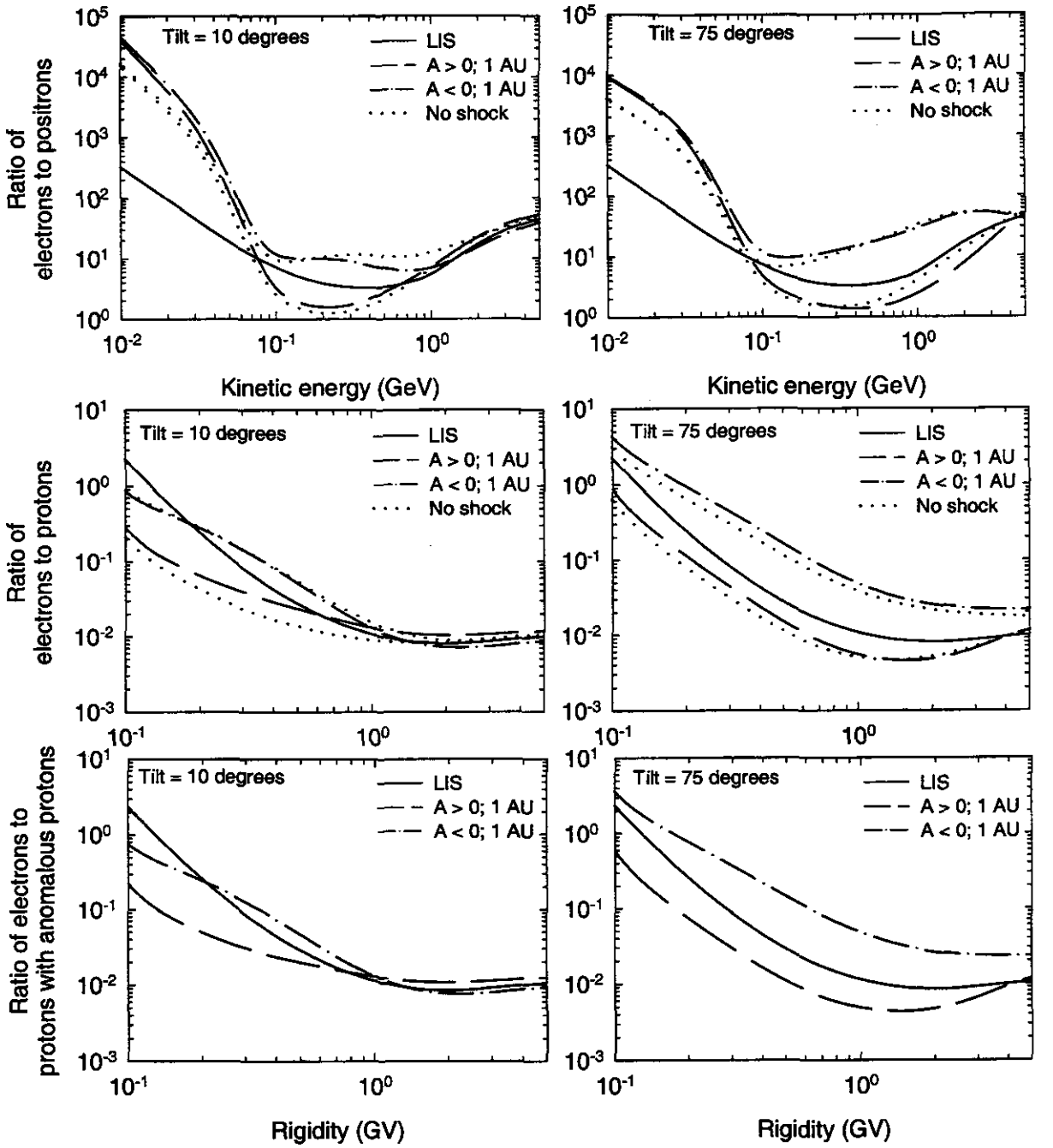

Figure 7.8. Intensity ratios, e^-/e^+ (top panels), e^-/p (middle panels) and e^-/p with an anomalous proton component (bottom panels) as a function of kinetic energy or rigidity in the equatorial plane at 1 AU for both polarity cycles with $\alpha = 10°$ (left panels) and $\alpha = 75°$ (right panels), respectively. All ratios are compared to the corresponding LIS values at 120 AU as a reference. Solutions without a TS are also shown in the four top panels as dotted lines, with the A < 0 solutions the higher values between 0.1 and 1.0 GeV (top panels) and 0.1 and 1.0 GV (middle panels).

e^- do not. Furthermore, e^- modulation becomes progressively independent of drifts with lower energies so that the e^-/p at 100 MV is a factor of ~200 at 90 AU. However, when the anomalous proton component is added, the e^-/p at 90 AU becomes significantly lower at low energies, e.g., only 10^{-2} at 100 MV since the anomalous protons dominate the galactic protons at these energies. The slight differences between the e^-/p and the e^-/p with anomalous protons at 1 AU and in comparison with the no shock ratios may be interpreted as an indication that anomalous protons may reach the Earth (e.g., MeWaldt et al., 1996).

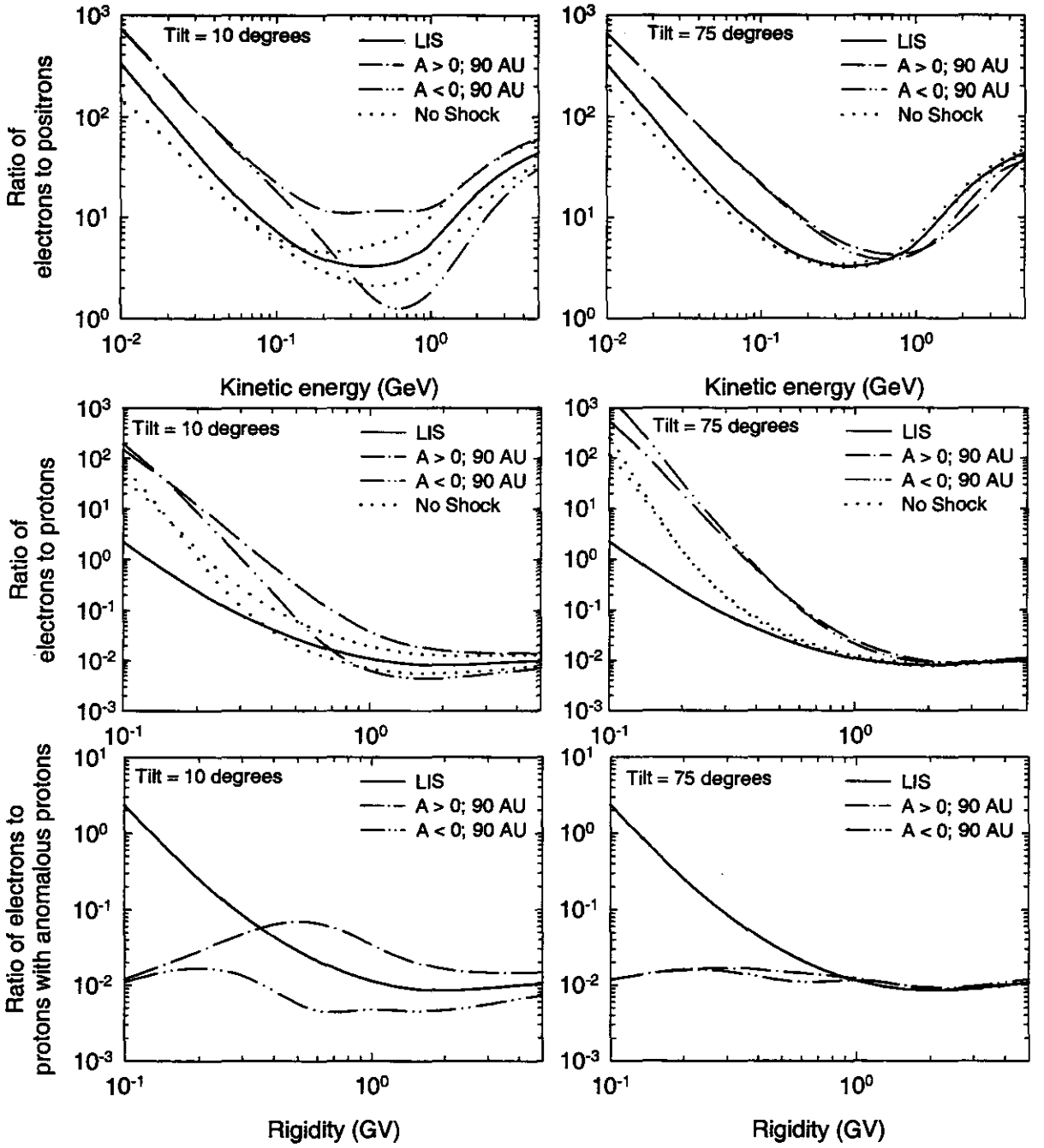

Figure 7.9. Similar to Figure 7.8, but at the TS ($r_s = 90$ AU). Solutions without a TS are also shown in the four top panels as dotted lines, with the A < 0 solutions the lower values between 0.1 and 1.0 GeV (top panels) and 0.7 and 1.0 GV (middle panels). Note the scale differences between the panels.

7.5.3. Tilt angle dependence of e^-/e^+

In Figure 7.10 the e^-/e^+ as a function of the tilt angle at 1 AU and 90 AU for both polarity cycles in the equatorial plane are shown at energies of 0.016, 0.05, 0.2, and 1.0 GeV, respectively. The characteristic 'Λ' and 'V' shapes are, as for $\bar{p}/p$, recognizable at 1 AU and 90 AU for the A > 0 and A < 0 polarity cycles, respectively, but only for $E \gtrsim 0.5$ GeV. For $E \lesssim 0.1$ GeV the shapes for the two polarity cycles become approximately the same because of the negligible drift effects at these energies, although with a different α-dependence at 1 AU than at 90 AU. An increase in the e^-/e^+ is evident for $\alpha \gtrsim 50°$ at 1 AU at these energies which is not present at larger energies. This

is because of decreasing drifts with increasing solar activity, which leads to a flatter energy dependence for the e^+ spectra at 1 AU for $E \leq 0.1$ GeV. These effects are also present at 90 AU, but clearly less prominent.

The neglect of drift effects at $E \lesssim 0.1$ GeV is also evident when comparing the transition found for A > 0 to A < 0 in Figure 7.10. At 1 AU the difference between the intensity ratios at $\alpha = 75°$ for the A > 0 and A < 0 cycle is negligible, causing a smooth transition with the changing in direction of the HMF. At 1 AU with $E \gtrsim 0.1$ GeV the differences between the intensity ratios from the A > 0 to the A < 0 cycle with $\alpha = 75°$ become larger, caused by increasing drifts. This indicate that too much drifts are allowed at even these moderate solar maximum conditions ($\alpha = 75°$) in this model, and that drifts must decrease with increasing solar activity towards extreme maximum conditions ($\alpha = 90°$). This aspect of heliospheric modulation has been considered and discussed in detail by Ferreira et al. (2001a, 2002) and is not pursued further in this work.

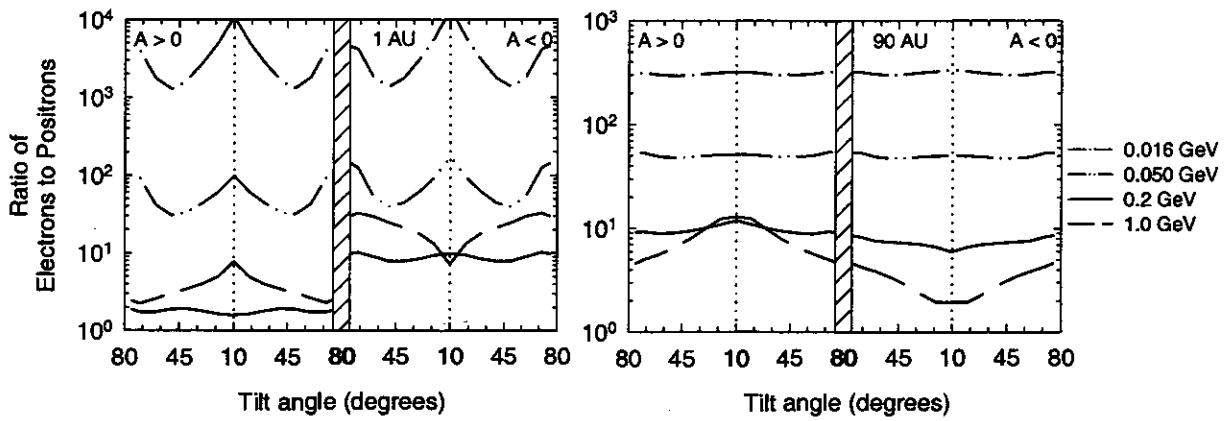

Figure 7.10. Ratios of e^-/e^+ as a function of the tilt angle in the equatorial plane at 1 AU (left panels) and at the TS ($r_s = 90$ AU) (right panels) for both polarity cycles at energies of 0.016, 0.05, 0.2, and 1.0 GeV. Note the scale differences between the panels. Legends are shown at the right side of the figures.

7.5.4. Tilt angle dependence of e^-/p, and e^-/p with an anomalous proton component

In Figure 7.11 the e^-/p, and e^-/p with an anomalous proton component, as a function of tilt angle at 1 AU and 90 AU for both polarity cycles in the equatorial plane are shown at rigidities of 0.05, 1.10, and 2.5 GV, respectively. The characteristic 'Λ' shape is again recognizable for 1 AU and 90 AU for the A > 0 cycle, but only for $R \gtrsim 0.1$ GV. For the A < 0 cycle the characteristic 'V' shape at 1 AU and 90 AU is present for all rigidities shown. For the A > 0 cycle the 'Λ' shape changes to a 'V' shape at $R \lesssim 0.1$ GV, which is caused by the almost constant tilt angle dependence for p at these rigidities between $\alpha = 10°$ to ~50°, and then a decrease in intensity towards higher tilt angles. For e^- at low rigidities the Jovian e^- source dominates in the inner heliosphere.

At 1 AU the ratios in the A < 0 cycle at $\alpha = 75°$ are larger than those for the A > 0 cycle, anticipating a large increase (approximately a factor of 10) in the ratios for the transition between the A > 0 and A < 0 cycles despite decreasing drifts with increasing solar activity. The intensities with $\alpha = 75°$ are not yet converging for the two polarity cycles in this model, but will if extreme solar maximum conditions without drifts are considered (Ferreira et al., 2002). At 90 AU this effect is less evident because drifts become already relatively small during moderate solar maximum conditions.

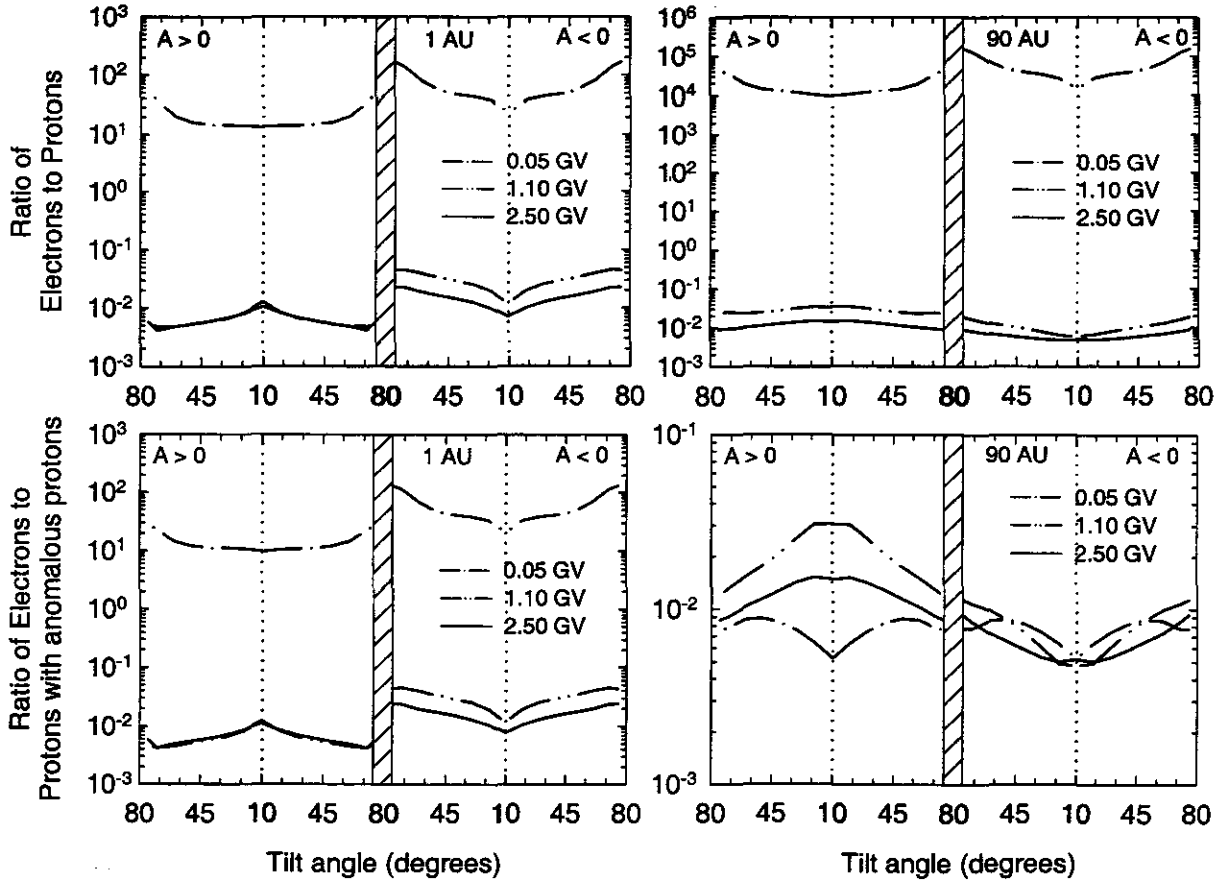

Figure 7.11. Ratios of e^-/p (top panels) and e^-/p with an anomalous proton component (bottom panels), as a function of the tilt angle in the equatorial plane at 1 AU (left panels) and at the TS (r_s = 90 AU) (right panels) for both polarity cycles at rigidities of 0.05, 1.10, and 2.5 GV, respectively. Note the scale differences between the panels.

7.6. Heliosheath modulation

The modulation computed to take place in the heliosheath, between r_b and r_s, is compared to what happens with the intensities between r_b and 1 AU (LIS to Earth) and between r_s and 1 AU (TS to Earth). This comparison is emphasized by showing in Figures 7.12 and 7.13 the intensity ratios of modulation occurring in the heliosheath (j_{LIS}/j_{90}) in comparison to what happens between the TS and Earth (j_{90}/j_1) and in total between the outer boundary and Earth (j_{LIS}/j_1) for the two species under consideration as a function of kinetic energy in the equatorial plane for both polarity cycles with $\alpha = 10°$ and 75°. Note that j_{LIS}/j_{90} becomes less than unity in some energy ranges, which is caused by the TS.

Note that for e^- in Figure 7.12 the factor modulation in the heliosheath becomes comparable to the factor between the TS and Earth ($j_{LIS}/j_{90} \gg j_{90}/j_1$) at low energies for both polarity epochs but not for e^+. During the A > 0 epoch, the e^- intensity ratios, $j_{LIS}/j_{90} < 1$ (or $j_{90}/j_1 > j_{LIS}/j_1$) from ~150 MeV to a few GeV so that the heliosheath cannot then be considered a modulation 'barrier' for electrons. During the A < 0 epoch this also happens for e^+ but at somewhat higher energies. The presence of the TS is thus more pronounced for e^- during A > 0 polarity cycles but for e^+ during A < 0 cycles.

In Figure 7.13 the intensity ratios as in Figure 7.12 are shown but with $\alpha = 75°$. From the figure follows that for electrons the modulation in the heliosheath is less conspicuous than for protons as has been shown in the previous

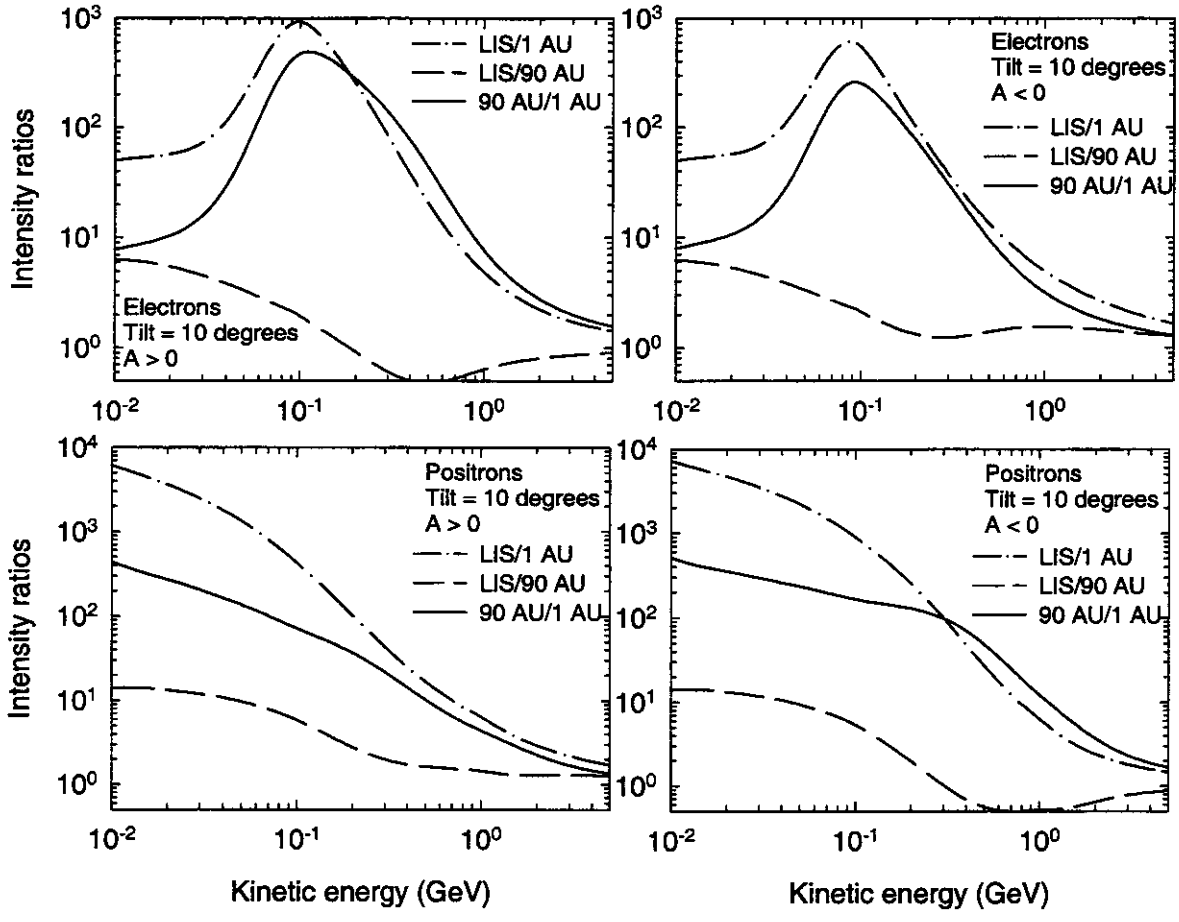

Figure 7.12. Intensity ratios j_{LIS}/j_1, j_{LIS}/j_{90} and j_{90}/j_1 (120 to 1 AU, 120 to 90 AU and 90 to 1 AU) for electrons (top panels) and positrons (bottom panels) as a function of kinetic energy in the equatorial plane with $\alpha = 10°$; for A > 0 (left panels), and for A < 0 (right panels). The LIS is at 120 AU and the TS at 90 AU. Note the scale differences between the panels.

chapter, and for positrons. For electrons the 'barrier' type modulation starts at ~200 MeV and increases with decreasing energies to a factor of ~3 at 1 MeV. The differences between the A > 0 and A < 0 cycles are small.

For positrons the heliosheath effect is larger, starting at ~500 MeV for both cycles to reach and maintain a maximum effect of a factor of ~5.5 from ~10 MeV and lower. As for protons the ratios become < 1 between 1 to 2 GeV which is caused by the TS. For moderate maximum conditions the heliosheath cannot be considered an effective modulation 'barrier' for e^- or e^+.

7.7. Summary and conclusions

Improved LIS for cosmic ray e^- and e^+ and a fundamental approach to diffusion coefficients have made it relevant to study the modulation for these species with a comprehensive numerical model including the TS and the Jovian e^- source. These aspects are considered for the first time for galactic positrons. The following heliospheric modulation aspects are highlighted: (1) The differences in the modulation of e^-, including a Jovian e^- source, and e^+, also with increased solar activity, and the consequent charge-sign dependence. (2) How the inclusion of a TS in the model alters this modulation and (3) the kind of modulation effects to be expected near the TS and in the heliosheath for e^- and e^+. The results confirm that the TS model reasonably reproduces the observed e^- modulation between the outer boundary and Earth. The TS model can therefore be applied with confidence to e^+ modulation. The

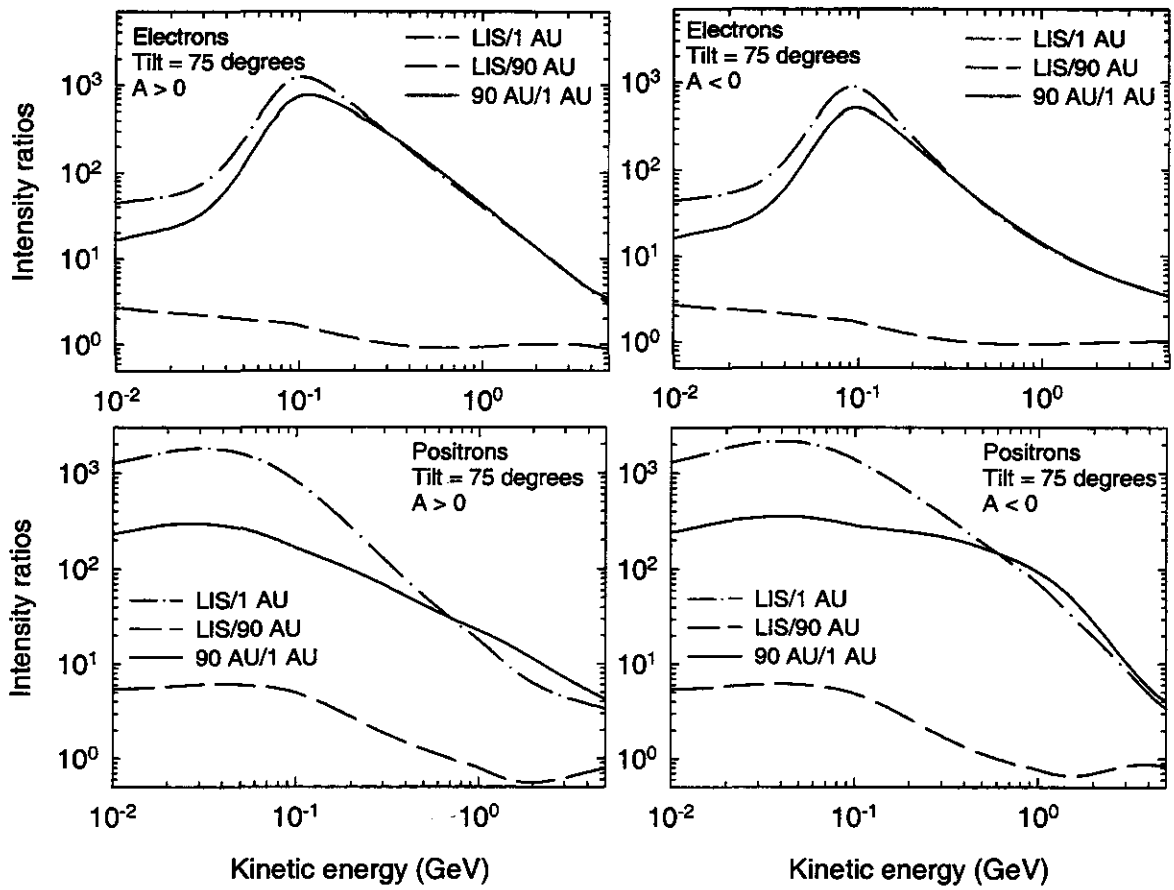

Figure 7.13. Similar to Figure 7.12 but for $\alpha = 75°$.

following have been found:

(1) The modulated spectra for e^- and e^+ at the TS may exceed the corresponding LIS at energies $\gtrsim$ 200 MeV. It becomes less pronounced when these particles drift in over the heliospheric poles towards the equatorial regions. With increased solar activity the effect becomes less evident for both polarity cycles.

(2) The modulation of e^- and e^+ becomes progressively independent of drifts with lower energies. Electrons and e^+ also experience significantly less adiabatic energy losses at energies $\gtrsim$ 1 MeV than p and $\bar{p}$ with the consequence that the rigidity dependence of the diffusion coefficients can easily be deduced from observations at lower energies. By studying the intensity ratios it is even possible to deduce the energy slopes of the corresponding LIS. Unfortunately, for e^- the situation at $E \lesssim 100$ MeV is complicated in the inner heliosphere by the dominating presence of the Jovian e^- source.

(3) With the inclusion of the TS, the largest modulation effects occur at/near the TS, as is expected. Intensities between 0.1 and 1.0 GeV are most affected and can be up to ~3 times higher at 90 AU than without a shock. A general effect of the inclusion of the TS is to decrease the intensities at lower energies at all radial distances while increasing it at mid-energy ranges. The energy where this adjustment occurs for e^+ is between 100-300 MeV depending on the radial distance and $\lesssim$ 1 MeV for electrons. The effect of the TS on modulation is the largest for e^- when A > 0, but for e^+ when A < 0. For both species the intensities are affected by the presence of the TS, even at Earth.

(4) The modulation in the heliosheath depends on the particle species, is strongly dependent on the energy of

the CRs - diminishes at higher energies but in a different manner for the different species - the polarity cycle and is enhanced by the inclusion of the TS. From the computations it is possible to estimate the ratio of modulation occurring in the heliosheath to the total modulation between the heliopause and Earth. For e^- the factor modulation in the heliosheath becomes comparable to the factor between the TS and Earth at low energies for both polarity epochs when $\alpha = 10°$. However, during the A > 0 epoch the heliosheath cannot really be considered a modulation 'barrier' above ~150 MeV for e^-, while for e^+ this occurs at somewhat higher energies during the A < 0 epoch. For $\alpha = 75°$ the heliosheath cannot be considered a modulation 'barrier'.

(5) For e^+, with a completely different shape LIS, the modulated spectra have very mild energy dependences below ~300 MeV, even at Earth, in contrast to e^-, p and $\overline{\text{p}}$ (Langner and Potgieter, 2003a, 2003b). These characteristic spectral features can be most helpful to distinguish between e^- and e^+ spectra when measured near and at Earth. These results can be of use for future missions to the outer heliosphere and beyond.

Chapter 8
Heliospheric modulation of galactic and anomalous Helium

8.1. Introduction

In this chapter the TS model applied to p, $\overline{p}$, e^-, and e^+ in the previous chapters, is expanded to include the heliospheric modulation of galactic Helium (He^{++}) and Helium with an anomalous component (He^+). Concerning modulation mechanisms, large-scale gradient, curvature and current sheet drifts that He experiences in the global HMF are most prominent. Drift models predict a clear charge-sign dependence for the modulation of cosmic ray e^- and He, which has been observationally confirmed (e.g., Heber et al., 2003). The effect of the TS on charge-sign dependent modulation as is experienced by He and anomalous He is the main topic of this chapter, and is complementary to the previous chapters.

Modelling the heliospheric modulation of He was done by various authors previously (e.g., Steenberg, 1998; Steenberg and Moraal, 1996). However, with a new and fundamental approach to diffusion coefficients and the TS model including a heliosheath and drifts that are very successful in explaining simultaneously the modulation of cosmic ray p, $\overline{p}$, e^-, and e^+ in the heliosphere, this study is extended to include He and anomalous He. This tests the generality of the TS model and the set of diffusion parameters for various species, both polarity cycles, and as modulation changes from solar minimum to moderate solar maximum conditions which together was not done before. The following topics are addressed in detail: (1) The effects of the TS on the modulation of galactic He and anomalous He in a simulated heliosphere for both HMF polarity cycles as modulation changes from minimum to moderate maximum conditions. (2) The differences in modulation between a model with and without a TS. (3) The level and the importance of modulation in the simulated heliosheath for galactic He, and (4) to establish the consequent charge-sign dependence and the effects of the TS on the modulated e^-/He and e^-/He with anomalous He.

Different isotopes for galactic He and anti-Helium were not considered for this study.

8.2. LIS for Helium and the anomalous Helium source

8.2.1. LIS for Helium

Protons and He are the most abundant species in cosmic radiation and knowledge of their absolute abundance and the exact shape of their energy spectra are of particular astrophysical importance. Their spectral shapes are sensitive indicators of the processes of particle acceleration in the Galaxy (e.g., Gaisser, 1990) and their fluxes are a primary measure of the energy density of CRs in the ISM. These spectra also serve as important input to calculations which aim to predict the γ-ray flux in the ISM because of π^0 decay or the secondary interstellar $\overline{p}$ or positron e^+ fluxes, all results of high energy interactions of p and He nuclei with the interstellar gas.

Unfortunately, neither the absolute fluxes nor the spectral shapes of these CR species are known with adequate precision in the ISM (e.g., Menn et al., 2000). The low-energy LIS for galactic protons, He and $\overline{p}$ cannot be measured directly deep inside the heliosphere because of modulation, especially the large adiabatic energy losses that these particles experience during their inward propagation in the heliosphere. The numerical modelling of He

plays therefore an essential role in understanding the modulation mechanisms that are involved and what to expect from observations. For this study the LIS for galactic He of Webber (1987) has been used, which is given by

$$j_{LIS} = \begin{cases} \exp\left(-1.47 - 1.55\ln E - 0.28\,(\ln E)^2\right) & \text{if } E \leq 5.54 \text{ GeV} \\ (0.52E^{-2.5}) & \text{if } E > 5.54 \text{ GeV} \end{cases} . \quad (8.1)$$

8.2.2. The anomalous source

For anomalous He a source was injected at the TS position at all θ at a rigidity of ~13.0 MV as a delta function with an arbitrary magnitude set to give reasonable compatibility to anomalous He observations at 60 AU and to He observations at Earth (e.g., Steenberg and Moraal, 1996; Steenberg, 1998). As for protons, the solutions are independent of this injection energy as long as it is lower than the TS cutoff energy for the ACRs, as has been discussed in Chapter 4. Since the mass-to-charge ratio, A/Z, is not the same for galactic He ($A/Z = 2$ for He^{++}) and anomalous He ($A/Z = 4$ for He^{+}), the model has to be run separately for these species, making it a very time consuming task. Solutions are therefore shown as a linear combination of solutions for galactic He and anomalous He. For protons the situation was simpler since $A/Z = 1$ for both galactic and anomalous protons (Langner and Potgieter, 2003b).

8.3. Comparison of the modulation of Helium and anomalous Helium

The results which will be shown in the following sections concentrate on four aspects of the heliospheric modulation of He: (1) The difference in the modulation of galactic He and He with anomalous He. (2) How the inclusion of a TS in the model alters the modulation of He and the subsequent effects of charge-sign dependent modulation on the e^-/He and e^-/He with anomalous He. (3) The nature of modulation effects to be expected near the TS and in the heliosheath. (4) The effects of increased solar activity and tilt angle dependence.

The left panels of Figures 8.1 and 8.5 show the modulation obtained with the TS model with respect to the LIS for He and for He with anomalous He, as a function of kinetic energy, respectively. This is done at 1, 60, 90 and 115 AU in the equatorial plane for the A > 0 and A < 0 polarity cycles with $\alpha = 10°$ and $\alpha = 75°$, respectively. The right panels of Figure 8.1 show the corresponding differential intensities at 0.016, 0.2 and 1.0 GeV as a function of radial distance in the equatorial plane, respectively for solutions with and without a TS. In Figure 8.5 the right panels also show the corresponding differential intensities at 0.016, 0.2 and 1.0 GeV as a function of radial distance in the equatorial plane, respectively but for solutions with the compression ratio $s = 3.2$ and $s = 2.0$. The spectra without a TS corresponding to the left panels of Figure 8.1 are repeated in Figure 8.2. The He with anomalous He spectra for a compression ratio of $s = 3.2$ and $s = 2.0$, are shown in Figures 8.4 and 8.3, and together in Figure 8.5 to emphasize the differences between these spectra. The decrease in s was necessary to obtain reasonable compatibility with the anomalous He observations at 60 AU as discussed in Chapter 4. The solutions in the inner heliosphere ($r \lesssim 40$ AU) are largely insensitive to this change. Decreasing s causes the peak in the modulated anomalous He spectra to shift to lower energies as the observations seem to require and can be caused by a decreasing shock strength with increasing solar activity, similar to protons. These quantitative aspects of anomalous He modulation were discussed in detail by Steenkamp and Moraal (1993), Steenkamp (1995), Steenberg (1998), and Steenberg et al. (1998) and were not pursued further in this work.

With the TS the modulated He spectra at large radial distances ($r \to r_s$) for the A < 0 cycle also exceed the corresponding LIS between ~200 MeV and a few GeV as has been noted for protons. This cannot happen

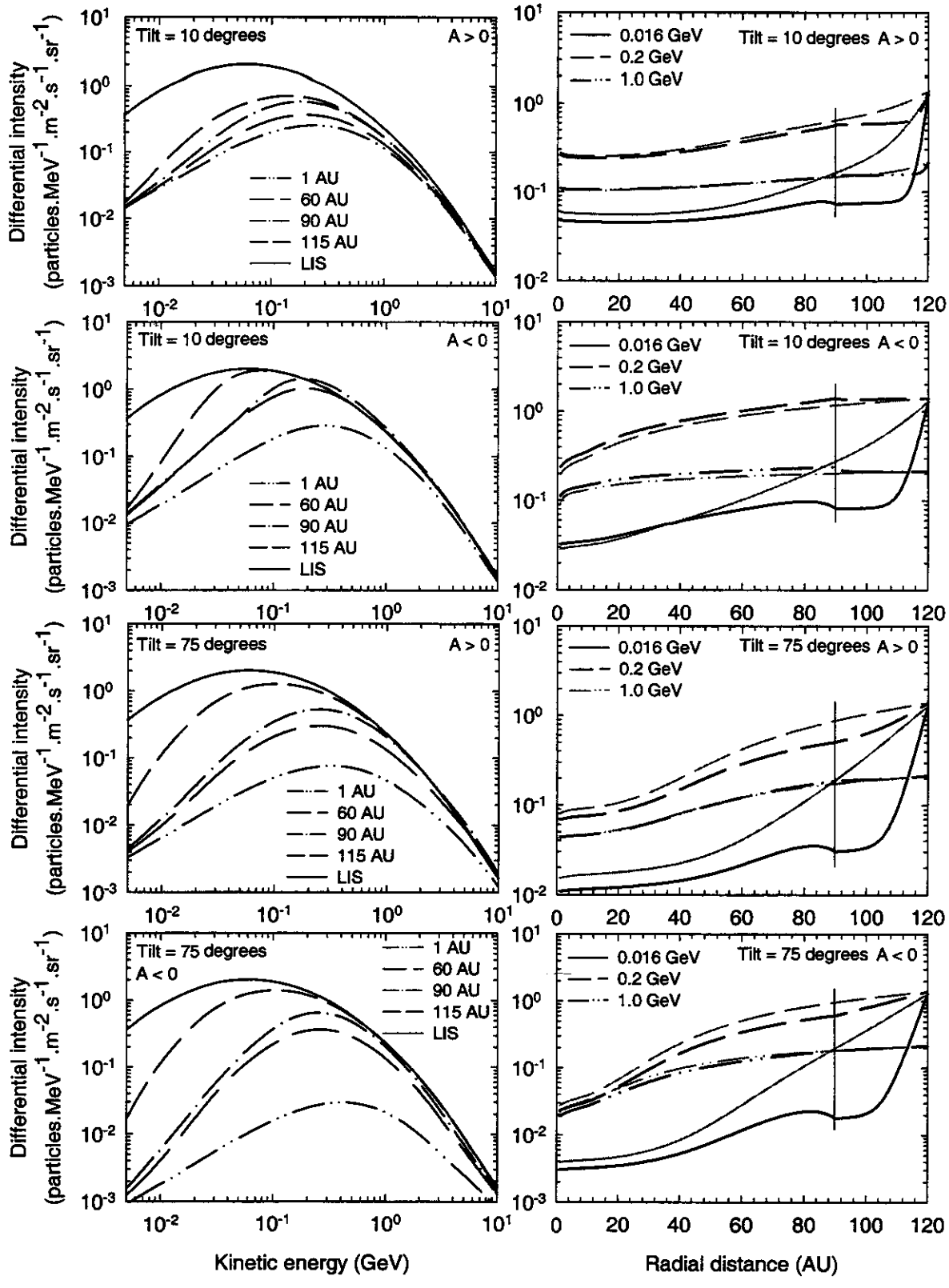

Figure 8.1. Left panels: Computed differential intensities for galactic He as a function of kinetic energy for both polarity cycles and solar minimum and moderate maximum conditions, at radial distances of 1, 60, 90 and 115 AU (bottom to top) in the equatorial plane. Right panels: Corresponding differential intensities as function of radial distance for 0.016, 0.2 and 1.0 GeV, respectively. Solutions without a TS are given here as thin grey lines at the same energies than solutions with a TS. In all panels the TS is at 90 AU, as indicated, and the LIS specified at 120 AU. The compression ratio $s = 3.2$.

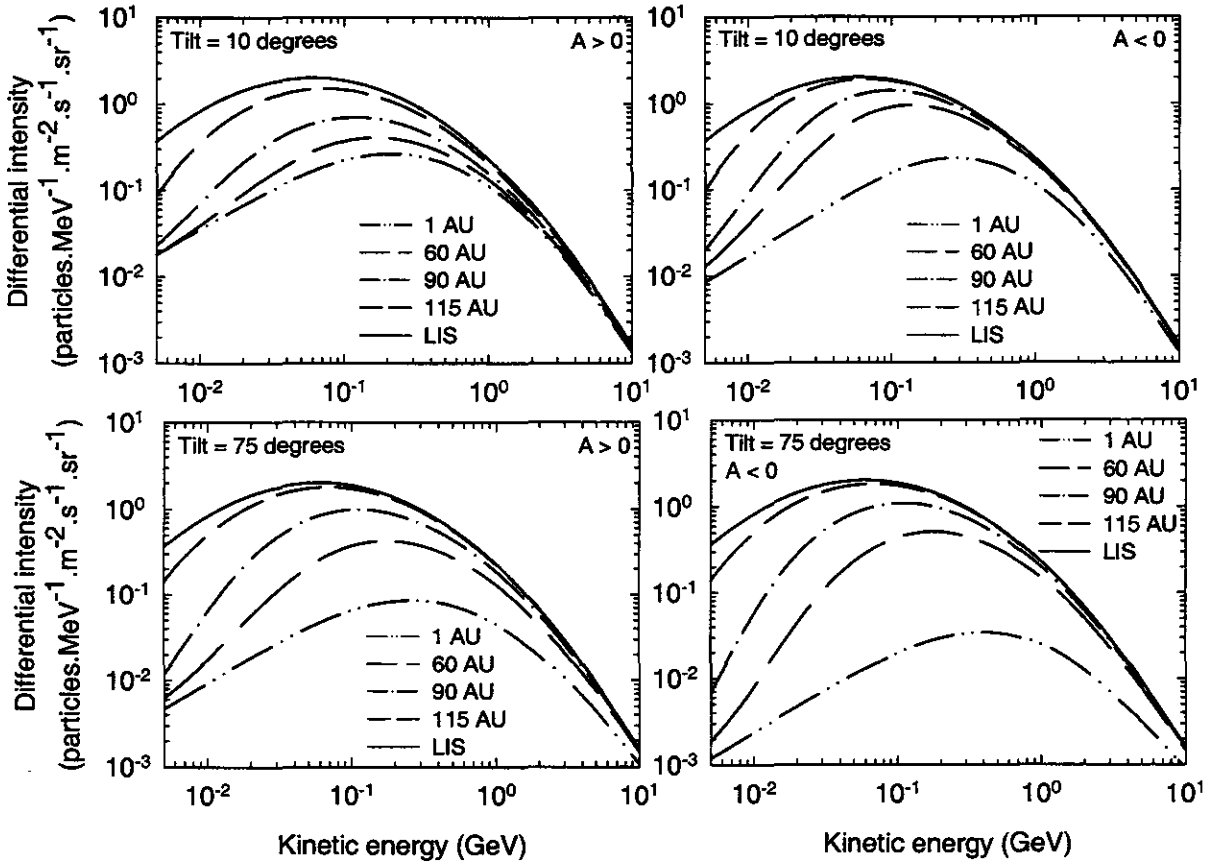

Figure 8.2. Differential intensities of galactic He computed without a TS as a function of kinetic energy for both polarity cycles and solar minimum (top panels) and moderate maximum (bottom panels) conditions, at radial distances of 1, 60, 90 and 115 AU (bottom to top) in the equatorial plane.

without a TS as is emphasized in Figure 8.2. This effect also seems absent for larger α's and clearly depends on the drift direction. The energy spectra in Figures 8.1 to 8.5 also depict how the slopes of the modulated He spectra systematically obtain the characteristic spectral index (energy slope) at lower energies which is caused by adiabatic 'cooling' with decreasing radial distance. Beyond the TS ($r > r_s$), the spectra obtain a much steeper energy slope at low energies and can cause rather strong negative radial gradients at very low energies, also evident for protons. This happens, however, at much lower energies ($E \lesssim 1.0$ MeV) than for protons, for the same reasons as has been discussed in Chapter 6. This implies that the LIS for galactic He may not be known at these low energies until a spacecraft actually approaches the heliopause. Differences between the spectra with and without a TS will be discussed in detail in the next section.

For He with anomalous He as is shown in Figure 8.5, the intensities at the TS where the anomalous He source is injected follow the characteristic $(E)^{-1.2}$ spectrum with $s = 3.2$ and $(E)^{-2.0}$ with $s = 2.0$, which is dictated by the acceleration of anomalous He at the TS with $E \lesssim 100$ MeV. The inclusion of a anomalous He component has a profound effect on the He intensities at larger radial distances ($r \gtrsim 60$ AU) at $E \lesssim 100$ MeV, but a relatively small effect on the intensities at Earth. This larger effect is because of the higher rigidity of He than that of protons for a given energy and should even be larger for heavier species (i.e., Oxygen, Boron, Carbon). Near the TS the spectrum is of course substantially different because of the injected anomalous He source. Note that the modulation for $r \gtrsim 50$ AU is much larger in the A < 0 cycle than for the A > 0 cycle if $\alpha = 10°$. This is also true for $\alpha = 75°$, although the modulation then is also larger for the A > 0 cycle than if $\alpha = 10°$. This effect is even

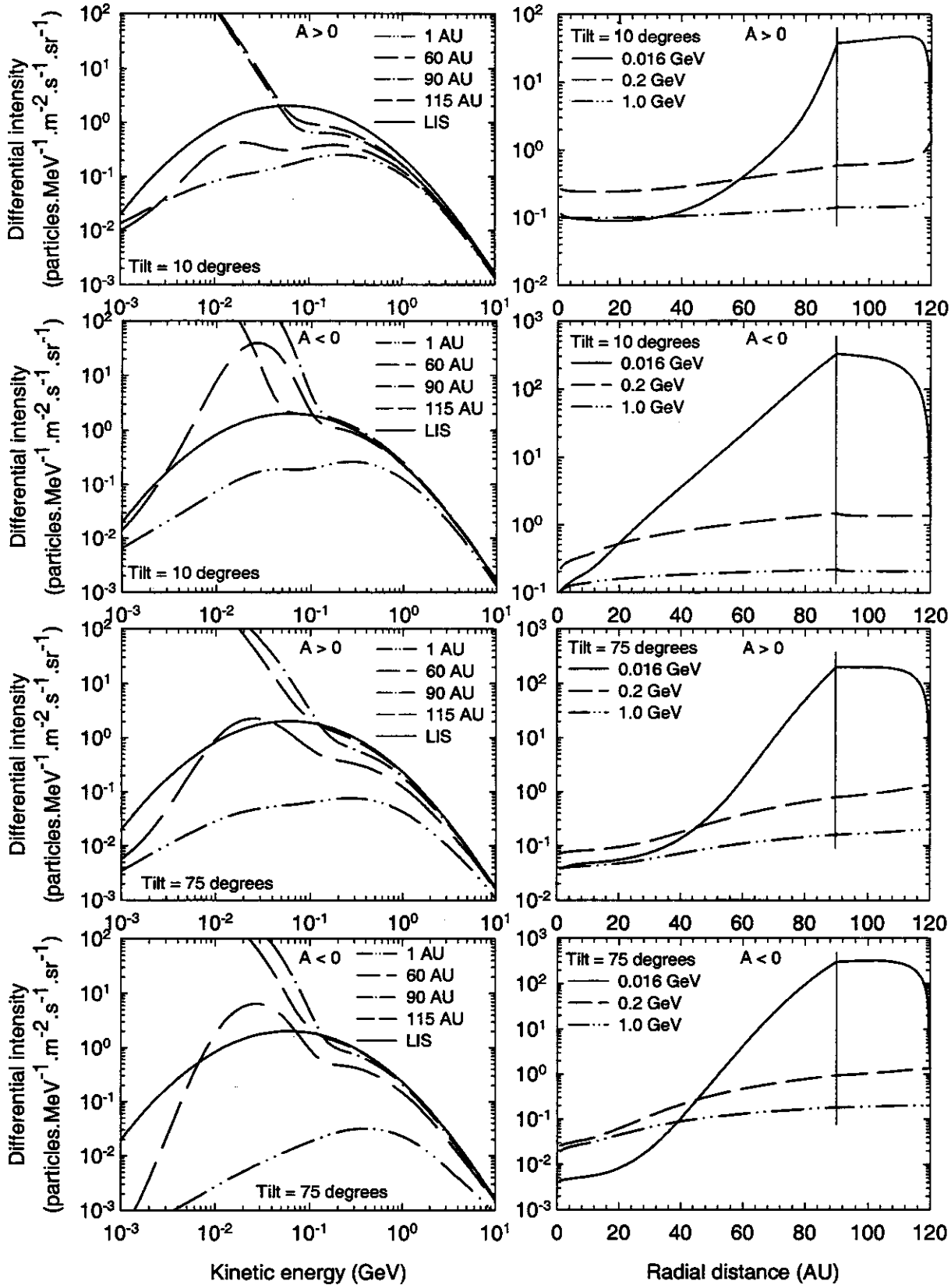

Figure 8.3. Similar to Figure 8.1 but for He with anomalous He and $s = 2.0$.

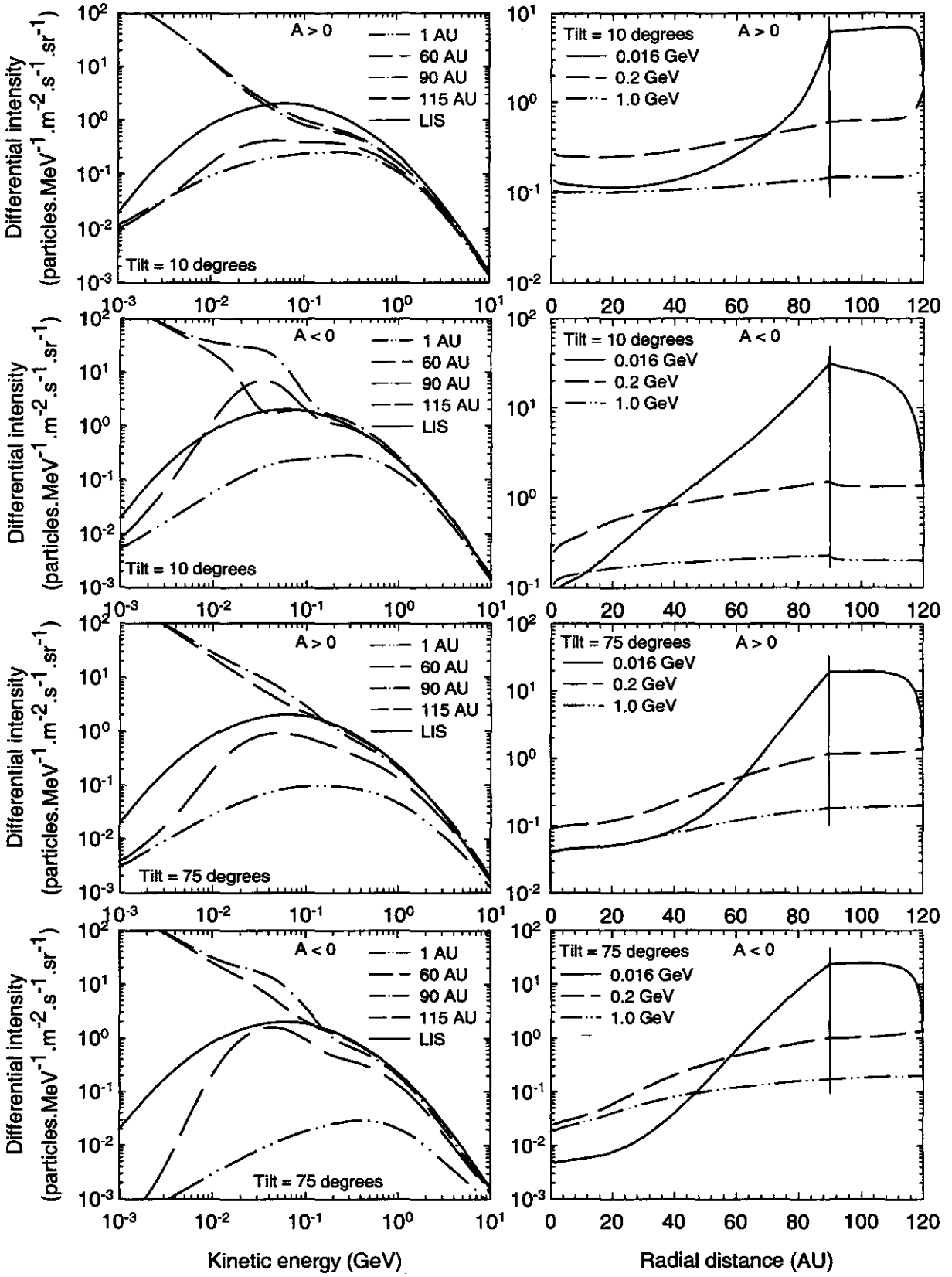

Figure 8.4. Similar to Figure 8.3 but for He with anomalous He and $s = 3.2$.

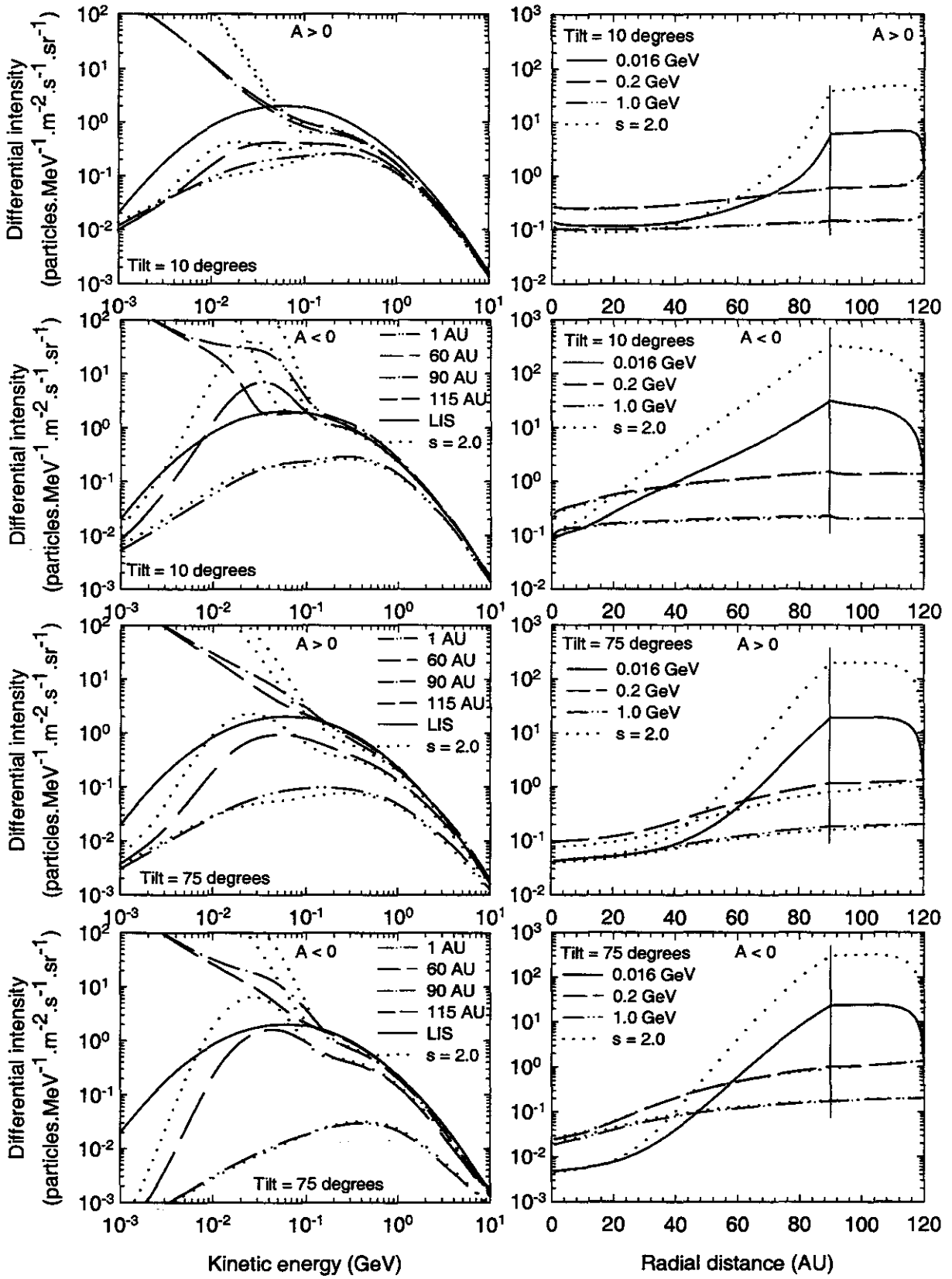

Figure 8.5. Similar to Figure 8.1 but for He with anomalous He. Here the dotted lines represent solutions with s = 2.0 (Figure 8.3) instead of s = 3.2 (Figure 8.4).

more enhanced as the compression ratio decreases from $s = 3.2$ to $s = 2.0$. At $E \approx 60$ MeV the cutoff energy of the anomalous He spectrum is quite evident for both values of α. The radial dependence of the 16 MeV intensity, that is shown in the right hand panels, is consequently significantly different, but at higher energies the effect diminishes as the acceleration cut-off energy is approached. The 'barrier' type modulation for this component at 16 MeV occurs inside the TS, and is not associated with the heliosheath, but occurring at smaller radial distances than have been predicted for protons, e.g., for the A > 0 cycle if $\alpha = 10°$ this is evident from ~40 AU already, while for the A < 0 cycle the 'barrier' effect disappears. This implicates that at these low energies a spacecraft should begin to observe a significant increase relatively far away from the TS for the A > 0 cycle. These aspects will be shown more quantitatively later in the chapter. Our results indicate that a s between 3.2 and 2.0 is preferred when anomalous He is also considered, and is consistent with the results that have been found for anomalous protons. Clearly, a strong shock with $s = 4$ is most unlikely (see also Potgieter and Langner, 2003a, 2003b).

8.4. Differences in modulation with and without a TS

In this section the differences in modulation with and without a TS are shown for galactic He. The differences between the spectra are evident from a comparison between Figures 8.1 and 8.2. In Figure 8.6 these differences are illustrated by depicting the ratio of intensities which have been obtained with and without a TS as a function of kinetic energy at radial distances of 1, 60, 90 and 115 AU, and as a function of radial distance at energies of 0.016, 0.2 and 1.0 GeV, respectively, in the equatorial plane for both polarity cycles when $\alpha = 10°$ and 75°. The modulation parameters of the two models were kept the same for these calculations in order to quantify the effects of the TS on the modulation of He. The ratios as a function of energy converge naturally at $E \gtrsim 10$ GeV because the TS has progressively less effect the higher the energy. The ratios as a function of radial distance approach unity at 120 AU where the LIS has been specified. These computed ratios indicate quantitatively how much the computed modulation for He changes when a TS is present.

Evidently, the effect of the TS on the modulation of galactic He with respect to the relevant LIS is profound. It decreases the intensities at lower energies (e.g., at 100 MeV) but increases it at higher energies (e.g., at 1 GeV) as the lower energy particles are being accelerated to higher energies, as have been emphasized by the ratios in Figure 8.6 which become larger than 1 for high energies. The differences between the two models can be significant, especially with $E <$ 100-300 MeV and $r \gtrsim 60$ AU for both $\alpha = 10°$ and 75°, similar to protons. For $\alpha = 10°$ the ratios have the lowest values at 115 AU for A > 0 at all energies, which indicates that the effect of the TS model is prominent at these larger distances. This is partly because of the assumed divergence free solar wind speed in the heliosheath region, causing the characteristic spectral slope which has been caused by adiabatic 'cooling' to be steeper for the TS model if $r \geq 90$ AU. The ratios at the different radial distances also have a minimum at a certain energy which becomes smaller as the radial distance increases, also related to the adiabatic 'cooling' that these particles experience which tends to have the ratios converge to a steady value at low energies. Combined these effects cause shifts in the minima of these ratios to lower energies, for increasing α and when the HMF polarity reverses.

The effect of the TS at Earth is not pronounced as has been expected, although the inclusion of the TS in the model can evidently influence the modulation of He even at Earth at low energies. The galactic He intensities are less at Earth at low energies with the TS than without it, because of the acceleration of these low energy particles to higher energies, as has been mentioned earlier. At these energies, this effect will of course not be observable

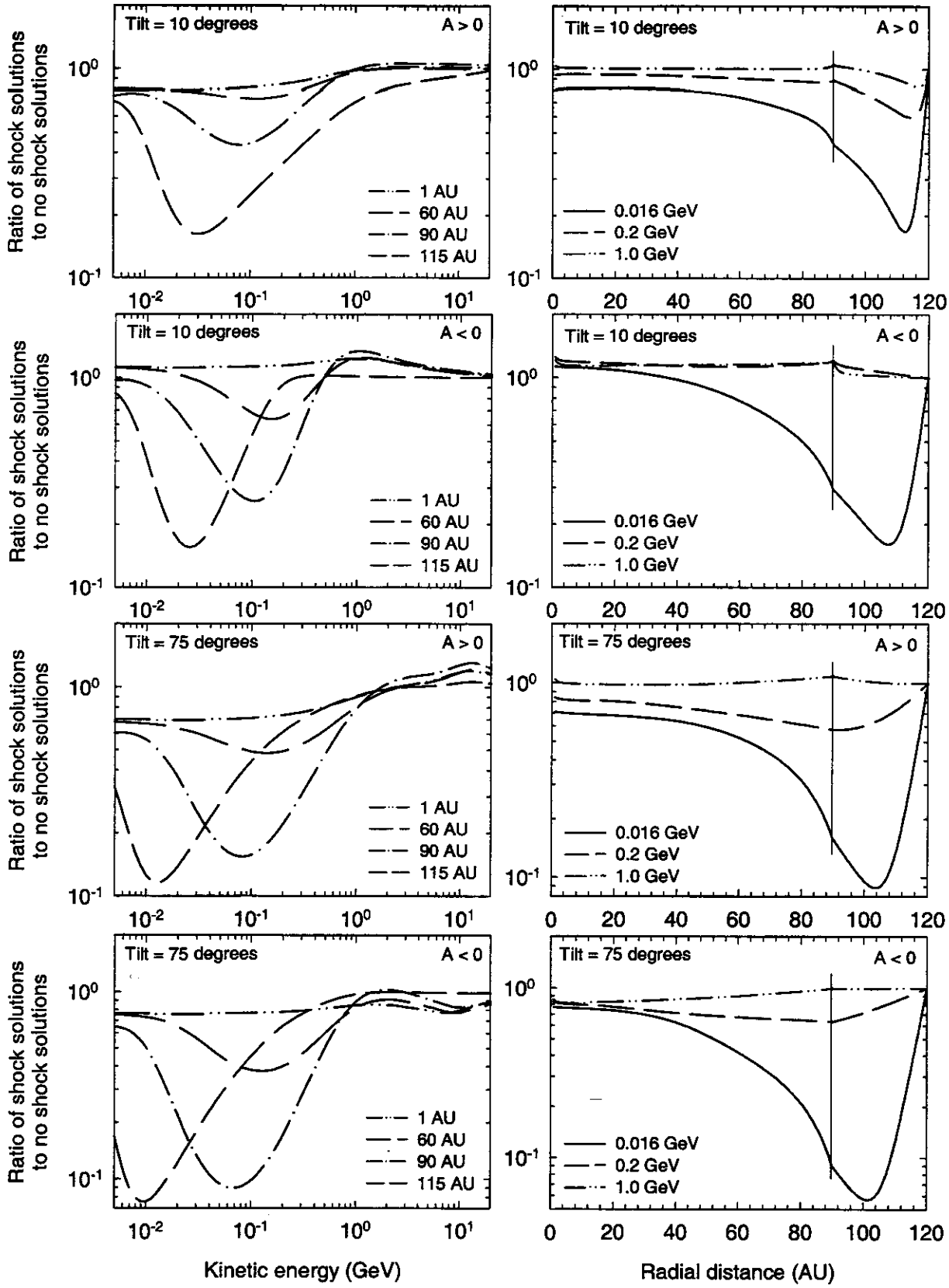

Figure 8.6. Intensity ratios of solutions for galactic He with a TS model compared to those without a TS as a function of kinetic energy at radial distances of 1, 60, 90 and 115 AU (left panels) and as function of radial distance at energies of 0.016, 0.2 and 1.0 GeV (right panels) for both polarity cycles in the equatorial plane. Top four panels are for solar minimum conditions ($\alpha = 10°$) and bottom four for moderate solar maximum conditions ($\alpha = 75°$). Note the scale differences between the panels.

because of the presence of anomalous He in the heliosphere.

8.5. Charge-sign dependence

8.5.1. Tilt angle dependence of Helium and Helium with anomalous Helium

Figure 8.7 shows differential intensities for He with and without anomalous He, as a function of the tilt angle in the equatorial plane at 1 AU for both polarity cycles at energies of 0.016 and 1.0 GeV. As has been noted for protons in Chapter 6, the model predicts a flattish tilt angle dependence for the A > 0 cycle for $\alpha \lesssim 50°$, but a steep decrease with larger tilt angles. For the A < 0 cycle a more gradual decrease with tilt angle is predicted. In Figure 8.7 it is also shown that theoretically the differential intensities with $\alpha = 90°$ converge if zero drifts have been assumed for extreme solar maximum activity. At $\alpha = 0°$ (not shown) the intensities for the A < 0 cycle are higher than that of the A > 0 cycle at $E = 1.0$ GeV, similar to protons, but the opposite happens at lower energies which is well known (see Reinecke et al., 1993).

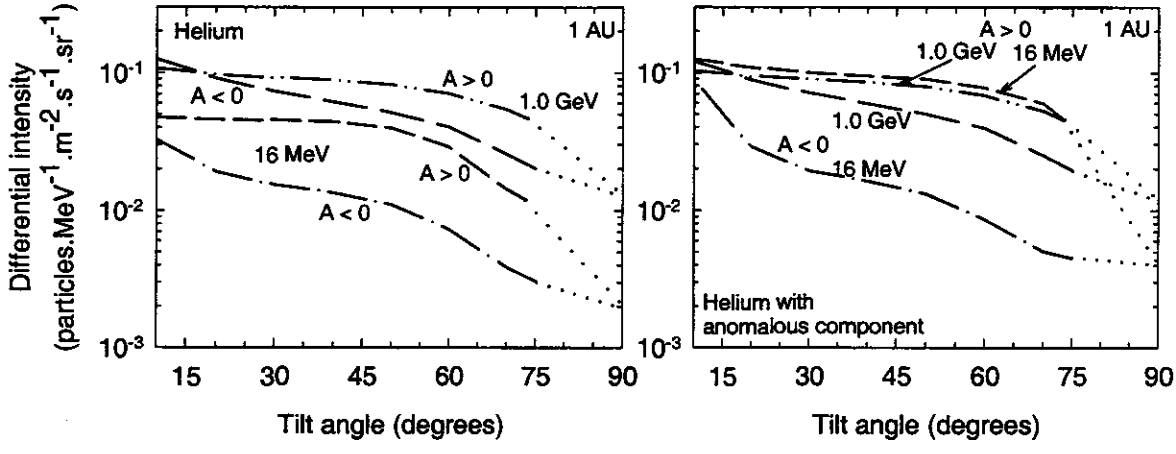

Figure 8.7. Differential intensities for He (left) and He with anomalous He (right), as a function of the tilt angle in the equatorial plane at 1 AU for both polarity cycles at energies of 0.016 and 1.0 GeV. The dotted lines are extrapolations to solutions with zero drifts at $\alpha = 90°$, when theoretically the HMF reverses.

8.5.2. Energy dependence of e^-/He and e^-/He with anomalous Helium

In Figure 8.8 the modulation differences between e^- and He are emphasized by plotting e^-/He and e^-/He with anomalous He, as a function of rigidity for both polarity cycles in the equatorial plane at 1 AU and 90 AU, with $\alpha = 10°$ and $\alpha = 75°$, respectively. As a reference, all the modulated ratios are compared to the corresponding (unmodulated) LIS ratios.

For the intensity ratios, e^-/He, and the e^-/He with anomalous He, one can expect to see effects similar to those of e^-/p and e^-/p with anomalous protons as has been discussed in the previous chapter. At low energies He experiences large adiabatic energy losses while e^- do not, and in addition e^- modulation becomes progressively independent of drifts so that the e^-/He is a factor of ~3000 for 100 MV at 90 AU. However, when the anomalous He component is added the e^-/He at 90 AU becomes significantly lower at low energies, e.g., only 6×10^{-2} at 100 MV since the anomalous He dominates the galactic He at these energies, which is similar to protons. The slight differences between the two cases at 1 AU indicates that anomalous He can reach the Earth. The cross-over

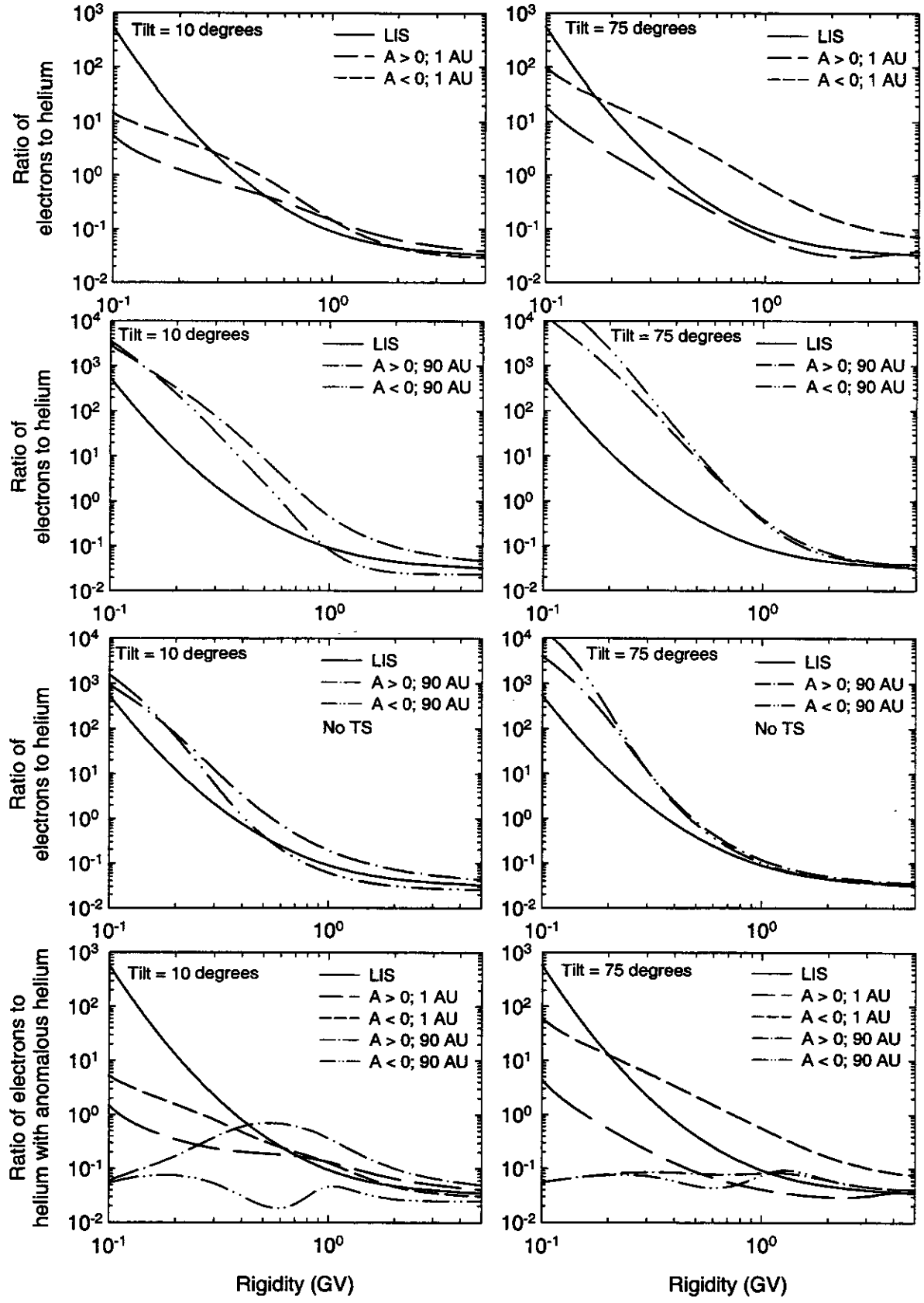

Figure 8.8. Ratios e^-/He and e^-/He with anomalous He as function of rigidity in the equatorial plane at 1 AU (top panels) and at the TS ($r_s = 90$ AU) for both polarity cycles with $\alpha = 10°$ (left panels) and $\alpha = 75°$ (right panels), respectively. All ratios are compared to the LIS e^-/He ratio (at 120 AU) as a reference. The ratios without a TS are shown only in the third row panels at 90 AU. Note the scale difference between the panels.

between the curves for the A > 0 and A < 0 polarity cycles for e^-/He evidently moves to lower rigidities with increasing radial distance, although this effect shifts to higher rigidities with increasing solar activity.

8.5.3. Tilt angle dependence of e^-/He, and e^-/He with anomalous Helium

In Figure 8.9 the e^-/He and e^-/He with anomalous He are shown as a function of the tilt angle at 1 AU and 90 AU for both polarity cycles in the equatorial plane at rigidities of 0.05, 1.10, and 2.5 GV. As has been noted for the e^-/p ratios, the characteristic 'Λ' shape are also clearly recognizable at 1 AU and 90 AU for the A > 0 cycle, but only for $R \gtrsim 0.1$ GV. For the A < 0 cycle the characteristic 'V' shape is visible for all rigidities shown at 1 AU and 90 AU. For the A > 0 cycle the tilt angle dependence becomes significantly less at $R \lesssim 0.1$ GV. For a discussion of these aspects see Chapter 7.

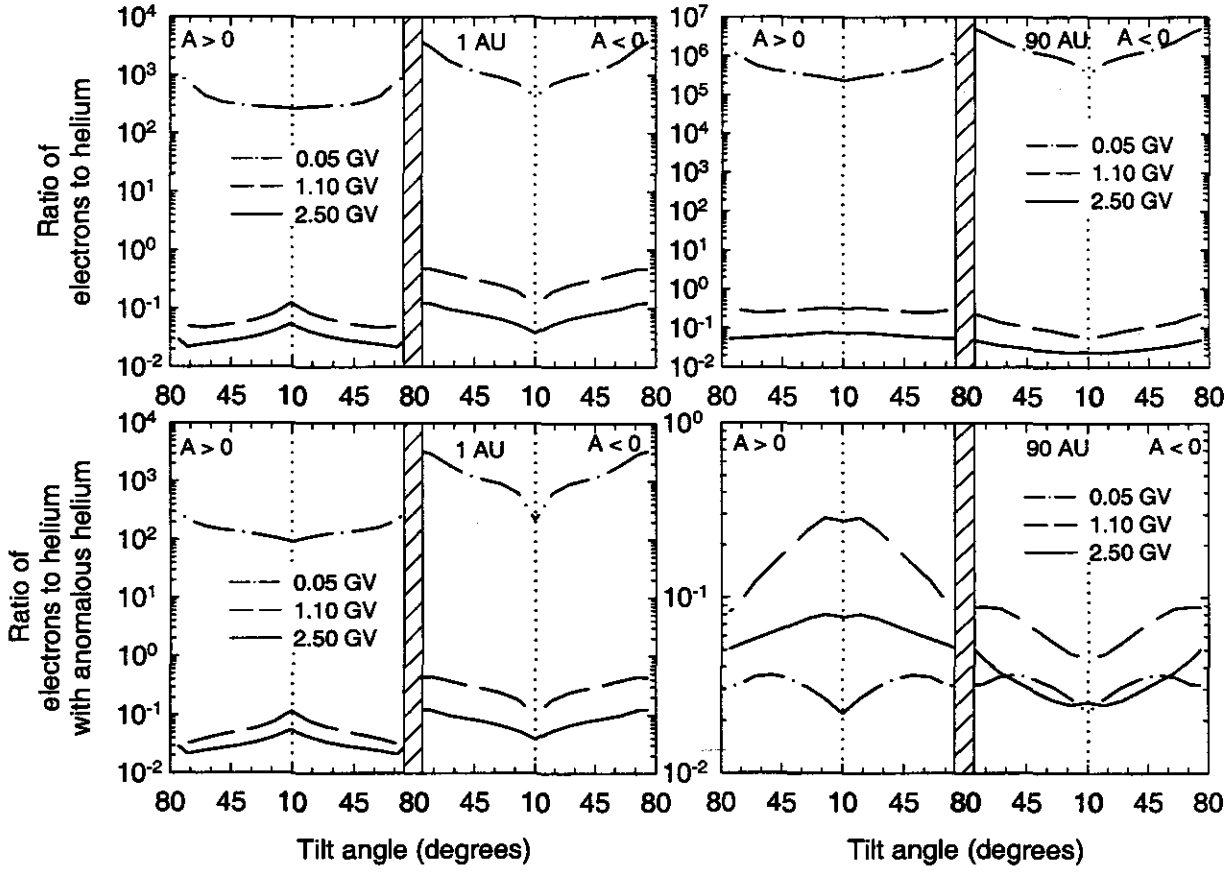

Figure 8.9: Ratios of e^-/He (top panels) and e^-/He with anomalous He (bottom panels), as a function of the tilt angle in the equatorial plane at 1 AU (left panels) and at the TS (r_s = 90 AU) (right panels) for both polarity cycles at rigidities of 0.05, 1.10, and 2.5 GV. Note the scale differences between the panels.

8.6. Heliosheath modulation

Next, the modulation computed to take place in the heliosheath, between r_b and r_s, is compared to what happens between r_b and 1 AU (LIS to Earth) and between r_s and 1 AU (TS to Earth). This comparison is emphasized by showing in Figures 8.10 and 8.11 the intensity ratios j_{LIS}/j_1, j_{LIS}/j_{90} and j_{90}/j_1 for He and He with anomalous He as a function of kinetic energy in the equatorial plane for both polarity cycles with $\alpha = 10°$ and 75°, respectively. For a few cases the ratios become less than unity, because of the acceleration of these particles at the TS.

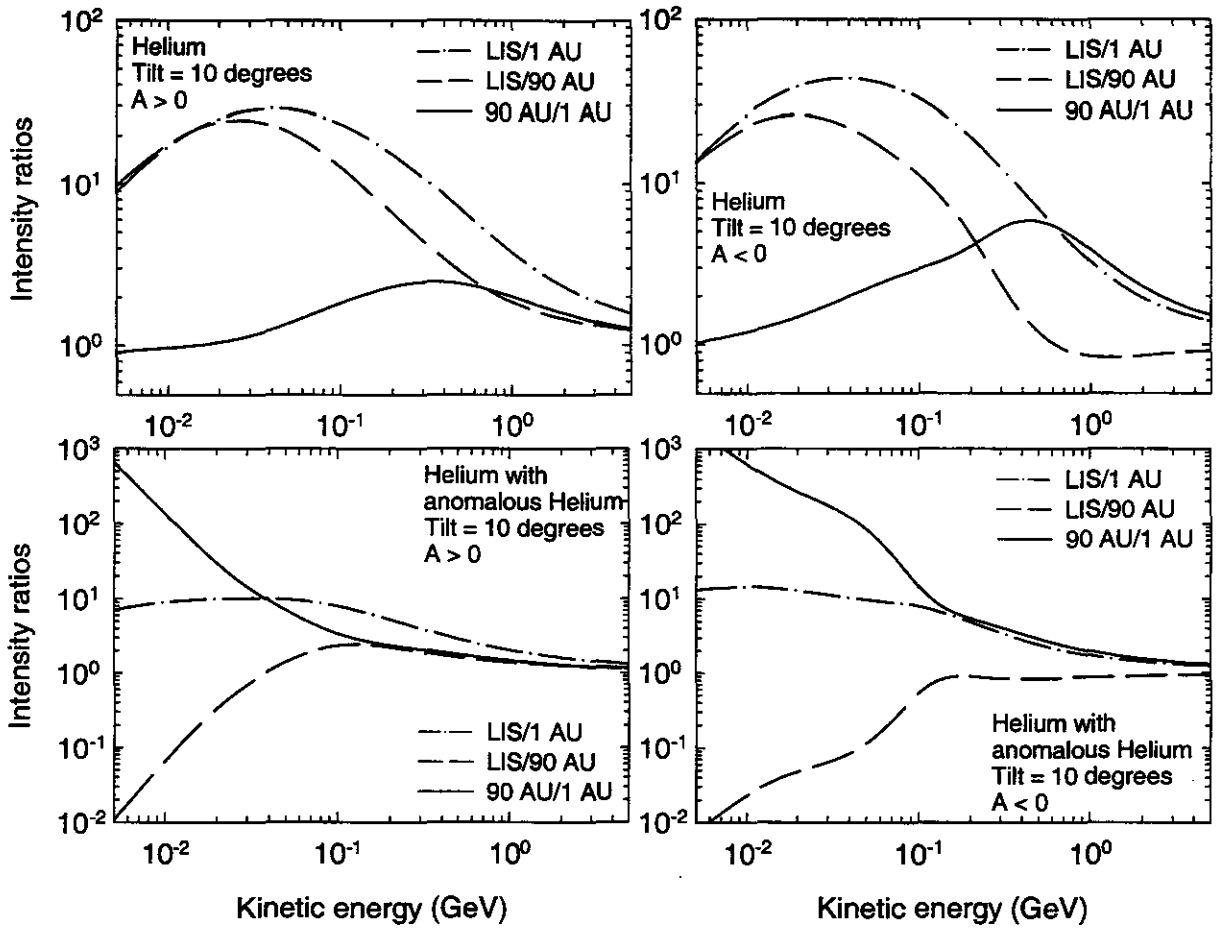

Figure 8.10. Intensity ratios j_{LIS}/j_1, j_{LIS}/j_{90} and j_{90}/j_1 (120 to 1 AU, 120 to 90 AU and 90 to 1 AU) for He (top panels) and He with anomalous He (bottom panels) as a function of kinetic energy in the equatorial plane with $\alpha = 10°$; left panels: for A > 0, right panels for A < 0. Note the scale differences between the panels.

According to Figures 8.10 and 8.11 a significant level of modulation occurs in the heliosheath for galactic He when A > 0 with $E \lesssim 200$ MeV for solar minimum ($\alpha = 10°$) and for moderate solar maximum ($\alpha = 75°$) conditions. This is also true for A < 0 but at a somewhat lower energy, similar to protons. For moderate solar maximum conditions the level of modulation in the heliosheath decreases significantly for $E > 200$ MeV in contrast with that of j_{90}/j_1. This is also true for solar minimum conditions in the A < 0 cycle and also to a lesser extent for the A > 0 cycle. Obviously, these ratios all converge at a high enough energy where no modulation is present.

The addition of the anomalous He component changes these ratios significantly for energies up to 1-2 GeV. The concept of 'barrier' or heliosheath modulation applicable to galactic CR species, changed when anomalous He and protons are considered. The heliosheath effects are still present at higher energies (rigidities) as the modelling indicates. Unfortunately, from an observational point of view clear indications of heliosheath modulation of galactic He and protons will be overwhelmed at low energies by the presence of the anomalous species. On the other hand, the presence of the anomalous particles should make the detection of the TS with particle detectors possible.

The modulation in the heliosheath is also an important part of the total modulation for galactic He and He with anomalous He as has been shown in the right panels of Figures 8.1 and 8.5. The TS in this regard plays a prominent role. For both species its effect becomes more pronounced the lower the energy. At higher energies, the 'barrier' effect progressively diminishes; the radial dependence beyond the shock may vanish or even become negative to

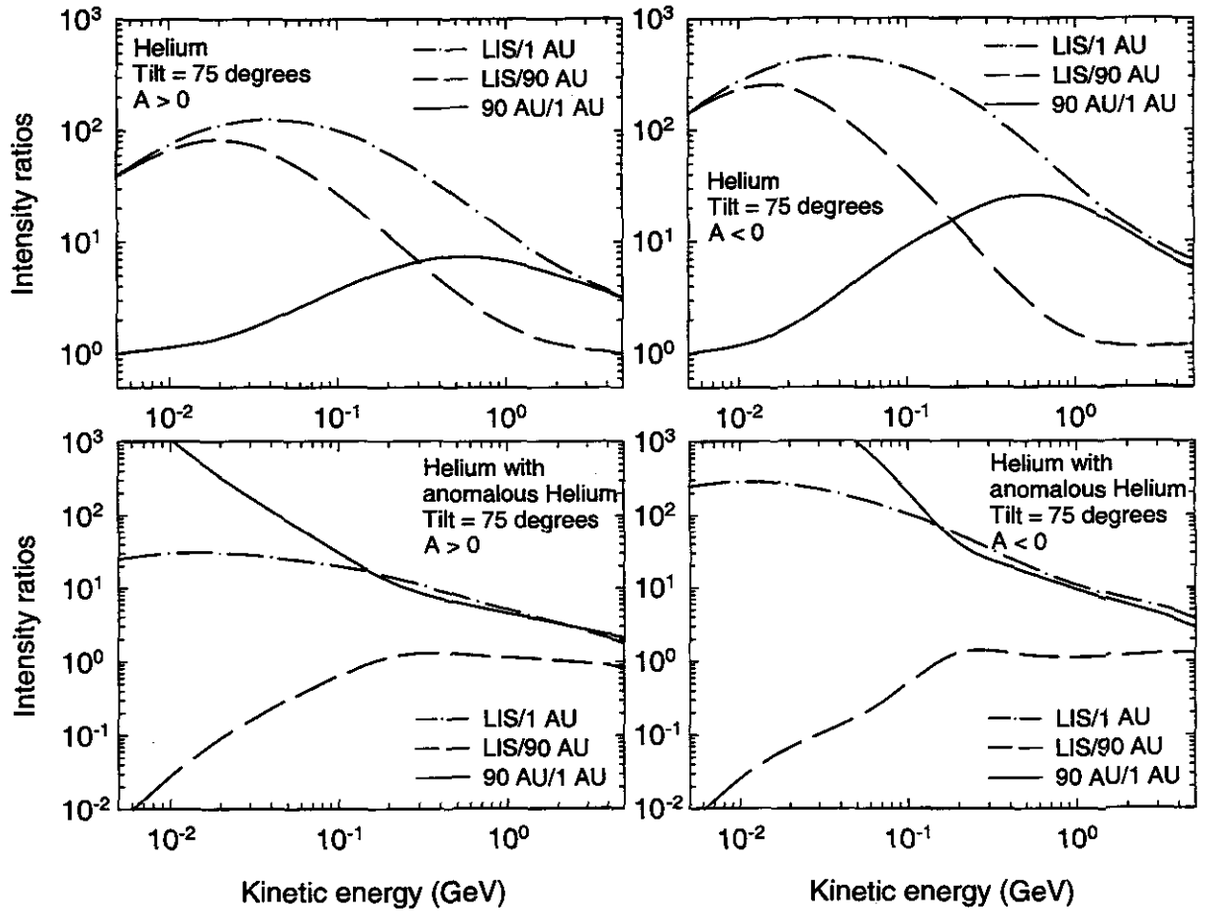

Figure 8.11. Similar to Figure 8.10 but for $\alpha = 75°$.

create a conspicuous shock effect on the radial intensity profiles. This effect is, however, strongly dependent on the HMF polarity cycles and is similar to that for protons.

8.7. Summary and conclusions

In this chapter four aspects of heliospheric modulation for He were highlighted: (1) The differences in the modulation of galactic He and He with anomalous He. (2) How the inclusion of a TS in the model altered this modulation and the consequent charge-sign dependence. (3) The kind of modulation effects to be expected near the TS and in the heliosheath; and (5) the effects of increased solar activity. Qualitatively, the results for He are similar to those of protons but there are quantitatively marked differences. These results confirm that this numerical model with a TS can reasonably reproduce the He modulation between the outer boundary and Earth and for a variety of species as it has been illustrated in the previous chapters. Although these results are most reasonable it seems unavoidable as has been noted before that the diffusion coefficients should change time-dependently, together with the 'tilt angle' and parameters like the compression ratio. These results indicate that a TS compression ration between 3.2 and 2.0 is preferred when anomalous He is also considered.

The modulation for galactic He that has been produced with and without a TS differs significantly, depending on the HMF polarity. These differences increase towards lower energies and larger radial distances. The slight differences between the e^-/He and the e^-/He with anomalous He at 1 AU indicate that anomalous He can reach the Earth.

The heliosheath can be considered a distinguishable modulation 'barrier' for galactic He with the overall effect clearly energy, polarity cycle and solar activity dependent, e.g., most of the modulation may occur in the heliosheath for $E \lesssim 200$ MeV at solar minimum during A < 0 cycles.

These results indicate as for protons that the LIS for galactic He may not be known at $E \lesssim 200$ MeV until a spacecraft actually approaches the heliopause because of the strong modulation that occurs in the heliosheath, the effect of the TS and the subsequent presence of anomalous He.

A detailed comparison with He observations at Earth and beyond was not done for this work - see Steenberg et al. (1998). Such a study may be well suited for a Masters thesis as follow-up and a further application of the TS model as has been presented in this work.

Chapter 9
Summary and conclusions

The interest in heliosheath modulation has leaped forward when it has become apparent, particularly from the Voyager and Pioneer spacecraft observations in the outer heliosphere, that the global modulation was significantly different in the A > 0 cycle than in the A < 0 cycle (Webber and Lockwood, 1995, 1997, 1998; McDonald, 1998; McDonald et al., 1998). The question of what happens beyond the solar wind termination shock has followed and has been the main motivation to address the issue of heliosheath modulation. The modulation, propagation and distribution of galactic and Jovian electrons, positrons, protons, anti-protons, Helium, and anomalous protons and Helium throughout the heliosphere and the effects of the solar wind termination shock on this modulation were therefore studied, using a two-dimensional termination shock model, referred to as the TS model, which was developed in this work. The solutions of this TS model were compared to a variety of observations from the Ulysses, Pioneer 10, and Voyager 1 and 2 missions.

A summary and the main conclusions that have been drawn from this study are given next:

After introducing the reader to this study in **Chapter 1**, a brief overview was given in **Chapter 2** of the major properties and the structure of the heliosphere. Topics discussed were the Sun, the solar wind, the solar activity cycle, the solar wind termination shock, the heliospheric magnetic field, and the Parker transport equation. What follows is an outline of the most important of these concepts which have been used in this study as is given in Chapter 2:

(1) The outer boundary (heliopause) of the heliosphere is assumed to be at $r_b = 120$ AU, while the location of the TS is assumed at $r_s = 90$ AU.

(2) The solar wind speed is assumed to change from 400 km.s^{-1} in the equatorial plane to 800 km.s^{-1} in the polar regions for solar minimum conditions, but to stay constant at 400 km.s^{-1} for moderate solar maximum conditions. Extreme solar maximum conditions are not considered.

(3) The heliospheric magnetic field is assumed to be a Parker spiral, but is significantly modified in the heliospheric polar regions, as are suggested by Jokipii and Kóta (1989).

(4) The heliosphere is divided into a northern and southern hemisphere with oppositely directed magnetic fields that change polarity every ~11 years. These hemispheres are separated by the wavy heliospheric current sheet along which charged particles experience drifts effects. Drift directions are different during the A > 0 and A < 0 cycles for a given species.

The distribution of cosmic rays in the heliosphere is the result of four different transport processes, namely diffusion, drifts, convection and adiabatic energy loss. The purpose of **Chapter 3** was therefore to give a short overview of the heliospheric transport processes, modulation theory, the numerical models developed by the Potchefstroom modulation group and for the present study, and in particular the diffusive shock acceleration process. In this work the locally one dimensional and the Wendroff's implicit method were used for solving the transport equation with a discontinuity at the assumed location of the solar wind termination shock. A suitable diffusion tensor was also constructed applicable to modulation of a variety of particles in the heliosphere. It has been shown that in two-dimensional modulation models three diffusion coefficients are of particular interest: $\kappa_{\parallel}$, $\kappa_{\perp r}$, and $\kappa_{\perp \theta}$, the diffusion coefficients parallel and perpendicular to the heliospheric magnetic field in the radial and polar direc-

tions, respectively. The 'drift coefficient' κ_A represents gradient, curvature and current sheet drifts. A $\kappa_{\|}$ was constructed based on theoretical calculations without the dissipation range but with slab/two-dimensional turbulence (Burger et al., 2000) and extended to lower rigidities for electrons and positrons, $R \leq 100$ MV, to have a near constant rigidity dependence ($R^{0.1}$) as predicted by observations and models including dynamical turbulence, e.g., the damping model (see Figures 3.5 and 3.8). Because of the complexity of $\kappa_{\perp}$, not much theoretical work exists, although currently it is seriously researched (e.g., Minnie, 2002; Teufel and Schlickeiser, 2002, 2003; Teufel et al., 2003; Stawicki, 2003; Shalchi, 2003; Parhi et al., 2003), illustrating that it is realized that $\kappa_{\perp}$ is important for the better understanding of CR modulation. In this work it was assumed that $\kappa_{\perp} \propto \kappa_{\|}$, and that $\lambda_{\perp r}/\lambda_{\|} \cong \lambda_{\perp \theta}/\lambda_{\|}$ between 0.003 - 0.2 for 0.5 MV - 5.0 GV (see Figure 3.13) at Earth. The 'drift coefficient' is the same as the one which has been used by Burger et al. (2000). Below ~1 GV, drifts are slightly reduced with respect to the weak scattering case for which $\lambda_A \propto R$, $\forall R$. In this work 50% drifts were assumed for all tilt angles. Without this assumption, the comparison between the computations and observations is very poor and it has become clear that full drifts are not possible as has been emphasized in many publications of the Potchefstroom group.

In **Chapter 4** characteristics of the improved and expanded two-dimensional TS modulation model developed and used for this study were shown. This model is an improvement of existing locally developed two-dimensional termination shock modulation models (e.g., Steenkamp, 1995; Haasbroek, 1997; Steenberg, 1998), but with a more general approach to handling the heliospheric current sheet in a two-dimensional model and the manner in which the solar wind speed transition at the termination shock is treated numerically. The WCS model of Hattingh (1993) was revisited, and a more general heliospheric current sheet approach was derived in order to accommodate a magnetic field with a modification, as was used in this work, and so that the TS model could be valid for all α.

The effects of continuous, discontinuous, and quasi-discontinuous transitions of the solar wind speed at the termination shock on the numerical solutions and the effect of the injection source spectrum at the termination shock were also studied. It was found that the spectra calculated for the continuous transition function of the solar wind speed differ from that of the discontinuous and quasi-discontinuous transitions. It became clear that although the continuous profile of the solar wind speed was easier to handle numerically, care had to be taken because the acceleration and modulation effects might be underestimated. In this work the quasi-discontinuous solar wind speed transition function was used with a compression ratio of $s = 3.2$ and a scale length of $L = 1.2$ AU inside of the termination shock. The deviation from the theoretically expected $E^{-1.18}$ dependence, for $s = 3.2$, of the shocked spectra for the anomalous cosmic rays and the quasi-discontinuous transition could clearly be seen in the 10 - 300 MeV range, and was prominent for the A < 0 cycle, but it was almost absent in the A > 0 cycle. This is similar to the effect that has been discussed by Steenkamp (1995) (see also Kóta and Jokipii, 1994), which causes the anomalous proton spectra in the A < 0 polarity cycle to be flatter than that of the A > 0 polarity cycle.

It was also shown that the TS model solutions were independent of the anomalous source injection energy, and that the accelerated spectrum at the termination shock was independent of the spectral form of the source spectrum, as long as the energy dependence was less than the expected energy dependence corresponding to the compression ratio used. For the TS model a delta function was injected at the termination shock with an arbitrary value which could be normalised by comparing the resulting spectra to observations. These aspects of the TS model are consistent to that of the Steenkamp (1995) model.

The effects of all these fundamental modulation processes and changes to the diffusion coefficients (discussed in Chapters 2 to 4) when applied to cosmic ray modulation in the heliosphere were shown through comparisons of

solutions to some major observations. These comparisons confirmed that the TS model used in this work could indeed reasonably reproduce the modulation in the heliosphere for a variety of galactic and anomalous particle species, and for Jovian electrons. Although the aim of this work was not to study the diffusion coefficients, it was evident that the chosen set gave reasonable comparisons to the observations for solar minimum, but for extreme solar maximum activity modification seemed necessary, e.g., by introducing transient 'barriers' like global merged interaction regions into the model to reproduce the observed radial gradients.

In **Chapter 5** it was shown that the inclusion of a termination shock in the modulation model for protons and for solar *minimum* conditions caused abrupt changes in the cosmic ray radial gradients at the termination shock, at almost all energies of interest to modulation studies. For $A > 0$ cycles, the radial gradients became typically very large (positive) inside the termination shock but almost zero at energies > 1.0 GeV beyond the termination shock, to increase again significantly close to the outer boundary. At lower energies, the radial gradients progressively became larger positive behind the termination shock. For the $A < 0$ cycle, the abrupt changes at the termination shock in the radial gradients were qualitatively similar, but they differed quantitatively, especially at low energies. For these cycles the intensity at the *termination* shock at energies $\gtrsim 0.5$ GeV could be higher than the corresponding value of the local interstellar spectrum for protons, so that the radial gradients might even be negative beyond the termination shock. Beyond the termination shock at energies < 10 MeV the slope of the spectra became much steeper than the adiabatic slope because the energy change term in the transport equation became negligible beyond the shock caused by the assumed divergence free solar wind in the heliosheath region.

For increased solar activity, the modulation in the heliosheath was quite different from minimum activity. The heliosheath no longer played the role of a distinguished 'barrier', although abrupt changes in the radial gradients at the termination shock might still occur, especially for $A > 0$ cycles, surprising more so for higher energies. The role of drifts manifested itself in the clear differences between the polarity cycles. Drifts in the heliosheath region had the effect to enhance the 'barrier' effect, while no drifts caused more gradual increases in the radial intensities. Qualitatively, these results for protons were consistent to those of Jokipii et al. (1993) but there were quantitatively marked differences (see also Langner et al., 2003).

In **Chapter 6** five aspects of heliospheric modulation for protons and anti-protons were highlighted: (1) The differences in the modulation of galactic protons and anti-protons. (2) How the inclusion of a termination shock in the model altered this modulation and the consequent charge-sign dependence. (3) How the inclusion of anomalous protons changes the modulation for protons. (4) The kind of modulation effects to be expected near the termination shock and in the heliosheath and (5) The effects of increased solar activity. The termination shock modulation results for anti-protons and the effects of the termination shock on charge-sign dependent modulation were new. Although the results were most reasonable it seemed unavoidable that the diffusion coefficients should change time-dependently, together with the 'tilt angle' and parameters like the compression ratio (see also Potgieter and Langner, 2003a, 2003b). These results indicated that a termination shock compression ration between 3.2 and 2.0 was preferred when anomalous protons were also considered, but that this ratio could not be determined effectively using only galactic proton and anti-proton spectra. A strong shock with $s = 4$ was most unlikely.

The modulation produced by a model with and without a termination shock could differ significantly, depending on the species and heliospheric magnetic field polarity. These differences increased toward lower energies and larger radial distances. The $\overline{\mathrm{p}}/\mathrm{p}$ approached a steady value at all radial distances for lower energies which was a manifestation of the adiabatic 'cooling' these species experienced in the heliosphere and was independent of the

shape of the local interstellar spectrum. Strong charge-sign dependent effects occurred for protons and anti-protons enhanced by the vastly different local interstellar spectra and the different effect the termination shock had on these cosmic ray particles.

It was also found that the heliosheath could be considered a distinguishable modulation 'barrier' for both protons and anti-protons with the overall effect clearly energy, polarity cycle and solar activity dependent. These results indicated that the proton local interstellar spectrum might not be known at $E \lesssim 200$ MeV until a spacecraft actually approached the heliopause because of the strong modulation that occured in the heliosheath, the effect of the termination shock and the presence of anomalous protons. For anti-protons, in contrast, these effects were less pronounced.

In **Chapter 7** the following heliospheric modulation aspects for electrons and positrons were highlighted: (1) The differences in the modulation of electrons, including a Jovian electron source, and positrons, also with increased solar activity, and the consequent charge-sign dependence. (2) How the inclusion of a termination shock in the model altered this modulation and (3) the kind of modulation effects to be expected near the termination shock and in the heliosheath for electrons and positrons. These aspects were considered for the first time for galactic positrons. The following were found:

(1) The modulated spectra for electrons and positrons at the termination shock might exceed the corresponding local interstellar spectrum at energies $\gtrsim 200$ MeV. It became less pronounced when these particles drifted in over the heliospheric poles towards the equatorial regions. With increased solar activity the effect became less evident for both polarity cycles.

(2) The modulation of electrons and positrons became progressively independent of drifts with lower energies. Electrons and positrons also experienced significantly less adiabatic energy losses at energies $\gtrsim 1$ MeV than protons and anti-protons with the consequence that the rigidity dependence of the diffusion coefficients could easily be deduced from observations at lower energies. By studying the intensity ratios it is even possible to deduce the energy slopes of the corresponding local interstellar spectrum. Unfortunately, for electrons the situation at $E \lesssim 100$ MeV was complicated in the inner heliosphere by the dominating presence of the Jovian electron source.

(3) With the inclusion of the termination shock, the largest modulation effects occured at/near the termination shock. Intensities between 0.1 and 1.0 GeV were most affected and could be up to ~3 times higher at 90 AU than without a shock. A general effect of the inclusion of the termination shock was to decrease the intensities at lower energies at all radial distances, while increasing it at mid-energy ranges. The energy where this adjustment occurred for positrons was between 100-300 MeV depending on the radial distance and $\lesssim 1$ MeV for electrons. The effect of the termination shock on modulation was the largest for electrons when $A > 0$, but for positrons when $A < 0$. For both species the intensities were affected by the presence of the termination shock, even at Earth.

(4) The modulation in the heliosheath depended on the particle species, was strongly dependent on the energy of the cosmic rays, the polarity cycle, and was enhanced by the inclusion of the termination shock. For electrons the factor modulation in the heliosheath became comparable to the factor between the termination shock and Earth at low energies for both polarity epochs when $\alpha = 10°$. However, during the $A > 0$ epoch the heliosheath could not really be considered a modulation 'barrier' above ~150 MeV for electrons, while for positrons this occured at somewhat higher energies during the $A < 0$ epoch. For $\alpha = 75°$ the heliosheath could not be

considered a modulation 'barrier'.

(5) For positrons the modulated spectra had very mild energy dependencies below ~300 MeV, even at Earth, in contrast to electrons, protons and anti-protons (Langner and Potgieter, 2003a, 2003b).

In **Chapter 8** four aspects of heliospheric modulation for Helium were highlighted: (1) The differences in the modulation of galactic Helium and Helium with an anomalous component. (2) How the inclusion of a termination shock in the model altered this modulation and the consequent charge-sign dependence between Helium and electrons. (3) The kind of modulation effects to be expected near the termination shock and in the heliosheath and (5) The effects of increased solar activity. Qualitatively, the results for Helium were similar to those of protons but there were quantitatively marked differences. The modulation for galactic Helium produced by the TS model with and without a termination shock differed significantly, depending on the heliospheric magnetic field polarity. These differences increased towards lower energies and larger radial distances. The slight differences between the e^-/He and the e^-/He with anomalous Helium at 1 AU indicated that anomalous Helium could reach the Earth.

The heliosheath could also be considered a distinguishable modulation 'barrier' for galactic Helium with the overall effect clearly energy, polarity cycle and solar activity dependent. These results indicated as for protons that the local interstellar spectrum for galactic Helium might not be known at $E \lesssim 200$ MeV until a spacecraft actually approached the heliopause because of the strong modulation that occured in the heliosheath, the effect of the termination shock and the subsequent presence of anomalous Helium.

The results of Chapters 5 to 8 confirmed that the two-dimensional numerical model with a termination shock, used in this work, could reasonably reproduce the modulation between the outer boundary and Earth for protons, anti-protons, electrons with a Jovian source, positrons, Helium, and anomalous protons and Helium. Although these results were most reasonable it seemed unavoidable that the diffusion coefficients should change time-dependently, together with the 'tilt angle' and parameters like the compression ratio. Modifications for extreme solar maximum activity also seemed necessary, e.g., by introducing transient 'barriers' like global merged interaction regions into the model to reproduce the observed radial gradients.

Comparing the findings summarized in this chapter to the list of topics discussed in Chapter 1, this work has successfully addressed these topics and can provide useful information for future spacecraft missions, especially to the outer heliosphere. The TS model can also be used for future studies, e.g.:

- Explaining the measurements by the Voyager missions in the region of the termination shock in more detail.
- A detailed comparison with Helium, Boron, and Carbon observations, and the calculation of the B/C ratio at Earth and beyond.
- The role and importance of drifts, and the structure of the heliospheric current sheet in the heliosheath.
- The inclusion of time-dependent parameters and different structures of the termination shock in the model.
- The development of a TS model with an asymmetric geometry for the heliosphere.
- The expansion of the TS model to three spatial dimensions.

References

[1] Alfven, H., Electric currents in cosmic plasmas, *Reviews of Geophysics and Space Physics, 15*, 271-284, 1977.

[2] Axford, W. I., Acceleration of Cosmic Rays by Shock Waves, *Proc. 17th Inter. Cosmic Ray Conf. (Paris), 12*, 155-158, 1981.

[3] Axford, W. I., E. Leer, and G. Skadron, The acceleration of cosmic rays by shock waves, *Proc. 15th Inter. Cosmic Ray Conf. (Plovdiv), 11*, 132-135, 1977.

[4] Balogh, A., E. J. Smith, B. T. Tsurutani, D. J. Southwood, R. J. Forsyth, and T. S. Horbury, The Heliospheric Magnetic Field Over the South Polar Region of the Sun, *Science, 268*(5213), 1007-1010, 1995.

[5] Balogh, A., R. G. Marsden, and E. J. Smith, (Eds.), *The Heliosphere Near Solar Minimum: The Ulysses Perspective*, 411 pp., Springer-Praxis, London, 2001.

[6] Baring, M. G., Cosmic ray origin, acceleration and propagation, *Proc. 26th Inter. Cosmic Ray Conf. (Salt Lake City): Invited, Rapporteur & Highlighted Papers*, 153-157, 1999.

[7] Belcher, J. W., A. J. Lazarus, R. L. McNutt, and G. S. Gordon, Solar wind conditions in the outer heliosphere and the distance to the termination shock, *J. Geophys. Res., 98*(A9), 15177-15183, 1993.

[8] Bell, A. R., The acceleration of cosmic rays in shock fronts - I, *Montly Notices of the Royal Astronomical Society, 182*, 147-156, 1978a.

[9] Bell, A. R., The acceleration of cosmic rays in shock fronts - II, *Montly Notices of the Royal Astronomical Society, 182*, 443-455, 1978b.

[10] Bieber, J. W., and W. H. Matthaeus, Cosmic ray pitch angle scattering in dynamical magnetic turbulence, *Proc. 22nd Inter. Cosmic Ray Conf. (Dublin), 3*, 248-251,1991.

[11] Bieber, J. W., W. H. Matthaeus, C. W. Smith, W. Wanner, M-B. Kallenrode, and G. Wibberenz, Proton and electron mean free paths: The Palmer consensus revisited, *Astrophys. J., 420*(1), 294-306, 1994.

[12] Biermann, L., Kometenschwiefe und solare Korpuskularstrahlung, *Zeit. Astrophys., 29*, 274-286, 1951.

[13] Biermann, L., The solar wind and the interplanetary media, in *Space Astrophysics*, edited by W. Liller, McGraw-Hill, New York, 150, 1961.

[14] Blandford, R. D., and J. P. Ostriker, Particle acceleration by astrophysical shocks, *Astrophys. J., 221*(2), L29-L32, 1978.

[15] Burger, R. A., On the theory and application of drift motion of charged particles in inhomogeneous magnetic fields, Ph.D. thesis, Potchefstroom University for CHE, South Africa, 1987.

[16] Burger, R. A., and M. Hattingh, Steady-State Drift-Dominated Modulation Models for Galactic Cosmic Rays, *Astrophysics and Space Science, 230*, 375-382, 1995.

[17] Burger, R. A., and M. Hattingh, Toward a Realistic Diffusion Tensor for Galactic Cosmic Rays, *Astrophys. J., 505*(1), 244-251, 1998.

[18] Burger, R. A., and M. Hattingh, Effect of Fisk-type heliospheric magnetic fields on the latitudinal transport of cosmic rays, *Proc. 27th Inter. Cosmic Ray Conf. (Hamburg), 9*, 3698-4001, 2001.

[19] Burger, R. A., and M. S. Potgieter, The calculation of neutral sheet drift in two-dimensional cosmic-ray modulation models, *Astrophys. J., 339*(1), 501-511, 1989.

[20] Burger, R. A., M. S. Potgieter, and B. Heber, Rigidity dependence of cosmic-ray proton latitudinal gradients measured by the Ulysses spacecraft: Implications for the diffusion tensor, *J. Geophys. Res., 105*(A12), 27447-27456, 2000.

[21] Burger, R. A., S. E. S. Ferreira, J. W. Bieber, R. Engel, T. K. Gaisser, and T. Stanev, The antiproton to proton ratio over a 22-year cycle: A time dependent approach, *Proc. 27th Inter. Cosmic Ray Conf. (Hamburg), 8*, 3661-3664, 2001.

[22] Burlaga, L. F., and N. F. Ness, Large-scale distant heliospheric magnetic field: Voyager 1 and 2 observations from 1986 through 1989, *J. Geophys. Res.*, *98*(A10), 17451-17460, 1993.

[23] Burlaga, L. F., N. F. Ness, E. C. Stone, F. B. McDonald, M. H. Acuña, R. P. Lepping, and J. E. P. Connerney, Search for the heliosheath with Voyager 1 magnetic field measurements, *Geophys. Res. Lett.*, *30*(20), SSC 9-1-SSC9-4, doi:10.1029/2003GL018291, 2003.

[24] Cecchini, S., and J. J. Quenby, Three-dimensional models of galactic cosmic ray modulation, *Proc. Inter. Cosmic Ray Conf. (Munich)*, *3*, 911-914, 1975.

[25] Chenette, D. L., T. F. Conlon, and J. A. Simpson, Bursts of relativistic electrons from Jupiter observed in interplanetary space with the time variation of the planetary rotation period, *J. Geophys. Res.*, *79*, 3551-3558, 1974.

[26] Cliver, E. W., Solar energetic particles: Acceleration and transport, *AIP Conference Proc.*, *516*(1), 103-119, 2000.

[27] Coroniti, F. V., C. F. Kennel, F. L. Scarf, and E. J. Smith, Whistler mode turbulence in the distrubed solar wind, *J. Geophys. Res.*, *87*, 6029-6044, 1982.

[28] Coutu, S., S. W. Barwick, J. J. Beatty, A. Bhattacharyya, C. R. Bower, C. J. Chaput, G. A. de Nolfo, M. A. Duvernois, A. Labrador, S. P. McKee, D. Müller, J. A. Musser, S. L. Nutter, E. Schneider, S. P. Swordy, G. Tarlé, A. D. Tomasch, and E. Torbet, Cosmic-ray positrons: are there primary sources ?, *Astroparticle Physics*, *11*(4), 429-435, 1999.

[29] Crooker, N. U., G. L. Siscoe, S. Shodhan, D. F. Webb, J. T. Gosling, and E. J. Smith, Multiple heliospheric current sheets and coronal streamer belt dynamics, *J. Geophys. Res.*, *98*(A6), 9371-9381, 1993.

[30] Cummings, A. C., R. A. Mewaldt, E. C. Stone, and W. R. Webber, Radial and latitudinal gradients of anomalous cosmic ray oxygen and helium from 1 to 41 AU, *Proc. 21st Inter. Cosmic Ray Conf. (Adelaide)*, *6*, 206-209, 1990.

[31] Czechowski, A., and S. Grzedzielski, Trapped VLF radiation as a signature of the dynamical processes in the heliosphere, *Adv. Space Res.*, *13*(6), 223-226, 1993.

[32] Davis, L., The interplanetary magnetic field, in *Solar Wind*, edited by C. P. Sonett, P. J. Coleman, and J. M. Wilcox., Scientific and Technical Information Office, NASA, Washington, 93, 1972.

[33] Donohue, D. J., and G. P. Zank, Steady state and dynamical structure of a cosmic-ray-modified termination shock, *J. Geophys. Res.*, *98*(A11), 19005-19025, 1993.

[34] Douglas, J., On the numerical integration of $\frac{\partial^2 u}{\partial x^2} + \frac{\partial^2 u}{\partial y^2} = \frac{\partial u}{\partial t}$ by implicit methods, *J. Soc. Indust. Appl. Math.*, *3*, 42-49, 1955.

[35] Douglas, J., Alternating direction implicit methods for three space variables, *Numerische Mathematik*, *4*, 41-47, 1962.

[36] Dröge, W., Particle scattering by magnetic fields, *Space Science Reviews*, *93*(1/2), 121-151, 2000.

[37] Drury, L., An introduction to the theory of diffusive shock acceleration of particles in tenuous plasmas, *Rep. Prog. Phys.*, *46*, 973, 1983.

[38] Du chateau, P., and W. D. Zachmann, *Theory and problems of partial differential equations*, McGraw-Hill, New York, 1986.

[39] Earl, J. A., The diffusive idealization of charged-particle transport in random magnetic fields, *Astrophys. J.*, *193*, 231-242, 1974.

[40] Eraker, J. H., Origins of the low-energy relativistic interplanetary electrons, *Astrophys. J.*, *257*(1), 862-880, 1982.

[41] Eraker, J. H., and J. A. Simpson, Jovian electron propagation close to the Sun (<0.5 AU), *Astrophys. J.*, *232*(2), L131-L134, 1979.

[42] Evenson, P., M. Garcia-Munoz, P. Meyer, K. R. Pyle, and J. A. Simpson, A quantitative test of solar

modulation theory - The proton, helium, and electron spectra from 1965 through 1979, *Astrophys. J.*, *275*(2), L15-L18, 1983.

[43] Exarhos, G., and X. Moussas, An estimation of the shape and location of the heliospheric termination shock, *Astrophys. J.*, *542*(2), 1075-1079, 2000.

[44] Ferrando, P., MeV to GeV electron propagation and modulation: Results of the KET-telescope onboard Ulysses, *Adv. Space Res.*, *19*(6), 905-915, 1997.

[45] Ferrando, P., R. Ducros, C. Rastoin, and A. Raviart, Jovian electron jets in interplanetary space, *Planetary and Space Science*, *41*, 839-843, 1993a.

[46] Ferrando, P., R. Ducros, C. Rastoin, A. Raviart, H. Kunow, R. Müeller-Mellin, H. Sierks, and G. Wibberenz, Propagation of jovian electrons in and out of the ecliptic, *Adv. Space Res.*, *13*(6), 107-110, 1993b.

[47] Ferrando, P., A. Raviart, L. J. Haasbroek, M. S. Potgieter, W. Dröge, B. Heber, H. Kunow, R. Müeller-Mellin, H. Sierks, G. Wibberenz, and C. Paizis, Latitude variations of ~7 MeV and >300 MeV cosmic ray electron fluxes in the heliosphere: Ulysses COSPIN/KET results and implications, *Astron. Astrophys.*, *316*, 528-537, 1996.

[48] Ferrando, P., A. Raviart, B. Heber, V. Bothmer, H. Kunow, R. Müeller-Mellin, and C. Paizis, Observation of a ~7 MeV electron super-flux at 5 AU by Ulysses, *Proc. 26th Inter. Cosmic Ray Conf. (Salt Lake City)*, *7*, 135-138, 1999.

[49] Ferraro, V. C. A., and C. Plumpton, *An introduction to magneto-fluid mechanics*, Clarendon Press., Oxford, 1966.

[50] Ferreira, S. E. S., A study of the modulation of cosmic ray electrons in the heliosphere, M.Sc. dissertation, Potchefstroom University for CHE, South Africa, 1998.

[51] Ferreira. S. E. S., The heliospheric transport of galactic cosmic rays and jovian electrons, Ph.D. thesis, Potchefstroom University for CHE, South Africa, 2002.

[52] Ferreira, S. E. S., and M. S. Potgieter, The modulation of 4- to 16-MeV electrons in the outer heliosphere: Implications of different local interstellar spectra, *J. Geophys. Res.*, *107*(A8), SSH 12-1-SSH12-10, doi:10.1029/2001JA000226, 2002.

[53] Ferreira, S. E. S., and M. S. Potgieter, Galactic cosmic rays in the heliosphere, *Adv. Space Res.*, in press, 2004.

[54] Ferreira, S. E. S., M. S. Potgieter, and R. A. Burger, Comparison of a two- and three-dimensional drift model, *Proc 26th Inter. Cosmic Ray Conf. (Salt Lake City)*, *7*, 77-80, 1999.

[55] Ferreira, S. E. S., M. S. Potgieter, R. A. Burger, and B. Heber, Modulation effects of anisotropic perpendicular diffusion on cosmic ray electron intensities in the heliopshere, *J. Geophys. Res.*, *105*(A8), 18305-18314, 2000.

[56] Ferreira, S. E. S., M. S. Potgieter, R. A. Burger, B. Heber, and H. Fichtner, Modulation of jovian and galactic electrons in the heliosphere 1. Latitudinal transport of a few MeV electrons, *J. Geophys. Res.*, *106*(A11), 24979-24988, 2001a.

[57] Ferreira, S. E. S., M. S. Potgieter, R. A. Burger, B. Heber, H. Fichtner, and C. Lopate, Modulation of Jovian and galactic electrons in the heliosphere: 2. Radial transport of a few MeV electrons, *J. Geophys. Res.*, *106*(A12), 29313-29322, 2001b.

[58] Ferreira, S. E. S., M. S. Potgieter, B. Heber, H. Fichtner, and R. A. Burger, Latitudinal transport of 7 MeV jovian and galactic electrons, *Proc. 27th Inter. Cosmic Ray Conf. (Hamburg)*, *8*, 3702-3705, 2001c.

[59] Ferreira, S. E. S., M. S. Potgieter, B. Heber, H. Fichtner, R. A. Burger, and P. Ferrando, A study of the compatibility between observations and model simulations for jovian and galactic electrons, *Adv. Space Res.*, *27*(3), 553-558, 2001d.

[60] Ferreira, S. E. S., M. S. Potgieter, and U. W. Langner, Effects of the heliospheric termination shock on possible local interstellar spectra for cosmic ray electrons and the associated heliospheric modulation, in *The Outer Heliosphere: The Next Frontiers*, edited by K. Scherer, H. Fichtner, H. J. Fahr, and E. Marsch, Pergamon, Amsterdam, 223, 2001e.

[61] Ferreira, S. E. S., M. S. Potgieter, U. W. Langner, and C. Lopate, Consequences of different local interstellar spectra on 16 MeV electron modulation, *Proc. 27th Inter. Cosmic Ray Conf. (Hamburg)*, *8*, 3653-3656, 2001f.

[62] Ferreira, S. E. S., M. S. Potgieter, and C. Lopate, Effects of the termination shock on 16 MeV electron modulation, *Proc. 27th Inter. Cosmic Ray Conf. (Hamburg)*, *8*, 3706-3709, 2001g.

[63] Ferreira, S. E. S., M. S. Potgieter, B. Heber, and H. Fichtner, Charge-sign dependent modulation over a 22-year cycle, *Annales Geophysicae*, *21*, 1359-1366, 2003.

[64] Fichtner, H., Anomalous Cosmic Rays: Messengers from the Outer Heliosphere, *Space Science Reviews*, *95*(3/4), 639-754, 2001.

[65] Fichtner, H., and K. Scherer, The heliosphere: A Brief Overview, in *The Outer Heliosphere: Beyond the Planets*, edited by K. Scherer, H. Fichtner, and E. Marsch, Copernicus Gesellschaft, Katlenburg-Lindau, 1, 2000.

[66] Fichtner, H., S. R. Sreenivasan, and H. J. Fahr, Cosmic ray modulation and a non-spherical shock, *Astron. Astrophys.*, *308*, 248-260, 1996.

[67] Fichtner, H., M. S. Potgieter, S. E. S. Ferreira, and R. A. Burger, On the propagation of Jovian electrons in the heliosphere: transport modelling in 4-D phase space, *Geophys. Res. Lett.*, *27*(11), 1611-1614, 2000.

[68] Fichtner, H., M. S. Potgieter, S. E. S. Ferreira, and B. Heber, Time-dependent 3D modelling of the heliospheric propagation of few-MeV electrons, *Proc. 27th Inter. Cosmic Ray Conf. (Hamburg)*, *8*, 3666-3669, 2001.

[69] Fisk, L. A., Solar modulation of galactic cosmic rays, *J. Geophys. Res.*, *76*, 221-226, 1971.

[70] Fisk, L. A., Modulation of Solar Cosmic RaysHigh Energy Phenomena on the Sun, in *Proc. at Goddard Space Flight Center*, edited by R. Ramaty and R. G. Stone, NASA, Washington, 418, 1973.

[71] Fisk, L. A., The anomalous component, its variation with latitude and related aspects of modulation, in *The sun and the heliosphere in three dimensions*, D. Reidel Publishing Co., Dordrecht, 401, 1986.

[72] Fisk, L. A., Motion of the footpoints of heliospheric magnetic field lines at the Sun: Implications for recurrent energetic particle events at high heliographic latitudes, *J. Geophys. Res.*, *101*(A7), 15547-15554, 1996.

[73] Fisk, L. A., B. Koslovsky, and R. Ramaty, An Interpretation of the Observed Oxygen and Nitrogen Enhancements in Low-Energy Cosmic Rays, *Astrophys. J.*, *190*, L35-L38, 1974.

[74] Florinski, V., and J. R. Jokipii, A Two-dimensional, Self-consistent Model of Galactic Cosmic Rays in the Heliosphere, *Astrophys. J.*, *523*(2), L185-L188, 1999.

[75] Florinski, V., G. P. Zank, and N. V. Pogorelov, Galactic cosmic ray transport in the global heliosphere, *J. Geophys. Res.*, *108*(A6), doi:10.1029/2002JA009695, SSH 1-1-SSH 1-16, 2003.

[76] Forbush, E., Three unusual cosmic ray increases probably due to charged particles from the Sun, *Physical Review 70*, 771-780, 1946.

[77] Forsyth, R. J., A. Balogh, E. J. Smith, G. Erdös, and D. J. McComas, The underlying Parker spiral structure in the Ulysses magnetic field observations, 1990-1994, *J. Geophys. Res.*, *101*(A1), 395-404, 1996.

[78] Gaisser, T. K., *Cosmic Rays and Particle Physics*, Cambridge Univ. Press., Cambridge, 1990.

[79] Garcia-Munoz, M., G. M. Mason, and J. A. Simpson, The Abundances of Galactic Cosmic-Ray Carbon, Nitrogen, and Oxygen and Their Astrophysical Implications, *Astrophys. J.*, *184*, 967-994, 1973a.

[80] Garcia-Munoz, M., G. M. Mason, and J. A. Simpson, A New Test for Solar Modulation Theory: the 1972 May-July Low-Energy Galactic Cosmic-Ray Proton and Helium Spectra, *Astrophys. J.*, *182*, L81-L84, 1973b.

[81] Garcia-Munoz, M., G. M. Mason, and J. A. Simpson, The Anomalous 1972 Low Energy Galactic Cosmic Ray Proton and Helium Spectra, *Proc. 13th Inter. Cosmic Ray Conf. (Denver)*, *2*, 1304-1307, 1973c.

[82] Gazis, P. R., A. Barnes, J. D. Mihalov, and A. J. Lazarus, The structure of the inner heliosphere from Pioneer, Venus and IMP observations, in *Solar Wind*, edited by E. Marsch and R. Schwenn, Pergamon Press., New-York, 183, 1991.

[83] Gazis, P. R., A. Barnes, J. D. Mihalov, and A. J. Lazarus, Solar wind velocity and temperature in the outer heliosphere, *J. Geophys. Res.*, *99*(A4), 6561-6573, 1994.

[84] Gervasi, M., P. G. Rancoita, and I. G. Usoskin, Transport of galactic cosmic rays in the heliosphere: Stochastic simulation approach, *Proc. 26th Inter. Cosmic Ray Conf. (Salt Lake City)*, *7*, 69-72, 1999.

[85] Giacalone, J., Cosmic-ray transport coefficients, *Space Science Reviews*, *83*(1/2) 351-363, 1998.

[86] Giacalone, J., and J. R. Jokipii, The Transport of Cosmic Rays across a Turbulent Magnetic Field, *Astrophys. J.*, *520*(1), 204-214, 1999.

[87] Giacalone, J., and J. R. Jokipii, The transport of energetic particles and cosmic rays in the heliosphere, *Adv. Space Res.*, *27*(3), 461-469, 2001.

[88] Giacalone, J., J. R. Jokipii, and J. Kóta, Particle drifts in a fluctuating magnetic field, *Proc. 26th Inter. Cosmic Ray Conf. (Salt Lake City)*, *7*, 37-40, 1999.

[89] Gil, A., and M. V. Alania, 27-day variations of cosmic rays for the minima epochs of solar activity: Experimental and 3-D drift modelling results, *Proc. 27th Inter. Cosmic Ray Conf. (Hamburg)*, *9*, 3725-3728, 2001.

[90] Gleeson, L. J., and W. I. Axford, Cosmic Rays in the Interplanetary Medium, *Astrophys. J.*, *149*, L115-L118, 1967.

[91] Gleeson, L. J., and W. I. Axford, The Compton-Getting effect, *Astrophysics and Space Science*, *2*, 431-440, 1968.

[92] Gloeckler, G., L. A. Fisk, and J. Geiss, Anomalously small magnetic field in the local interstellar cloud, *Nature*, *386*, 374-377, 1997.

[93] Goldstein, M. L., A nonlinear theory of cosmic-ray pitch-angle difusion in homogeneous magnetostatic turbulence, *Astrophys. J.*, *204*, 900-919, 1976.

[94] Goldstein, M. L., A. J. Klimas, and G. Sandri, Mirroring in the Fokker-Planck coefficient for cosmic-ray pitch-angle scattering in homogeneous magnetic turbulence, *Astrophys. J.*, *195*, 787-799, 1975.

[95] Gombosi, T. I., K. Lorencz, and J. R. Jokipii, Combined first- and second-order Fermi acceleration in cometary environments, *J. Geophys. Res.*, *94*, 15011-15023, 1989.

[96] Gurnett, D. A., and W. S. Kurth, Heliospheric 2-3 kHz radio emissions and their relationship to large Forbush decreases, *Adv. Space Res.*, *16*(9), 279-290, 1995.

[97] Gurnett, D. A., and W. S. Kurth, Radio Emissions from the Outer Heliosphere, *Space Science Reviews*, *78*(1/2), 53-66, 1996.

[98] Gurnett, D. A., W. S. Kurth, S. C. Allendorf, and R. L. Poynter, Radio Emission from the Heliopause Triggered by an Interplanetary Shock, *Science*, *262*(5131/OCT8), 199-203, 1993.

[99] Haasbroek, L. J., Modulation of cosmic rays in the heliosphere: A model study for the Ulysses mission (in Afrikaans), M.Sc. dissertation, Potchefstroom University for CHE, South Africa, 1993.

[100] Haasbroek, L. J., The transport and acceleration of charged particles in the heliosphere, Ph.D thesis, Potchefstroom University for CHE, South Africa, 1997.

[101] Haasbroek, L. J., and M. S. Potgieter, The modulation of cosmic rays in the high latitude heliosphere: A computer simulation, *Space Science Reviews*, *72*, 385-388, 1995.

[102] Haasbroek, L. J., and M. S. Potgieter, A new model to study galactic cosmic ray modulation in an asymmetrically bounded heliosphere, *J. Geophys. Res.*, *103*, 2099-2104, 1998.

[103] Haasbroek, L. J., M. S. Potgieter, and J. A. le Roux, The time-dependent recovery after the large cosmic ray decrease in 1991, *Proc. 24th Inter. Cosmic Ray Conf. (Rome)*, *4*, 710-713, 1995a.

[104] Haasbroek, L. J., M. S. Potgieter, and W. R. Webber, Cosmic-ray electron modulation using current knowledge of the heliosphere, *Proc. 24th Inter. Cosmic Ray Conf. (Rome)*, *4*, 706-709, 1995b.

[105] Haasbroek, L. J., M. S. Potgieter, and J. A. le Roux, Acceleration of galactic and Jovian electrons at the heliospheric solar wind termination shock, *Adv. Space Res.*, *19*(6), 953-956, 1997a.

[106] Haasbroek, L. J., M. S. Potgieter, and J. A. le Roux, Some modulation effects of termination shock accelerated galactic and jovian electrons, *Proc. 25th Inter. Cosmic Ray Conf. (Durban)*, *2*, 29-32, 1997b.

[107] Hall, D. T., D. E. Shemansky, D. L. Judge, P. Gangopadhyay, and M. A. Gruntman, Heliospheric hydrogen beyond 15 AU: Evidence for a termination shock, *J. Geophys. Res.*, *98*(A9), 15185-15192, 1993.

[108] Hamilton, D. C., and J. A. Simpson, Jovian electron propagation out of the solar equatorial plane - Pioneer 11 observations, *Astrophys. J.*, *228*(2), L123-L127, 1979.

[109] Harding, A. K., and R. Ramaty, The pulsar contribution to galactic cosmic-ray positrons, *Proc. 20th Inter. Cosmic Ray Conf. (Moscow)*, *2*, 6.2-2, 1987.

[110] Hasselmann, K., and G. Wibberenz, Scattering of charged particles by random electromagnetic fields, *Zeitschrift für Geophysik*, *34*, 353-360, 1968.

[111] Hasselmann, K., and G. Wibberenz, A note on the parallel diffusion coefficient, *Astrophys. J.*, *162*, 1049-1051, 1970.

[112] Hattingh, M., Drift of cosmic rays at a wavy neutral sheet in the heliosphere (in Afrikaans), M.Sc. dissertation, Potchefstroom University for CHE, South Africa, 1993.

[113] Hattingh, M., The modulation of galactic cosmic rays in a three-dimensional heliosphere, Ph.D thesis, Potchefstroom University for CHE, South Africa, 1998.

[114] Hattingh, M., and R. A. Burger, A new simulated wavy neutral sheet drift model, *Adv. Space Res.*, *16*(9), 213-216, 1995a.

[115] Hattingh, M., and R. A. Burger, Some properties of a fully three-dimensional drift model for the modulation of galactic cosmic rays, *Proc. 24th Inter. Cosmic Ray Conf. (Rome)*, *4*, 337-340, 1995b.

[116] Hattingh, M., and R. A. Burger, Towards a realistic diffusion tensor for galactic cosmic rays, *Proc. 25th Inter. Cosmic Ray Conf. (Durban)*, *2*, 13-16, 1997.

[117] Heber, B., Modulation galaktischer kosmischer protonen und alpha-teilchen in der inneren dreidimensionalen heliosphäre: Messungen des Kiel Electron Telescopes an bord der raunsonde Ulysses, Ph.D. thesis, Christian-Albrechts-Universität, Kiel, Germany, 1997.

[118] Heber, B., Modulation and propagation of cosmic rays in the inner three-dimensional heliosphere: Ulysses observations, habilitatsion study, Universität Osnabrück, Germany, 2002.

[119] Heber B., W. Dröge, P. Ferrando, L. J. Haasbroek, H. Kunow, R. Müller-Mellon, C. Paizis, M. S. Potgieter, A. Raviart, and G. Wibberenz, Spatial variation of >40MeV/n nuclei fluxes observed during the ULYSSES rapid latitude scan, *Astron. Astrophys.*, *316*, 538-546, 1996.

[120] Heber, B., M. S. Potgieter, and P. Ferrando, Solar modulation of galactic cosmic rays: The 3D heliosphere, *Adv. Space Res.*, *19*(5), 795-804, 1997.

[121] Heber B., P. Ferrando, A. Raviart, C. Paizis, R. Müller-Mellin, and H. Kunow, Propagation of 3 - 10 MeV electrons in the inner heliosphere: Ulysses observations, *Adv. Space Res.*, *27*(3), 547-552, 2001.

[122] Heber, B., G. Wibberenz, M. S. Potgieter, R. A. Burger, S. E. S. Ferreira, R. Müller-Mellon, H. Kunow, P.Ferrando, A. Raviart, C. Paizis, C. Lopate, F. B. McDonald, and H. V. Cane, Ulysses Cosmic Ray and Solar Particle Investigation/Kiel Electron Telescope observations: Charge sign dependence and spatial gradients during the 1990-2000 A > 0 solar magnetic cycle, *J. Geophys. Res.*, *107*(A10), SSH 2-1-SSH 2-10, doi:10.1029/2001JA000329, 2002.

[123] Heber, B., J. M. Clem, R. Müller-Mellon, H. Kunow, S. E. S. Ferreira, and M. S. Potgieter, Evolution of the galactic cosmic ray electron to proton ratio: Ulysses COSPIN/KET observations, *Geophys. Res. Lett.*, *30*(19), ULY 6-1-ULY 6-10, doi:10.1029/2003GL017356, 2003.

[124] Hess, V. F., *Physikal. Zeits.*, *12*, 998, 1911.

[125] Hess, V. F., *Physikal. Zeits.*, *13*, 1084, 1912.

[126] Higbie, P. R., J. D. Peterson, J. M. Rockstroh, and W. R. Webber, Calculations of the < 1 GeV electron spectrum using a Monte Carlo diffusion program and a comparison with the low energy galactic g-ray spectrum, *Proc. 26th Inter. Cosmic Ray Conf.*, *4*, 245-248, 1999.

[127] Hovestadt, D., O. Vollmer, G. Gloeckler, and C. Y. Fan, Measurement of Elemental Abundance of Very Low Energy Solar Cosmic Rays, *Proc. 13th Inter. Cosmic Ray Conf. (Denver)*, *2*, 1498-1501, 1973.

[128] Hundhausen, A. J., An interplanetary view of coronal holes, in *Coronal Holes and High Speed Streams*, edited by J. B. Zirker, Colorado Associated Univ. Press., Colorado, 114, 1977.

[129] Jokipii, J. R., Cosmic-ray propagation. I. Charged particles in a random magnetic field, *Astrophys. J.*, *146*, 480-487, 1966.

[130] Jokipii, J. R., Propagation of cosmic rays in the solar wind, *Review of Geophysics and Space Physics*, *9*, 27-35, 1971.

[131] Jokipii, J. R., Particle acceleration at a termination shock. 1 - Application to the solar wind and the anomalous component, *J. Geophys. Res.*, *91*, 2929-2932, 1986.

[132] Jokipii, J. R., The physics of cosmic-ray modulation, *Adv. Space Res.*, *9*(12), 105-119, 1989.

[133] Jokipii, J. R., Latitudinal heliospheric magnetic field: Stochastic and causal components, *J. Geophys. Res.*, *106*(A8), 15841-15848, 2001.

[134] Jokipii, J. R., and J. Giacalone, The theory of anomalous cosmic rays, *Space Science Reviews*, *83*(1/2), 123-136, 1998.

[135] Jokipii, J. R., and D. A. Kopriva, Effects of particle drift on the transport of cosmic rays. III - Numerical models of galactic cosmic-ray modulation, *Astrophys. J.*, *234*, 384-392, 1979.

[136] Jokipii, J. R., and J. Kóta, The polar heliospheric magnetic field, *Geophys. Res. Lett.*, *16*, 1-4, 1989.

[137] Jokipii, J. R., and J. Kóta, On the interpretation of the high cosmic-ray electron fluxes observed in 1986, *Proc. 22nd Inter. Cosmic Ray Conf. (Dublin)*, *3*, 569-572, 1991.

[138] Jokipii, J. R., and J. Kóta, The maximum energy of anomalous cosmic rays, *Proc. 24th Inter. Cosmic Ray Conf. (Rome)*, *4*, 718-721, 1995.

[139] Jokipii, J. R., and J. Kóta, Galactic and anomalous cosmic rays in the heliosphere, *Proc. 25th Inter. Cosmic Ray Conf. (Durban): Invited, Rapporteur & Highlighted Papers*, *8*, 151-155, 1997.

[140] Jokipii, J. R., and F. B. McDonald, Quest for the Limits of the Heliosphere, *Scientific American*, *272*(4/APR), 62-67, 1995.

[141] Jokipii, J. R., and E. N. Parker, On the convection, diffusion and adiabatic deceleration of cosmic rays in the solar wind, *Astrophys. J.*, *160*, 735-744, 1970.

[142] Jokipii, J. R., and B. Thomas, Effects of drift on the transport of cosmic rays. IV - Modulation by a wavy interplanetary current sheet, *Astrophys. J.*, *243*, 1115-1122, 1981.

[143] Jokipii, J. R., E. H. Levy, and W. B. Hubbard, Effects of particle drift on cosmic ray transport. I - General properties, application to solar modulation, *Astrophys. J.*, *213*, 861-868, 1977.

[144] Jokipii, J. R., J. Kóta, and E. Merényi, The gradient of galactic cosmic rays at the solar wind termination shock, *Astrophys. J.*, *405*, 782-786, 1993.

[145] Jokipii, J. R., J. Kóta, J. Giacalone, T. S. Horbury, and E. J. Smith, Interpretation and consequences of large-scale magnetic variances observed at high heliographic latitude, *Geophys. Res. Lett.*, *22*(23), 3385-3388, 1995.

[146] Jones, F. C., and D. C. Ellison, The plasma physics of shock acceleration, *Space Science Reviews*, *58*(3-4), 259-346, 1991.

[147] Kojima, M., H. Washmimi, H. Misawa, and K. Hakamada, Solar wind observed within 0.3 AU with interplanetary scintilation, in *Solar Wind*, edited by E. Marsch, and R. Schwenn, Pergamon Press., New York, 201, 1991.

[148] Kóta, J., Diffusion, drifts and modulation of galactic cosmic rays in the heliopshere, in *Physics of the outer heliosphere*, edited by S. Grzedzielski, and D. E. Page, Pergamon Press., New York, 119, 1990.

[149] Kóta, J., and J. R. Jokipii, Effects of drift on the transport of cosmic rays. VI - A three-dimensional model including diffusion, *Astrophys. J.*, *265*, 573-581, 1983.

[150] Kóta, J., and J. R. Jokipii, The role of corotating interaction regions in cosmic-ray modulation, *Geophys. Res. Lett.*, *18*, 1797-1800, 1991.

[151] Kóta, J., and J. R. Jokipii, Diffusive shock acceleration in the presence of current sheets, *Astrophys. J.*, *429*(1), 385-390, 1994.

[152] Kóta, J., and J. R. Jokipii, 3-D distribution of cosmic rays in the outer heliosphere, *Proc. 24th Inter. Cosmic Ray Conf. (Rome)*, *4*, 680-683, 1995.

[153] Kóta, J., and J. R. Jokipii, 3-D simulation of heliospheric transport: A comparison of models, *Proc. 25th Inter. Cosmic Ray Conf. (Durban)*, *2*, 25-28, 1997.

[154] Kóta, J., and J. R. Jokipii, Modelling of 3-D corotating Cosmic-ray Structures in the Heliosphere, *Space Science Reviews*, *83*(1/2), 137-145, 1998.

[155] Kóta, J., and J. R. Jokipii, Cosmic ray modulation and the structure of the heliospheric magnetic field, *Proc. 26th Inter. Cosmic Ray Conf. (Salt Lake City)*, *7*, 9-12, 1999.

[156] Kóta, J., and J. R. Jokipii, Recurrent depressions of galactic cosmic rays in CIR's: 22-year cycle, *Proc. 27th Inter. Cosmic Ray Conf. (Hamburg)*, *9*, 3577-3580, 2001.

[157] Koyama, K., R. Petre, E. V. Gotthelf, U. Hwang, M. Matsuura, M. Ozaki, and S. S. Holt, Evidence for Shock Acceleration of High-Energy Electrons in the Supernova Remnant SN:1006, *Nature*, *378*(6554/NOV16), 255-258, 1995.

[158] Krainev, M. B., and W. R. Webber, The galactic cosmic rays near the solar activity minimum. II. The model for the behaviour of positive and negative cosmic rays near the current sheet, *Proc. 23rd Inter. Cosmic Ray Conf. (Calgary)*, *3*, 555-558, 1993.

[159] Krieger, A. S., A. F. Timothy, and E. C. Roelof, A Coronal Hole and Its Identification as the Source of a High Velocity Solar Wind Stream, *Solar Physics*, *29*, 505-512, 1973.

[160] Krimigis, S. M., R. B. Decker, E. C. Roelof, and D. Lario, Energetic particle intensity increases at Voyagers 1 and 2 durin 2002-03, *Proc. 28th Inter. Cosmic Ray Conf. (Tsukuba)*, 3769-3772, 2003.

[161] Krymski, G. F., A regular mechanism for the acceleration of charged particles on the front of a shock wave, *Sov. Phys. Dokl.*, *243*, 1306-1312, 1977.

[162] Lagage, P. O., and C. J. Cesarsky, The maximum energy of cosmic rays accelerated by supernova shocks, *Astron. Astrophys.*, *125*(2), 249-257, 1983.

[163] Langner, U. W., Effects of different local interstellar spectra on the heliospheric modulaiton of cosmic rays, M.Sc. dissertation, Potchefstroom University for CHE, South Africa, 2000.

[164] Langner, U. W., and M. S. Potgieter, Differences in proton and anti-proton modulation in the heliosphere, *Proc. 27th Inter. Cosmic Ray Conf. (Hamburg)*, *4*, 3657-3660, 2001a.

[165] Langner, U. W., and M. S. Potgieter, Heliospheric modulation of cosmic rays computed with new local interstellar spectra, *Proc. 27th Inter. Cosmic Ray Conf. (Hamburg)*, *4*, 3686-3689, 2001b.

[166] Langner, U. W., and M. S. Potgieter, Effects of the solar wind termination shock on charge-sign dependent cosmic ray modulation, *Adv. Space Res.*, in press, 2003a.

[167] Langner, U. W., and M. S. Potgieter, Solar wind termination shock and heliosheath effects on the modulation of protons and anti-protons, *J. Geophys. Res.*, *109*(A01103), doi:10.1029/2003JA010158, 2003b.

[168] Langner, U. W., O. C. de Jager, and M. S. Potgieter, Proposed local interstellar spectra for cosmic ray electrons, *Proc. 27th Inter. Cosmic Ray Conf. (Hamburg)*, *4*, 3992-3995, 2001a.

[169] Langner, U. W., O. C. de Jager, and M. S. Potgieter, On the local interstellar spectrum for cosmic ray

electrons, *Adv. Space Res.*, *27*(3), 517-522, 2001b.

[170] Langner, U. W., M. S. Potgieter, and W. R. Webber, Modelling of 'barrier' modulation for cosmic ray protons in the outer heliosphere, *Adv. Space Res.*, in press, 2003a.

[171] Langner, U. W., M. S. Potgieter, and W. R. Webber, Modulation of cosmic ray protons in the heliosheath, *J. Geophys. Res.*, *108*(A10), 8039-8048, doi:10.1029/2003JA009934, 2003b.

[172] Lapidus, L., and G. F. Pinder, *Numerical solution of partial differential equations in science and engineering*, Wiley, New York, 1982.

[173] le Roux, J. A., The solar modulation of galactic cosmic rays as described by a time-dependent drift model, Ph.D. thesis, Potchefstroom University for CHE, South Africa, 1990.

[174] le Roux, J. A., and H. Fichtner, A self consistent determination of the heliospheric termination shock structure in the presence of pickup, anomalous, and galactic cosmic ray protons, *J. Geophys. Res.*, *102*(A8), 17365-17380, 1997.

[175] le Roux, J. A., and H. Fichtner, The simulation of step decreases in the cosmic ray intensity with a cosmic-ray-hydrodynamic model, *Adv. Space Res.*, *23*(3), 501-504, 1999.

[176] le Roux, J. A., and M. S. Potgieter, The simulation of complete 11 and 22 year modulation cycles for cosmic rays in the heliosphere using a drift model with global merged interaction regions, *Astrophys. J.*, *442*(2), 847-851, 1995.

[177] le Roux, J. A., M. S. Potgieter, and V. S. Ptuskin, A transport model for the diffusive acceleration and modulation of anomalous cosmic rays in the heliosphere, *J. Geophys. Res.*, *101*(A3), 4791-4804, 1996.

[178] Levy, E. H., The interplanetary magnetic field structure, *Nature*, *261*, 394-395, 1976.

[179] Linde, T. J., T. I. Gombosi, P. L. Roe, K. G. Powell, and D. L. Dezeeuw, Heliosphere in the magnetized local interstellar medium - Results of a three-dimensional MHD simulation, *J. Geophys. Res.*, *103*(A2), 1889-1904, 1998.

[180] Lockwood, J. A., and W. R. Webber, An estimate of the location of the modulation boundary for E greater than 70 MeV galactic cosmic rays using Voyager and Pioneer spacecraft data, *Astrophys. J.*, *442*(2), 852-860, 1995.

[181] Longair, M. S., Cosmic rays and the Galactic radio background emission, in *Low Frequency Astrophysics from Space*, Springer-Verlag, 227, 1990.

[182] Lopate, C., Jovian and galactic electrons (2-30 GeV) in the heliosphere from 1 to 50 AU, *Proc. 23rd Inter. Cosmic Ray Conf. (Calgary)*, *3*, 415-418, 1991.

[183] Lopate, C., Pioneer-10 measurements of relativistic electrons in the outer heliosphere, *J. Geophys. Res.*, submitted, 2001.

[184] Marsch, E., Kinetic physics of the solar wind plasma, in *Physics of the Inner Heliosphere*, edited by R. Schwenn and E. Marsch, Springer-Verlag, Berlin, 45, 1991.

[185] Marsch, E., W. I. Axford, and J. F. McKenzie, Solar wind, in *Dynamic Sun*, edited by B. N. Dwivedi, Cambridge University Press., Cambridge, 374, 2003.

[186] Marsden, R. G., The intrepid heliospheric explorer, *Physics World*, *6*(11), 36-40, 1993.

[187] Marsden, R.G. (Ed.), The High Latitude Heliosphere, *Space Science Reviews*, *72*(1/2), 1995.

[188] Marsden, R.G. (Ed.), The 3-D Heliosphere at Solar Maximum, *Space Science Reviews*, *97*(1-4), 2001.

[189] McComas, D. J., Ulysses observations of the three-dimensional solar wind over the solar cycle and their implications for the outer heliosphere, *EOS*, *81*, F983, 2000.

[190] McDonald, F. B., Cosmic-Ray Modulation in the Heliosphere A Phenomenological Study, *Space Science Reviews*, *83*(1/2), 33-50, 1998.

[191] McDonald, F. B., T. L. Cline, and G. M. Simnett, Multifarious temporal variations of low-energy relativistic

cosmic ray electrons, *J. Geophys. Res.*, *77*, 2213-2231, 1972.

[192] McDonald, F. B., B. J. Teegarden, J. H. Trainor, and W. R. Webber, The Anomalous Abundance of Cosmic-Ray Nitrogen and Oxygen Nuclei at Low Energies, *Astrophys. J.*, *187*, L105-L108, 1974.

[193] McDonald, F. B., H. Moraal, J. P. L. Reinecke, N. Lal, and R. E. McGuire, The cosmic radiation in the heliosphere at successive solar minima, *J. Geophys. Res.*, *97*, 1557-1570, 1992.

[194] McDonald, F. B., N. Lal, and R. E. McGuire, Cosmic ray recovery and solar minimum phase of solar cycle 22 - An interim report, *J. Geophys. Res.*, *103*(A1), 373-380, 1998.

[195] McDonald, F. B., B. Heikkila, N. Lal, and E. C. Stone, The relative recovery of galactic and anomalous cosmic rays in the distant heliosphere: Evidence for modulation in the heliosheath, *J. Geophys. Res.*, *105*(A1), 1-8, 2000.

[196] McDonald, F. B., B. Klecker, R. E. McGuire, and D. V. Reames, Relative recovery of galactic and anomalous cosmic rays at 1 AU: Further evidence for modulation in the heliosheath, *J. Geophys. Res.*, *107*(A8), SSH 2-1-SSH 2-9, doi:10.1029/2001JA000206, 2002.

[197] McKibben, R.B., Reanalysis and confirmation of positive latitude gradients for anomalous helium and Galactic cosmic rays measured in 1975-1976 with Pioneer II, *J. Geophys. Res.*, *94*, 17021-17033, 1989.

[198] Menn, W., M. Hof, O. Reimer, M. Simon, A. J. Davis, A. W. Labrador, R. A. Mewaldt, S. M. Schindler, L. M. Barbier, E. R. Christian, K. E. Krombel, J. F. Krizmanic, J. W. Mitchell, J. F. Ormes, R. E. Streitmatter, R. L. Golden, S. J. Stochaj, W. R. Webber, and I. L. Rasmussen, The absolote flux of protons and helium at the top of the atmosphere using IMAX, *Astrophys. J.*, *533*(1), 281-297, 2000.

[199] Mewaldt, R. A., R. S. Selesnick, J. R. Cummings, E. C. Stone, and T. T. von Rosenvinge, Evidence for Multiply Charged Anomalous Cosmic Rays, *Astrophys. J.*, *466*, L43-L46, 1996.

[200] Minnie, J., Observational constraints on the heliospheric diffusion tensor for galactic cosmic rays, M.Sc. dissertation, Potchefstroom University for CHE, South Africa, 2002.

[201] Möbius, E., Pick-up of interstellar neutrals by the solar wind, *Adv. Space Res.*, *6*(1), 199-208, 1986.

[202] Möbius, E., D. Hovestadt, B. Klecker, M. Scholer, and G. Gloeckler, Direct observation of He(+) pick-up ions of interstellar origin in the solar wind, *Nature*, *318*, 426-429, 1985.

[203] Moraal, H., Proton modulation near solar minimum periods in consequtive solar cycles, *Proc. 21st Inter. Cosmic Ray Conf. (Adelaide)*, *6*, 140-143, 1990.

[204] Moraal, H., and W. I. Axford, Cosmic ray acceleration in supernova blast waves, *Astron. Astrophys.*, *125*(2), 204-216, 1983.

[205] Moraal, H., and L. J. Gleeson, Three-dimensional models of galactic cosmic ray modulation, *Proc. 14th Inter. Cosmic Ray Conf. (Munich)*, *12*, 4189-4192, 1975.

[206] Moraal, H., L. J. Gleeson, and G. M. Webb, Effects of charged particle drifts on the modulation of the intensity of galactic cosmic rays, *Proc. 16th Inter. Cosmic Ray Conf. (Kyoto)*, *3*, 1-4, 1979.

[207] Moraal, H., J. R. Jokipii, and R. A. Mewaldt, Heliospheric effects on cosmic-ray electrons, *Astrophys. J.*, *367*, 191-199, 1991.

[208] Moses, D., Jovian electrons at 1 AU - 1978-1984, *Astrophys. J.*, *313*, 471-486, 1987.

[209] Moskalenko, I. V., and A. W. Strong, Production and propagation of cosmic-ray positrons and electrons, *Astrophys. J.*, *493*, 694-707, 1998.

[210] Moskalenko, I. V., A. W. Strong, J. F. Ormes, M. S. Potgieter, and U. W. Langner, Secondary antiprotons in cosmic rays, *Proc. 27th Inter. Cosmic Ray Conf. (Hamburg)*, *4*, 1868-1871, 2001.

[211] Moskalenko, I. V., A. W. Strong, J. F. Ormes, and M. S. Potgieter, Secondary antiprotons and propagation of cosmic rays in the galaxy and heliosphere, *Astrophys. J.*, *565*, 280-296, 2002.

[212] Moskalenko, I. V., A. W. Strong, S. G. Mashnik, and J. F. Ormes, Challenging cosmic-ray propagation with antiprotons: Evidence for a "fresh" nuclei component?, *Astrophys. J.*, *586*, 1050-1066, 2003.

[213] Myasnikov, A. V., V. V. Izmodenov, D. B. Alexashov, and S. V. Chalov, Self-consistent model of the solar wind interaction with two-component circumsolar interstellar cloud: Mutual influence of thermal plasma and galactic cosmic rays, *J. Geophys. Res.*, *105*(A3), 5179-5188, 2000.

[214] Odstrcil, D., Modeling 3-D solar wind structure, *Adv. Space Res.*, *32*(4), 497-506, 2003.

[215] Palmer, I. D., Transport coefficients of low-energy cosmic rays in interplanetary space, *Reviews of Geophysics and Space Physics*, *20*, 335-351, 1982.

[216] Parhi, S., R. A. Burger, J. W. Bieber, and W. H. Matthaeus, Challenges for an ab initio theory of cosmic ray modulation, *AGU Spring Meet.*, Abstract SH22F-06, 2001.

[217] Parhi, S., J. W. Bieber, W. H. Matthaeus, and R. A. Burger, Improved Representation of Heliospheric Magnetic Field Fluctuations in Ab Initio Models of Cosmic Ray Modulation, *AGU Fall Meet.*, Abstract SH11A-0380, 2002.

[218] Parhi, S., J. W. Bieber, W. H. Matthaeus, and R. A. Burger, Toward an Ab Initio Theory of the Solar Modulation of Cosmic Rays, *Astrophys. J.*, *585*(1), 502-515, 2003.

[219] Parker, E. N., Cosmic ray modulation by the solar wind, *Physical Reviews*, *110*, 1445, 1958.

[220] Parker, E. N., Sudden expansion of the corona following a large solar flare and the attendant magnetic field and cosmic-ray effects, *Astrophys. J.*, *133*, 1014, 1961.

[221] Parker, E. N., *Interplanetary dynamical processes*, Interscience, New York, 1963.

[222] Parker, E. N., The passage of energetic charged particles through interplanetary space, *Planetary and Space Science*, *13*, 9, 1965.

[223] Pauls, H. L., and G. P. Zank, Interaction of a nonuniform solar wind with the local interstellar medium, *J. Geophys. Res.*, *101*(A8), 17081-17092, 1996.

[224] Pauls, H. L., and G. P. Zank, Interaction of a nonuniform solar wind with the local interstellar medium 2. A two-fluid model, *J. Geophys. Res.*, *102*(A9), 19779-19788, 1997.

[225] Pauls, H. L., G. P. Zank, and L. L. Williams, Interaction of the solar wind with the local interstellar medium, *J. Geophys. Res.*, *100*(A11), 21595-21604, 1995.

[226] Perko, J. S., and L. A. Fisk, Solar modulation of galactic cosmic rays. V - Time-dependent modulation, *J. Geophys. Res.*, *88*, 9033-9036, 1983.

[227] Pesses, M. E., J. R. Jokipii, and D. Eichler, Cosmic ray drift, shock wave acceleration and the anomalous component of cosmic rays, *Astrophys. J.*, *246*, L85-L88, 1981.

[228] Peterson, J. D., P. R. Higbie, J. M. Rockstroh, and W. R. Webber, A New look at galactic polar radio emission and the local interstellar electron spectrum, *Proc. 26th Inter. Cosmic Ray Conf. (Salt Lake City)*, *4*, 251-254, 1999.

[229] Phillips, J. L., A. Balogh, S. J. Bame, B. E. Goldstein, J. T. Gosling, J. T. Hoeksema, D. J. McComas, M. Neugebauer, N. R. Sheeley, and Y. M. Wang, Ulysses at 50° south: constant immersion in the high-speed solar wind, *Geophys. Res. Lett.*, *21*(12), 1105-1108, 1994.

[230] Phillips, J. L., S. J. Bame, A. Barnes, B. L. Barraclough, W. C. Feldman, B. E. Goldstein, J. T. Gosling, G. W. Hoogeveen, D. J. McComas, M. Neugebauer, and S. T. Suess, Ulysses solar wind plasma observations from pole to pole, *Geophys. Res. Lett.*, *22*(23), 3301-3304, 1995.

[231] Potgieter, M. S., The modulation of galactic cosmic rays as described by a three-dimensional drift model, Ph.D thesis, Potchefstroom University for CHE, South Africa, 1984.

[232] Potgieter, M. S., Heliospheric terminal shock acceleration and modulation of the anomalous cosmic-ray component, *Adv. Space Res.*, *9*(12), 21-24, 1989.

[233] Potgieter, M. S., Heliospheric modulation of galactic electrons: Consequences of new calculations for the mean free path of electrons between 1 MeV and ~10 GeV, *J. Geophys. Res.*, *101*(A11), 24411-24422, 1996.

[234] Potgieter, M. S., Implications of enhanced perpendicular diffusion in the heliosphereric modulation of cosmic

rays, *Proc. 25th Inter. Cosmic Ray Conf. (Durban)*, *2*, 1-4, 1997.

[235] Potgieter, M. S., The modulation of galactic cosmic rays in the heliosphere: Theory and models, *Space Science Reviews*, *83*(1/2), 147-158, 1998.

[236] Potgieter, M. S., The heliospheric modulaiton of cosmic ray protons: The role of enhanced perpendicular diffusion during periods of minimum solar modulation, *J. Geophys. Res.*, *105*(A8), 18295-18304, 2000.

[237] Potgieter, M. S., and R. A. Burger, The modulation of cosmic-ray electrons, positrons and helium nuclei as predicted by a drift model with a simulated wavy neutral sheet, *Astron. Astrophys.*, *233*(2), 598-604, 1990.

[238] Potgieter, M. S., and S. E. S. Ferreira, The importance of perpendicular diffusion in the heliospheric modulation of cosmic ray electrons, *Adv. Space Res.*, *23*(3), 463-466, 1999a.

[239] Potgieter, M. S., and S. E. S. Ferreira, Implications of cosmic ray electron observations on the modeling of electron modulation in the heliopshere, *Proc. 26th Inter. Cosmic Ray conf. (Salt Lake City)*, *7*, 21-24, 1999b.

[240] Potgieter, M. S., and L. J. Haasbroek, The simulation of base-line cosmic ray modulation for the Ulysses trajectory, *Proc. 23rd Inter. Cosmic Ray Conf. (Calgary)*, *3*, 457-460, 1993.

[241] Potgieter, M.S., and U. W. Langner, Modulation of anomalous protons with increasing solar activity, *Adv. Space Res.*, *32*(4), 687-692, doi:10.1016/S0273-1177(03)00359-4, 2003a.

[242] Potgieter, M.S. and U. W. Langner, Modulation and acceleration of anomalous protons in the outer heliopshere, *Adv. Space Res.*, in press, 2003b

[243] Potgieter, M. S., and U. W. Langner, Heliospheric modulation of cosmic ray positrons and electrons: Effects of the heliosheath and the solar wind termination shock, *Astrophys. J.*, *602*, 993-1001, 2003c.

[244] Potgieter M. S., and J. A. le Roux, A numerical model for a cosmic-ray modulation barrier in the outer heliosphere, *Astron. Astrophys.*, *209*, 406-410, 1989a.

[245] Potgieter M. S., and J. A. le Roux, More on a possible modulation barrier in the outer heliosphere, *Adv. Space Res.*, *9*(4), 121-124, 1989b.

[246] Potgieter, M. S., and J. A. le Roux, The long-term heliospheric modulation of galactic cosmic rays according to a time-dependent drift model with merged interaction regions, *Astrophys. J.*, *423*, 817-827, 1994.

[247] Potgieter, M. S., and H. Moraal, A drift model for the modulation of galactic cosmic rays, *Astrophys. J.*, *294*, 425-440, 1985.

[248] Potgieter, M. S., and H. Moraal, Acceleration of cosmic rays in the solar wind termination shock. I - A steady state technique in a spherically symmetric model, *Astrophys. J.*, *330*, 445-455, 1988.

[249] Potgieter, M. S., J. A. le Roux, and R. A. Burger, Interplanetary cosmic ray radial gradients with steady state modulation models, *J. Geophys. Res.*, *94*, 2323-2332, 1989.

[250] Potgieter, M. S., L. J. Haasbroek, P. Ferrando, and B. Heber, The modeling of the latitude dependence of cosmic rays protons and electrons in the inner heliosphere,*Adv. Space Res.*, *19*(6), 917-920, 1997.

[251] Potgieter, M. S., S. E. S. Ferreira, and B. Heber, The heliospheric modulation of cosmic ray electrons: Rigidity dependence of the perpendicular diffuion coefficient, *Proc. 26th Inter. Cosmic Ray conf. (Salt Lake City)*, *7*, 57-60, 1999a.

[252] Potgieter, M. S., S. E. S. Ferreira, B. Heber, P. Ferrando, and A. Raviart, Implications of the heliospheric modulation of cosmic ray electrons observed by Ulysses, *Adv. Space Res.*, *23*(3), 467-470, 1999b.

[253] Potgieter, M. S., U. W. Langner, and S. E. S. Ferreira, New cosmic ray electron to positron ratios in the heliosphere, *Proc. 27th Inter. Cosmic Ray Conf. (Hamburg)*, *4*, 3690-3693, 2001a.

[254] Potgieter, M. S., U. W. Langner, and S. E. S. Ferreira, Cosmic ray electron to positron ratios in the heliosphere, *Adv. Space Res.*, *27*(3), 523-528, 2001b.

[255] Potgieter, M. S., R. A. Burger, and S. E. S. Ferreira, Modulation of Cosmic Rays in the Heliosphere From Solar Minimum to Maximum: a Theoretical Perspective, *Space Science Reviews*, *97*(1/4), 295-307, 2001c.

[256] Quenby, J. J., J. A. Lockwood, and W. R. Webber, Cosmic ray gradient measurements and modulation beyond the inner solar wind termination shock, *Astrophys. J.*, *365*, 365-371, 1990.

[257] Rastoin, C., Jovian and galactic electrons in the heliosphere: Observations of the KET experiment on board the Ulysses spacecraft, Ph.D. thesis, University of Paris VII, France, 1995.

[258] Ratkiewicz, R., and L. Ben-Jaffel, Effects of interstellar magnetic field B and constant flux of neutral H on the heliosphere, *J. Geophys. Res.*, *107*(A1), SSH 2-1-SSH 2-13, doi:10.1029/2001ja000092, 2002.

[259] Reinecke, J. P. L., and H. Moraal, On the form of the 1987 hydrogen spectrum in the outer heliosphere, *Astrophys. J.*, *392*, 272-276, 1992.

[260] Reinecke, J. P. L., H. Moraal, and F. B. McDonald, The cosmic radiation in the heliosphere at successive solar minima - Steady state no-drift solutions of the transport equation, *J. Geophys. Res.*, *98*(A6), 9417-9431, 1993.

[261] Reinecke, J. P. L., H. Moraal, M. S. Potgieter, F. B. McDonald and W. R. Webber, Different Crossovers?, *Proc. 25th Inter. Cosmic Ray Conf. (Durban)*, *2*, 49-52, 1997.

[262] Rice, W. K. M., and G. P. Zank, Shock propagation in the outer heliosphere 3. Pickup ions, MHD, cosmic rays, and energetic particles, *J. Geophys. Res.*, *105*(A3), 5157-5166, 2000.

[263] Richardson, J. D., C. Wang, and K. I. Paularena, The solar wind: From solar minimum to solar maximum, *Adv. Space Res.*, *27*(3), 471-479, 2001.

[264] Scherer, K., and H. J. Fahr, Solar cycle induced variations of the outer heliospheric structures, *Geophys. Res. Lett.*, *30*(2), 17-1 - 17-4, doi:10.1029/2002GL016073, 2003.

[265] Schlickeiser, R., On the interplanetary transport of solar cosmic rays, *J. Geophys. Res.*, *93*, 2725-2729, 1988.

[266] Schulz, M., Interplanetary sector structure and the heliomagnetic equator, *Astrophysics and Space Science*, *24*, 371, 1973.

[267] Schwenn, R., The average solar wind in the inner heliosphere: Structures and slow variations, in *Solar Wind Five*, edited by M. Neugebauer, NASA CP-2280, 489, 1983.

[268] Shalchi, A., Transport geladener Teilchen in der anisotropen Turbulenz, Ph.D. Thesis, Ruhr-Universität Bochum, 2003.

[269] Sheeley, N. R., Y. M. Wang, S. H. Hawley, G. E. Brueckner, K. P. Dere, R. A. Howard, M. J. Koomen, C. M. Korendyke, D. J. Michels, S. E. Paswaters, D. G. Socker, O. C. St. Cyr, D. Wang, P. L. Lamy, A. Llebaria, R. Schwenn, G. M. Simnett, S. Plunkett, and D. A. Biesecker, Measurements of Flow Speeds in the Corona between 2 and 30 R sub sun, *Astrophys. J.*, *484*, 472-478, 1997.

[270] Siluszyk, M., and M. V. Alania, On the internal boundary condition problem for the Parker's transport equation of galactic cosmic rays, *Proc. 27th Inter. Cosmic Ray Conf. (Hamburg)*, *9*, 3722-3725, 2001.

[271] Simpson, J. A., Cosmic radiation: Particle astrophysics in the heliosphere, in *Frontiers in cosmic physics: Symposium in memory of Serge Korff*, edited by R. B. Mendell, and A. J. Mincer, New York Academy of Sciences, New York, 97, 1992.

[272] Simpson, J. A., The cosmic radiation: Reviewing the present and future, *Proc. 25th Inter. Cosmic Ray Conf. (Durban): Invited, Rapporteur & Highlighted Papers*, 4-8, 1997.

[273] Simpson, J. A., D. Hamilton, G. Lentz, R. B. McKibben, A. Mogro-Campero, M. Perkins, K. R. Pyle, A. J. Tuzzolino, and J. J. O'Gallagher, Protons and electrons in Jupiter's magnetic field: Results from the university of Chigago experiment on Pioneer 10, *Science*, *183*(4122), 306-309, 1974.

[274] Simpson, J. A., D. Hamilton, G. Lentz, R. B. McKibben, M. Perkins, K. R. Pyle, A. J. Tuzzolino, and J. J. O'Gallagher, Jupiter revisited - First results from the University of Chicago charged particle experiment on Pioneer 11, *Science*, *188*, 455-459, 1975.

[275] Simpson, J. A., J. D. Anglin, A. Balogh, J. R. Burrows, S. W. H. Cowley, P. Ferrando, B. Heber, R. J. Hynds, H. Kunow, and R. G. Marsden, Energetic charged-particle phenomena in the Jovian magnetosphere - First results from the ULYSSES COSPIN collaboration, *Science*, *257*(5076), 1543-1550, 1992a.

[276] Simpson, J. A., J. D. Anglin, A. Balogh, M. Bercovitch, J. M. Bouman, E. E. Budzinski, J. R. Burrows, R. Carvell, J. J. Connell, R. Ducros, P. Ferrando, J. Firth, M. Garcia-Munoz, J. Henrion, R. J. Hynds, B. Iwers, R. Jacquet, H. Kunow, G. Lentz, R. G. Marsden, R. B. Mckibben, R. Meuller-Mellin, D. E. Page, M. Perkins, A. Raviart, T. R. Sanderson, H. Sierks, L. Treguer, A. J. Tuzzolino, K. P. Wenzel, and G. Wibberenz, The ULYSSES Cosmic Ray and Solar Particle Investigation, *Astron. Astrophys. Supp. Series*, *92*(2), 365-399, 1992b.

[277] Smith, C. W., and J. W. Bieber, Solar cycle variation of the interplanetary magnetic field spiral, *Astrophys. J.*, *370*, 435-441, 1991.

[278] Smith, C. W., W. H. Matthaeus, G. P. Zank, N. F. Ness, S. Oughton, and J. D. Richardson, Heating of the low-latitude solar wind by dissipation of turbulent magnetic fluctuations, *J. Geophys. Res.*, *106*(A5), 8253-8272, 2001.

[279] Smith, E. J., Interplanetary magnetic field over two solar cycles and out to 20 AU, *Adv. Space Res.*, *9*(4), 159-164, 1989.

[280] Smith, E. J., Magnetic fields in the heliosphere - Pioneer observations, in *Physics of the outer heliosphere*, Pergamon Press., Oxford, England and Elmsford, New York, 253, 1990.

[281] Smith, E. J., The Sun, solar wind and magnetic field. I, in *Proceedings of the International School of Physics "Enrico Fermi" Course CXLII*, edited by B. Coppi, A. Ferrari, and E. Sindoni, IOS Press., Amsterdam, 179, 2000.

[282] Smith, E. J., The heliospheric current sheet, *J. Geophys. Res.*, *106*(A8), 15819-15832, 2001.

[283] Smith, E. J., and R. G. Marsden, Ulysses Observations at Solar Maximum: Introduction, *Geophys. Res. Lett.*, *30*(19), ULY 1-1-ULY 1-3, doi:10.1029/2003GL018223, 2003.

[284] Snodgrass, H. B., Magnetic rotation of the solar photosphere, *Astrophys. J.*, *270*, 288-299, 1983.

[285] Stawicki, O., On magnetic fluctuations in the solar wind and their influence on the transport of charged particles, Ph.D. Thesis, Ruhr-Universität Bochum, 2003.

[286] Steenberg, C. D., Modelling of anomalous and galactic cosmic ray modulation in the outer heliosphere, Ph.D thesis, Potchefstroom University for CHE, South Africa, 1998.

[287] Steenberg, C. D., and H. Moraal, An Acceleration/Modulation Model for Anomalous Cosmic-Ray Hydrogen in the Heliosphere, *Astrophys. J.*, *463*, 776-783, 1996.

[288] Steenberg, C. D., H. Moraal, and F. B. McDonald, Modulation of the anomalous and galactic components of cosmic ray H and He as described by a full-drift two-dimensional acceleration model, in *Cosmic Rays in the heliosphere*, *Space Science Reviews*, *83*, 269-275, 1998.

[289] Steenkamp, R., Shock acceleration as source of the anomalous component of cosmic rays in the heliosphere, Ph.D thesis, Potchefstroom University for CHE, South Africa, 1995.

[290] Steenkamp, R., and H. Moraal, Acceleration and modulation of anomalous helium and oxygen in 1977 and 1987, *Proc. 23th Inter. Cosmic Ray Conf. (Calgary)*, *3*, 539-542, 1993.

[291] Stone, E. C., and A. C. Cummings, A tilt model for anomalous cosmic rays and the location of the solar wind termination shock, *Proc. 26th Inter. Cosmic Ray Conf. (Salt Lake City)*, *7*, 500-503, 1999.

[292] Stone, E. C., and A. C. Cummings, Estimate of the location of the solar wind termination shock, *Proc. 27th Inter. Cosmic Ray Conf. (Hamburg)*, *10*, 4263-4266, 2001.

[293] Stone, E. C., and A. C. Cummings, The approach of Voyager 1 to the termination shock, *Proc. 28th Inter. Cosmic Ray Conf. (Tsukuba)*, 3889-3992, 2003.

[294] Stone, E. C., A. C. Cummings, and W. R. Webber, The distance to the solar wind termination shock in 1993 and 1994 from observations of anomalous cosmic rays, *J. Geophys. Res.*, *101*(A5), 11017-11026, 1996.

[295] Strong, A. W., and I. V. Moskalenko, New constraints on galactic cosmic-ray propagation, *10th European Cosmic Ray Symposium*, OG 2.3, 1998.

[296] Strong, A. W., K. Bennett, H. Bloemen, R. Diehl, W. Hermsen, D. Morris, V. Schoenfelder, J. G. Stacy,

C. de Vries, M. Varendorff, C. Winkler, and G. Youssefi, Diffuse continuum gamma rays from the galaxy observed by COMPTEL, *Astron. Astrophys.*, *292*(1), 82-91, 1994.

[297] Strong, A. W., I. W. Moskalenko, and O. Reimer, Diffuse continuum gamma rays from the galaxy, *Astrophys. J.*, *537*(2), 763-784, 2000.

[298] Suess, S. T., The heliopause, *Reviews of Geophysics*, *28*, 97-115, 1990.

[299] Suess, S.T., Temporal variations in the termination shock distance, *J. Geophys. Res.*, *98*(A9), 15147-15155, 1993.

[300] Tanimori, T., Y. Hayami, S. Kamei, S. A. Dazeley, P. G. Edwards, S. Gunji, S. Hara, T. Hara, J. Holder, A. Kawachi, T. Kifune, R. Kita, T. Konishi, A. Masaike, Y. Matsubara, T. Matsuoka, Y. Mizumoto, M. Mori, M. Moriya, H. Muraishi, Y. Muraki, T. Naito, K. Nishijima, S. Oda, S. Ogio, J. R. Patterson, M. D. Roberts, G. P. Rowell, K. Sakurazawa, T. Sako, Y. Sato, R. Susukita, A. Suzuki, R. Suzuki, T. Tamura, G. J. Thornton, S. Yanagita, T. Yoshida, and T. Yoshikoshi, Discovery of TeV Gamma Rays from SN 1006: Further Evidence for the Supernova Remnant Origin of Cosmic Rays, *Astrophys. J.*, *497*, L25-L28, 1998.

[301] Teegarden, B. J., F. B. McDonald, J. H. Trainor, W. R. Webber, and E. C. Roelof, Interplanetary MeV electrons of jovian origin, *J. Geophys. Res.*, *79*, 3615-3622, 1974.

[302] Teufel, A., and R. Schlickeiser, Analytic caculation of the parallel mean free path of interplanetary cosmic rays I. Dynamical magnetic slab turbulence and random sweeping model, *Astron. Astrophys.*, *393*, 703-715, 2002.

[303] Teufel, A., and R. Schlickeiser, Analytic caculation of the parallel mean free path of heliospheric cosmic rays II. Dynamical magnetic slab turbulence and random sweeping slab turbulence with finite wave power at small wavenumbers, *Astron. Astrophys.*, *397*, 15-25, 2003.

[304] Teufel, A., I. Lerche, and R. Schlickeiser, Cosmic ray transport in anisotropic magnetohydrodynamic turbulence II. Shear Alfvén waves, *Astron. Astrophys.*, *397*, 777-788, 2003.

[305] Thomas, B. T., and E. J. Smith, The structure and dynamics of the heliospheric current sheet, *J. Geophys. Res.*, *86*, 11105-11110, 1981.

[306] Van Niekerk, Y., An investigation into the causes and consequences of north-south asymmetries in the helioshere, M.Sc. dissertation, Potchefstroom University for CHE, South Africa, 2000.

[307] Von Rosenvinge, T. T., and F. B. McDonald, IMP 6, 7 and 8 observations of the composition and time variations of low energy cosmic rays, *Proc. 14th Inter. Cosmic Ray Conf.(Munich)*, *2*, 92-97, 1975.

[308] Wang, Y. M., and N. R. Sheeley, Solar implications of Ulysses interplanetary field measurements, *Astrophys. J.*, *447*, L143-L146, 1995.

[309] Washimi, H., and T. Tanaka, MHD structure of the heliosphere and its response to the 11-year solar cycle variations, *Adv. Space Res.*, *23*(3), 551-560, 1999.

[310] Webber, W. R., Cosmic ray proton and helium spectra from 5-200 GV measured with a magnetic spectrometer, *Proc. 21th Inter. Cosmic Ray Conf.(Moscow)*, *1*, 325-328, 1987.

[311] Webber, W. R., and J. A. Lockwood, Interplanetary radial cosmic ray gradients and their implication for a possible large modulation effect at the heliospheric boundary, *Astrophys. J.*, *317*, 534-542, 1987.

[312] Webber, W. R., and J. A. Lockwood, Intensity variations of >70 MeV cosmic rays measured by Pioneer 10, Voyager 1 and 2 and IMP in the heliosphere during the recovery period from 1992-1995, *Geophys. Res. Lett.*, *22*(19), 2669-2672, 1995.

[313] Webber, W. R., and J. A. Lockwood, Intensities of anomalous and galactic cosmic rays in the outer heliosphere near the heliospheric equator in 1987 and during the period from 1994 to 1996, *J. Geophys. Res.*, *102*, 9773-9780, 1997.

[314] Webber, W. R., and J. A. Lockwood, The inner heliosphere – outer heliosphere comparison for cosmic ray modulation, *Space Science Reviews*, *83*(1/2), 159-167, 1998.

[315] Webber, W. R., and J. A. Lockwood, Voyager and Pioneer spacecraft measurements of cosmic ray intensities in

the outer heliosphere: Toward a new paradigm for understanding the global modulation process: 1. Minimum solar modulation (1987 and 1997), *J. Geophys. Res.*, *106*(A12), 29323-29332, 2001a.

[316] Webber, W. R., and J. A. Lockwood, Voyager and Pioneer spacecraft measurements of cosmic ray intensities in the outer heliosphere: Toward a new paradigm for understanding the global modulation process: 2. Maximum solar modulation (1990-1991), *J. Geophys. Res.*, *106*(A12), 29333-29340, 2001b.

[317] Webber, W. R., J. A. Lockwood, F. B. McDonald, and B. Heikkila, Using transient decreases of cosmic rays observed at Voyagers 1 and 2 to estimate the location of the heliospheric termination shock, *J. Geophys. Res.*, *106*(A1), 253-260, 2001.

[318] Wenzel, K. P., Ulysses - it's status and prospects, *Adv. Space Res.*, *13*(6), 275-280, 1993.

[319] Whang, Y. C., and L. F. Burlaga, Anticipated Voyager crossing of the termination shock, *Geophys. Res. Lett.*, *27*(11), 1607-1610, 2000.

[320] Whang, Y. C., L. F. Burlaga, and N. F. Ness, Locations of the termination shock and the heliopause, *J. Geophys. Res.*, *100*(A9), 17015-17024, 1995.

[321] Wilcox, J. M., and N. F. Ness, Quasi-Stationary Corotating Structure in the Interplanetary Medium, *J. Geophys. Res.*, *70*, 5793-5805, 1965.

[322] Williams, T., The influence of the wavy heliospheric neutral sheet on the modulation of cosmic rays (in Afrikaans), M.Sc. dissertation, Potchefstroom University for CHE, South Africa, 1990.

[323] Williams, T., and M. S. Potgieter, The length of the wavy heliospheric neutral sheet as a modulation parameter, *Proc. 22nd Inter. Cosmic Ray Conf. (Dublin)*, *3*, 545-548, 1991.

[324] Withroe, G. L., W. C. Feldman, and H. S. Ahluwalia, The solar wind and its coronal origins, in *Solar interior and atmosphere*, edited by A. N. Cox, W. C. Livingstone, and M. S. Mathews, University of Arizona Press., Tucson, 1087, 1992.

[325] Yamada, Y., S. Yanagita, and T. Yoshida, A stochastic simulation method for the solar cycle modulation of cosmic rays, *Adv. Space Res.*, *23*(3), 505-508, 1999.

[326] Zank, G. P., Interaction of the solar wind with the local interstellar medium: A theoretical perspective, *Space Science Reviews*, *89*(3/4), 413-688, 1999.

[327] Zank, G. P., and H. R. Müller, The dynamical heliosphere, *J. Geophys. Res.*, *108*(A6), SSH 7-1-SSH 7-15, doi:10.1029/2002JA009689, 2003.

[328] Zank, G. P., I. H. Cairns, D. J. Donohue, and W. H. Matthaeus, Radio emissions and the heliospheric termination shock, *J. Geophys. Res.*, *99*(A8), 14729-14735, 1994.

[329] Zank, G. P., W. H. Matthaeus, and C.W. Smith, Evolution of turbulent magnetic fluctuation power with heliospheric distance, *J. Geophys. Res.*, *101*(A8), 17093-17108, 1996.

[330] Zank, G. P., W. H. Matthaeus, J. W. Bieber, and H. Moraal, The radial and latitudinal dependence of the cosmic ray diffusion tensor in the heliosphere, *J. Geophys. Res.*, *103*(A2), 2085-2098, 1998.

[331] Zank, G. P., W. K. M. Rice, I. H. Cairns, J. W. Bieber, R. M. Skoug, and C. W. Smith, Predicted timing for the turn-on of radiation in the outer heliosphere due to the Bastille Day shock, *J. Geophys. Res.*, *106*(A12), 29363-29372, 2001.

[332] Zhang, M., A path integral solution to the stochastic differential equation of the Markov process for cosmic ray transport, *Proc. 26th Inter. Cosmic Ray Conf. (Salt Lake City)*, *7*, 1-4, 1999.

[333] Zirker, J. B., Coronal holes: An overview, in *Coronal Holes and High Speed Wind Streams*, edited by J. B. Zirker, Colorado Associated Univ. Press., Colorado, 1, 1977.

[334] Zurbuchen, T. H., N. A. Schwadron, and L. A. Fisk, Direct observational evidence for a heliospheric magnetic field with large excursions in latitude, *J. Geophys. Res.*, *102*(A11), 24175-24182, 1997.

[335] Zwillinger, D., *Handbook of differential equations*, Academic Press., San Diego, 1989.

Acknowledgements

I wish to use this opportunity to express my gratitude to, and acknowledge several people and institutions who have aided me in different ways to let this thesis materialise. They are in no particular order:

- Our Heavenly Father, to whom I am eternally grateful for His grace to have allowed me to complete this work, and to study a small portion of his magnificent universe.
- Prof. Marius Potgieter, my supervisor, for his guidance, motivation and assistance with this work, and for the long hours he has spent poring over my work despite his busy schedule. I would also like to thank him for the opportunity he has given me to lecture during my final year.
- Prof. Adri Burger, Prof. Harm Moraal, and Dr. Stefan Ferreira for their insight, useful discussions and assistance on various occasions.
- Ms. Petro Sieberhagen and Ms. Lizelle le Roux for all their indispensable administrative assistance, and a perennial willingness to assist in matters big or small.
- Ms. Anne Mans for her valuable assistance on various occasions with the IBM RS/6000 Scalable POWER-parallel Systems (SP) computer.
- Mr. Matthew Holleran and Mr. Jaco Minnie for their aid with computer related problems and queries.
- The academic staff of the School of Physics, most of whom have been my lecturers at one time or another.
- Ms. Nanette Beneke for evaluating the grammar and spelling of this thesis.
- The Unit for Space Physics at the Potchefstroom Univeristy for CHE, the South African National Research Foundation and the Department of Labour of South Africa for financial support.
- The School of Physics for the use of their facilities.

A special thanks to :

- My parents, Ulrich and Marieke, for their love, support, encouragement, and countless prayers and who have made many sacrifices to allow me to be where I am today.
- My wife, Annette, for her love, support, encouragement, and endless faith in me and for sharing my dreams.
- My in-laws, for their love and support.

Soli Deo gloria!

Ulrich Langner

January, 2004